X-ray characterisation of multi-scale damage mechanisms in carbon-fibre-reinforced polymers at extreme thermomechanical conditions



Xiyao Sun
Lady Margaret Hall

A thesis submitted for the degree of
Doctor of Philosophy

Supervised by
Professor Daniel Eakins & Doctor David Chapman

Department of Engineering Science
University of Oxford

Michaelmas Term, 2025

Dedicated to all my family members in the past, present and future

Declaration

I declare that this thesis is entirely my own work and, except where stated, describes my own research.

Xiyao Sun
Lady Margaret Hall

Acknowledgements

This four-year DPhil at the University of Oxford has been a unique journey in my life - one that I could not have completed without the tremendous help and support I received along the way.

First, I would like to thank my supervisors, Prof. Daniel Eakins and Dr David Chapman, who provided me with the opportunity to pursue a DPhil study and degree at one of the best universities in the world. Their encouragement and support were essential for my success in this DPhil research. They consistently provided direction and guidance while leaving room for independence and curiosity. The research group they built and guarded is filled with warm and supportive air, which helped me navigate the early transition and continuously sustained my progress. In addition, I also wish to record my gratitude to the late Prof. Nik Petrinic, who, although not my listed supervisor, offered me generous advice and support across many aspects of my research.

I am deeply grateful to my senior colleagues in the lab - Dr Kai Liu, Dr David Sory, Dr Liam Smith, Dr Huifang Liu, Dr Yanhong Chen, Dr Ziwen Xu, Dr Maria Lißner, Dr Justus Hoffmann, Dr Lukasz Farbaniec, Dr Simone Falco, Dr Longhui Zhang, Dr Yuan Xu, Dr Guohua Zhao, and Dr Maureen Aceves Lopez - for their continuous help and support. They taught me theories, trained me in skills, supported me in experiments, reviewed my drafts, attended my presentation rehearsals, and shared their perspectives. They are “first responders” whenever problems arose and were essential accelerators of my research.

My sincere thanks also go to our lab management and support team, they are Dr David Townsend, Mr Graham Hillsdon (lab support), Mrs Karen Bamford (office manager), Mr Hisham Elamin (IT support), and, very importantly, the Department workshop team at Begbroke Science Park - Mr Stuart Carter, Mr Derek Robinson, Mr Peter Tantrum, and Mr Jeffrey Fullerton. Their help and assistance made possible the experiments, meetings, travel, and events over the past four years.

I am indebted to my collaborators at the European Synchrotron Radiation Facility - Dr Bratislav Lukić and Dr Alexander Rack - for enabling access to critical facilities and for their guidance in experiments and data analysis. Together, we established cutting-edge experimental methodologies that allowed novel damage inspection under extreme testing conditions.

Last but not least, my wonderful lab mates - Mr Xuefei Liang, Mr Jasper Threadingham, Mr David Simonian, Mr Kwan Wong, Mr Simranjeet Singh, Mr Edward Leggett, Dr Mila Fitzgerald, Dr David Wason, Dr Kin Chan, Dr Govind Gour, Dr Yue Chen, and Dr Indrajeet Sahu - who were my companions and fellow travellers along this road. We supported each other’s experiments, discussed each other’s challenges, joined each other’s presentations, attended conferences together, and visited tourist sites together. We studied and travelled, we ate, drank, laughed, and shared both successes and setbacks as a team. My DPhil study and life could not have been more fruitful and meaningful without their presence. Thank you for travelling alongside me.

Xiyao Sun
January, 2026
In Oxford, UK

Abstract

In the context of sustainable development, carbon-fibre-reinforced polymer (CFRP) is widely adopted across modern industries owing to its favourable balance of performance and cost. In civil aerospace applications, their high specific strength, tailorable anisotropy, corrosion resistance, design flexibility, and industrial maturity have led to more than 50% of the structural components in the latest generation of aircraft being manufactured from CFRP. During service, CFRP structures are subjected to complex mechanical loading and harsh environmental conditions, which pose significant challenges to structural integrity and safety design. In particular, during cruise, high-velocity impact events may occur at low ambient temperatures of approximately -50 °C. However, the damage mechanisms of CFRP laminates under such extreme combined loading and environmental conditions remain insufficiently characterised and understood.

Recent advances in synchrotron X-ray, including MHz phase-contrast imaging and high-resolution phase-contrast μ-CT scanning, enabled novel subsurface probing of damage in CFRP laminates *in situ*. Tracking the onset and development of internal damage in CFRP laminates under high-strain-rate loading became possible through carefully designed equipment and setups. Therefore, this thesis establishes a practical investigation protocol that involves experimental design and data analysis to, first, capture the internal damage development of CFRP laminates together with their mechanical response under high-strain-rate loading and low temperatures using synchrotron X-ray. Then, the retrieved damage and mechanical data are analysed integratively to elucidate their correlations and the governing physics. The primary objective is to enhance the understanding of damage mechanisms in CFRP laminates under high-strain-rate loading and extreme temperatures with direct experimental evidence.

This DPhil research was conducted in three stages, spanning damage observation and characterisation at the meso-, micro-, and micron-scale. The work reported in Chapter 3 and Paper I used synchrotron-based X-ray phase-contrast imaging (XPCI) to capture the initiation and evolution of meso-scale damage in CFRP laminates on sequential radiographies. The potential roots of damage, with respect to stress and strain concentrations, were proposed based on observation and analysis. Building on this framework, Chapter 4 and Pa-

per II combined interrupted high-rate loading with synchrotron-based X-ray phase-contrast μ-CT to investigate the micro-scale damage mechanisms of CFRP laminates, qualitatively and quantitatively resolving the initiation and growth at high strain-rate and low temperatures. It provided additional evidence at a smaller scale and in higher dimensions to understand mechanical responses, damage mechanisms, and their correlations on top of the previous chapter. Finally, Chapter 5 and Paper III targeted micron-scale damage and strain localisation using pre- and post-loading scanning, interrupted loading, and digital volume correlation (DVC). The achieved experimental and analysis results added unique insight by unravelling CFRP's local stress-strain states at the onset of different types of damage, further consolidating and enriching previous observations from a micro-mechanical point of view.

By integrating the results across multiple metrics, this thesis mapped the damage initiation and development of the tested CFRP laminates from the micron- to meso-scale, supported by qualified and quantified evidence. Local stress-strain states were associated with observed damage at the microscopic level to explain changes in global mechanical behaviour during loading. The developed investigation protocol and obtained datasets can be further used to facilitate the validation, calibration and development of composite failure criteria and damage models in numerical analysis. To promote continuous advancement in understanding complex composite damage under extreme conditions, future directions were outlined on the basis of the established methodology and findings at the end of the thesis.

List of publications

The following is a list of articles, book chapters, and patents that were published as a result of the research carried out for this thesis.

Articles

- Sun, X., Sory, D., Liu, K., Lukić, B., Simonian, D., Wong, K. L., Rack, A., Chapman, D., Petrinic, N., & Eakins, D. (2024). Effect of temperature on high strain-rate damage evolving in CFRP studied by synchrotron-based MHz X-ray phase contrast imaging. Composites Part B: Engineering, 279.

  https://doi.org/10.1016/j.compositesb.2024.111445

- Sun, X., Lukić, B., Liu, K., Sory, D., Lißner, M., Hoffmann, J., Chapman, D., Petrinic, N., & Eakins, D. (2026). Role of temperature in the development of micro-scale damage in CFRP laminates through interrupted high-rate loading and synchrotron phase-contrast μ-CT. Composites Part A: Applied Science and Manufacturing, 109284.

  https://doi.org/10.1016/j.compositesa.2025.109284

- Sun, X., Lukić, B., Chen, Y., Xu, Z., Chapman, D., & Eakins, D. (2026). “3D micro-mechanics of a CFRP laminate under high-rate and varying temperature loading using digital volume correlation,” Composites Part B: Engineering, 321.

  https://doi.org/10.1016/j.compositesb.2026.113693.

Table of contents

Table of contents xiii

List of figures xvi

List of tables xxv

Glossary xxvi

1 Introduction 1

1.1 Motivation 1

1.1.1 Composites development overview 1

1.1.2 Fibre-reinforced composites 3

1.1.3 Laminated fibre-reinforced composites 4

1.1.4 CFRP and its failure study 5

1.2 Problem statement and research objectives 7

1.3 Thesis structure 8

2 Literature review 11

2.1 CFRP ply design 11

2.2 Quasi-static behaviours of CFRP 13

2.2.1 Quasi-static property testing 13

2.2.2 Quasi-static damage probing 14

2.2.3 Challenges in CFRP testing 20

2.3 Dynamic behaviour of CFRP 22

2.3.1 Loading setups in dynamic testing 23

2.3.2 Mechanical properties in dynamic loading 23

2.3.3 Damage characterisation in dynamic loading 26

2.4 Moisture and temperature effects 34

2.4.1 *In-situ* temperature 34

2.4.2 Environmental cycling 36

2.5 Concluding remarks 38

3 CFRP's damage at meso-scale 40

3.1 Background and motivations 40

3.1.1 Challenges of CFRP's anisotropy 40

3.1.2 Challenges of high-strain-rate damage probing 41

3.1.3 Challenges of temperature control 42

3.1.4 Objectives of the chapter 42

3.2 Summary of Paper I 43

3.2.1 Material and specimen 43

3.2.2 Methodology 44

3.2.3 Research findings 47

3.3 Chapter remarks 52

3.4 Paper I: Effect of temperature on high strain-rate damage evolving in carbon-fibre-reinforced polymer (CFRP) studied by synchrotron-based MHz X-ray phase contrast imaging 52

4 CFRP's damage at micro-scale 65

4.1 Background and motivation 65

4.1.1 Limitation in in-plane spatial resolution 65

4.1.2 Limitation in the out-of-plane spatial resolution 66

4.1.3 Objectives of the chapter 67

4.2 Summary of Paper II 67

4.2.1 Material and specimen 68

4.2.2 Methodology 68

4.2.3 Research findings 74

4.3 Chapter remarks 82

4.4 Paper II: Role of temperature in the development of micro-scale damage in CFRP laminates through interrupted high-rate loading and synchrotron phase-contrast μ-CT 82

5 CFRP's damage at micron-scale 97

5.1 Background and motivation 97

5.1.1 Micron-scale damage characterisation 98

5.1.2 Micro-mechanics measurement and analysis 98

5.1.3 Objectives of the chapter 99
5.2 Summary of Paper III 101
5.2.1 Material and specimen 101
5.2.2 Methodology 101
5.2.3 Research findings 108
5.3 Chapter remarks 113
5.4 Paper III: 3D micro-mechanics of a CFRP laminate under high-rate and varying temperature loading using digital volume correlation 114

6 Conclusion and outlook **132**
6.1 Research aim, scope, and challenges 132
6.2 Methodological contributions and new capabilities 133
6.3 Integrated multi-scale mechanistic conclusions 134
6.4 Limitations 136
6.5 Future work 137
6.6 Concluding remarks 138

Bibliography **139**

List of figures

1.1 Advanced composites used in the Boeing 787 Dreamliner. More than 50% of the body is made of carbon fibre composites [3]. 1

1.2 Newly developed Ultra-fan system by Rolls-Royce plc (currently on testing) using composites as the fan blade material [5]. 2

1.3 Composition of laminated composites. (a) CFRP laminates manufactured by laying up unidirectional prepreg [38]. (b) Laying up undirectional prepreg in different directions [39]. 4

1.4 Examples of brittle failure of CFRP composites. (a) Visible examination of the brittle failure morphology [50]. (b) Typical mechanical responses of CFRP and glass-fibre-reinforced polymers (GFRP) compared to those of steel [51]. 5

1.5 Damage to civil aeroplanes after encountering foreign object impacts in service poses a direct and critical threat to the aeroplanes' safety [52, 53, 54]. 6

1.6 Research and reporting structures of the technical contents in this Doctor of Philosophy (DPhil) and thesis. 9

2.1 Different types of continuous CFRP laminates based on the ply layup methods [56, 57, 58]. 11

2.2 (a) Chopped fibre composites [59]. (b) CFRP sandwich laminates [60]. (c) Hybrid composite laminates made of polyimide fibre laminates and CFRP laminates [62]. 12

2.3 Comparison of the specific stiffness and strength between unidirectionaly (UD) CFRP and other engineering materials [70]. 14

2.4 Failure mechanism of UD CFRP. (a) UD CFRP specimens after tensile tests [72]. (b) Micro-scale damage morphology of tensile failure inside the UD CFRP specimens [72]. (c) Sketch of the micro-mechanism of tensile failure for UD CFRP [73]. 15

2.5 Fibre breakage in UD CFRP specimens under tensile loading [77]. 15

2.6 scanning electron microscope (SEM) examination of the fibres in a UD CFRP specimen under tension [72]. (a) Fibre fracture line can be inclined to the loading direction in the apparently undamaged area. (b) Fibres in the UD CFRP laminates with low volume fracture fail as bundles. 16

2.7 X-ray images of UD CFRP damaged in compression obtained using micro-computed tomography (μ-CT) : (a) 3D volume rendering of the damage zone. (b) A XZ cross-section slice in the damage zone with explanations of fibre failure mechanisms. In the figure, kinking band width, boundary angle and fibre rotation angle are shown in white, red and yellow, respectively [78]. 17

2.8 Two subsequent frames from the images taken by the *in-situ* SEM. (a) The frame right before the kinking band started to propagate. (b) Kinking band formed [81]. 18

2.9 Micro-scale damage characterisation of UD GFRP using *in-situ* CT. (a) Schematic of GFRP specimen geometry for *in-situ* compression and X-ray computed tomography (CT) scanning. (b) Photography illustrating the compression test rig accommodated at the Swiss Light Source (SLS). (c) X-ray CT slices of the UD GFRP specimen acquired at three load steps while loading in compression: before loading (0% failure load), just before failure (99.9% failure load) and after failure (Failed) [84]. 19

2.10 Tracking fibre movement on xz and yz planes based on *in-situ* CT image as a function of loading steps. (a) Trajectories of fibre clusters. (b) Displacement of fibre clusters with the original fibre position normalised as 0. It can be seen that all the displayed fibre clusters displaced toward the positive x direction. The fibre displacement was much more obvious on the xz plane [84]. 20

2.11 Variation in the loading methods and results of the CFRP's mechanical testing. Different loading configuration in tensile tests according to (a) American Society for Testing and Materials (ASTM) D3039 for 0 ° UD CFRP, (b) ASTM D3039 for 90 ° UD CFRP, and (c) International Standardisation Organisation (ISO) 527 for 0 ° UD CFRP [88]. (d) Compressive testing results of the same group of CFRP laminates obtained from seven different laboratories [75]. Different symbols (e.g., ○ and □) represent different laboratories. 21

2.12 Stress-strain curves of UD CFRP laminates under tensile loading at different strain rates, demonstrating a clear strain rate sensitivity. The mechanical properties of the tested specimens were enhanced by increasing the strain rate [128]. 24

2.13 Stress-strain curves of CFRP laminates in compressive tests with different strain rates. (a) quasi-isotropic (QI) CFRP laminates [129]. (b) UD CFRP laminates [130]. Both indicate that raising strain rates can increase the strength of CFRP specimens. 25

2.14 Damage in woven CFRP caused by ballistic impact showing a comparison between experimental results (from ultrasonic C-scan) and model predictions [140]. 27

2.15 Micro-scale damage of woven CFRP under axial and off-axial loading characterised using CT. Damage morphology and volume changes between the specimens with different off-axial angles (0, 60, and 90 °) are presented and highlighted in red [143]. 28

2.16 Experimental method of the high-strain-rate tension on UD CFRP specimens conducted at Beamline 32-ID-B, the Advanced Photon Source (APS). (a) Schematics of the high-strain-rate loading and X-ray phase-contrast imaging (XPCI) systems setup [150]. (b) Camera triggering time and voltage waves recorded by the strain gauge and the load cell [149]. 29

2.17 Results of the high-strain-rate tension on UD CFRP specimens with 0.3 mm diameter void [149]. (a) Stress-strain curve measured using the strain gauge and load cell. (b) Specimen and loading geometry. (c) Captured X-ray phase-contrast images at the representative time steps labelled on the stress-strain curve. 30

2.18 Setups of dynamic X-ray phase-contrast imaging at the ID19, the European Synchrotron Radiation Facility (ESRF) [151]. 31

2.19 Sequential radiographic images showing failure mechanisms of a Ti-6A1-4V specimen under high-strain-rate loading with split Hopkinson pressure bars (SHPB). (A) damage initiation at $t = 74.1$ µs and damage progression $t = 86.5$ µs [151]. 32

2.20 Stress-strain curves of 90° UD CFRP 20 and -60 °C with a loading strain rate of 890 s^{-1} recovered from the strain gauge signal obtained using SHPB [166]. 35

2.21 SEM images on the tensile failure of 90° UD CFRP specimens at (a) room temperature, (b) 173 K and (c) 77 K [169]. 36

2.22 Cycling effects on CFRP laminates. The comparison of internal defects between cycled and uncycled CFRP specimens: (a) UD, (b) QI CFRP volume rendering, and (c) defect volume fractions. Mechanical performance changes due to thermal cycling: (d) 0 ° UD tension, (e) QI tension, (f) unidirectional-0 flexural and (g) quasi-isotropic flexural [169]. 37

3.1 CFRP specimens used in this research showing their geometry, dimensions, and ply stacking sequence of $[\pm 45]_{4s}$. The symmetry axis is indicated between the two plies in the middle with $+45$ ° fibre direction (FD). 43

3.2 SHPB loading setups at beamline ID19, ESRF. The loading is perpendicular to the X-ray propagation direction. 45

3.3 Temperature control system and its main components. (a) Gas flow pipeline panel used to condition and deliver the heating and cooling gases. (b) proportional–integral–derivative (PID) controllers for automatic temperature adjustment and maintenance. (c) Double-layer loading/environmental chamber, which has an inner chamber and an outer chamber. Windows on both sides of the chamber allow nearly non-obstructive transmission of X-rays. The development of this temperature-control system was led by Dr David Sory. 46

3.4 Dynamic X-ray imaging setup at synchrotron beamline. (a) Photo of the setup at the beamline ID19, the ESRF. (b) Schematic demonstrating the positions of the X-ray source, SHPB, X-ray beam, lens and cameras. 47

3.5 Stress-strain curves of the specimens in dry and hygrothermal cycled conditions under quasi-static compression obtained by using a universal loading machine. 48

3.6 Stress-strain curves of the specimens under high-strain-rate compression tested on the SHPB loading platform: (a) dry specimens, and (b) hygrothermal cycled specimens. 48

3.7 *In-situ* damage probing of the specimens using XPCI at the synchrotron facility. (a) Stress-time plot of the specimens as a reference for damage development characterisation using X-ray images. (b) Representative X-ray radiographies of a specimen at room temperature. (c) Representative X-ray radiographies of a specimen at low temperature. Damage initiated earlier and evolves more rapidly at low temperature. Evident stress drops can be found after the observable damage in XPCI images. Ply delamination also initiated earlier at low temperatures. 49

3.8 Tracking damage orientations based on the *in-situ* XPCI images: (a) specimen at room temperature and (b) specimen at the low temperature. The initiated intra-ply cracks rotated with the angle change of fibres in the plies. Intra-ply cracks at both $+45$ and $-45\,^{\circ}$ fibre direction can be found in the low-temperature specimen, whereas the intra-ply cracks in the room-temperature specimen are mainly in $-45\,^{\circ}$ fibre direction. 50

3.9 Schematic showing the mechanisms of damage initiation and evolution in tested CFRP laminates with ply breakdowns. (a) Micro-scale damage that is difficult to detect under the current XPCI setup. (b) Micro-cracks coalesce and broaden, forming detectable cracks in surface plies. (c) As compression continues, detectable cracks emerge in subsurface plies and in both fibre directions. (d) Detectable cracks grow and cause breakage of the surface plies and ply delamination. 51

4.1 Comparison between the size of XPCI pixels and carbon fibres. The initiated matrix cracking might be smaller than the fibres, taking into consideration the epoxy's brittle behaviour. The resolution of XPCI is not sufficient for visualising damage at the micro-scale. 66

4.2 Superposition effects in XPCI 2D projects. (a) An example XPCI frame demonstrates the damage in both $+45$ and -45° plies. (b) Schematic illustrates the ply layup of the specimen along depth (X-ray propagation direction). 67

4.3 Strain interruption setups implemented on the SHPB loading system. (a) A collar is installed near the interface between the incident bar and specimen. (b) A gap is created between the end of the incident bar and the collar face to allow the desired specimen deformation. (c) Detailed dimensions of the strain control collars. 70

4.4 An example of a synchrotron CT setup. The produced X-ray beam is emitted from the storage ring and propagates through the specimens sitting on a rotation platform. The specimens will be rotated for 360° to allow the detector to capture X-ray radiation with specimens at different angles for the three-dimensional (3D) volume reconstruction [161]. 71

4.5 Configuration of lighting and imaging systems in the impact loading region on the SHPB platform. The camera is placed perpendicular to the loading direction, facing toward the specimens. Two flashlights were adopted, producing both front light reflection and backflash. Both the flashlights and the camera were triggered by the strain gauges on the incident bar with a set delay using delay generators. A control laptop was connected to the camera for adjusting camera parameters and recording the captured images during loading. 72

4.6 Example of captured images using the high-speed camera. Before the loading arrived at the bar/specimen interface, a clear gap can be seen between the input bar and the collar face. This gap allows the specimen to deform freely. At the interruption strain, the bar end and the collar came into contact, which stopped the load transfer to the specimen and hence interrupted the specimen deformation. The ends of the bars were painted with a white background and black speckles for tracking the displacement of the bars and the engineering strain of the specimens. 73

4.7 Evaluation of the specimen strain through image-based digital image correlation (DIC) measurement and strain-gauge-based wave measurement. (a) Image of the loading region before the impact arrived. (b) Image of the loading region at the interruption strain of the specimen. (c) The bar end displacement and distance tracking. The strain converted from the distance tracking for (d) the room-temperature specimens and (e) the low-temperature specimens. The stress-strain plots estimated from the wave measurement of the bars using strain gauges for (f) the room-temperature specimens and (g) the low-temperature specimens. Stable strains are shown after a rapid rise in the engineering strain-time measurements, indicating a successful interruption of the specimen strains. The sudden rises in the engineering stress-strain plot represent the same from a different measurement technique. Good agreement is seen between the two types of measurement. 77

4.8 Macroscopic dimension change in the bulk specimens measured after the tests. (a) Specimen geometry, including dimension labels and ply layup. The permanent dimension change occurs after the loading for (b) the room-temperature specimens and (c) the low-temperature specimens. No width change can be seen at the room temperature until RM4, whereas evident expansion in width occurred starting from the specimen with the lowest interruption strain (i.e., CL1). 78

4.9 Micro-scale damage initiation and evolution in the specimens at (a) room and (b) low temperatures. The observed damage was categorised in six classes. The damage initiates and evolves more rapidly at low temperatures. Similar damage mechanisms can be seen at the early damage stages between the room and low temperature specimens, while different ones are shown at the late damage stages. 79

4.10 Volume statistics of the opened damage and their developments with the strain increases in the room and low temperature specimens. The volume increase of damage is more rapid in the low-temperature specimens. The damage in CL5 is significantly larger owing to the surface ply detachment on both sides of the specimens. 80

4.11 Opened damage in specimens with large interruption strain - RM4, RM5 and CL5 - visualised in 3D space. (a, c and e) are presented with solid specimen bodies to reveal the surface damage morphology and distribution, whereas those in (b, d and f) were made transparent to show the internal damage propagation. At a similar strain level, evidently larger damage can be seen in the low-temperature specimens. Prominent ply delamination at the low temperature seems to be the cause of the ply detachment in the surface plies. Discrete damage can be found in CL5, while the damage in RM5 demonstrates an interconnected pattern, forming obvious damage bands. 81

5.1 Comparison between the opened and closed cracks in a single X-ray radiography. Void regions can be seen inside the opened cracks, whereas the edges on both sides of the closed cracks have come back in contact after removing the load. 99

5.2 Difficulties of segmenting closed cracks with conventional thresholding methods. (a) The original tomography slice with both closed and opened cracks. (b) Segmenting the slice with a thresholding range from 0 to 18761. (c) Segmenting the slice with a thresholding range from 0 to 31611. Closed cracks cannot be accurately differentiated from the background material owing to the similar intensity between the closed cracks and the matrix. 100

5.3 Data acquisition, image processing, strain computation, and damage analysis flowchart in three stages: image pre-processing (including image acquisition strategy), image registrations, and image post-processing. 102

5.4 Internal microstructures of the tested CFRP specimens in the cross-sectional direction perpendicular to the loading. A clear textured structure can be seen created by the impregnation of the carbon fibres in the epoxy matrix. 103

5.5 Change of recoverability of polymers at elevated temperatures. J_r (solid lines with circle markers) is the recoverable shear compliance of the polymer material. Dashed lines represent the total creep compliance, J. It can be seen that at high temperatures, J_r and J have obvious differences even at early loading stages, indicating a poor recoverability [176]. 104

5.6 Comparison between pre- and post-scan slices in roughly the same location in a specimen. (a) Pre-scan: CT scan performed before loading. (b) Post-scan: CT scan performed after loading. (c) Grey value distribution for pre- and post-scan slices. Although the same scanning parameters were implemented, differences in the resulting images can still be seen. 105

5.7 An example demonstrating the effectiveness of image pre-processing. (a) Pre-processed pre-scan image. (b) Pre-processed post-scan image. (c) The grey value distribution of the pre-scan image after normalisation. (d) The grey value distribution of the post-scan image. The pre-processed images are in a much more comparable state compared to those in Fig.5.6. 107

5.8 Development of local displacement vectors for the specimens at (a) room and (b) low temperatures. The local displacement and its development show clear directional features regardless of temperatures and loading stages in the tested CFRP laminates. Local displacement evolves more rapidly at low temperatures. Degrees noted are the fibre directions instead of the absolute directions. 109

5.9 Distribution and development of (a) the micron-scale damage, (b) the deviatoric strain, and (c) the volumetric strain in low temperature specimens. The locations of the intra-ply cracks coincide with the shear strain localisation. At the locations of inter-ply delamination, prominent volumetric strain can be seen. 111

5.10 Deviatoric and volumetric strain distribution of a 2D slice in CL3, with the location and the fibre direction of the slice demonstrated on the top. Both deviatoric and volumetric strain bands are visualised along the fibre direction of the current ply. In addition, a shear localisation band can also be seen perpendicular to the fibre direction of the current ply but along the fibre direction of the neighbouring plies, which is caused by the inter-ply shear transfer effect. 113

List of tables

4.1 Specimen details and testing conditions. All specimens were dynamically compressed along the plane of the laminates at an approximate strain-rate of 2500 s^{-1}. The specimens that were loaded without strain interruption were labelled as “IF”, while the specimens loaded with strain interruption at room and low temperatures were labelled as “RM” and “CL”, respectively. 69

Glossary

2D	Two-dimensional
3D	Three-dimensional
AP	Angle-ply
APS	Advanced Photon Source
ASTM	American Society for Testing and Materials
BS	British Standard
CFRP	Carbon-fibre-reinforced polymer
CP	Cross-ply
CT	Computed tomography
DIC	Digital image correlation
DIHPB	Direct-impact Hopkinson pressure bar
DPhil	Doctor of Philosophy
DVC	Digital volume correlation
EN	European Standard
ESRF	European Synchrotron Radiation Facility
FD	Fibre direction
FDK	Feldkamp-Davis-Kress
FEA	Finite element analysis beam melting
FIB	Focused ion beam
FoV	Field of view
FPS	Frames per second
GFRP	Glass-fibre-reinforced polymers
He	Helium gas
ISO	International Standardisation Organisation

LN2 Liquid nitrogen

mSHPB Miniature split-Hopkinson pressure bar

N2 Nitrogen gas

ORNL Oak Ridge National Laboratory

PID Proportional–integral–derivative

QI Quasi-isotropic

RoI Region of interest

RVEs Representative volume elements

SEM Scanning electron microscope

SHPB Split Hopkinson pressure bars

SLS Swiss Light Source

UD Unidirectional

XPCI X-ray phase-contrast imaging

µ-CT Micro-computed tomography

Chapter 1

Introduction

1.1 Motivation

1.1.1 Composites development overview

Global energy and environmental concerns have put greater demands on engineering design and manufacturing in the modern transportation industry. The introduction of lightweight materials is deemed to be a straightforward and efficient answer to the challenge of sustainable development, as weight reduction can lead to lower fuel consumption. Engineers and researchers in the transportation industry started to explore building transportation vehicles such as automobiles and boats with composites after the Second World War due to their high strength-to-weight ratio and high radio frequency transparency [1].

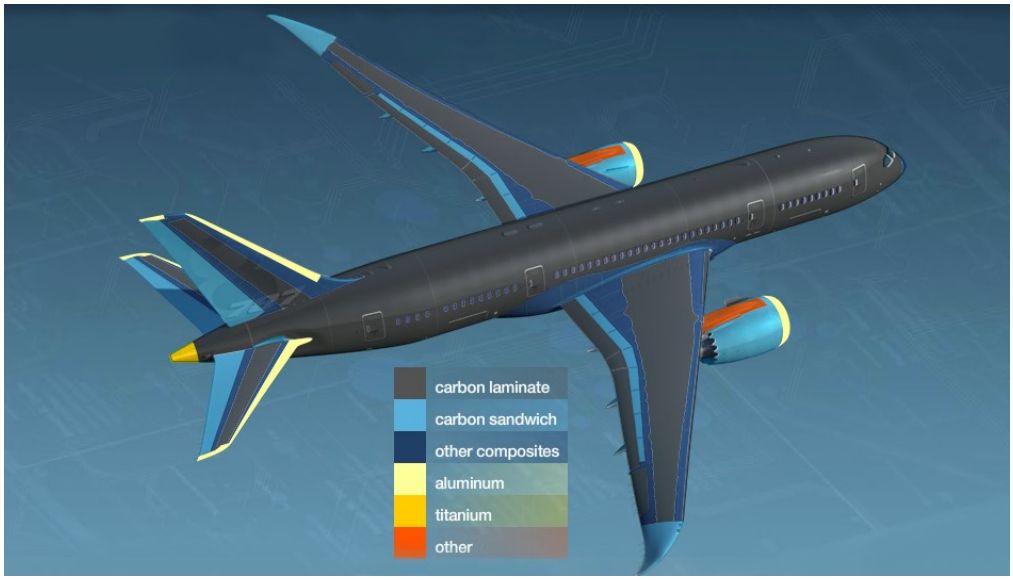


Figure 1.1: Advanced composites used in the Boeing 787 Dreamliner. More than 50% of the body is made of carbon fibre composites [3].

After entering the 21st century, to respond to pervasive concerns of environmental

damage and associated global environmental policies such as climate protection and sustainable energy development, the transportation industry has invested heavily in composite research and application, and significant progress has been made accordingly. Nearly half of the airframe of the newly developed aeroplane model Boeing 787 Dreamliner is made of carbon-fibre-reinforced polymer (CFRP) and other advanced composites (please see Fig.1.1), which has led to a weight savings of about 20% on average [2, 3]. Similarly, the Airbus A350 incorporates approximately 53% CFRP in its primary structures, contributing to considerable reductions in fuel consumption. These lightweight composites drive down aircraft mass, which directly translates into lower fuel burn and emissions [4]. Not only in aeroplane structures, the latest aero-engine products, such as the Ultra-fan system (Rolls-Royce plc) and GE-9X engine (General Electric Company), all intensively incorporate composites in their design for a high energy efficiency Fig.1.2 [5]. Furthermore, research from Oak Ridge National Laboratory (ORNL) indicates that up to 60% of an automobile's weight can be reduced by replacing metal components with composites, significantly improving fuel efficiency [6]. In the rail sector, high-performance composite materials, such as CFRP and glass-fibre-reinforced polymers (GFRP), are being tested in critical structural components such as bogie frames and roof-mounted pantograph platforms [7, 8]. Experimental prototypes exhibit not only substantial weight savings but also meet the demanding fatigue and performance requirements of rail operations [9].

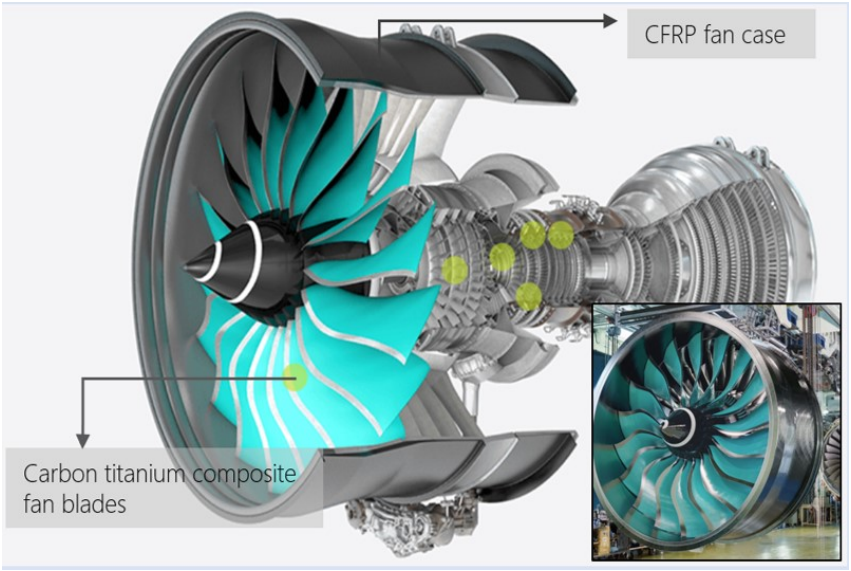


Figure 1.2: Newly developed Ultra-fan system by Rolls-Royce plc (currently on testing) using composites as the fan blade material [5].

Beyond the sectors mentioned above, composite materials are widely used in other transportation modes such as boats and bicycles [10, 11, 12], in military applications like firearms and missiles [13, 14, 15], in aerospace systems including satellites, launch vehicles, and exploration rovers [16, 17, 18], as well as in modern infrastructure such as bridges and wind turbines [19, 20, 21]. Among these, high-speed vehicles — particularly aerospace craft — are constantly exposed to the threat of high-strain-rate loading at extreme temperatures in service [22, 23, 24, 25, 26]. Unlike quasi-static loading scenarios, damage modes in high-strain-rate loading events can evolve rapidly and interact non-linearly, significantly affecting the load-bearing capacity and residual strength of the composite structure [27].

However, the behaviour of composites under such complex conditions is still not fully understood. Traditional continuum models often fail to capture such convoluted and time-sensitive damage mechanisms, prompting the development of advanced experimental techniques and a vast characterisation of high-rate damage at multi-scale. This inadequate understanding and lack of accurate simulation models pose major challenges to the broader and more advanced application of composites in future industrial systems.

1.1.2 Fibre-reinforced composites

The idea of reinforcing a material with fibres can be traced back thousands of years, when the indigenous people used straws and animal hair to reinforce their clay structures, representing early forms of composite materials. This rudimentary fibre–matrix composite effectively improved the toughness and dimensional stability of clay-based materials, reducing shrinkage, deformation and cracking during drying, firing and long-term use [28]. In the 20th century, the rapid development and successful commercialisation of glass fibres largely promoted the use of GFRP in a wide range of applications, including aircraft, automobiles and boats [29]. Later in the 1960s, the development of a fibrous material with higher stiffness and strength - the carbon fibres - brought along CFRP, which is now one of the most widely used structural composites in the modern industry [30].

The reason that fibrous materials can effectively enhance the strength of matrix materials is that, for many materials, their material strength is much higher in fibre form compared to their bulk form [31]. Instead of being randomly oriented in bulk form, polymer chains in fibrous polymers or grain structures in carbon fibres are highly aligned along one direction, producing significant tensile resistance in that direction [32, 33]. However, fibrous materi-

als are normally very poor at providing longitudinal compressive and transverse resistance without binding together in practice. Thus, binder or matrix materials are applied and form a combination with fibrous material to produce optimised mechanical properties in the application [34]. By orienting fibres at various angles inside the matrix materials, the composites can be designed to resist stresses in different directions [35]. In addition, the matrices can also prevent fibre from being damaged by external factors such as weathering and impacts [36].

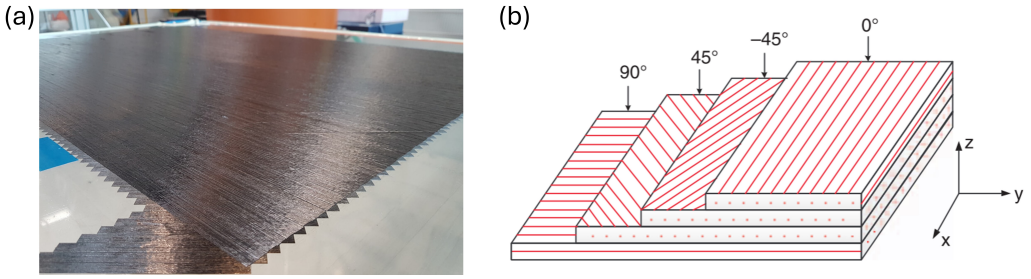


Figure 1.3: Composition of laminated composites. (a) CFRP laminates manufactured by laying up unidirectional prepreg [38]. (b) Laying up undirectional prepreg in different directions [39].

1.1.3 Laminated fibre-reinforced composites

The laminated-form composites also emerged around the mid-20th century, with the early production of carbon and glass fibres. This laminated layup method allows engineers to tailor the mechanical properties and damage mechanisms of CFRP composites in different application scenarios. This flexibility effectively improves the anisotropy of fibre-reinforced composites and thus gains traction in aerospace, automotive and marine industries. Fibre-reinforced composites exhibit advantages in multiple aspects in laminated forms [37]. By laying up the CFRP or GFRP prepreg (a thin CFRP sheet consists of unidirectional fibres and matrix shown in 1.3a [38]) in different directions, such as $0\,°$, $\pm 45\,°$, and $90\,°$ (1.3b [39]), the composited laminates can have high stiffness and strength in multiple directions and in different loading scenarios (e.g., compression, tension and shear) [40]. Through the layup process, the produced laminates can be moulded in complex geometries with relatively low costs for different applications, for example, the aircraft fuselages and wings, and automotive body panels and chassis. Therefore, it is still the mainstream of the manufacturing process of the CFRP composites in the present industry [41].

1.1.4 CFRP and its failure study

Carbon is an extensively investigated element in the science community owing to its excellent ability to establish various bonds [42]. In the 1970s, scientists and engineers started to use carbon as the reinforcement in composites by structuring the bonded carbon atom in one dimension to form an ultrahigh-strength fibre [43, 44]. The remarkable properties exhibited by polymers reinforced by carbon fibres make this artificial material one of the primary composite materials that is widely used in the present aerospace industry [45]. Commercial CFRP materials can easily have a tensile strength that is $6 - 10$ times stronger than mild steel, with approximately one-fifth of the weight. Although the cost of CFRP is one of the main hindrances to its wider application in other industrial sectors, this shortcoming is not that prominent in aerospace manufacturing if it can save a substantial amount of energy consumption in the product's service life.

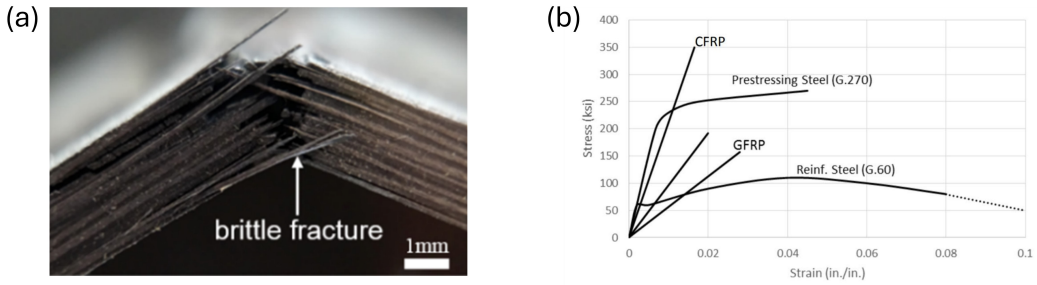


Figure 1.4: Examples of brittle failure of CFRP composites. (a) Visible examination of the brittle failure morphology [50]. (b) Typical mechanical responses of CFRP and GFRP compared to those of steel [51].

However, another main challenge of using CFRP is their brittle behaviour compared to metallic materials [46]. A number of previous experiments demonstrate that CFRP materials exhibit high strength and stiffness before reaching their pseudo-yield point [47, 48, 49]. Upon pseudo-yielding, a sharp drop in stress can normally be discovered without obvious strain hardening processes, especially for unidirectional CFRP, as shown in Fig.1.4 (a and b) [50, 51]. Hence, the failure of CFRP materials could be sudden and catastrophic without sufficient warning. Nevertheless, various CFRP applications, such as in automotive and aerospace, might frequently face threats from unexpected situations in service due to their complex and uncontrolled working environment. Consequently, studying the failure mechanisms and proposing subsequent failure prediction and mitigation are crucial subjects for the application of CFRP materials in transportation and other relevant industries.



Figure 1.5: Damage to civil aeroplanes after encountering foreign object impacts in service poses a direct and critical threat to the aeroplanes' safety [52, 53, 54].

The dynamic failure mechanisms of CFRP under high-strain-rate loadings are a subtopic of failure that needs considerable attention owing to the fact that foreign body and detached part impact on aerospace vehicles might result in disastrous losses in life and assets (Fig.1.5) [52, 53, 54]. A detached CFRP aero-engine fan blade impacting the casing at high velocity can generate strong in-plane compression in the fan structure. Although foreign object impact is often initially associated with localised, through-thickness loading normal to the laminate surface, the structural response of thin-walled composite components can rapidly evolve into complex in-plane stress states due to stress wave propagation and geometric constraints. For instance, foreign body impact on a barrel-shaped aero-engine casing can lead to circumferential propagation of compressive waves, resulting in in-plane compressive stresses along the laminate.

In-plane compression is known to be a relatively weak deformation mode in CFRP laminates, as it can promote inter-ply delamination and matrix-dominated failure. Therefore, understanding this loading condition is important for industrial design and failure prediction under impact scenarios. In this study, ± 45 ° laminates are adopted because they provide a well-established means of characterising the in-plane shear response of composite materials under uniaxial loading, following the American Society for Testing and Materials (ASTM) D3518/D3518M standard [55]. Through coordinate transformation, the applied uniaxial compressive load can be related to an effective in-plane shear stress state, enabling the investigation of shear-dominated failure mechanisms while avoiding fibre-dominated responses associated with loading along principal material directions.

Furthermore, harsh service environments, such as extreme temperatures caused by the weather, altitude and engine heat, could complicate the CFRP's high-strain-rate failure mechanism even more. Extensive research in this area is demanded by the industry to

ensure a safe and efficient CFRP application in the present and future. Promisingly, the recent advancement in synchrotron-based X-ray imaging provides an excellent opportunity to probe the multi-scale subsurface failure initiation and progression *in-situ*. The observed phenomena are expected to fill the gap in understanding the failure evolution in CFRP materials under high-strain-rate loading and extreme temperatures.

1.2 Problem statement and research objectives

Research on *in-situ* damage mechanisms in CFRP laminates, particularly those with $\pm$ 45 ° layups, under extreme loading and temperature conditions remains limited due to the complexity and constraints of specimen loading and measurement technologies. Therefore, the aim of this Doctor of Philosophy (DPhil) research is to establish a time-resolved experimental framework using synchrotron X-ray imaging for the multi-scale characterisation of damage mechanisms in CFRP laminates under coupled high-strain-rate loading and temperature effects, thereby advancing the understanding of these mechanisms and their relationship to mechanical response. The scope of this thesis is limited to the experimental investigation of damage mechanisms in $\pm$ 45 ° CFRP laminates under extreme loading conditions. While the results provide insight into damage evolution and its relationship to mechanical response, this work does not attempt to establish generalised predictive models and focuses on mechanistic understanding at this stage. The aim is addressed through the following objectives:

• To characterise the internal microstructure of the CFRP laminates to provide a structural basis for interpreting damage initiation and evolution.

• To quantify the global mechanical response of the laminates across a range of loading rates and temperatures, establishing the macroscopic behaviour under coupled thermomechanical conditions.

• To develop and implement bespoke experimental setups integrating synchrotron X-ray imaging for time-resolved and multi-scale observation of damage processes under high-strain-rate loading and varying temperatures.

• To establish robust analysis methodologies for processing synchrotron X-ray data and quantifying subsurface damage mechanisms in relation to the measured mechanical response.

• To elucidate the relationship between multi-scale damage mechanisms and the corresponding global and local mechanical responses under extreme conditions.

For future extension of this work, the achieved outcomes can be used to promote numerical model validation and improve shear property characterisation of CFRP laminates under combined high-strain-rate loading and extreme temperature conditions.

1.3 Thesis structure

This DPhil thesis contains six main chapters. The scientific research flow of the present DPhil work is demonstrated in Fig.1.6, and thus the same is the case in the technical chapters (Chapters 3 – 5) of the present thesis.

In this thesis, the terms meso-, micro-, and micron-scale damage are used to distinguish different levels of damage characterisation. As these terms are not universally standardised, they are explicitly defined here in the context of the present work. Meso-scale damage refers to damage at the ply or sub-laminate level, where the composite architecture (e.g., plies and their interfaces) is explicitly involved. This includes large intra-ply cracking and inter-ply delamination that are typically observable at length scales on the order of approximately 0.5 to 5 mm. Micro-scale damage corresponds to the constituent level, where individual fibres, matrix, and their interfaces can be distinguished. Damage that can be quantitatively characterised at this scale is typically above approximately 50 μm, including matrix cracks with a clear void region within the crack contour. In addition, the term micron-scale damage is used in this thesis to refer specifically to very fine cracks with characteristic dimensions on the order of a few micrometres (typically 2 - 10 μm). These cracks may close or become difficult to detect upon unloading and, therefore, require a bespoke imaging and analysis pipeline to quantitatively extract and analyse. This term is introduced as a subcategory of micro-scale damage for clarity in describing experimentally observed features. It should be noted that, although each chapter primarily focuses on a specific length scale, interactions across different scales may be discussed where necessary to provide a comprehensive understanding of the damage mechanisms.

The present thesis begins with an introduction section. The definition, application and development of CFRP laminates are briefly reviewed, which also unfolds the motivation to characterise the multi-scale damage mechanisms of CFRP laminates at high-strain-rate and extreme temperatures.

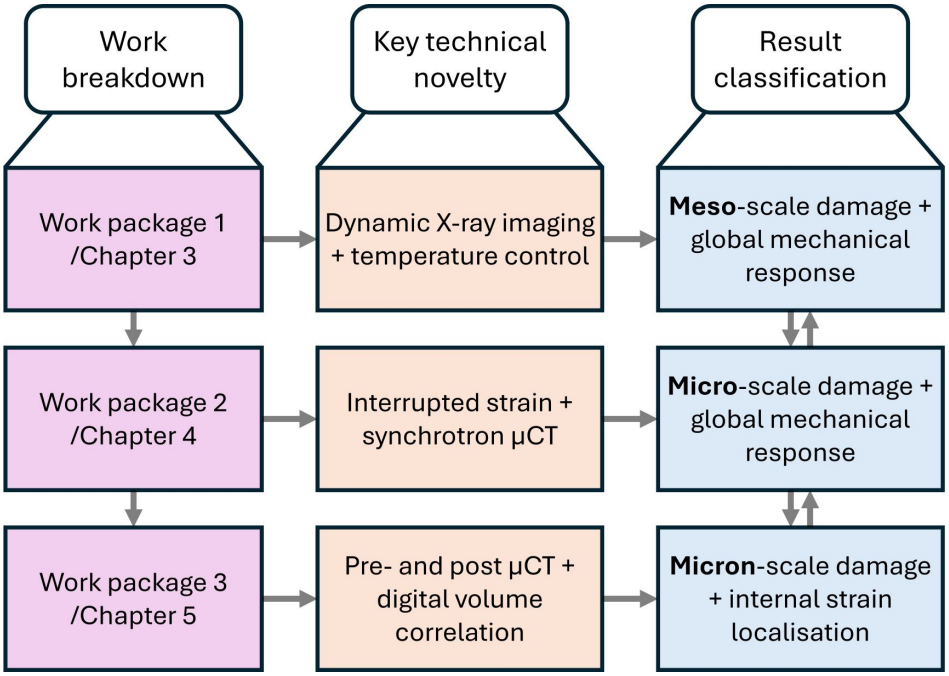


Figure 1.6: Research and reporting structures of the technical contents in this DPhil and thesis.

Then, a comprehensive review of existing research in relevant areas has been summarised, covering the preparation, testing, property measurement and damage probing of CFRP laminates under different strain rates (e.g., quasi-static and high strain rate) and environmental conditions (e.g., hygrothermal cycling and *in-situ* temperatures).

Next, Chapter 3 focuses on the mechanical behaviour and damage mechanisms of the studied CFRP laminates at the meso-scale level under high-strain-rate loading and low temperatures. The experimental realisation is mainly through a combination of a traditional high-rate loading system, a bespoke temperature control and recording system, and a synchrotron-based dynamic X-ray imaging system. The interactive analysis between the measured mechanical responses and the observed internal structural changes reveals the damage mechanisms of the tested CFRP with respect to time and global strain under high-strain-rate loading and low temperatures.

Chapter 4 addresses the limitations of the two-dimensional (2D) and three-dimensional (3D) resolution (planar and through-thickness space, respectively) in dynamic X-ray imaging by incorporating the interrupted strain technique and high-resolution synchrotron-based computed tomography (CT). The results of this work package characterise the relationship between global mechanical behaviour and damage development of the studied CFRP lam-

inates at the micro-scale level under similar testing conditions.

Chapter 5 describes the content in work package 3, which extends the investigation of damage mechanisms further into a finer scale. By performing synchrotron-based phase-contrast CT before and after high-strain-rate loading and implementing advanced digital volume correlation (DVC) analysis, fine cracks at early loading stages in a width around $2-4$ µm are extracted and quantified, which, in association with the computed strain localisation, elucidate the damage nucleation and development mechanisms under complex and extreme loading conditions.

Finally, a concluding chapter is presented, summarising the results and contributions of this DPhil research, together with further perspectives and outlooks that prompt the continuous development in the investigation of composite damage mechanisms under extreme loading conditions.

Chapter 2

Literature review

2.1 CFRP ply design

Carbon fibres often have inert structures and nonpolar surface areas owing to their highly crystallised graphite basal planes [42]. Consequently, interfacial adhesion is often considered a limitation of carbon fibres when used as reinforcement in composites. The overall mechanical properties of CFRP can be significantly influenced by the properties of the fibres, matrix, and their interaction. Thus, the ply design and manufacturing technology become crucial, which can considerably affect the bulk performance of the material in practice.

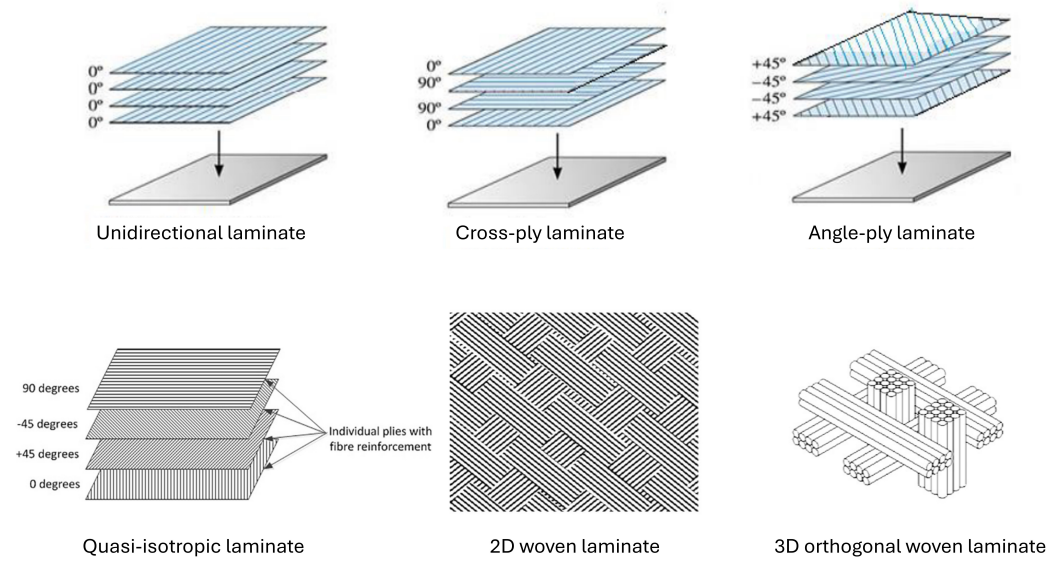


Figure 2.1: Different types of continuous CFRP laminates based on the ply layup methods [56, 57, 58].

Structures that take heavy loads are generally made of continuous fibre composite laminate [45] because the continuous fibres can provide exceptional loading bearing capacities. Aeroplane structure parts made of continuous CFRP can offer significantly higher strength-to-weight ratios compared to conventional metallic structures [45]. By manipulat-

ing the fibre direction, the composed continuous CFRP can demonstrate distinct mechanical behaviours under load. The most common ply layups are unidirectionaly (UD), cross-ply (CP), angle-ply (AP), quasi-isotropic (QI), 2D woven, and 3D orthogonal woven laminates (Fig.2.1) [56, 57, 58].

In UD CFRP laminates, all the carbon fibres align in the same direction, normally designed to be parallel to the loading direction and noted as 0 °. Research shows that the tensile strength of the 0 ° UD CFRP can be as high as 30 times that of the 90 ° UD CFRP laminates (fibres perpendicular to the loading direction), and the compressive strength of 0 ° UD CFRP laminates are normally 4 to 5 times higher than that of 90 ° UD CFRP laminates [45]. CP laminates [0/90] contain fibres that are both parallel and perpendicular to the principal load direction. In such a way, the mechanical properties of the composites can be balanced in both directions. AP laminates [+45/-45] refer to the continuous CP CFRP under the principal loads that are at 45 ° to the fibre direction. To further average the strength in all directions, in some applications with loads coming from multiple directions, the CFRP laminates are designed as [0/+45/90/-45] to provide adequate reinforcement in all directions, which are called QI laminates. Despite various laminate layups to address different loading conditions, the major concerns of using continuous fibre composite laminates are delamination due to the low strength of the matrix and the fibre de-bonding resulting from the poor adhesion of carbon fibres.

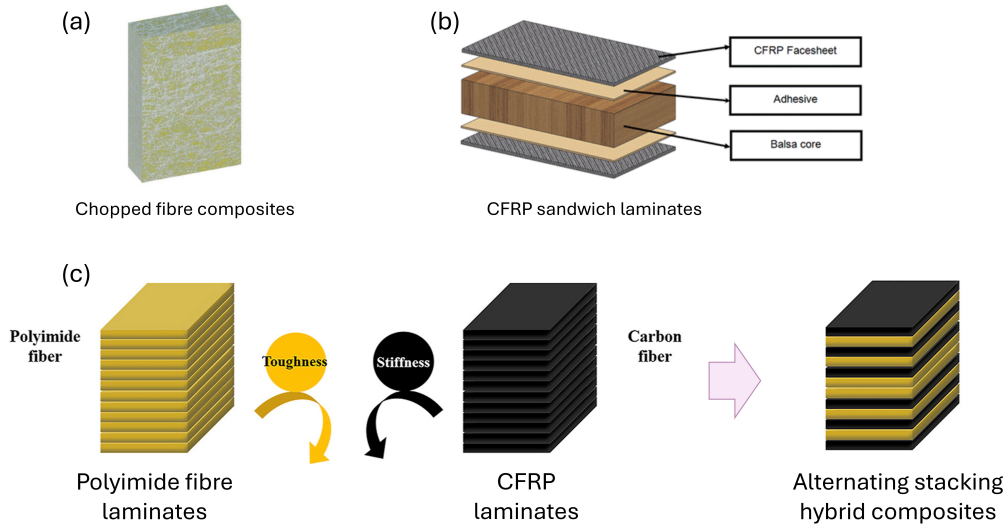


Figure 2.2: (a) Chopped fibre composites [59]. (b) CFRP sandwich laminates [60]. (c) Hybrid composite laminates made of polyimide fibre laminates and CFRP laminates [62].

Woven fibre composites, on the other hand, perform better in ply delamination since fibre tows in warp and weft directions cross over and are perpendicular to each other. However, waviness will simultaneously lead to considerable reductions in material strength and stiffness as the fibres are not aligned straight and in-plane.

Chopped fibre composites are less commonly used in primary load-bearing aeronautical structures because they have the lowest mechanical strength compared to continuous fibre composites (Fig.2.2a) [59]. The benefits of discrete fibres embedded in the matrix include low cost and high suitability for large volume production.

Sandwich composite panels normally consist of a low-density core bonded with thin face skins, as illustrated in Fig.2.2b [60, 42]. They have good performance in bending resistance, impact resistance and energy absorption, but are often subjected to tension and compression due to their soft core. Thus, Sandwich composites are usually used for lightly loaded structures where they provide adequate strength with lighter weight [45, 61].

Matrix materials combining two or more types of reinforcement are called hybrid composites, as the example shown in Fig.2.2c [62, 63]. Hybrid composites have received increasing attention from industrial engineers and academic researchers as they can exhibit various advantages by integrating multiple reinforcements. However, introducing more types of reinforcing materials will generally lead to enhanced overall performance but weakened prominent advantages that the matrix with a single type of reinforcement previously had [64].

2.2 Quasi-static behaviours of CFRP

2.2.1 Quasi-static property testing

Extensive research has been conducted on the quasi-static mechanical properties of continuous CFRP over the past decades. Continuous CFRP is usually very strong in tension due to the high tensile resistance of carbon fibres (3.5 to 5 GPa in general) [46]. As a consequence, the tensile strength of 0 ° UD CFRP is generally between 1 to 3.5 GPa, depending on the type of carbon fibre, matrix, fibre content and manufacturing technology [46, 65, 66], whereas that of 90 ° UD CFRP, which largely depends on the strength of the matrix materials, might be less than 100 MPa [67]. The compressive strength of 0 ° UD CFRP is normally around 800 MPa [68], and this strength value could reduce to one or a

few hundred MPa when the loading is perpendicular to the fibre direction, mainly subjected to the matrix property. The mechanical performance of Angle-ply CFRP is, in essence, between the 0 ° and 90 ° UD CFRP [69], which could offer excellent overall load-bearing ability. However, one of the main limitations of CFRP is its brittleness. The specific stiffness of UD CFRP is generally higher than that of conventional metallic materials such as mild steel, owing to its low density and high fibre stiffness, as shown in Fig.2.3 [70]. However, their tensile failures can be sudden and abrupt. The failure mechanisms of UD CFRP in tension are the combination of ply delamination, matrix breakage, fibre pullout and fibre breakage Fig.2.4 [71, 72, 73, 74], and sufficient experimental evidence indicates that the UD CFRP fails in compression because of fibre buckling rather than the failure of fibre in compression [75, 76].

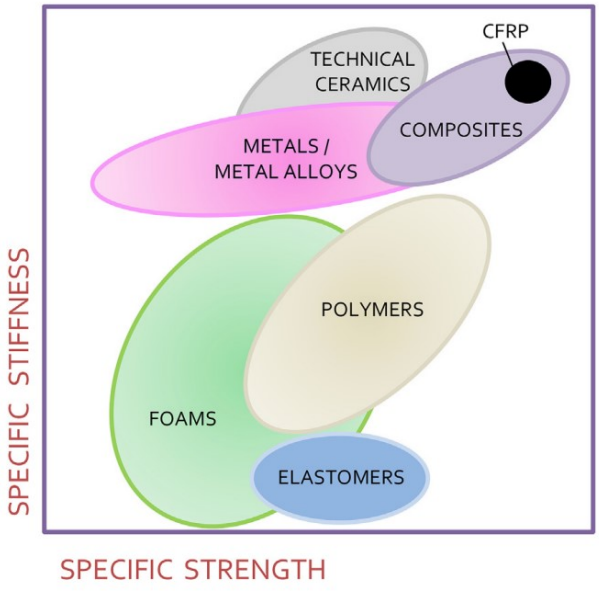


Figure 2.3: Comparison of the specific stiffness and strength between UD CFRP and other engineering materials [70].

2.2.2 Quasi-static damage probing

Postmortem damage inspection

The conventional failure morphology examination is generally performed by visual, scanning electron microscope (SEM), and X-ray CT inspection. Visual inspection is a common approach to study the failure morphology of the composite material, either by performing inspections after the test or by monitoring the failure development during the tests using

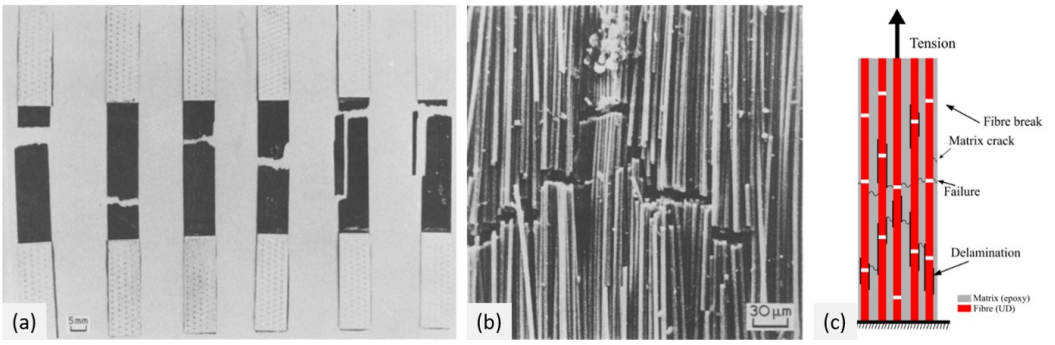


Figure 2.4: Failure mechanism of UD CFRP. (a) UD CFRP specimens after tensile tests [72]. (b) Micro-scale damage morphology of tensile failure inside the UD CFRP specimens [72]. (c) Sketch of the micro-mechanism of tensile failure for UD CFRP [73].

high-speed cameras [49, 72]. Based on the visual inspection results, Zhang et al. [49] found that the failure area of UD CFRP specimens is evidently larger than woven CFRP specimens. Fuwa et al. [72] describe the failure mode of UD CFRP in tension as the failure was in a brittle manner, and the specimens broke into two or more pieces at random locations throughout the specimen.

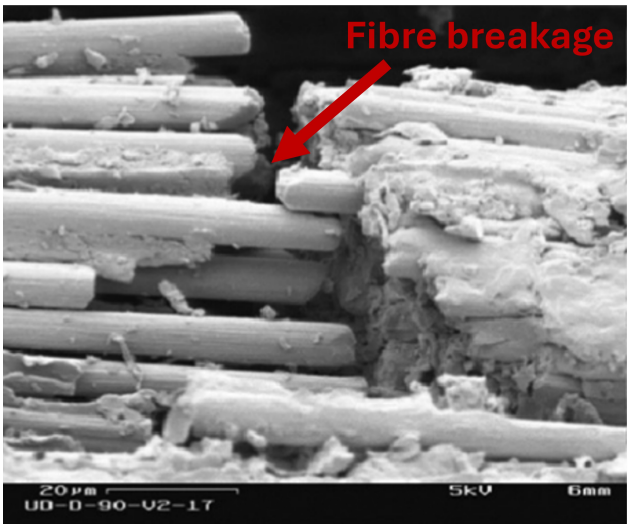


Figure 2.5: Fibre breakage in UD CFRP specimens under tensile loading [77].

In order to have detailed information at the micro-scale level, it is also common practice to use equipment such as SEM [72, 77]. With the help of SEM, the failure mechanism of UD CFRP in tension was found to be fibre breakage (Fig. 2.5), ply split, and delamination [72, 77]. The succession of fibre breaks does not necessarily occur at or near the final site of complete failure, although fibre breaks appear to be more localised near the final failure

point. However, fibre fractures observed in the apparently undamaged regions are not at right angles to the fibre and loading directions (Fig.2.6a). In addition, fibres of weaker CFRP specimens that have average or low fibre volume content tend to fail in bundles. Some fibre bundles might fail simultaneously, create shear to neighbouring bundles, and then lead to a fractured layer throughout the specimen thickness (Fig.2.6b). While SEM can provide high-resolution images, its utility is limited to surface inspection. The materials' internal structural examination using SEM might be destructive and can only be done by removing their surface layers mechanically (e.g., cutting or grinding) or chemically (e.g., sulphuric acid), which could introduce serious interference and alteration to the specimens' internal structure.

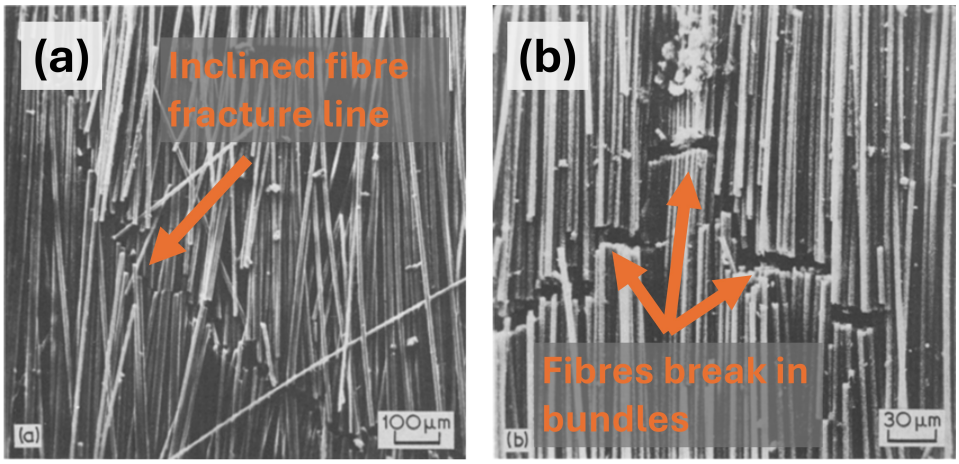


Figure 2.6: SEM examination of the fibres in a UD CFRP specimen under tension [72]. (a) Fibre fracture line can be inclined to the loading direction in the apparently undamaged area. (b) Fibres in the UD CFRP laminates with low volume fracture fail as bundles.

X-ray CT is an effective tool to study the internal material failure morphology by examining the post-damaged CFRP specimens. In contrast to SEM, X-ray imaging is able to examine the internal structure of composites non-destructively. The difference in X-ray absorption when X-ray passes through the material can be detected and reconstructed to reveal the material's internal structures [78]. The damage morphology of the UD CFRP rods was investigated by Wang et al. using CT scan [79] after compression tests. The reconstruction was done using the Feldkamp-Davis-Kress (FDK) algorithm [80], and 3D visualisation and analysis were carried out on Avizo software [79]. Greyscale differences caused by X-ray attenuation were adopted as the method to differentiate cracks and specimen bodies. By analysing the features disclosed by micro-computed tomography (µ-CT), Wang et al.

[79] show that clear fibre kinking bands were formed by compression load and eventually led to the failure of UD CFRP specimens, as shown in Fig.2.7. The boundaries of those kinking bands were inclined at 11 to 40 ° to the horizontal axis. The width of the kinking bands was found to be from 20 to 320 µm, and the fibre rotation angles were between 18 and 52 °. Additionally, micro-mechanism features such as longitudinal fibre splitting, matrix micro-cracks and fibre breakage were identified on X-ray µ-CT images.

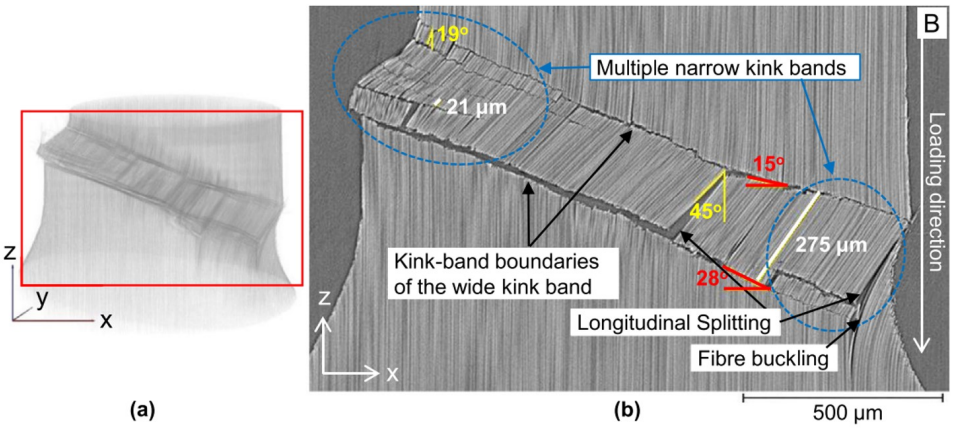


Figure 2.7: X-ray images of UD CFRP damaged in compression obtained using µ-CT : (a) 3D volume rendering of the damage zone. (b) A XZ cross-section slice in the damage zone with explanations of fibre failure mechanisms. In the figure, kinking band width, boundary angle and fibre rotation angle are shown in white, red and yellow, respectively [78].

In-situ damage inspection

In-situ SEM is a newly developed technique which can monitor the microstructural changes while loading the specimens and correlate those changes with load-displacement behaviours [81]. Hapke et al. [81] adopted *in-situ* SEM to track the microstructural changes of UD CFRP under compression. To ensure the failure occurs within the SEM's field of view (FoV), a notch was machined on the specimens. However, it is worth noting that pre-notching does disturb the material structure and makes the stress state in that area non-uniform while loading. Fig.2.8 shows two subsequent frames from the images taken by the *in-situ* SEM that reveal the surface structures of the specimen just before and after the first visible fracture occurred near the notch. It can be seen that in Fig.2.8a, the evident plastic matrix shearing had already been produced in the matrix before kinking bands emerged. However, in the state shown in 2.8a, no longitudinal splitting can be observed, indicating that the fibre-matrix bonding was still very stable. With the compressive loading gradually increasing, the fibre inclination also increased until a kinking band began to propa-

gate (Fig.2.8b). According to the subsequent images captured by *in-situ* SEM, the initiation of the kinking band was found to be sudden and catastrophic.

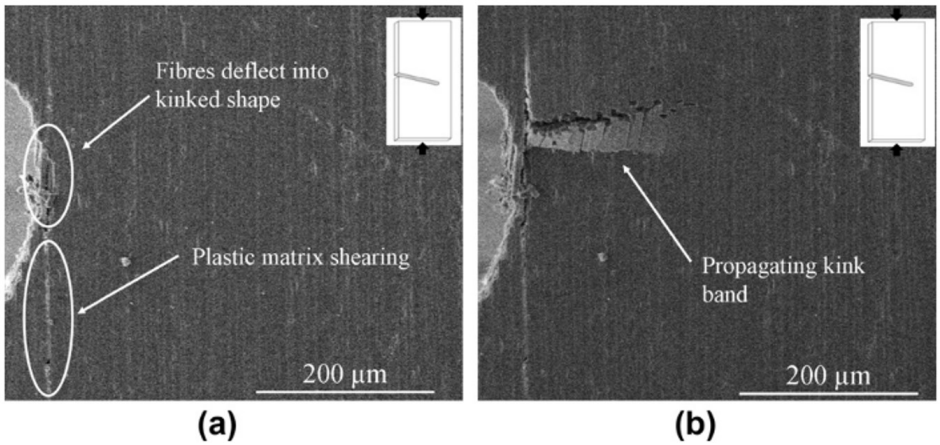


Figure 2.8: Two subsequent frames from the images taken by the *in-situ* SEM. (a) The frame right before the kinking band started to propagate. (b) Kinking band formed [81].

While conventional SEM is often limited to surface examination, Volkert et al. [82] introduced a modified SEM which integrates a focused ion beam (FIB) instrument on an SEM system that allows subsurface microstructure examination by cross-sectional milling and polishing to expose the features that are hidden underneath the surface. To achieve this, the surface material must be removed, which is irreversible and can cause disturbance to the test specimens. And the investigation region is normally at the nano-metre to micro-metre level, and therefore, might not be suitable for investigating the damage of CFRP laminates [83].

Compared to FIB, *in-situ* X-ray CT could be a more preferable micro-damage examination technique that can qualitatively and quantitively reveal the fibres and matrix, but in the meantime, extend the FoV to the micro- to milli-metre level. In such a way, it can inspect a wider area of specimens more efficiently. Wang et al. [84] conducted a pioneering exploration on UD fibre-reinforced polymer composites with *in-situ* compression loading and X-ray CT scanning. The material they tested was UD GFRP composed of 12 µm E-glass fibres and Araldite® LY 564/Aradur® 3486 epoxy. The specimen was cylindrical with a $\sim$1.6 mm reduced gauge section and a groove notch to lead the failure initiation (Fig.2.9a). E-glass is a standard type of glass fibres, whose mechanical strength, reported by many existing studies and industrial product data sheets, is generally weaker than standard carbon fibres, such as TORAYCA® T700 carbon fibres [85]. However, the investigation strategy

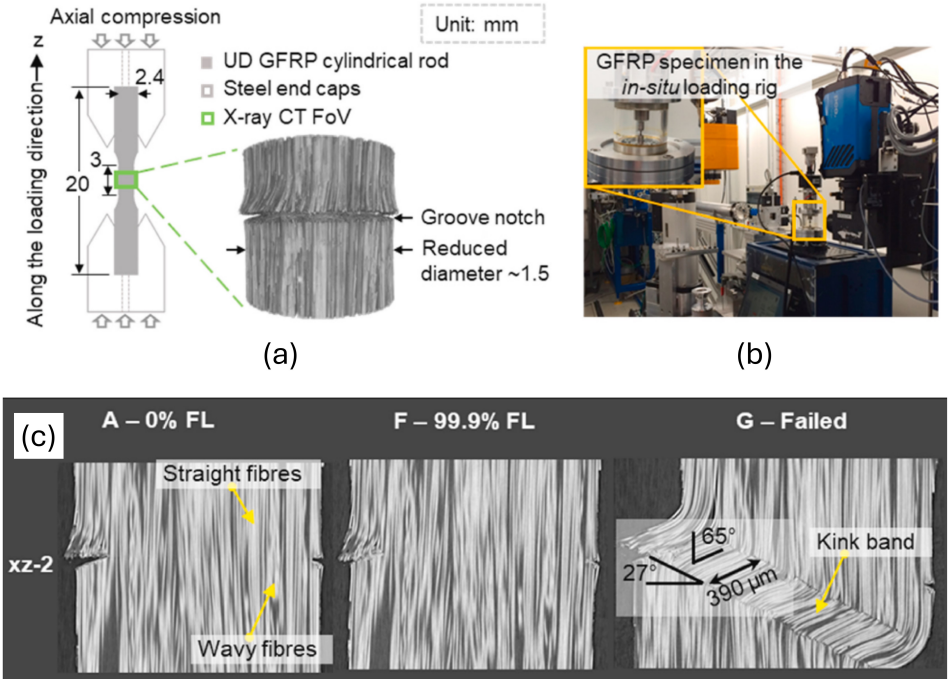


Figure 2.9: Micro-scale damage characterisation of UD GFRP using *in-situ* CT. (a) Schematic of GFRP specimen geometry for *in-situ* compression and X-ray CT scanning. (b) Photography illustrating the compression test rig accommodated at the SLS. (c) X-ray CT slices of the UD GFRP specimen acquired at three load steps while loading in compression: before loading (0% failure load), just before failure (99.9% failure load) and after failure (Failed) [84].

and equipment should not be different between UD GFRP and UD CFRP. *In-situ* X-ray CT scan was performed at the SLS with a 20 keV monochromatic beam. In order to detect fine cracks and facilitate X-ray attenuation imaging, the specimen-detector distance was designed to form a degree of phase contrast. An *in-situ* loading rig was developed by Maire et al. [86], as shown in Fig.2.9b. In addition, a toolbox named Insegt Fibre [87] was used to track the movement of individual fibres in the specimens while loading by analysing the acquired CT scans. Fig.2.9c shows the X-ray CT images captured at three different load steps during compressive loading, namely before loading, just before failure and after failure. It can be seen that the kinking band is not evident even at 99.9% of the failure load. Immediately after failure, a 390 µm kinking band with 27 ° kinking band inclination and 65 ° fibre rotation angle is observed. By introducing the fibre reorientation tracking method developed by Emerson et al. [87], the fibres were classified into 10 clusters according to their kinking direction and analysed as the function of load steps (Fig.2.10). They found that although the fibres did not originally orientate and tilt in the same direction, they all reoriented

and deflected similarly toward the same direction. Fibre deformation primarily happened in the xz plane, whereas its deformation in the yz plane was trivial.

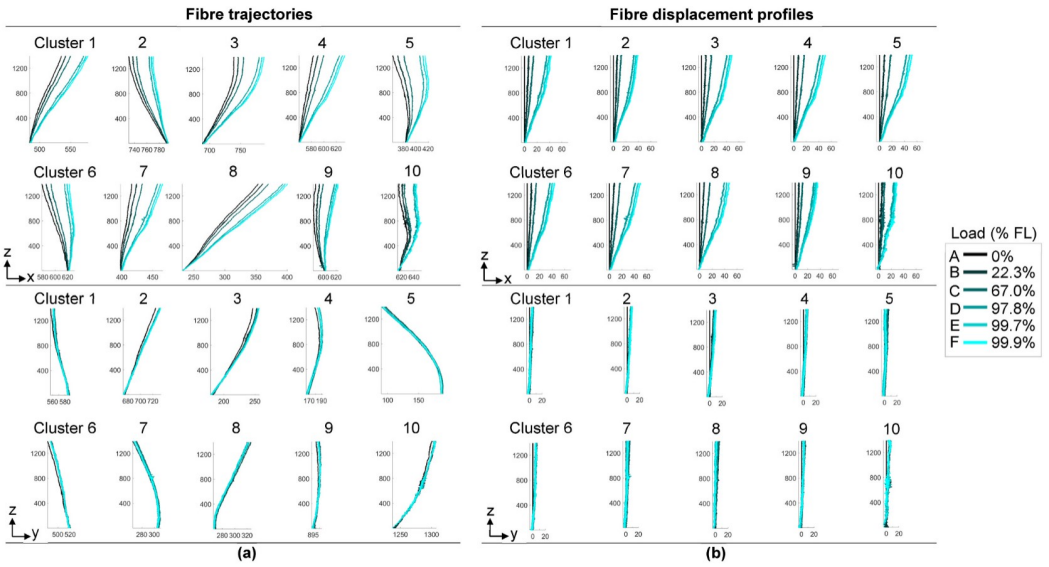


Figure 2.10: Tracking fibre movement on xz and yz planes based on *in-situ* CT image as a function of loading steps. (a) Trajectories of fibre clusters. (b) Displacement of fibre clusters with the original fibre position normalised as 0. It can be seen that all the displayed fibre clusters displaced toward the positive x direction. The fibre displacement was much more obvious on the xz plane [84].

2.2.3 Challenges in CFRP testing

Due to the heterogeneous nature of composites and the distinct properties of their constituents, accurate measurement of the mechanical properties of CFRP remains challenging. The choice of loading method can significantly influence the measured response. For instance, conventional dog-bone specimens, commonly used for metallic materials, may fail prematurely in shear before reaching the tensile strength of the laminate [88]. As a result, tensile testing of CFRP is typically conducted in accordance with established standards such as ASTM D3039M [89, 90, 91] and British Standard (BS) European Standard (EN) International Standardisation Organisation (ISO) 527 Part 5 [92, 93, 94], with representative specimen geometries shown in Fig.2.11(a - c). Compression testing is further complicated by the dominance of instability-driven failure mechanisms, such as fibre microbuckling and ply delamination, rather than fibre fracture [75]. This leads to strong sensitivity to test configuration and procedure. As illustrated in Fig.2.11d, significant discrepancies (up to a factor of two in measured strength) can arise for the same material when tested by

different laboratories [75]. To address this, a range of standardised loading methods have been developed, including end loading, shear loading, and combined loading approaches. These are defined in standards such as ASTM D695, D3410, and D6641, BS EN 2850 and ISO 14126 (M1 and M2), as well as industrial protocols including Boeing BSS 7260 T III/IV and Airbus AITM 1.0008 [95, 96, 97, 55]. The selection of an appropriate method remains dependent on laminate configuration and prior benchmarking [75].

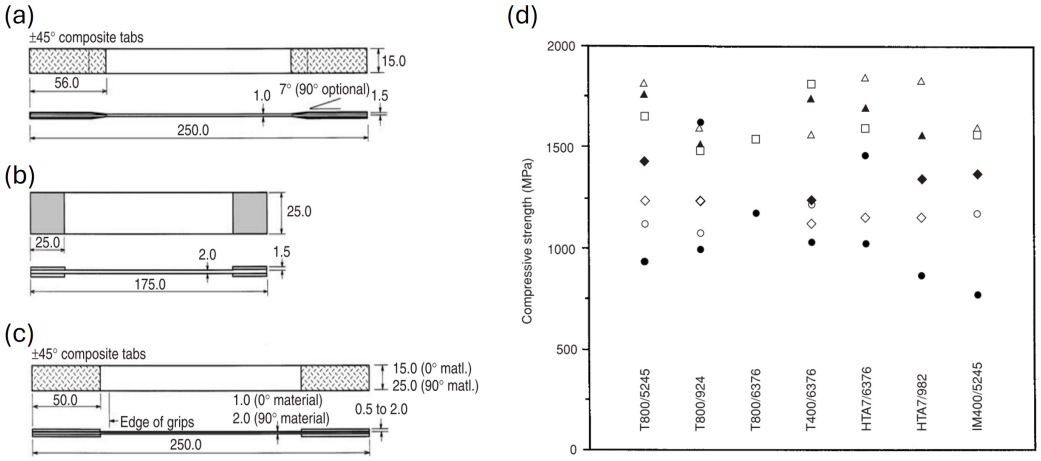


Figure 2.11: Variation in the loading methods and results of the CFRP's mechanical testing. Different loading configuration in tensile tests according to (a) ASTM D3039 for 0 ° UD CFRP, (b) ASTM D3039 for 90 ° UD CFRP, and (c) ISO 527 for 0 ° UD CFRP [88]. (d) Compressive testing results of the same group of CFRP laminates obtained from seven different laboratories [75]. Different symbols (e.g., ○ and □) represent different laboratories.

The characterisation of shear properties is particularly important for CFRP laminates because shear deformation is strongly matrix-dominated and is closely associated with matrix cracking, fibre-matrix debonding, and delamination [98, 99, 100]. Under quasi-static conditions, the ± 45 ° uniaxial test is one of the most widely adopted methods for deriving the in-plane shear stress-strain response, shear modulus, and shear strength of fibre-reinforced composites, as specified in standards such as ASTM D3518 [101] and ISO 14129 [102]. In this method, a uniaxial load applied to a balanced ± 45 ° laminate generates a nominal in-plane shear state in the material coordinates, allowing the global response to be transformed into an equivalent shear response.

At high strain rates, the same principle is often extended using high-speed loading systems or split Hopkinson pressure bars (SHPB)-based configurations to investigate the strain-rate sensitivity of matrix-dominated shear properties [103, 99, 104]. These studies

generally indicate that the in-plane shear response of CFRP is strain-rate sensitive, with shear strength and, in some cases, shear modulus increasing as strain rate increases, reflecting the rate-sensitive response of the polymer matrix [104, 105]. However, dynamic ± 45 ° tests still largely provide global or nominal shear properties, while the internal damage processes responsible for the measured response remain difficult to observe directly [99, 106, 105]. In particular, the transient nature of high-strain-rate loading makes it challenging to determine whether the assumed nominal shear response is maintained throughout deformation, and how matrix cracking, fibre-matrix debonding and delamination develop in relation to the measured macroscopic response. This limitation motivates the need for time-resolved damage characterisation under dynamic loading conditions.

2.3 Dynamic behaviour of CFRP

Despite CFRP's numerous merits, its current research and application are primarily limited by the fact that it has relatively lower ductility and impacts damage tolerance due to its brittle components, anisotropic properties and layered configuration [107, 108, 109, 110]. However, the application scenarios of CFRP, such as the structural materials of aeroplanes, sports cars and earth satellites, often travel at very high speed, and can thus be exposed to the threat of foreign object impacts. In light of this, understanding the dynamic properties and failure mechanisms of CFRP at various strain rates is of great significance to the development of modern transportation engineering [111]. Nevertheless, as yet, the dynamic behaviour of CFRP remains not fully understood, not only because of the complex architectures of CFRP itself but also because of the current limitations of investigating methods in high-strain-rate tests. Commonly used numerical approaches for modelling the dynamic response of CFRP, such as those based on the Hashin failure criteria [112], are often adapted from quasi-static failure formulations. The simulated subsurface failure mechanisms of CFRP under high-strain-rate loading have not yet been validated by solid experimental evidence. Thus, in this section, which reviews the existing approaches to examine the properties and failure of CFRP at high-strain-rate loading, a technology-originated narrative layout is adopted.

2.3.1 Loading setups in dynamic testing

Commonly used dynamic loading setups include drop tower machines, high-pressure gas guns, high-rate servo-hydraulic machines, and SHPB systems. Among these dynamic loading platforms, drop tower and servo-hydraulic machines normally offer low to moderate loading speed (below 24 m/s) [113, 114, 115, 116, 117], whereas SHPB and gas guns are often used to provide high-speed loadings.

The present research was mainly conducted by using SHPB systems because they can exert a wide range of strain rates from 1×10^2 to 1×10^5 s^{-1} [118, 119, 120]. For some newly developed miniature miniature split-Hopkinson pressure bar (mSHPB) systems with bar diameter as small as 100 μm, the strain rate can achieve up to 1×10^6 s^{-1} [121]. Meanwhile, high-pressure gas gun tests on CFRP laminates can also be planned in the future to investigate their ballistic impact and spallation behaviours in ultra-high-strain-rate states. Taking into consideration that the travel speed of commercial aircraft is from 200 (taking off) to 1000 (cruising) $km\,h^{-1}$ [122], SPHB should be the optimised choice of loading platforms among them to create similar impact loading situations.

2.3.2 Mechanical properties in dynamic loading

Several previous studies have proved that the mechanical properties of CFRP are strain-rate sensitive. Hou and Ruiz [103] investigated the strain-rate dependency of the CFRP's mechanical properties in tension, compression and in-plane shear. The material used was woven CFRP composed of T300 carbon fibre and 914 epoxy resin. The results indicate that both matrix-dominated (i.e. compression strength, shear strength, in-plane shear modulus and Poisson's ratio) and fibre-dominated (tensile strength and modulus) properties are strain-rate dependent. Epoxy resins are highly cross-linked thermoset polymers. Their molecular architecture limits chain mobility and energy dissipative mechanisms, leading to pronounced rate-dependent mechanical responses [123]. At high strain rates, chain relaxation mechanisms cannot keep up with loading, resulting in reduced ductility and increased brittleness due to suppressed viscous flow and enhanced formation of micro-voids and craze [124]. In contrast to that, carbon fibres exhibit negligible strain-rate sensitivity in the longitudinal direction [125, 126]. However, changes in the performance of the epoxy matrix can affect the stress states of carbon fibres, causing structural instability such as fibre micro-bulking and splitting. Consequently, strain-rate-dependent behaviour can also

be shown in fibre-dominated loading cases [127].

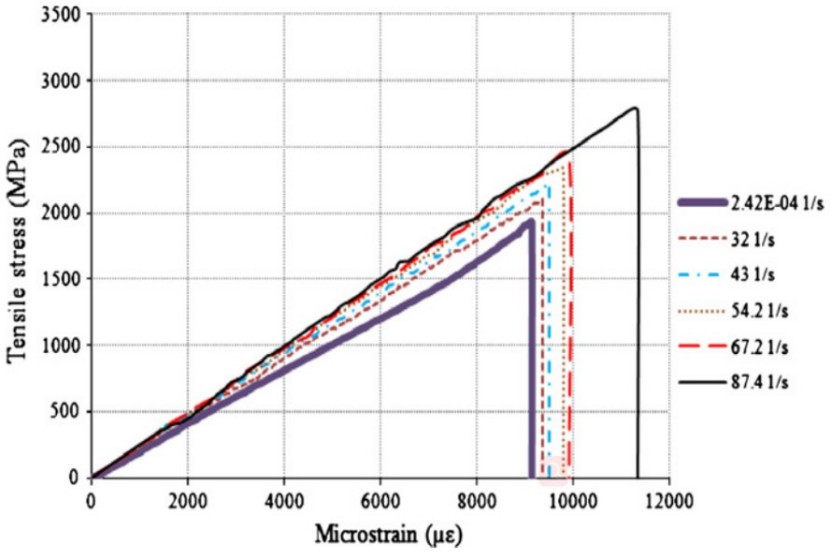


Figure 2.12: Stress-strain curves of UD CFRP laminates under tensile loading at different strain rates, demonstrating a clear strain rate sensitivity. The mechanical properties of the tested specimens were enhanced by increasing the strain rate [128].

Tension

The experimental results obtained by Al-Zubaidy et al. [128] were in good agreement with the research conducted by Hou and Ruiz in terms of CFRP's strain-rate sensitivity [103], although the material used was UD CFRP composed of CF130 carbon fibres and Araldite 420 matrix. Fig.2.12 demonstrates the stress and strain data recorded while loading [128]. It clearly indicates that, for the tested CFRP specimens, both their tensile strength and modulus are strain rate dependent. The failure strength and strain of the specimen are indicated by the curves' turning points at which the stresses start to drop rapidly. It can be seen that, as the strain rate increases, the tensile strength, Young's modulus, failure strain and energy absorption all increase considerably. This suggests that the mechanical performance of the CFRP material might be enhanced with the increase in strain rate.

Compression

Guedes et al. [129] performed a series of compression tests on QI $[0/90/+45/-45]_{2s}$ CFRP specimens using a universal testing machine and a SHPB system. The test results indicate that the tested CFRP specimens became stronger in terms of compressive strength as the strain rate increased (Fig.2.13a), which agrees with the findings obtained in dynamic tensile tests of CFRP specimens. These results also coincide with the dynamic

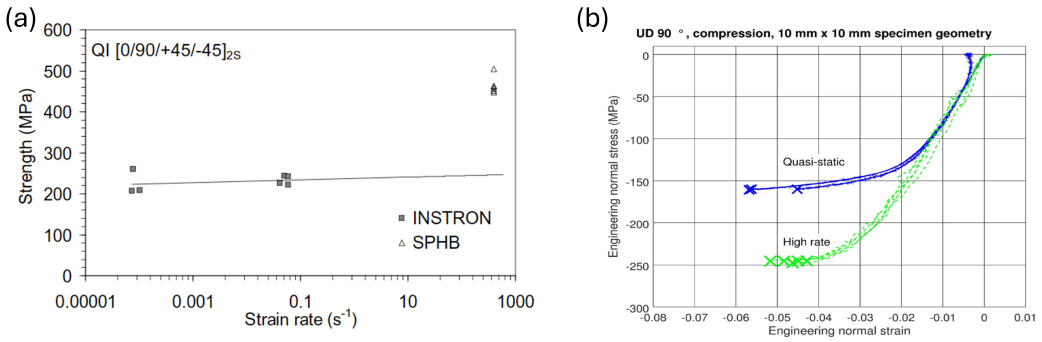


Figure 2.13: Stress-strain curves of CFRP laminates in compressive tests with different strain rates. (a) QI CFRP laminates [129]. (b) UD CFRP laminates [130]. Both indicate that raising strain rates can increase the strength of CFRP specimens.

and quasi-static compressive test results on UD CFRP conducted by Paul et al. [130], although the dynamic loading method used by the latter was a direct-impact Hopkinson pressure bar (DIHPB). Fig.2.13b displays a significant difference in compressive strength of UD CFRP specimens in quasi-static and high strain rates. However, Young's modulus of the tested CFRP specimens acquired by their experiments seems somewhat similar between both strain rates. Sawamura et al. [131] tested cylindrical hollow CFRP specimens with transverse and longitudinal fibre directions. All the experimental results point toward the same trend, which the compressive strength of CFRP gets enhanced at dynamic strain rates compared to that under quasi-static loading.

Shear

The in-plane shear response of CFRP laminates is commonly characterised using ± 45 ° off-axis specimens, where the applied axial load is transformed into a nominal shear stress-strain response in the material coordinates. Under quasi-static loading, this method has been widely used to determine the shear modulus, shear strength, and non-linear shear behaviour of fibre/matrix laminates [132, 133]. Under dynamic conditions, the same principle has been extended using high-speed servo-hydraulic machines and SHPB systems configurations to quantify the strain-rate sensitivity of matrix-dominated shear properties [103, 134, 99, 104]. These studies generally show that the in-plane shear response of CFRP is strain-rate sensitive, with shear strength and, in some cases, shear modulus increasing at higher strain rates. This behaviour is usually attributed to the rate-dependent response of the polymer matrix and fibre-matrix interface, since in-plane shear deformation is primarily governed by matrix shearing, fibre rotation, and interfacial damage rather than

direct fibre stretching [135, 136].

Despite these findings, the current understanding of the mechanical response of CFRP under dynamic loading remains less comprehensive than that under quasi-static conditions. While strain-rate sensitivity of material properties has been widely reported, there is still a lack of time-resolved experimental evidence that directly links such behaviour to the underlying damage mechanisms and their evolution across different length scales. This is largely due to the transient nature of high-strain-rate loading experiments and the limitations of damage observation techniques.

2.3.3 Damage characterisation in dynamic loading

Meso-scale damage charaterisation

Ballistic impact tests of CFRP can create similar loading conditions as foreign object impact events in CFRP's application in the aeronautics industry. The CFRP's delamination is a crucial parameter and can be examined using ultrasonic C-scan after the tests. This technique is widely used because it is non-destructive, affordable, easy to implement and good at detecting subsurface damage in materials [137, 138, 139]. By observing the drop or change in the amplitude of reflection pulses, internal defects can be detected and located [137]. The time-of-flight of the ultrasonic pulse can be analysed alongside the wave amplitude to obtain the defect dimension in thickness. Fig.2.14 shows a group of C-scan images of CFRP plates after ballistic impact tests [140]. Reconstructed ultrasonic images clearly show that the damage caused by ballistic impact is larger with the higher impact velocities, especially in $[0/90]$ laminates. Although improvements in ultrasonic C-scan have been made in recent years regarding image quality and spatial resolution, X-ray is still the better choice for internal structure examination in scientific research since it can provide much more details and features with higher image resolutions [141].

Despite its widespread use, ultrasonic C-scan is primarily effective in detecting delamination and large-scale subsurface damage. However, it lacks the spatial resolution required to resolve fine microstructural features and cannot capture the evolution of damage during loading. As a result, it provides limited insight into the mechanisms of damage initiation and progression under dynamic conditions.

Micro-scale damage characterisation

Microscale failure characterisation of CFRP is commonly conducted by post-damage

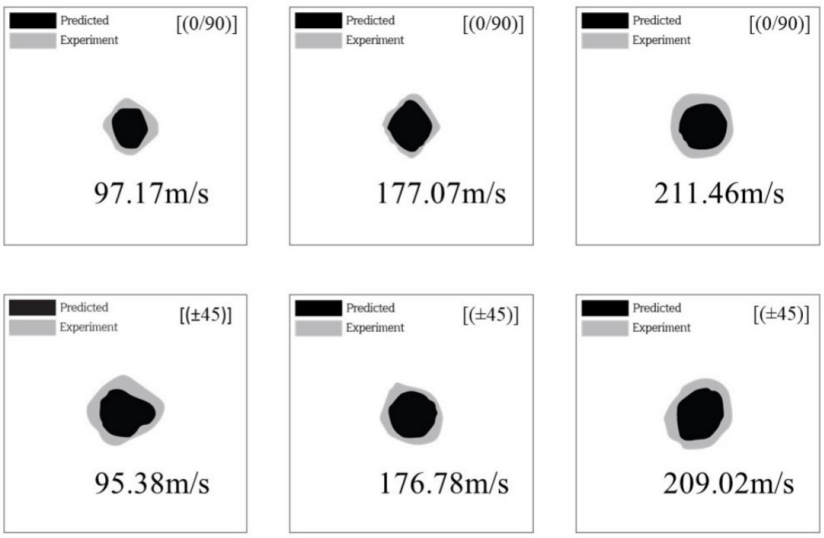


Figure 2.14: Damage in woven CFRP caused by ballistic impact showing a comparison between experimental results (from ultrasonic C-scan) and model predictions [140].

X-ray CT inspection in previous research [142, 143]. Xiao et al. [143] conducted in-plane high-strain-rate compression on woven CFRP specimens with three different off-axial angles between fibre yarns using an SHPB. The tested specimens were labelled as OA00 (i.e., off-axis at $0\ °$), OA60 and OA90 according to the angles between fibre yarns and loading directions. X-ray CT was adopted to carry out postmortem damage inspection on the tested specimens. X-ray CT results, as the images shown in Fig.2.15, provide good insights into the internal microstructures of damaged specimens. By quantifying the detected damages inside the specimens, they found that the failure of OA60 and OA90 specimens was dominated by interlaminar damage, whereas that of the OA00 specimens was mainly a result of intralaminar damage, such as fibre splitting and debonding. The damage volumes inside the specimens were 15.3, 31 and 19.6 mm^2 for OA00, OA60 and OA90, respectively. The researchers suggest the observed fibre buckling in OA60 and OA90 can be attributed to the delamination of the outermost layer at the beginning, and the shear bands were formed by the connection of intralaminar fibre fracture. However, the stated failure evolution was obtained based on reverse deductions in light of the post-mortem CT results. Without the real-time probing of the subsurface microstructural changes under impact load, those findings cannot be validated by direct evidence.

While post-mortem X-ray CT provides detailed insights into internal damage morphology, the interpretation of damage evolution relies heavily on indirect inference. Without

time-resolved measurements, the sequence of damage initiation and propagation cannot be directly observed, limiting the ability to establish causal relationships between loading conditions and failure mechanisms.

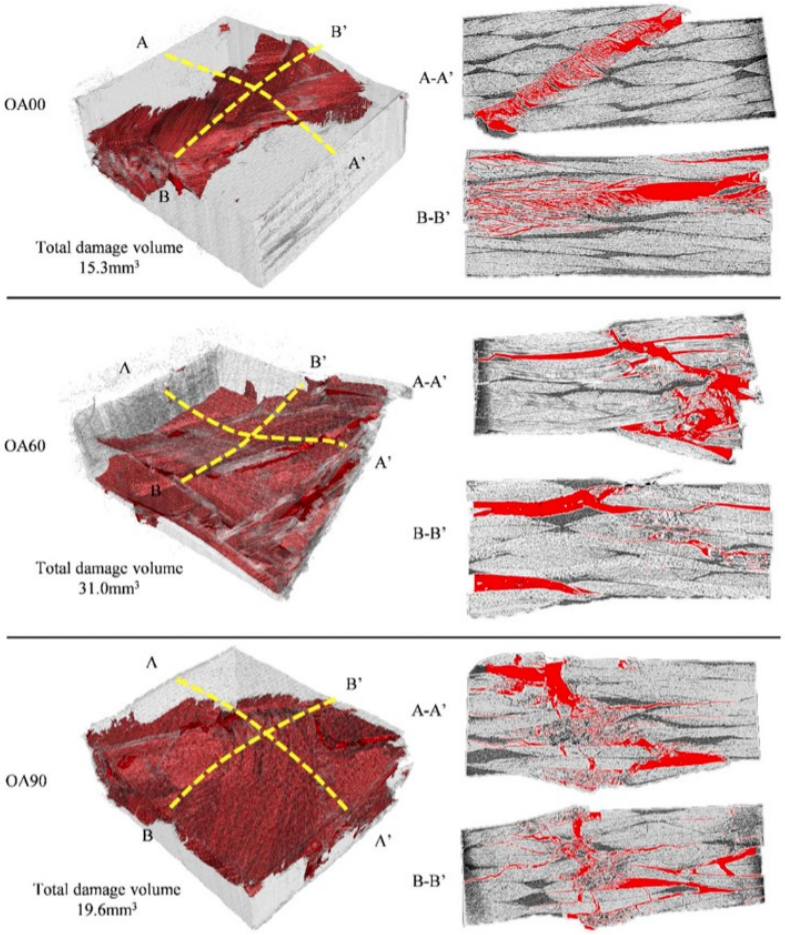


Figure 2.15: Micro-scale damage of woven CFRP under axial and off-axial loading characterised using CT. Damage morphology and volume changes between the specimens with different off-axial angles (0, 60, and 90 °) are presented and highlighted in red [143].

In-situ damage characterisation using dynamic X-ray imaging

In-situ X-ray phase-contrast imaging (XPCI) is a state-of-the-art technique that can provide direct evidence of the subsurface structural changes in opaque specimens when undergoing high-strain-rate loading. This technology has flourished over the past decade. By virtue of extremely high energy requirements [144, 145, 146], very few laboratories are able to perform such experiments around the world. In recent years, this type of experiment has been mainly performed at the European Synchrotron Radiation Facility (ESRF) [147] in France and the APS at Argonne National Laboratory of the United States [148]. Nie et

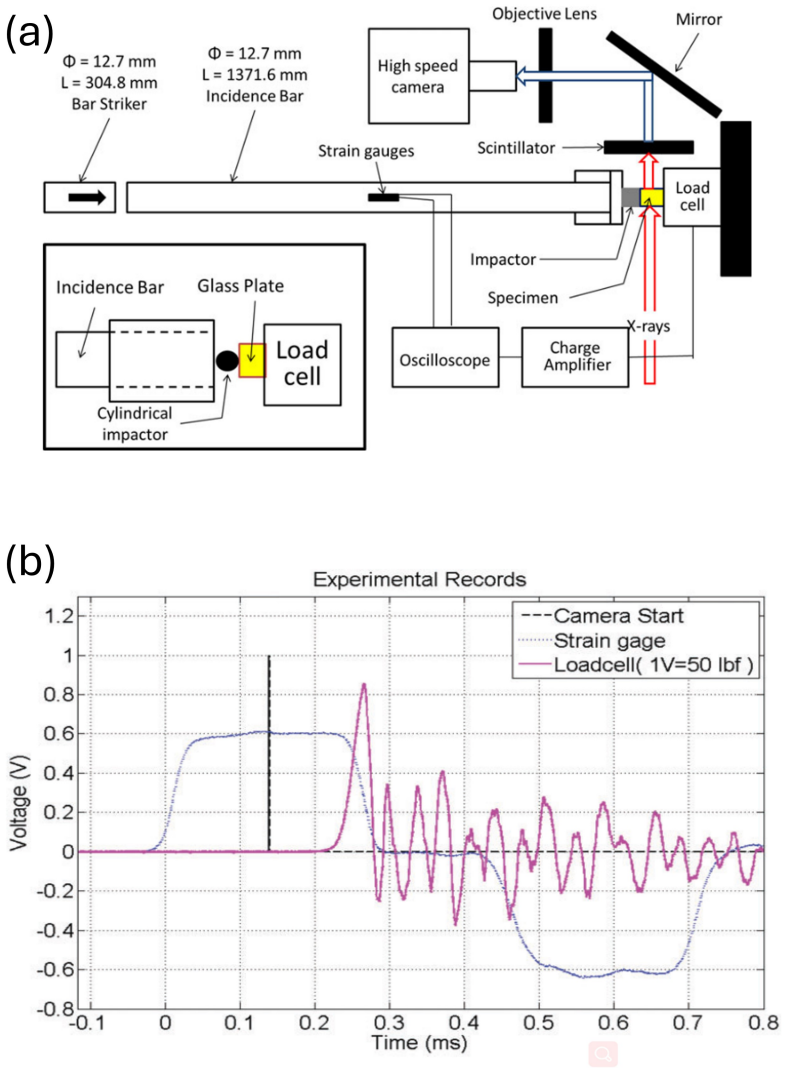


Figure 2.16: Experimental method of the high-strain-rate tension on UD CFRP specimens conducted at Beamline 32-ID-B, the APS. (a) Schematics of the high-strain-rate loading and XPCI systems setup [150]. (b) Camera triggering time and voltage waves recorded by the strain gauge and the load cell [149].

al. [149] reported one of the first synchrotron-based XPCI studies of failure mechanisms in UD CFRP under high-strain-rate loading.

The SHPB system is normally placed perpendicular to the X-ray beam, which propagates through the test specimens, as shown in Fig.2.16. A scintillator (single crystal Lu3Al5O12:Ce) mounted downstream of the X-ray has the property of luminescence in the visible light spectrum when stimulated by X-ray radiation [150]. The visible light converted from the X-ray beam by the scintillator continues to travel and is reflected by a 45 ° mirror downstream and captured by a high-speed camera. The specimens Nie et al. [149]

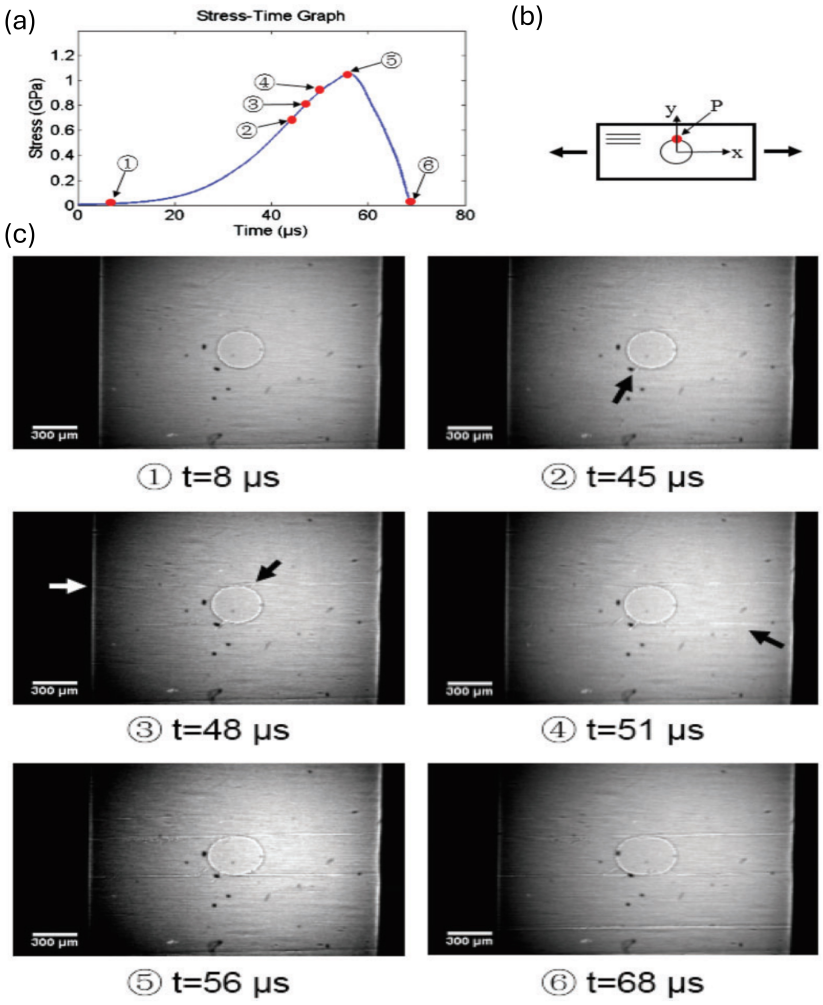


Figure 2.17: Results of the high-strain-rate tension on UD CFRP specimens with 0.3 mm diameter void [149]. (a) Stress-strain curve measured using the strain gauge and load cell. (b) Specimen and loading geometry. (c) Captured X-ray phase-contrast images at the representative time steps labelled on the stress-strain curve.

tested were single-ply UD CFRP with circular defects in tensile loading exerted by an SHPB. The specimens were in the size of 15×1.5 mm^2 with circular defects ranging from 0.08 to 0.5 mm diameter in the centre. The curves shown in Fig.2.16b present voltage wave data logged by the strain gauge and load cell when testing a longitudinal UD CFRP specimen with a 0.3 mm diameter void. The camera was triggered at an approximate time of 0.13 ms by the voltage signals detected by the strain gauge, which represents the most common way of camera triggering in SHPB tests. This triggering method will also be considered in the high-speed imaging design of the present research. In Fig.2.17, the stress-strain curve (a), specimen configuration (b), and captured X-ray phase contrast images at different time

steps (c) for single-ply UD CFRP specimens are illustrated. These demonstrate the use of synchrotron-based XPCI to capture dynamic failure processes in UD CFRP under high-strain-rate loading, revealing crack initiation and propagation in real time.

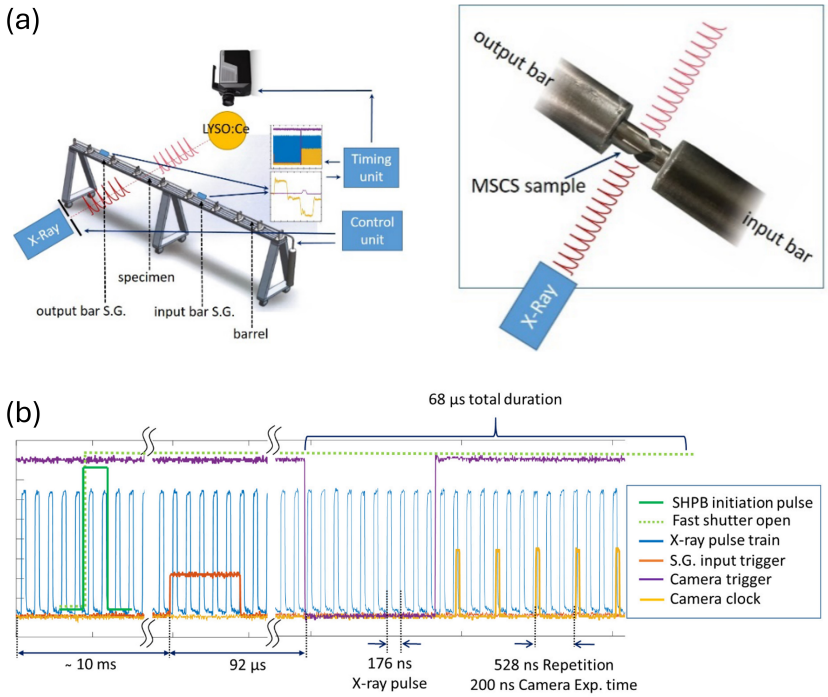


Figure 2.18: Setups of dynamic X-ray phase-contrast imaging at the ID19, the ESRF [151].

Similar synchrotron-based dynamic imaging systems have also been developed at facilities such as the ESRF, enabling high-temporal-resolution observation of material behaviour under high-strain-rate loading [151, 152]. These systems further demonstrate the potential of X-ray imaging for real-time damage characterisation, although they remain experimentally complex and limited in accessibility. Similar to the setup at APS, a bespoke SHPB system was designed, accommodated in the beamline hatch and aligned perpendicular to the X-ray pulse path, allowing the X-ray pulse to penetrate through the samples from the targeting area, as shown in Fig.2.18a. The SHPB system was originally designed to have input and output steel bars in 12.7 mm diameters, but can accommodate bars with different materials and diameters. Launching of the striker is driven by a simple gas gun system and can be controlled remotely from the control unit set up in the hatch room or a computer code compiled on the computers in the control room.

X-ray phase contrast real-time examination is achieved by single-bunch imaging. The

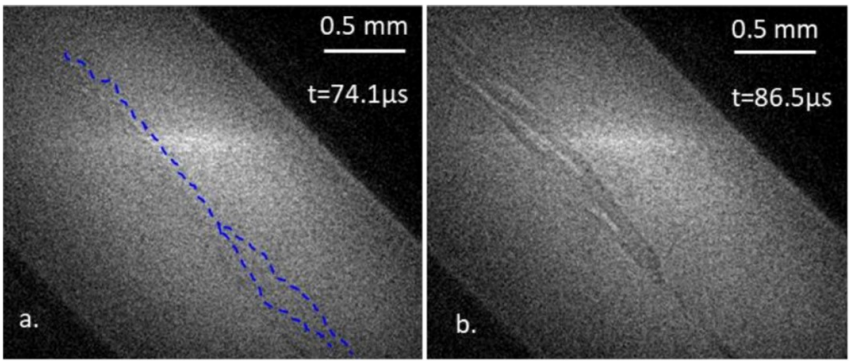


Figure 2.19: Sequential radiographic images showing failure mechanisms of a Ti-6A1-4V specimen under high-strain-rate loading with SHPB. (A) damage initiation at $t = 74.1$ µs and damage progression $t = 86.5$ µs [151].

bunch modes used at ID19 include 4-bunch and 16-bunch modes, corresponding to ∼100 ps X-ray flashes delivered within ∼2.816 µs, producing time intervals of 704 ns and 176 ns, respectively [152]. The FoV can be up to 20×10 mm^2 (horizontal $\times$ vertical), and an LYSO:Ce single-crystal scintillator with a 40 ns decay time and a magnifying optics with 0.2 numerical aperture is adopted to convert each transmitted X-ray pulse into visible light and captured by a Shimadzu HPV-X2 high-speed camera placed downstream. In Cohen et al.'s experiment [151], the high-speed camera was set to have a 530 ns inter-frame temporal sampling, and was synchronised to capture the X-ray pulse in every three bunches (Fig.2.18b). The specimens were exposed to the X-ray pulse once the fast shutter was opened. The scintillator was mounted ∼8 m downstream of the specimen to allow the forming of sufficient phase-contrast for crack detection [152]. Upon the fire command of the gas gun, the high-speed camera was triggered when the stress wave arrived at the strain gauge. Fig.2.19 demonstrates an example image result that was obtained using the setups at the ESRF for Ti-6A1-4V specimens with modified shear compression specimen geometry. It is worth mentioning that a gas gun system has also been developed and tested at ESRF. This loading platform and testing method could be useful if testing specimens at higher strain rates in the future [153, 154, 155].

In-situ X-ray phase contrast imaging offers a unique capability to directly observe sub-surface damage evolution during high-strain-rate loading with high temporal resolution. However, such experiments are limited to a small number of specialised facilities, and often involve constraints on specimen geometry, FoV, image resolution, and experimental complexity. Consequently, while XPCI provides unprecedented insight into dynamic damage

processes, its application remains limited and not yet widely accessible.

Overall, current methods for damage characterisation in dynamic loading exhibit a clear trade-off between spatial resolution, temporal resolution, and experimental accessibility. Techniques such as ultrasonic C-scan are effective for large-scale damage detection but lack resolution and time-resolved capability, while post-mortem X-ray CT provides detailed structural information but cannot capture damage evolution. In contrast, *in-situ* X-ray imaging techniques enable direct observation of damage processes in real time, but are constrained by experimental complexity, 3D resolution, and limited availability. As a result, although significant progress has been made in characterising damage in CFRP under dynamic loading, there remains a lack of comprehensive, time-resolved, and multi-scale understanding of damage initiation and evolution. Addressing this gap requires experimental approaches that can bridge spatial scales while capturing transient damage processes, which form the focus of this research.

High-rate damage mechanisms of $\pm$45 CFRP

For $\pm$45 ° and other AP CFRP laminates under high-strain-rate compression, existing studies have primarily focused on measuring the rate-dependent compressive response and constructing failure envelopes rather than directly resolving the internal damage sequence. The current understanding is therefore that damage in AP CFRP under dynamic compression is governed by matrix-dominated shear deformation, fibre rotation, fibre kinking, fibre-matrix debonding, and delamination [98, 100]. Although intra-ply cracking and delamination have been reported as important failure modes in AP CFRP laminates under dynamic loading [156, 104], the available evidence is often obtained from post-mortem inspection or numerical inference [157, 158]. Surface-based techniques such as high-speed imaging, digital image correlation (DIC), and infrared thermography have demonstrated strain localisation, local heating, and rate-dependent hardening or softening during dynamic shear/compression loading, but these methods cannot fully resolve subsurface damage evolution [159, 105]. *In-situ* synchrotron XPCI studies on dynamically compressed CFRP have recently demonstrated that internal shear fracture and crack propagation can be captured in real time [159, 149]. However, such work remains limited in material systems, loading configurations, and laminate architectures. Consequently, for $\pm$45 ° CFRP laminates, the key limitation in the literature is not the absence of dynamic mechanical data, but the lack of direct, time-resolved, and multi-scale evidence linking the onset and development of internal

damage to specific stages of the macroscopic and local mechanical response.

2.4 Moisture and temperature effects

2.4.1 *In-situ* temperature

Numerous studies have demonstrated that *in-situ* test temperature can induce substantial changes in the internal microstructure, mechanical properties, and failure mechanisms of CFRP. These effects are primarily attributed to the strong temperature sensitivity of the polymer matrix and the mismatch in thermomechanical properties between the polymer matrix and carbon fibres. At elevated temperatures, polymer molecular chains acquire additional thermal energy from the surrounding environment, enabling increased segmental mobility by overcoming energy barriers more easily [160]. At the constituent level, changes in epoxy segmental mobility and relaxation with temperature alter matrix stiffness, ductility, and energy dissipation, exerting direct impacts on global mechanical and damage behaviours of CFRP laminates. In addition, previous studies have shown that the fibre/matrix coupling is also highly sensitive to temperature variations originating from thermomechanical property mismatch [161]. Variations in matrix properties, together with residual thermal stresses retained at the fibre/matrix interface during temperature changes, can significantly alter interfacial strength and toughness, ultimately affecting the macroscopic performance and failure behaviour of CFRP composites [162, 163].

Soutis and Turkmen [164] studied the compressive strength and failure mechanisms of epoxy-based UD CFRP specimens at elevated temperatures (20, 50, 80 and 100 °C). The results suggest that the compressive strength of the tested CFRP specimens is weaker, associated with more out-of-plane micro-buckling at higher temperatures, due to the reduction in the strength of the matrix material at the ply interface as the temperature increases. Similar results were obtained by Korbelin et al. [165]. Existing research on the change of CFRP's mechanical properties at different temperatures under high strain rates is relatively scarce. The trends of property change at high-strain-rate loading reported by Gómez-del Río et al. [166], Castres et al. [167], and Jia et al. [168] are in good agreement with the test results at quasi-static loading conditions. They suggest that the CFRP's mechanical strength is higher when the temperature is lower (Fig.2.20). Moreover, their experiments indicate that increasing the loading rate can pose a similar effect on the mechanical performance of

CFRP as decreasing temperature, where the mechanical strength can be improved when the loading rate is higher.

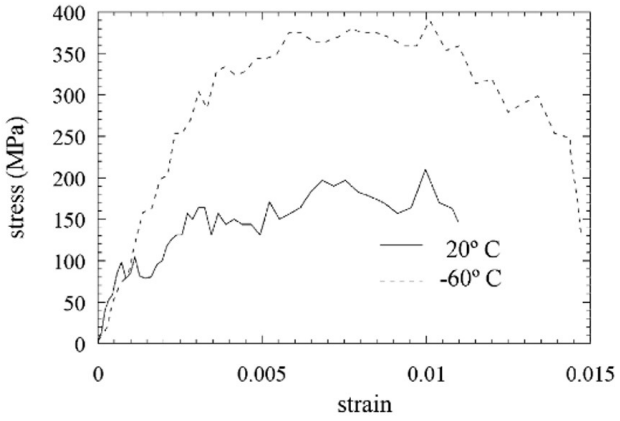


Figure 2.20: Stress-strain curves of 90° UD CFRP 20 and -60 °C with a loading strain rate of 890 s^{-1} recovered from the strain gauge signal obtained using SHPB [166].

Meng et al. [169] present a systematic study on the effects of extreme *in-situ* temperatures on the UD and QI CFRP laminates used for aerospace crafts under tensile and flexural loadings. The results of testing CFRP specimens at 77 K, 173 K, and room temperature show a significant tensile strength drop due to the *in-situ* temperature decrease. In addition, the failure mode was identified as fibre/matrix debonding at their interfaces. They attribute this strength drop to the matrix-dominated behaviour of the tested laminates at the low temperatures, and the tensile strength of the matrix material (epoxy, TED-86®) is lower when the temperature is lower. Fig.2.21 shows SEM inspection on the failure morphology of 90 ° UD CFRP specimens at different *in-situ* testing temperatures. It can be seen that there are matrix flakes adhered to the fibres on the failure and debonding surfaces at cryogenic temperatures, indicating that, despite the strength reduction in the matrix materials, the interfacial bonding between fibres and matrix might be improved as the temperature drops by virtue of thermal contraction.

While the findings reported by Meng et al. [169] on the changes in mechanical properties at varying temperatures are supported by Islam et al. [170] and Morkavuk et al. [171], some studies obtained contrary results. Yang et al. [172] tested the tensile strength of UD CFRP specimens with ambient temperature ranging from room to -180 °C. The experimental data indicate that the tested CFRP specimens possess evident higher tensile strength at the lower ambient temperatures. These opposite results could be attributed to

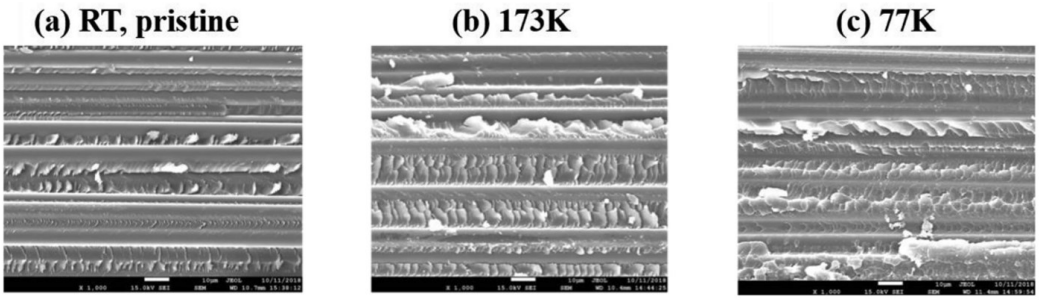


Figure 2.21: SEM images on the tensile failure of 90° UD CFRP specimens at (a) room temperature, (b) 173 K and (c) 77 K [169].

the difference in fibre/loading arrangement and matrix materials, as in Yang et al. [172], the polymer matrix material they used (bisphenol F epoxy) in longitudinal tension. The contraction of the matrix at low temperature might enhance the fibre/matrix interfacial bonding and strengthen the overall tensile performance of the specimens when the fibre is the main load-taking component.

2.4.2 Environmental cycling

Meng et al. [169] also characterised the internal microstructural change of thermally cycled and uncycled CFRP specimens using X-ray CT (Fig.2.22). Prior to the CT scan, specimens were cycled 50, 100 and 150 times between 77 K (hold for 10 min) and 298 K (hold for 30 min). Fig.2.22b demonstrates that the voids and defects of the QI specimens are mainly distributed between plies. Furthermore, the performed thermal cycling not only resulted in the growth of the size of voids inside the specimens but also increased the number of voids, as shown in Fig.2.22c. The volume fraction of detected defects increased 7.75 and 5 times for UD and QI CFRP specimens, respectively.

The experiments on thermally cycled UD and QI CFRP presented by Meng et al. [169] indicate tensile strength reductions of 2.4% for 0° UD CFRP and 1.4% for QI CFRP (Fig.2.22 (a and b). The degradation in flexural performance was found to be more significant than in tensile performance. The approximate reduction of 10% was obtained for both 0 ° UD and QI CFRP specimens because of the difference in the coefficient of thermal expansion of fibre and matrix materials (Fig.2.22 (c and d)). However, the changes in tensile and flexural moduli for both UD and QI CFRP were not evident after cycling, owing to the low cooling rates (7 $\mathrm{K\,min^{-1}}$). A low cooling rate was suggested to create rougher matrix surfaces, thereby enhancing the interfacial bonding between fibre and matrix [169].

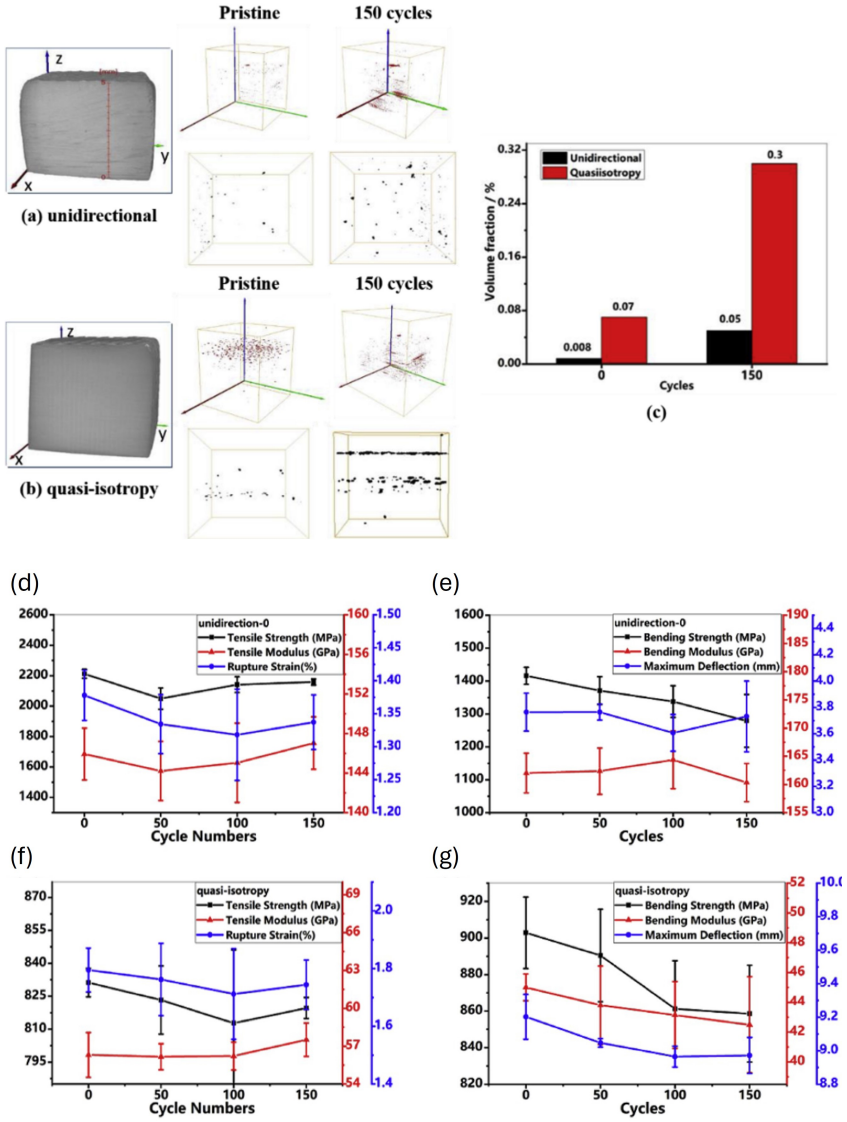


Figure 2.22: Cycling effects on CFRP laminates. The comparison of internal defects between cycled and uncycled CFRP specimens: (a) UD, (b) QI CFRP volume rendering, and (c) defect volume fractions. Mechanical performance changes due to thermal cycling: (d) 0 ° UD tension, (e) QI tension, (f) unidirectional-0 flexural and (g) quasi-isotropic flexural [169].

Di Ludovico et al. [173] conducted similar research on the tensile performance of CFRP specimens with different matrix materials and different numbers of freeze-thaw cyclings. The results show that, although there is a slight strength increase after some CFRP specimens were cycled 80 times, a uniform strength drop was observed for all 210-time cycled CFRP specimens. Nevertheless, Young's moduli of the specimens with different matrix materials have different changing trends after cycling.

2.5 Concluding remarks

Investigating CFRP's mechanical properties and failure mechanisms can be a challenging subject at both quasi-static and high-strain-rate states by virtue of the anisotropy in its internal structures. Continuous CFRP is one of the most common CFRP types in the aerospace industry, benefiting from its excellent mechanical performance, relatively low manufacturing cost and high structural designability.

Extensive research has been done regarding the quasi-static mechanical properties and failure assessment of continuous CFRP with different ply designs and loading directions. In addition to the fibres and matrix materials, the ply design does significantly influence its mechanical behaviour. CFRP performs best when the loading directions are along its fibre directions. Although the continuous CFRP can offer excellent overall mechanical strength when it is reinforced by fibres in multiple directions, its brittle failure mechanism deters it from being used in wider industrial applications. The investigation of CFRP's failure mechanism includes post-mortem methods such as visual inspection, SEM and CT scanning, and *in-situ* methods such as *in-situ* SEM and CT scanning. The dominant failure mechanisms of 0 ° UD CFRP at quasi-static tensile loading are ply delamination, matrix breakage, fibre pullout and fibre breakage, whereas those at compressive loading are mainly fibre buckling.

Among the available high-strain-rate loading apparatuses, SHPB systems were selected for the present research because of their accessible strain-rate range and compatibility with high-speed data acquisition. Previous studies have established that CFRP is commonly strain-rate sensitive, as resin behaviours, which are prominently rate-dependent, can also be involved in the composites' structural performances even in fibre-dominated loading configurations. This implies the necessity to individually investigate the failure mechanisms of CFRP at high strain rates. Due to technical limitations on high-strain-rate subsurface probing, the common practice to study the subsurface failure mechanisms of CFRP materials at high-rate loading is to simulate the process using finite element analysis (FEA) models or post-mortem inspection and reverse inference. The former is mostly developed and validated based on experimental observation in quasi-static loading conditions, and the latter cannot provide adequate scientific evidence of subsurface failure initiation and progression. Thus, *in-situ* damage visualisation and quantitative characterisation are essential to unveil the subsurface failure mechanisms of anisotropic composite materials, such as CFRP, in the high-rate domain. The experimental protocols and multi-scale datasets developed in

this thesis are intended to provide valuable physical benchmarks for validating existing failure criteria and calibrating continuum damage models. In doing so, they help address the enduring challenge of achieving reliable and physically grounded damage predictions for CFRP subjected to high-strain-rate loading and extreme temperatures.

In addition, the microstructural characterisation, mechanical properties and failure mechanisms of CFRP can be susceptible to environmental conditions, such as hygrothermal cycling and testing temperatures. However, existing research that investigates the coupling effects of loading rates and environmental conditions is far from sufficient in terms of both quantity and depth. A systematic study of CFRP's high-strain-rate subsurface failure mechanisms driven by both scientific knowledge gaps and specific industrial application needs is required.

Chapter 3

CFRP's damage at meso-scale

3.1 Background and motivations

For fibre-reinforced composites, such as CFRP, the strain-rate sensitivity of their constituents leads to mechanical responses and damage mechanisms that can differ significantly from those observed under quasi-static conditions. In recent decades, various experimental methods have been developed to measure the mechanical properties of CFRP at high-strain-rate loading. Although further refinement is still required, particularly for complex fibre architectures and laminate configurations, existing techniques are generally capable of providing reliable macroscopic mechanical data. Such data have supported the development of numerical models for predicting the global response of CFRP under conventional conditions, for example, in standard specimen geometries and at room temperature. However, increasing demands for energy efficiency and structural reliability in modern engineering applications have highlighted the need for more accurate predictions under extreme conditions, such as high strain rates and varying temperatures. In this context, there is a growing need for evidence-driven modelling approaches that integrate mechanical behaviour with damage evolution. Achieving such integration remains challenging, particularly due to the limited availability of direct and time-resolved experimental observations of subsurface damage processes under dynamic loading conditions.

3.1.1 Challenges of CFRP's anisotropy

The challenges associated with developing full-process evidence-driven modelling for CFRP in safety-critical applications, such as aerospace, lie mainly in the following aspects: complex and anisotropic material structures, internal damage observation during transient loadings, and implementation of extreme temperature environments. CFRP is a typical heterogeneous material composed of components with different properties and layouts. Therefore,

understanding CFRP's internal damage mechanisms cannot solely rely on surface observations. Except in a UD configuration, CFRP with most other ply layups, such as QI, CP and AP laminates, have surface ply and subsurface ply in different fibre arrangements. Due to the distinct physical and mechanical properties between the fibres and the matrix, the damage in each ply is highly susceptible to the fibre directions under loading. Thus, different damage morphologies can often be found through the depth of CFRP laminates.

3.1.2 Challenges of high-strain-rate damage probing

One of the obvious features of high-strain-rate loading is its short duration. While measuring the mechanical response of specimens at quasi-static loading is well-established in existing studies, acquiring force and displacement in high-strain-rate loading tests involves additional layers of complexities, such as specimen inertia and wave propagation effects. The SHPB system measures the mechanical response of specimens by synchronising wave propagation in a set of bars with identical, uniform diameters. Meanwhile, the common practice to examine the damage of specimens in this transient loading event on a SHPB setup is incorporating visible-light high-speed cameras facing the specimens and recording images during the rapid loading of specimens. The cameras are normally synchronised to the SHPB loading with high accuracy and tuned accordingly with the length of the loading events, enabling effective damage capture in specimens. Specimens are sometimes painted with black speckles on a white background to facilitate the local displacement and strain correlations based on acquired images. However, due to the anisotropy of composites, the observed surface damage often does not reflect the damage through the thickness of specimens. Therefore, new approaches are needed that can simultaneously accommodate the anisotropy of CFRP and the transient nature of high-strain-rate loading.

Promisingly, advances in synchrotron X-ray in recent years have provided a novel solution for tackling this challenge. It uses high-energy and focused X-ray beams to propagate through the specimens during high-strain-rate loading, producing attenuation and phase shifts. The altered X-ray is then converted into visible light and captured by high-speed cameras. This dynamic X-ray technology enables subsurface damage probing in a 2D stacking fashion. Thus, in this chapter, the methodology and experimental results of using dynamic X-ray on the high-strain-rate testing of CFRP are presented. The reported experiments were carefully designed according to the loading and specimen features to obtain

valid information to the greatest extent, because of the current limitation on spatial resolution (both in-plane and out-of-plane directions).

3.1.3 Challenges of temperature control

The third challenge is effectively implementing extreme testing environments (i.e., high and low temperatures) during the high-strain-rate loading and dynamic X-ray probing. This environmental setup needs to satisfy a few requirements, such as stable temperature maintenance, non-interference with SHPB loading, and nearly complete transparency to X-ray propagation. To bring the specimens' internal temperature to the testing conditions, it is necessary to leave the specimens in a stable testing environment for a sufficient amount of time. This requires good temperature control and maintenance in the loading/environmental chamber. Then, the loading/environmental chamber needs to be mounted to the SHPB loading system, allowing the free deformation and sliding of the bars for elastic wave propagation. Lastly, the chamber needs to have two windows, one in the front and the other in the back of the chamber. The X-ray beam should be able to transmit through these window sections without obstruction from the window materials or the frost forming on the windows caused by low temperatures.

3.1.4 Objectives of the chapter

In light of this, the first objective of this chapter is to establish an effective experimental methodology, which involves specimen design, loading setup, temperature control, and dynamic X-ray imaging. This combination of systems is expected to achieve mechanical measurements, damage visualisation, and temperature recording with high accuracy and efficiency. Then, the data obtained across different metrics needs to be analysed integratively in a time-synchronised and resolved manner. This requires data exploration and processing in individual metrics (such as the imaging data obtained from dynamic X-rays) and a combination of multi-metrics (such as the synchronised combination between curves and images). The mapped mechanical and damage development with respect to time should be able to inform the damage mechanisms under the tested conditions, producing unique experimental evidence that can be used to validate and improve existing numerical simulation modes and extend their valid applications to extreme loading cases.

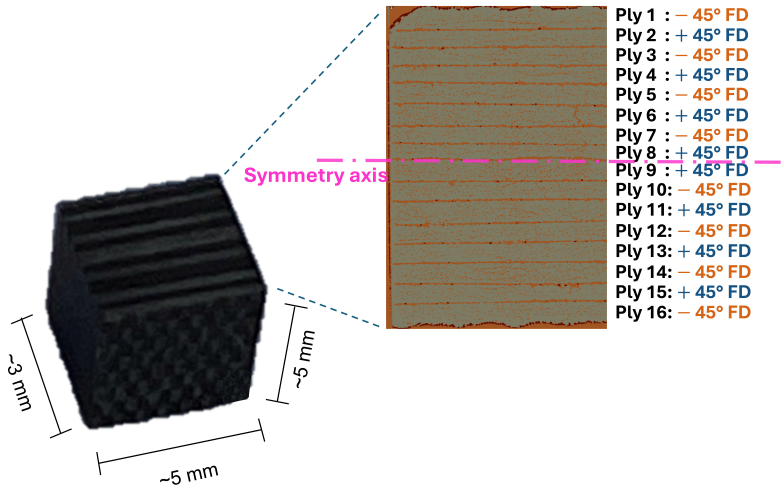


Figure 3.1: CFRP specimens used in this research showing their geometry, dimensions, and ply stacking sequence of $[\pm 45]_{4s}$. The symmetry axis is indicated between the two plies in the middle with $+45$ ° FD.

3.2 Summary of Paper I

3.2.1 Material and specimen

The material tested in this chapter is an aerospace-grade CFRP laminate comprising "standard modulus" carbon fibres supplied by Toray Industries, Inc., and a high-performance epoxy matrix provided by Hexcel Corporation. The layup of the CFRP laminate follows a stacking sequence of $[\pm 45]_{4s}$ using UD CFRP pre-pregs and was implemented by the hand-laying method (Fig.3.1). The stacked pre-pregs were then placed into an autoclave machine and cured according to procedures of 1-2 °C/min heating rate, 2-5 °C/min cooling rate, and 120-min duration at 180 °C. Afterwards, the cured CFRP laminate panel will be cut into small cubic blocks ($5 \times 5 \times 3$ mm^3) for environmental ageing and high-strain-rate loading.

The ± 45 ° laminate configuration was selected because axial loading of this layup generates a strong matrix-dominated in-plane shear response in the material coordinates. This makes the specimen particularly suitable for investigating shear-driven damage mechanisms, including matrix cracking, ply splitting, and delamination, which are essential to the objectives of the present study [101]. An end-loaded specimen design was adopted to ensure compatibility with the SHPB-based high-strain-rate loading system and synchrotron

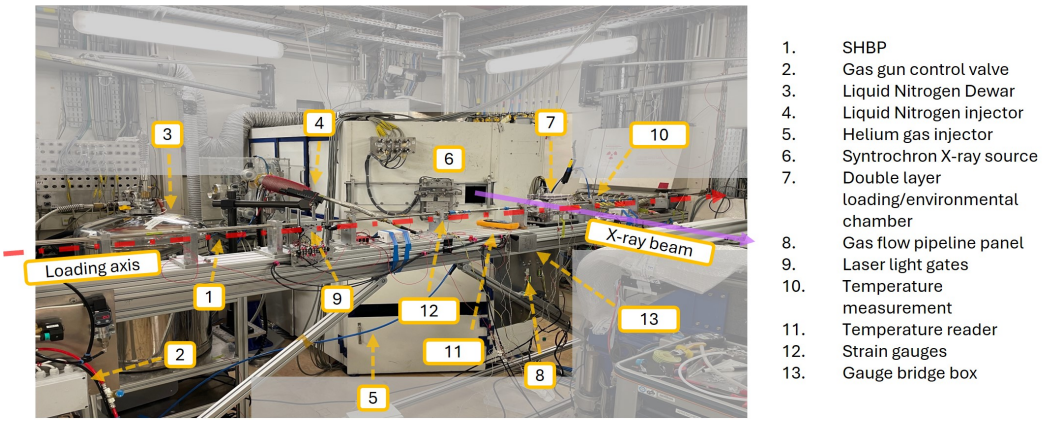
X-ray imaging setup. Compared with more complex shear or combined-loading fixtures, the end-loaded configuration provides a simpler load path, facilitates stress-wave transmission through the specimen, minimises obstruction of the X-ray beam path, and allows the gauge region to remain accessible for time-resolved damage observation. Therefore, the specimen design represents a practical compromise between achieving a shear-dominated damage state, maintaining dynamic loading reliability, and enabling direct internal damage characterisation. It should be noted that this specimen design was not intended to provide a general standardised compressive or shear strength measurement for CFRP laminates. Instead, it was designed to generate and observe representative shear-dominated damage processes in $\pm$45 ° CFRP laminates under high-strain-rate and low-temperature conditions.

To represent the potential service conditions of CFRP components, such as aero-engine fan blades and casings, hygrothermal ageing and *in-situ* low-temperature conditions were incorporated as experimental parameters. The selected temperature range reflects typical operating environments, where components may experience ambient temperatures during ground operation and sub-zero temperatures at high altitudes. The hygrothermal cycling condition (−50 to 90 °C) was designed to simulate repeated thermal fluctuations and environmental exposure during service, which can induce matrix degradation, residual stress accumulation, and interfacial weakening. ASTM standard 5229 [174] was used to prepare the specimens under two ageing conditions - dry and hygrothermally cycled. The dry specimens were oven dried at 70 °C until no further weight could be reduced, and the hygrothermally cycled specimens were subjected to 250 temperature cycles between -50 and 90 °C (please refer to the paper for more details [147]). In addition, two *in-situ* testing temperatures were designed, namely, room temperature (23 ± 2 °C) and the low temperatures (-30 ± 2 °C). Before any loading, the internal micro-structures of the conditioned specimens were characterised using micro-CT with a slice pixel size of 2.1 µm at beamline ID19 at the ESRF.

3.2.2 Methodology

The experiment implementation system is primarily composed of 3 sub-systems - high-strain-rate loading platform, temperature control chamber and device, and synchrotron-based dynamic X-ray imaging setup. A traditional SHPB system is introduced to exert high-strain-rate loading on the specimens, as shown in Fig.3.2. This SHPB loading plat-

form consists of a striker (sometimes called a projectile), incident bar, and transmitted bar. All of these bars are 12.7 mm in diameter and made of Ti-6Al-4V titanium alloy. A 150 mm length striker was selected based on the wave propagation properties of the specimens, and the incident and transmitted bars were 1300 and 1100 mm long, respectively. In addition, two sets of strain gauges were mounted with one 60 mm upstream of the bar/specimen interface on the incident bar and the other 40 mm downstream of the bar/specimen interface on the transmitted bar. These strain gauges measured the elastic wave propagation in the incident and transmitted bars. Thereafter, a classical one-dimensional wave propagation theory [175] can be applied to analyse the measured waves and produce the stress-strain responses of the specimens (refer to Paper I for more details [147]).



1. SHBP
2. Gas gun control valve
3. Liquid Nitrogen Dewar
4. Liquid Nitrogen injector
5. Helium gas injector
6. Syntrochron X-ray source
7. Double layer loading/environmental chamber
8. Gas flow pipeline panel
9. Laser light gates
10. Temperature measurement
11. Temperature reader
12. Strain gauges
13. Gauge bridge box

Figure 3.2: SHPB loading setups at beamline ID19, ESRF. The loading is perpendicular to the X-ray propagation direction.

Temperature control was achieved by installing a temperature control device in the SHPB loading system. This temperature control device comprises three parts - a gas-flow pipeline panel, a set of proportional–integral–derivative (PID) controllers, and a double-layer loading/environmental chamber. The primary use of the gas flow pipeline panel (Fig.3.3a) is to convert liquid nitrogen (LN2) into nitrogen gas (N2) and heat the gases in the pipeline to the target temperatures, while allowing a controlled gas flow. The heating of the gases was achieved by a set of PID controllers (Fig.3.3b). The loading/environmental chamber has an inner chamber and an outer chamber. The inner chamber was where loading and cooling took place, and the outer chamber was used to establish an isolation between the cold space in the inner chamber and the room-temperature space in the ambient environment. In such a way, frosting of the windows on the chamber walls, which was used to enable the non-obstructive penetration of X-ray beams, can be prevented (Fig.3.3c). The pipeline panel has

two channels, and thus two pairs of inlets and outlets. During the experiments, one channel received room-temperature helium gas (He), heated it to high temperatures in the pipeline, and delivered it to the outer chamber to form an isolation. In the experiments presented in Chapters 4 and 5, N2 was used in this outer chamber channel due to laboratory constraints associated with the gas supply system. The other channel received LN2, converted it into N2, heated the N2 to the target low temperature, and injected the N2 into the inner chamber as a coolant. The original development of this in-house temperature-control system was led by a former group member - Dr David Sory.

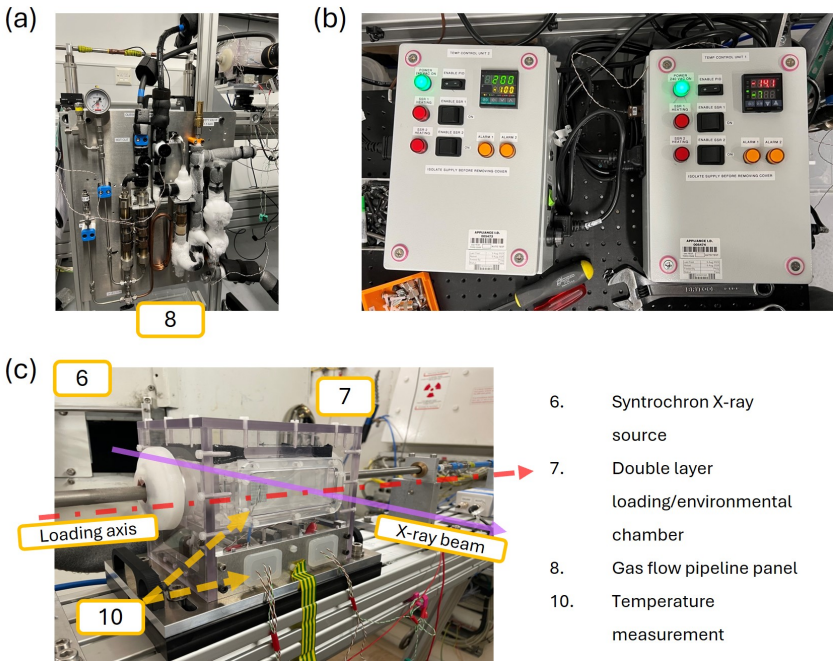


Figure 3.3: Temperature control system and its main components. (a) Gas flow pipeline panel used to condition and deliver the heating and cooling gases. (b) PID controllers for automatic temperature adjustment and maintenance. (c) Double-layer loading/environmental chamber, which has an inner chamber and an outer chamber. Windows on both sides of the chamber allow nearly non-obstructive transmission of X-rays. The development of this temperature-control system was led by Dr David Sory.

A XPCI system established at synchrotron light sources was implemented to visualise subsurface damage of CFRP laminates *in situ* during high-strain-rate loading. The SHPB loading system was placed downstream of the synchrotron X-ray light source and perpendicular to the X-ray propagation direction (Fig.3.2), allowing the X-ray beam to transmit through the specimen laterally during loading (Fig.3.3c). After that, the X-ray beam travelled downwards to the imaging setups, as shown in Fig.3.4a. A scintillator is located downstream of the specimen and facing the inbound X-ray. When the X-ray passes through, the scintillator

is stimulated and emits visible-light photons. The visible-light photons are then reflected into two high-speed cameras by two pellicle beamsplitters placed upstream and downstream of the scintillator (Fig.3.4b). The X-ray used in this study was generated in a 4-bunch fill mode with a pair of aligned U32 undulators. This setup produces a train of polychromatic ("white-beam") X-ray pulses with a 704 ns time separation and about 23 keV. The cameras were operated in an interleaved manner with an exposure time of 600 ns and acquired images every 1410 ns, thus capturing each pulse of the X-ray train. Under these settings, the frequency mismatch between the cameras and X-rays can lead to a slight image drift of about 2 ns. However, given the relatively long camera exposure time in the present experiments, this effect is considered negligible. They were triggered by strain gauge signals when the voltage reached target levels. For more details, refer to the paper in Section 2.4 [147].

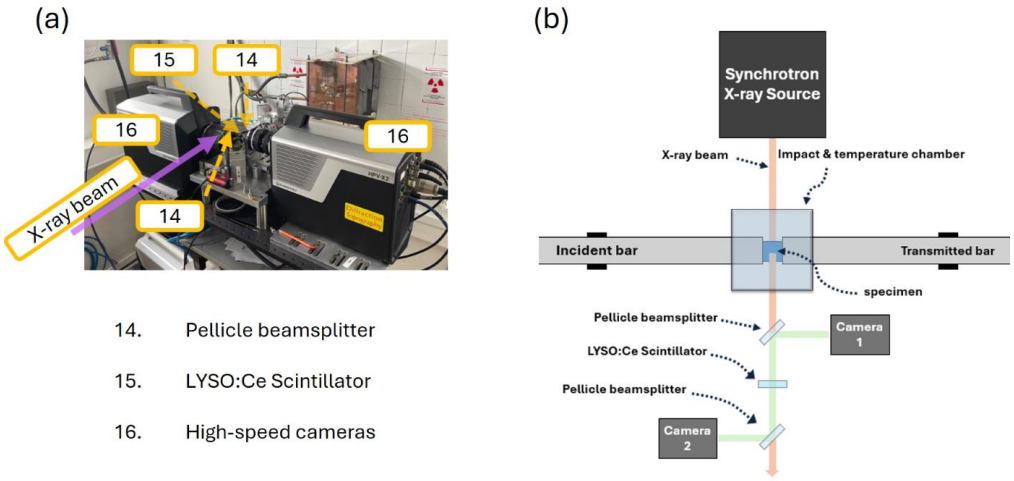


Figure 3.4: Dynamic X-ray imaging setup at synchrotron beamline. (a) Photo of the setup at the beamline ID19, the ESRF. (b) Schematic demonstrating the positions of the X-ray source, SHPB, X-ray beam, lens and cameras.

3.2.3 Research findings

Prior to high-strain-rate loading tests, the mechanical responses of the specimens at quasi-static loading were measured using a universal loading machine at a specimen strain rate of 3.3×10^{-3} s^{-1} to establish a baseline for comparison and analysis. It can be seen that, despite similar stiffness and modulus, dry specimens have an obviously higher strength compared to cycled ones (Fig.3.5). However, the overall mechanical behaviour of the specimens under these two different conditions is similar. Fig.3.6 demonstrates the mechanical

measurements of the specimens at high-strain-rate loading acquired using the SHPB platform. Compared with specimens tested under quasi-static loading, high-strain-rate loading can trigger significantly higher strength responses in specimens under both dry and hydrothermal cycled conditions. In addition, it was found that, at high strain-rates, specimens have a higher strength at low temperature in both ageing conditions, of which the cycled specimens demonstrate a more obvious difference, as shown in Fig.3.6. A more rapid stress drop can be seen after the peak stress in the low-temperature specimens, whereas the room-temperature specimens entered a “flow stress” region.

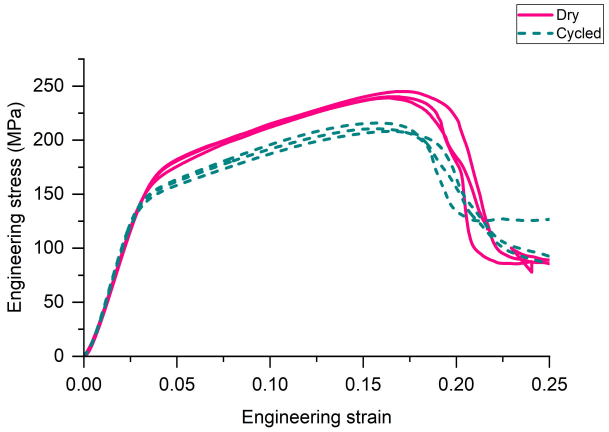


Figure 3.5: Stress-strain curves of the specimens in dry and hygrothermal cycled conditions under quasi-static compression obtained by using a universal loading machine.

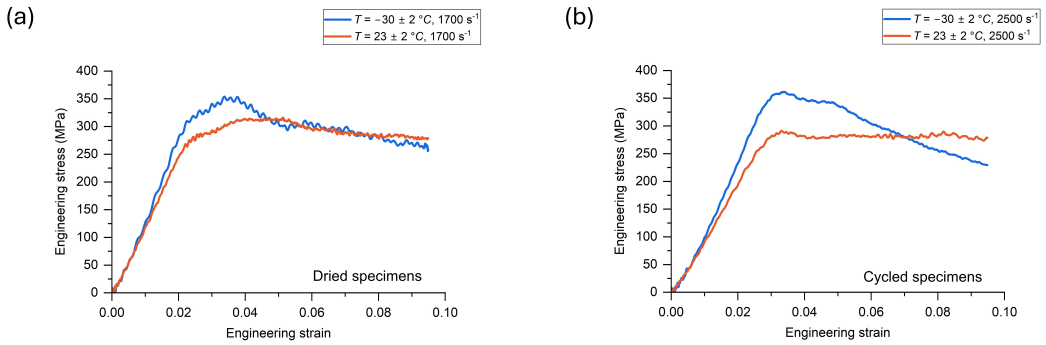


Figure 3.6: Stress-strain curves of the specimens under high-strain-rate compression tested on the SHPB loading platform: (a) dry specimens, and (b) hygrothermal cycled specimens.

Fig.3.7a shows the stress-time curve of two of the cycled specimens, one at room temperature and the other at low temperatures. It again shows the trend observed in the stress-strain plots: low-temperature specimens have higher strength but a more rapid stress drop

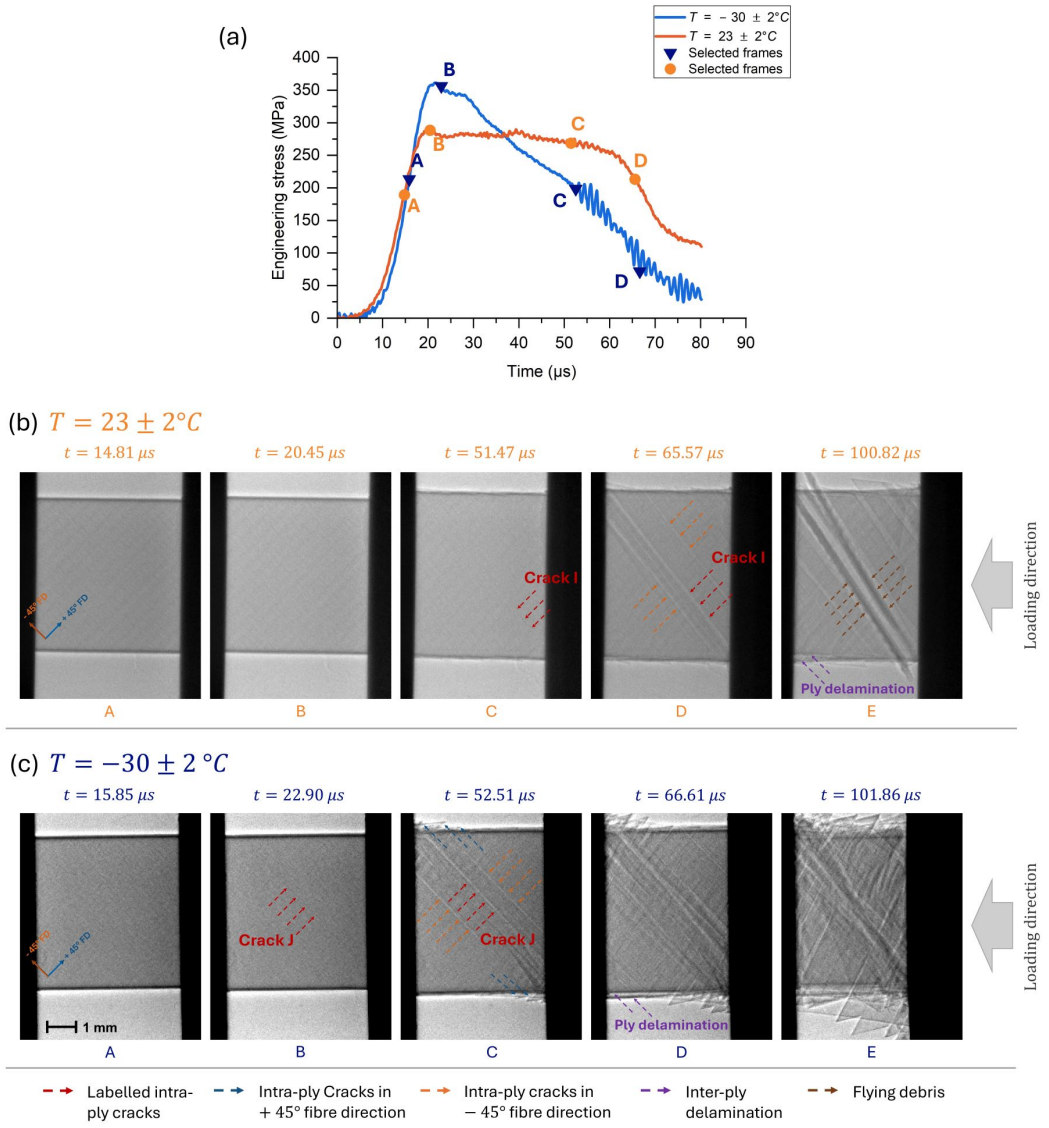


Figure 3.7: *In-situ* damage probing of the specimens using XPCI at the synchrotron facility. (a) Stress-time plot of the specimens as a reference for damage development characterisation using X-ray images. (b) Representative X-ray radiographies of a specimen at room temperature. (c) Representative X-ray radiographies of a specimen at low temperature. Damage initiated earlier and evolves more rapidly at low temperature. Evident stress drops can be found after the observable damage in XPCI images. Ply delamination also initiated earlier at low temperatures.

after the peak. Using the synchrotron-based XPCI system, *in-situ* X-ray radiographies were obtained. Several key frames are presented in Fig.3.7 (b and c) in a time sequence with label marks made on the curves in Fig.3.7a as reference. It can be seen that the first observable damage occurred at $t = 51.47$ μs in the room-temperature specimen, while the earliest crack was found at $t = 22.90$ μs at low temperatures. After the occurrence of damage, a

stress drop can be seen in both specimens, as displayed in Fig.3.7a. This indicates that damage can initiate earlier and develop more rapidly in low-temperature specimens compared to their counterparts at room temperature. Evident ply delamination is seen in Frame D ($t = 66.61$ µs) at low temperature, while room-temperature specimens only had slight ply delamination even in Frame E ($t = 100.82$ µs). The strain development in low-temperature specimens in the late loading stages is evidently more rapid than that in room-temperature specimens. This can be noticed by comparing the residual length of specimens in Frame E at both temperatures.

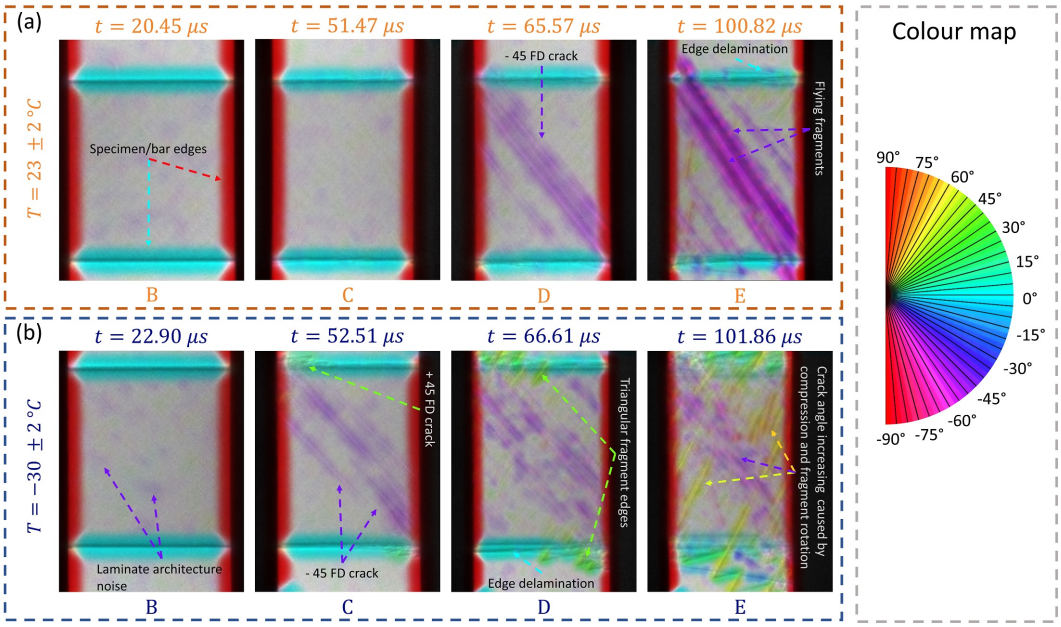


Figure 3.8: Tracking damage orientations based on the *in-situ* XPCI images: (a) specimen at room temperature and (b) specimen at the low temperature. The initiated intra-ply cracks rotated with the angle change of fibres in the plies. Intra-ply cracks at both $+45$ and -45 ° fibre direction can be found in the low-temperature specimen, whereas the intra-ply cracks in the room-temperature specimen are mainly in -45 ° fibre direction.

Performing orientation analysis on the obtained XPCI radiographies reveals that the initiated intra-ply crack rotated with the fibre direction in each ply, indicating that the damage produced is in the form of intra-ply matrix cracking between the fibres at this stage. The observed intra-ply cracks were about -45 ° due to the fibre direction in the surface plies. With compression progress, intra-ply cracks in both $+45$ and -45 ° fibre directions (not the absolute ± 45 ° directions) are seen at low temperatures at the late loading stage (e.g., Frames D and E). This suggests that the intra-ply cracks with observable size were not only in the surface plies (all in -45 ° fibre direction) but also in the subsurface plies (some in $+45$

° fibre direction). Meanwhile, no obvious cracks in $+45$ ° fibre direction can be found in the room-temperature specimen, even at the late loading stages (e.g., Frames D and E). That is to say, the intra-ply cracks with the observable size might not yet have been generated in the subsurface plies.

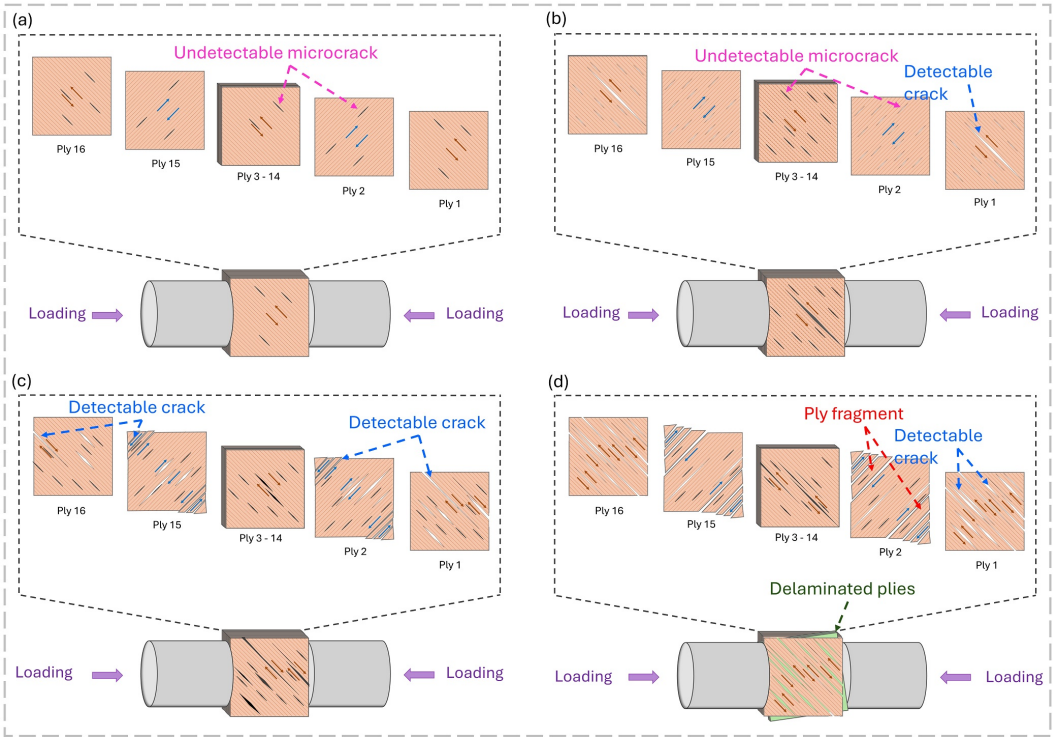


Figure 3.9: Schematic showing the mechanisms of damage initiation and evolution in tested CFRP laminates with ply breakdowns. (a) Micro-scale damage that is difficult to detect under the current XPCI setup. (b) Micro-cracks coalesce and broaden, forming detectable cracks in surface plies. (c) As compression continues, detectable cracks emerge in subsurface plies and in both fibre directions. (d) Detectable cracks grow and cause breakage of the surface plies and ply delamination.

Despite differences in the damage timescale across temperatures, their meso-scale damage mechanisms (on the order of 100 µm) seem similar. As illustrated in Fig.3.9a, the damage might initiate in the form of micro-scale intra-ply cracks due to the excessive intra-ply shear between the fibres and also the potential fibre micro-buckling during loading. It was not detectable under the current XPCI setup due to resolution limitations, but it was subsequently confirmed in Paper II [176]. Then, the micro-scale cracks in the surface plies first developed into large and thus detectable intra-ply cracks owing to the lack of shear and lateral restraints on the surface (Fig.3.9b). With compression and deformation progression, the damage initiated continuously evolves, and meso-scale intra-ply cracks are generated

in the subsurface plies (Fig.3.9c), indicated by the cracks in the $+45\,^{\circ}$ fibre direction. At the late loading stages, specimen lateral expansion, excessive inter-ply shear, and fibre lateral buckling have continuously developed. These effects combine and lead to ply delamination. In terms of the mechanical reflection of the damage development. The onset of surface intra-ply cracks at the meso-scale stops the stress from increasing in the specimens. The stress in the room-temperature specimens enters a “flow stress” region, whereas prominent stress drops can be seen in the specimens at low temperatures. At the time of forming observable delamination, the specimens have lost a considerable amount of their load-bearing capacity, which can be seen as a complete failure of the specimens.

3.3 Chapter remarks

The work presented in this chapter provides, for the first time, direct visualisation of internal damage initiation and evolution in CFRP laminates under the combined extreme conditions of high strain-rate loading and low temperature. By correlating the time-resolved damage progression with the measured global mechanical response, this study offers unique insight into the temperature sensitivity of failure processes in CFRP laminates.

Despite establishing a time-resolved damage characterisation framework, the current limitations of XPCI technology, more specifically its limited spatial resolution in both the in-plane and through-thickness directions, preclude detailed interpretation of damage morphology and interactions within the laminate volume at finer length scales. Consequently, in order to develop a clearer and more comprehensive understanding of the temperature effects on different damage modes and morphologies in CFRP laminate structures, alternative experimental strategies are required to complement the datasets obtained in this work.

3.4 Paper I: Effect of temperature on high strain-rate damage evolving in CFRP studied by synchrotron-based MHz X-ray phase contrast imaging

Composites Part B 279 (2024) 111445

Contents lists available at ScienceDirect

Composites Part B

journal homepage: www.elsevier.com/locate/composites

Effect of temperature on high strain-rate damage evolving in CFRP studied by synchrotron-based MHz X-ray phase contrast imaging

Xiyao Sun [a], David Sory [a], Kai Liu [a], Bratislav Lukić [b,c], David Simonian [a], Kwan Lok Wong [a], Alexander Rack [b], David Chapman [a], Nik Petrinic [a], Daniel Eakins [a,*]

[a] Department of Engineering Science, University of Oxford, Parks Road, Oxford, OX1 3PJ, UK
[b] European Synchrotron Radiation Facility, 71 Av. des Martyrs, Grenoble, 38000, France
[c] Henry Royce Institute for Advanced Materials, Department of Materials, The University of Manchester, Manchester, M13 9PL, UK

ARTICLE INFO

Keywords:
A. Polymer-matrix composites (PMCs)
B. Impact behaviour
B. Low-temperature properties
C. Damage mechanics
Synchrotron X-ray phase-contrast

ABSTRACT

The present study demonstrates experimental evidence of subsurface mesoscale damage initiation and evolution in angle-ply CFRP laminates under high strain-rate loading at low temperatures using synchrotron-based X-ray MHz radiography. A bespoke set of loading, temperature control and *in-situ* X-ray imaging systems were applied to simultaneously correlate high strain-rate mechanical response with observed subsurface damage in a time-resolved manner. The results demonstrate that independent of temperature, damage evolved following a specific sequence; firstly intra-ply shear cracking along the fibre direction, developing into multi-layer cracking with continued deformation, and finally culminating in inter-ply delamination and complete failure of the specimen. The timescale for this sequence, however, was observed to strongly depend upon temperature, with low temperatures resulting in more rapid damage evolution and loss of mechanical strength.

1. Introduction

To respond to global environmental policies, a wide range of modern transport industries, such as aerospace, automobile and maritime, have invested heavily in the research and application of carbon-fibre reinforced polymer (CFRP) composites due to their high stiffness and strength-to-weight ratio over conventional metal-based alternatives [1–3]. In such applications, CFRP components can be exposed to a multitude of adverse conditions, including extremes of mechanical loading, humidity and temperature. However, understanding of the behaviour of CFRP under such complex and often combined conditions is incomplete, which is hindering CFRP composites from being more widely used in future industrial products.

There are ample studies exploring the strain-rate sensitivity of epoxy-based CFRP laminates at room temperature [4–7]. For extreme temperatures, it has been found that the tensile [8–13] and bending [14] performance of CFRP is susceptible to temperature change. In addition, thermal cycling can also lead to strength degradation for CFRP laminates because of the generated micro-damage between fibre and matrix as the result of their differing thermal expansion characteristics [15].

The failure of CFRP could be sudden and catastrophic due to its well-known brittleness [16–19]. [0/90] cross-ply (CP) [4], [±45] angle-ply (AP) [20], quasi-isotropic (QI) [5] and 90° off-axis biaxial braided (BB) [21] CFRP laminates have been observed to fail by inter-ply delamination under in-plane compression with different strain-rates (confirmed via post-mortem examination using visual and computed tomography (CT), and *in-situ* examination using visible light and infrared thermal imaging). Previous investigation of CFRP laminates tested at *in-situ* extreme temperature indicates both high and low temperatures can weaken the fibre/matrix bonding at the interface. Where, for example under tensile loading at quasi-static (QS) and intermediate strain-rates, more pronounced fibre debonding and laminate delamination was observed in postmortem inspection relative to room temperature testing [8,13]. Under flexural loading (three-point bending), damage in CFRP specimens has been shown to propagate faster and expand wider at lower temperatures, causing more severe delamination [14].

X-ray imaging, especially X-ray CT, has become an important technique to non-destructively investigate the internal structures of composite components and damage [22,23]. Instead of only performing post-mortem scanning, recent developments have enabled *in-situ* CT scanning to characterise internal structural changes under loading induced

* Corresponding author.
E-mail addresses: xiyao.sun@eng.ox.ac.uk (X. Sun), daniel.eakins@eng.ox.ac.uk (D. Eakins).
URL: https://shock.eng.ox.ac.uk (D. Eakins).

https://doi.org/10.1016/j.compositesb.2024.111445
Received 22 January 2024; Received in revised form 5 March 2024; Accepted 9 April 2024
Available online 20 April 2024
1359-8368/© 2024 The Author(s). Published by Elsevier Ltd. This is an open access article under the CC BY license (http://creativecommons.org/licenses/by/4.0/).

Table 1
Specimen pretreatment and testing conditions.

Specimen label	Pretreatment condition	Appx. impact velocity, m/s	Testing temperature, °C
Dry_Room	Oven dried	11.0	23 ± 2
Dry_Low	Oven dried	11.0	-30 ± 2
Cycled_Room	250-time HTC cycled	15.5	23 ± 2
Cycled_Low	250-time HTC cycled	15.5	-30 ± 2

* HTC: hygrothermally cycled.

by tension [24], compression [25], flexure [26] and wedge indentation [27]. Apart from that, some recent research has also demonstrated that synchrotron-based dynamic X-ray imaging has a great potential to probe the subsurface damage of composites under high strain-rate (HSR) loading [28,29].

While a limited number of studies have visualised the initiation and evolution of damage in CFRP laminate under HSR loading [28,29], no studies have resolved the *in-situ* progression of mesoscale subsurface damage at low temperatures. Direct experimental evidence would greatly enhance both existing and future simulation models used to predict the HSR failure of CFRP laminates. In this study, a synchrotron-based X-ray source, together with a bespoke set of synchronised loading, temperature control, strain measurement, ultra-fast X-ray imaging and data acquisition system, was implemented to achieve real-time mesoscale damage probing and property measurement for tested specimens at HSR loading. Synchrotron-based X-ray phase-contrast imaging (XPCI) was introduced as it facilitates the visualisation of damage and fine features (*e.g.*, newly generated interface) due to phase contrast enhancement. A group of AP CFRP specimens with different ageing conditions were prepared and tested under HSR in-plane compression at room and low temperatures. The subsurface damage development and associated mechanical behaviours were characterised and analysed integratively in a time-resolved manner. Finally, the failure micromechanics and models of tested CFRP laminates were deduced and discussed.

2. Materials and methods

2.1. Material and specimen

The material studied in this work is an aerospace-grade epoxy-based carbon-fibre reinforced polymer composite (CFRP) that is comprised of autoclave-cured laminates with a curing cycle of 1–2 °C/min heating rate, 2–5 °C/min cooling rate, and 120-min duration at 180 °C. It was manufactured by using the hand lay-up method with $[\pm 45]_{4s}$ AP laminations and cut into a size of $5 \times 5 \times 3$ mm^3 for effective environmental ageing and HSR loading. Two ageing conditions were considered in the present research — dry and hygrothermally cycled (see Table 1). The dried specimens were oven-dried following ASTM standard 5229 [30] at 70 °C for four weeks until no further weight could be reduced. The cycled CFRP specimens were saturated in an environmental chamber following the same ASTM standard at 70 °C with a constant relative humidity of 85% for four weeks to ensure complete saturation before cycling. After full saturation, the CFRP specimens were subjected to 250 sequential temperature cycles between −50 and 90 °C. Each cycle took about 150 min, with the 250 cycles therefore taking approximately 1 month to complete. Specimens with a higher number of cycles were also prepared, tested and analysed. However, their differences in terms of mechanical properties and damage mechanisms were found to be trivial compared to 250-time cycled specimens. Thus, only the results of 250-time cycled specimens are presented and discussed as a representation of cycled specimens in this work. Following controlled ageing, the internal configuration for each component (fibres, matrix and voids) and possible defects caused by manufacture and ageing were inspected by synchrotron-based X-ray μCT (2.1 μm) at beamline ID19 at the ESRF.

2.2. High strain-rate loading

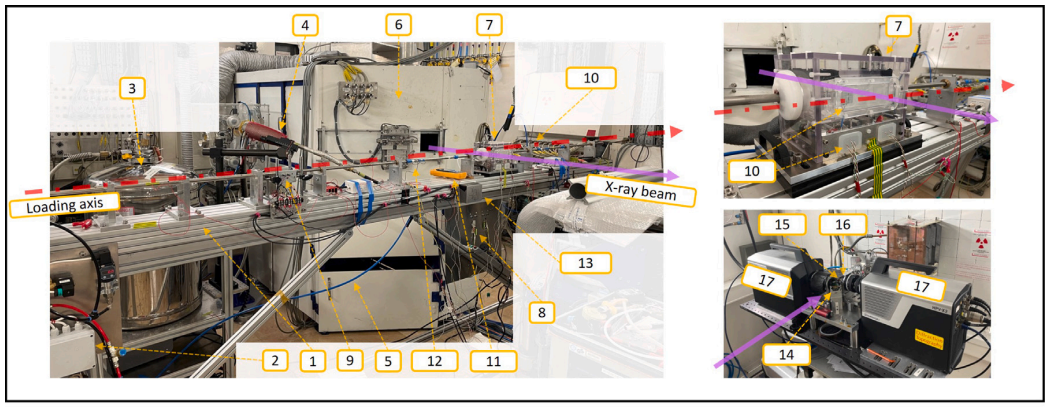
HSR loading was applied using a split-Hopkinson pressure bar (SHPB) system [31]. As shown in Figs. 1 and 2, this SHPB setup consisted of a striker, input and output bars made of titanium alloy (Ti-6Al-4V) with a diameter of 12.7 mm. Ti-6Al-4V was adopted considering the high strength and mechanical impedance of the CFRP specimen studied in this work. The striker was 150 mm in length, and the input and output bars were 1300 mm and 1100 mm long, respectively. Before loading, two 3 mm-thick loading platens made of the same material and diameter as the bars were attached at the bar ends and in contact with the specimens to avoid damage to the bars. The specimens were sandwiched between the input and output bars with a thin layer of grease applied at the specimen/platen and bar/platen interfaces to reduce friction. A set of strain gauges was mounted 60 mm uprange of the specimens on the input bar and 40 mm downrange of the specimens on the output bar to record the incident, reflected, and transmitted strain pulses.

2.3. Test temperature control

A bespoke cryogenic chamber was designed and manufactured to enable good temperature isolation and impact debris containment whilst ensuring minimal X-ray beam attenuation. The chamber was constructed of Perspex and consisted of an inner and outer chamber. During the tests the temperature within the inner chamber was controlled by injecting cooled nitrogen gas using a Cobra Nitrogen Cooler from Oxford Cryosystems. The outer chamber was filled with room-temperature helium gas to prevent frost from forming on the X-ray window and introducing phase artefacts at the detector plane perturbing the X-ray image (Figs. 1 and 2). The temperature in the inner and outer chambers was measured and recorded from multiple measurement points and monitored from both the experimental hutch and control room.

2.4. High-speed X-ray imaging

Real-time visualisation of the evolution of impact initiated damage was performed at the ID19 beamline of the ESRF [32]. The SHPB system was aligned perpendicular to the X-ray beam path, as illustrated in Figs. 1 and 2, allowing the X-ray pulse train to propagate through the specimens normal to the direction of loading. In the present study, the 4 bunch fill mode was used, and the X-ray source at ID19 was a pair of aligned U32 undulators, producing a train of polychromatic X-ray pulses separated in time by 704 ns (“white-beam” with peak in the X-ray spectrum at about 23 keV). The indirect single-bunch X-ray imaging strategy employed in the current study is discussed in greater detail by Escauriza et al. [33]. Briefly however, the imaging system employed a 500 μm thick LYSO:Ce (Ce-dopped $Lu_{1-x}Y_xSiO_5$, Hilger Crystals, UK) single-crystal scintillator with 40 ns decay time, optically relayed to a pair of Shimadzu HPV-X2 high-speed cameras as illustrated in Figs. 1 and 2. Each optical relay consisted of a pair of Nikon 50 mm F/1.4 lenses producing an effective 1 × magnification with 0.34 numerical aperture. This indirect X-ray detector assembly was placed ∼9 m downstream of the specimen to allow sufficient propagation distance for phase-contrast to form and hence enhance the



1. SHBP
2. Gas gun control valve
3. Liquid Nitrogen Dewar
4. Liquid Nitrogen injector
5. Helium gas injector
6. Synchrotron X-ray source
7. Double layer impact and temperature control chamber
8. Bespoke temperature control panel
9. Laser light gates
10. Temperature measurement
11. Temperature reader
12. Strain gauges
13. Gauge bridge box
14. Pellicle beamsplitter
15. LYSO:Ce Scintillator
16. Mirror
17. High-speed cameras

Fig. 1. Photos of the experimental setup, comprising the SHPB system, cryogenic impact chamber, and imaging system, at ID19, ESRF.

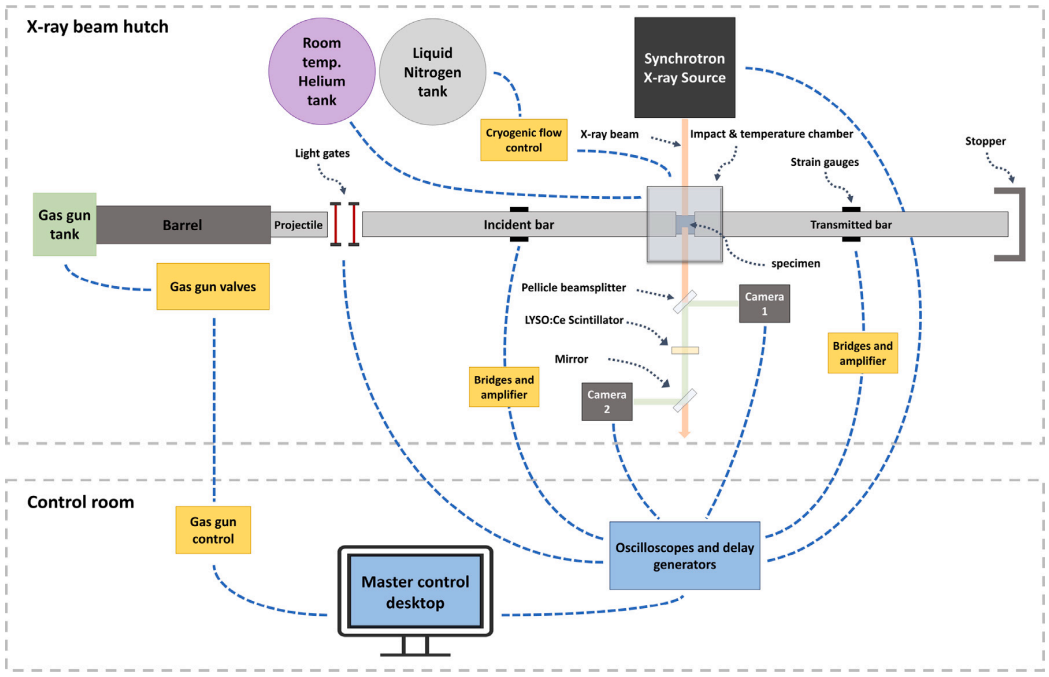


Fig. 2. Schematic of the experimental setup at ID19, ESRF, illustrating the key devices, components, connections, and beam paths of the SHPB and diagnostic systems.

visualisation of crack interfaces. The Shimadzu cameras were synchronised to the X-ray pulse train using the methods described in [33]. The 600 ns exposure of each camera captured scintillator emission primarily from a single X-ray bunch, and the camera triggering and frame rate (interframe time 1410 ns) were implemented such that the image sequences from the two cameras were interleaved in time to capture every bunch. The Shimadzu cameras were triggered from the voltage signals produced by the strain gauges on the input bar of the SHPB, enabling synchronisation of the radiography to the load history of the specimen. Finally, a fast X-ray shutter, gated open during the dynamic event, was used to reduce the total X-ray exposure duration to approximately 200 ms to minimise radiation-induced degradation of the specimen.

2.5. Mechanical property analysis

The stress–strain response of the specimens during HSR loading was estimated by assuming one-dimensional wave propagation [31]. The force recorded in the input and output bars was compared to evaluate force equilibrium. The engineering strain of the tested specimens obtained by processing the strain gauge signals was checked against the image measurements of the captured XPCI radiography. The bar energy

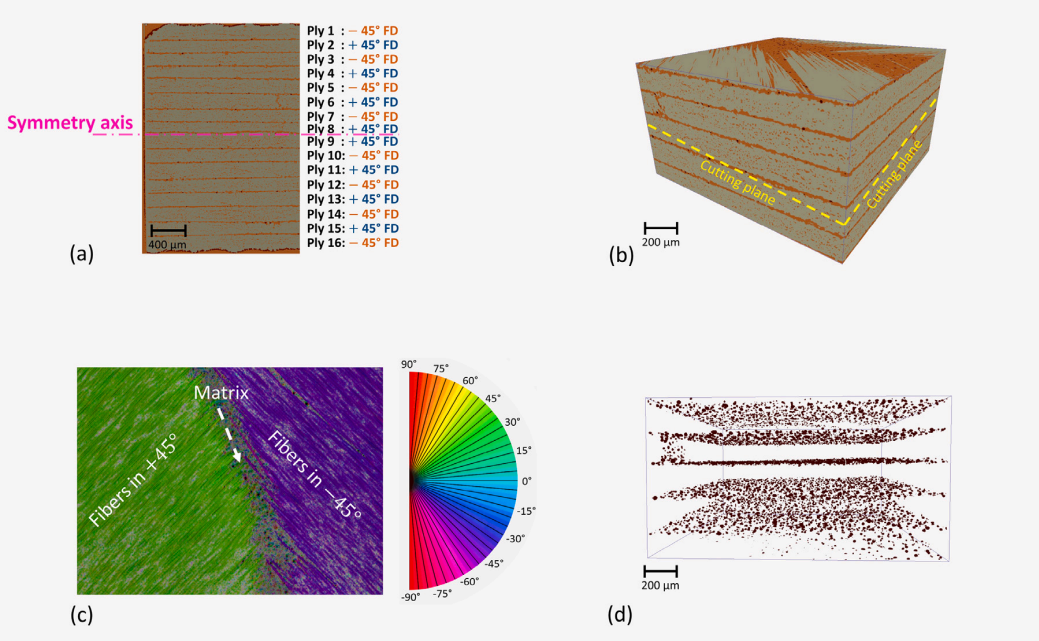


Fig. 3. Internal structural characterisation and defect checking for XPCI by using X-ray CT scanning: (a) an orthogonal slice with ply lay-ups, (b) volume rendering of a small specimen section with image segmentation, (c) fibre orientation identification on the cutting plane with the colour code performed by using OrientationJ plugin in ImageJ, and (d) segmented voids that distribute in the glue layers between plies. (For interpretation of the references to colour in this figure legend, the reader is referred to the web version of this article.).

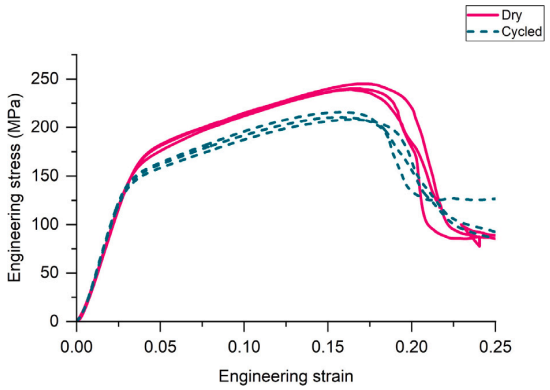


Fig. 4. Stress–strain curve of dried and cycled specimens under quasi-static (3.3×10^{-3} s^{-1}) uni-axial compression at room temperature setting a baseline for high strain-rate property analysis.

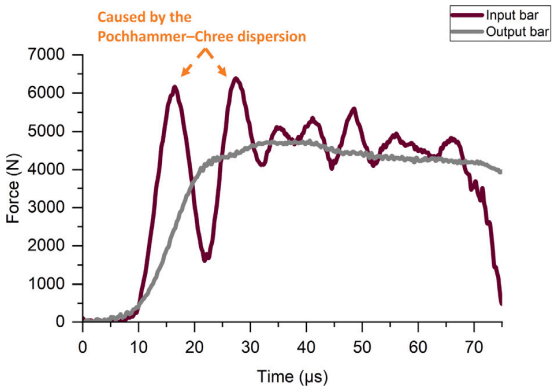


Fig. 5. Force equilibrium demonstrated by comparing force recorded in the input (incident and reflected wave) and output (transmitted wave) bar. Pochhammer–Chree dispersion was recorded in the input bar because no pulse shaper was used.

dissipated through the specimens, W, was also analysed by integrating the load–displacement curve, *i.e.*,

$$W = \int_0^{\delta_i} F_i(\delta_i)\, d\delta_i, \tag{1}$$

where F_i is the load acting on the material associated with the displacement δ_i.

2.6. Resolved damage analysis

Synchrotron-based dynamic XPCI is susceptible to fixed-pattern noise which can arise from aging and damage of optical elements (windows, lenses, scintillators), non-uniformities in the sensors (*i.e.*, the cameras in the present study) and in-homogeneities in the X-ray beam [34]. In order to aid crack identification, the obtained X-ray radiographs were subjected to a flat-field correction following,

$$I_c(t) = \frac{I_r(t) - \overline{I}_d}{\overline{I}_f - \overline{I}_d}, \tag{2}$$

where I_c stands for the 2D intensity of the flat-field corrected image at impact time t. I_r is the image intensity of the recorded image. Average flatfield $\overline{I}_f$ and darkfield $\overline{I}_d$ images were constructed from images taken with X-ray illumination but without objects, and images without both X-ray illumination and objects respectively.

Identification of the observed cracks at their initiation stage was performed by using a modified 2D image intensity analysis [27], while further details of their propagation and damage evolution was achieved

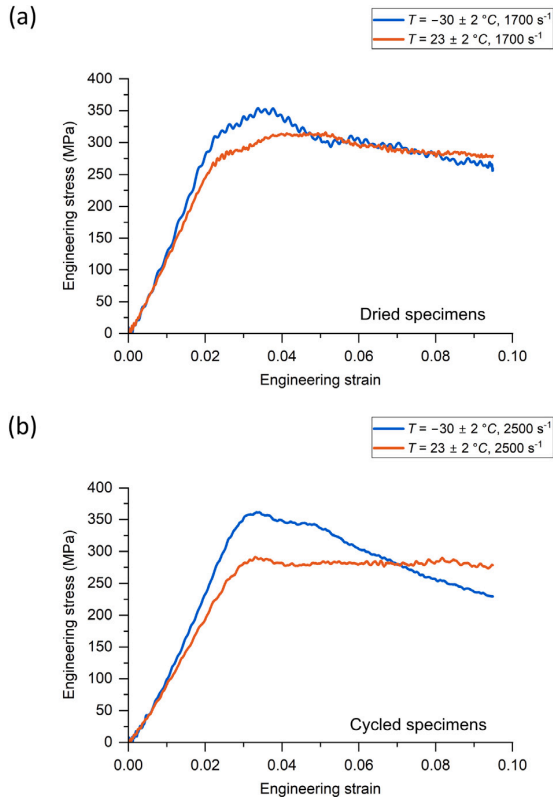


Fig. 6. Stress–strain curve of (a) dried and (b) cycled specimens at room and low temperatures.

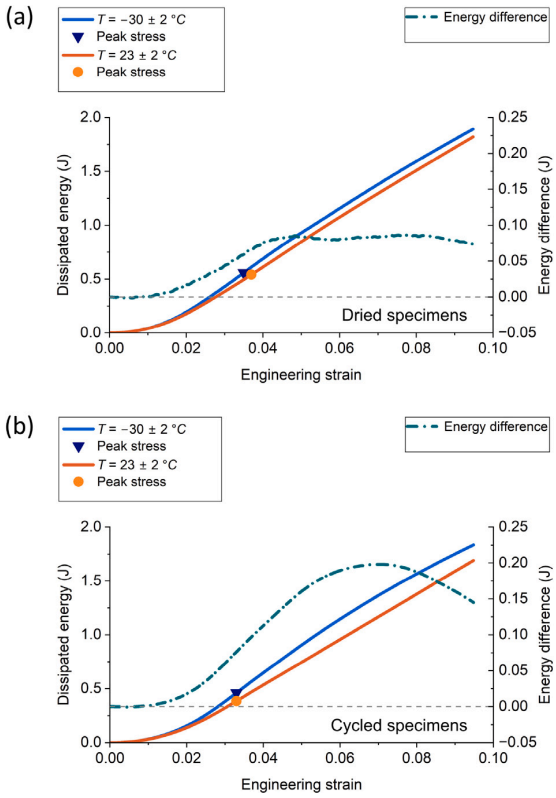


Fig. 7. Energy dissipated through the specimens as the function of strain: (a) dried and (b) cycled specimens.

using a directional image analysis method [35] facilitated by the ImageJ OrientationJ plugin. Explicit explanation of these two analyses is presented in the following section.

3. Results and discussion

3.1. Specimen microstructures

Fig. 3 presents the internal microstructure of the tested CFRP laminates examined by using synchrotron-based X-ray μCT prior to the HSR loading. It shows the tested laminates consist of 16 layers of CFRP plies (Fig. 3a) with densely packed (around 80%) 5 μm-diameter carbon fibres (Figs. 3b) in the orientations of ±45° and symmetrically arranged about the central axis. By making a cutting plane across two adjacent plies on either side of the symmetry axis (Figs. 3b) and applying directional image analysis (Fig. 3c) [35], it can be seen that the +45° and −45° fibre plies were laid up in turn. Each ply is approximately 170 μm in thickness and glued by a thin layer (about 15 μm) of the matrix material, which leads to a total thickness of ~3000 μm. Spherical voids with diameter in the range 5 to 20 μm are spread evenly within the inter-ply glue layers without coalescence to each other (Fig. 3d). No obvious defects can be identified in the dried and cycled CFRP specimens. It should be noted that the voids are too small to be resolved by the indirect MHz XPCI in the dynamic experiments (1× magnification).

3.2. Mechanical properties

QS uni-axial compression tests on both dried and cycled specimens were performed and analysed (Fig. 4) to establish a baseline for HSR mechanical property analysis in the present research. An example of force recorded from the input and output bar during HSR loading tests is present in Fig. 5 which demonstrates equilibrium was reached during the dynamic loading.

The obtained specimen stress σ versus strain ε curves in Fig. 6 show that there is a significant strength increase at room temperature for both dried and cycled specimens under HSR loading compared to the ones tested at QS loading. For the HSR loading tests, the specimens tested at low temperatures have noticeably higher strength (about 10% for dried and 20% for cycled specimens) and apparent stiffness than their room temperature counterparts, although they all reached their maximum stress at approximately $\varepsilon = 3.5\%$. Similar findings were also reported by Liu et al. [9] and Wang et al. [36]. After the peak, the flow stress in the low-temperature specimens dropped rapidly with increasing strain, whereas the room-temperature specimens maintained a stable flow stress. This observation is more prominent for the cycled specimens, as shown in Fig. 6b. Regarding the cycling effect on the specimen strength, the dried specimen at room temperature has a higher strength than the cycled specimen, although the test strain rate was lower for the dry specimen compared to the cycled. This agrees with the experimental results on the tensile tests of a unidirectional-90 CFRP laminate reported by Meng et al. [15]. A similar trend can also be observed from the QS test results shown in Fig. 4. However, the cycling effect on the specimens tested at low temperatures (both dried and cycled) is not very obvious in terms of strength.

This observed difference in behaviour should mainly be driven by the thermophysical behaviour of the epoxy matrix, since the mechanical properties of carbon fibres are comparatively insensitive at temperatures below 400 °C [14,37]. The matrix on the other hand

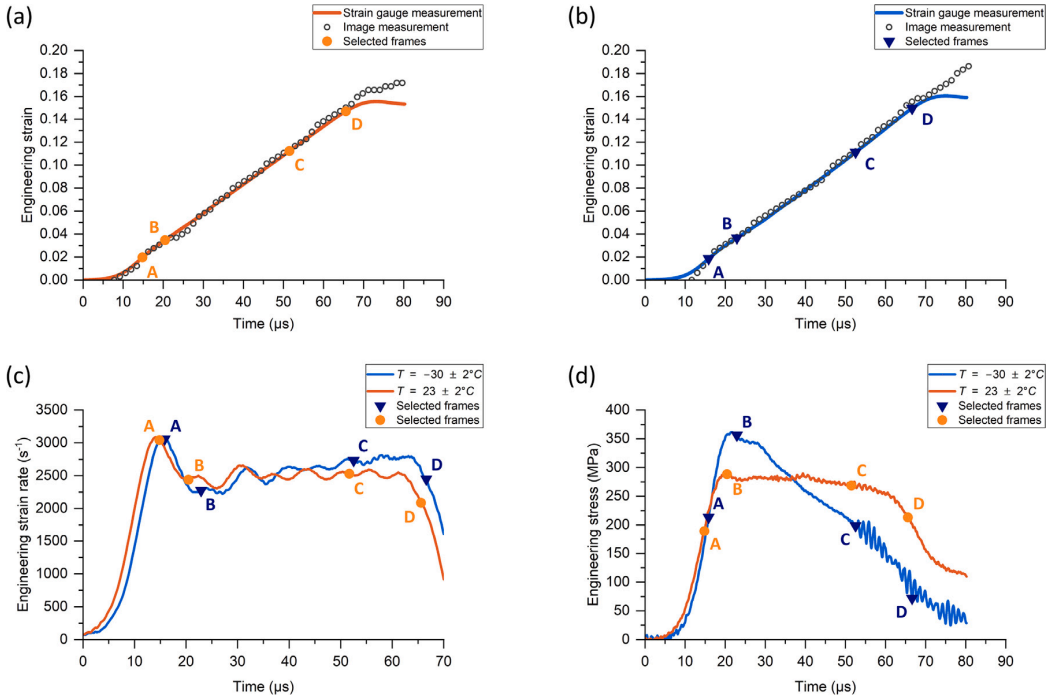


Fig. 8. Mechanical response of the cycled specimens as a function of time t: (a) engineering strain at room temperature, (b) engineering strain at low temperature; (c) engineering strain rate, and (d) engineering stress. t is referenced to the first loading of the specimen.

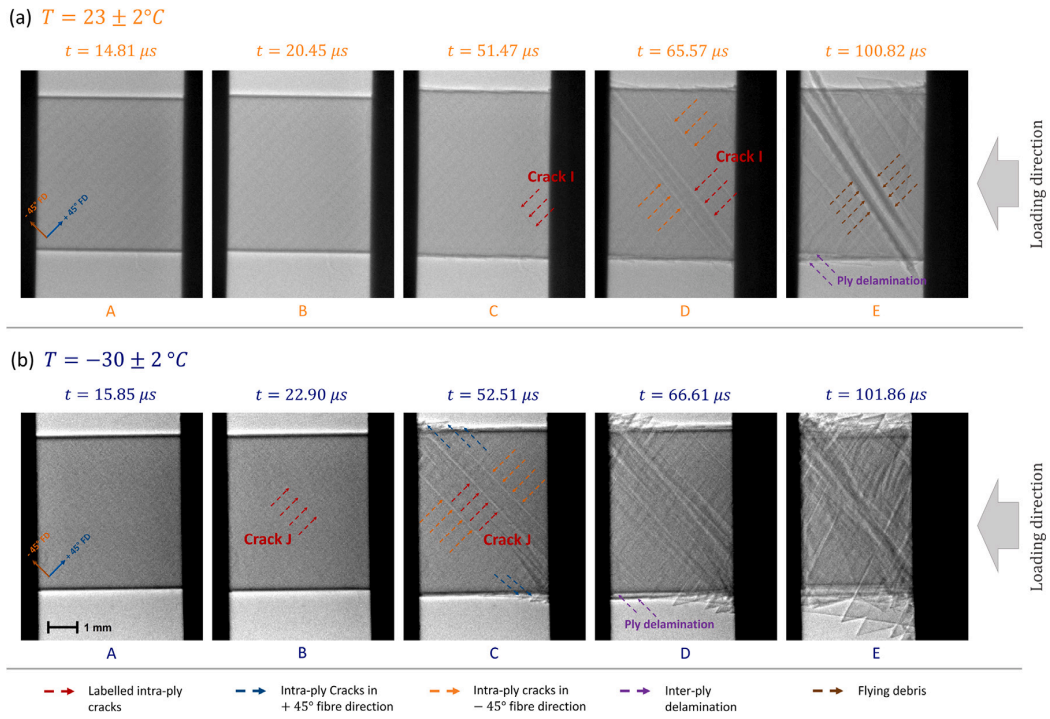


Fig. 9. Subsurface failure initiation and evolution for the (a) room- and (b) low-temperature specimens under HSR loading presented by five key frames captured using synchrotron-based MHz XPCI. The selected frames from the room- and low-temperature specimens are approximately equivalent in time and strain. Damage in the low-temperature specimen initiated earlier and developed faster than that in the room-temperature specimen. The earliest damage that can be observed for the room-temperature specimen is in Frame C (t = 51.47 μs, $\varepsilon \simeq 11.2\%$), whereas that for the low-temperature specimen is in Frame B (t = 22.90 μs, $\varepsilon \simeq 3.7\%$).

Table 2
Summary of mechanical response and damage state for the (a) room- and (b) low-temperature specimens with impact progression. Fibre direction (FD) shown was estimated based on the overall deformation of the specimens measured from the images in both parallel and perpendicular directions to the loading.

(a) $T = 23 \pm 2$ °C					
Frame label	A	B	C	D	E
Time after impact t, μs	14.81	20.45	51.47	65.57	100.82
Gauge strain ε, % (Fig. 8)	2.0	3.5	11.2	14.7	–
Image strain ε_I, % (Fig. 8)	1.8	3.4	11.4	15.0	16.0
Gauge stress σ, MPa (Fig. 8)	189.03	288.30	268.35	212.98	–
Stress state (Fig. 8)	Raising elastically	Peak stress	6% strength lost	27% strength lost	–
Damage state (Figs. 9, 10 and 11)	No crack	No crack	Intra-ply crack emerged	Minor inter-ply delamination	Inter-ply delamination
Fibre direction (FD) (based on ε_I)	±45.5°	±46.0°	±48.1°	±49.0°	±49.2°
Crack direction (Figs. 10 and 11)	–	–	−47.0°	$-50.0 \pm 2°$	$\pm 51 \pm 2°$
(b) $T = -30 \pm 2$ °C					
Frame label	A	B	C	D	E
Time after impact t, μs	15.85	22.90	52.51	66.61	101.86
Gauge strain ε, % (Fig. 8)	1.9	3.7	11.1	15.0	–
Image strain ε_I, % (Fig. 8)	1.9	3.7	11.2	15.5	24.8
Gauge stress σ, MPa (Fig. 8)	213.28	356.31	198.55	71.82	–
Stress state (Fig. 8)	Raising elastically	Peak stress	50% strength lost	80% strength lost	–
Damage state (Figs. 9, 10 and 11)	No crack	Intra-ply crack emerged	Intra-ply cracks in both directions	Inter-ply delamination	Structure collapsed
Fibre direction (FD) (based on ε_I)	±45.5°	±46.0°	±48.4°	±49.8°	±53.0°
Crack direction (Figs. 10 and 11)	–	−45.5°	$\pm 47.0 \pm 2°$	$\pm 50.0 \pm 2°$	$\pm 56.0 \pm 5°$

becomes stiffer at low temperatures owing to the reduced internal energy and mobility of molecule chain segments [38]. Consequently, the interaction between fibre and matrix might be less important compared to that at room temperature, as the increased matrix strength forms most of the load resistance in low-temperature specimens before the peak stress. Additionally, the absolute coefficient of thermal expansion (CTE) of epoxy resin and ice introduced by hygrothermal cycling can be significantly higher than that of carbon fibres [39], which will alter the state and distribution of residual stress within the material at low temperature, and may influence the mechanical response.

3.3. Energy dissipation

The energy dissipated through specimen deformation and damage, W, is shown with respect to engineering strain, ε, for each tested condition in Fig. 7. In the case of the dried specimens, it can be seen that W exhibits a quicker rise when tested at low temperatures before levelling off after the peak stress is achieved. This is a consequence of the higher apparent stiffness and peak stress for the cooled specimen, as shown in Fig. 6a. A similar behaviour is observed for the cycled specimens, where a greater degree of strain energy is initially dissipated at the lower temperature. A notable key difference here however is the reversal in energy dissipation which arises due to the much steeper drop in load-carrying capacity for the low-temperature specimen. The testing temperature seems to have a more prominent effect in cycled specimens indicated by the higher energy difference shown in Fig. 7b possibly resulting from the presence of moisture. In terms of overall energy dissipation, no significant difference can be found up to $\varepsilon \simeq 9.5\%$ between dried and cycled specimens. Although the low specimens still demonstrate higher energy dissipation for both ageing cases relative to their room-temperature counterparts, the stress declines more rapidly after the peak in the cycled specimens, suggesting room-temperature specimens might overtake at larger strain.

Previous studies on the behaviour of CFRP during impact loading indicate that this drop in toughness can be attributed to the reduced ductility of the matrix at low temperature, resulting in a decreased threshold for damage [12,40]. This effect is particularly evident in the ±45° CFRP laminates tested in the present study, implying that the mechanical response and failure are dominated by the matrix material [41]. However, the conventional strain gauge measurement cannot provide further information or direct indication to elaborate damage mechanisms associated with this behavioural difference at different temperatures under HSR. Therefore, synchrotron-based MHz XPCI was introduced in this study to perform *in-situ* observation of this impact and subsurface failure event.

3.4. Observed damage initiation

Real-time X-ray phase contrast imaging, synchronised to the HSR loading, was used to investigate the nature and evolution of damage with respect to the bulk mechanical conditions measured using the strain gauges. X-ray images of the cycled specimens were selected and analysed in this section since they demonstrated the clearest difference in response between low and room temperature possibly by virtue of the moisture present. Fig. 8a and 8b show the comparison between axial strain history as measured by the strain gauges and XPCI for the room- and low-temperature specimens, respectively. It can be seen that there is good agreement between the two measurement techniques from ~ 15–70 μs, during which time the strain-rate was stable (see Fig. 8c). Thus, all time-based damage analyses were selected within these regions.

Fig. 9 demonstrates the subsurface damage progression in both room- and low-temperature specimens with respect to time t by presenting five key XPCI frames — Frames A to E. Table 2 summarises the main damage observation with the associated stress and strain states. Although the similar strain development between two specimens before $t = 70$ μs, the cracks in the low-temperature specimen can be clearly identified earlier than that in the room-temperature specimen. At the very early impact stage (Frame A for both specimens in Fig. 9), no internal structural change can be observed from the images regardless of temperature. The first evidence of cracks in the low-temperature specimen can be found at approximately $t = 22.90$ μs (Crack J in Frame B, Fig. 9b), at which time the specimen was near its peak stress (Fig. 8d) at $\varepsilon \simeq 3.7\%$. In comparison, no similar features can be recognised at a similar time and strain in the room-temperature specimen (Frame B, Fig. 9a), where cracks are not visible until $t = 51.47$ μs and $\varepsilon \simeq 11.2\%$ (Crack I in Frame C, Fig. 9a). At Frame C (first observed crack) in Fig. 9a, the stress in the room-temperature specimen had experienced a slight drop (about 6%) relative to Frame B (peak stress), but it was still maintained at roughly the same level.

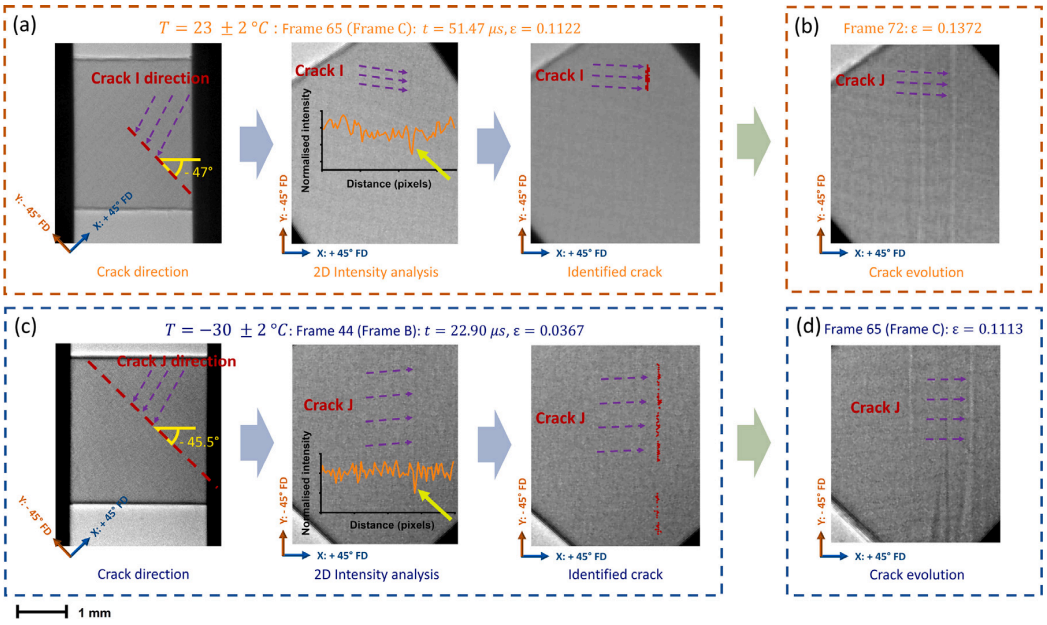


Fig. 10. Identifying the initiated cracks and their later stage development in obtained X-ray radiography. (a) Initiated crack identification and (b) its development for the room-temperature specimen, and (c) initiated crack identification and (d) its development for the low-temperature specimen. By calculating the average intensity along the crack directions, and plotting it along the perpendicular distance, the initiated narrow cracks can be visualised by sudden intensity changes, as shown in (a) and (c).

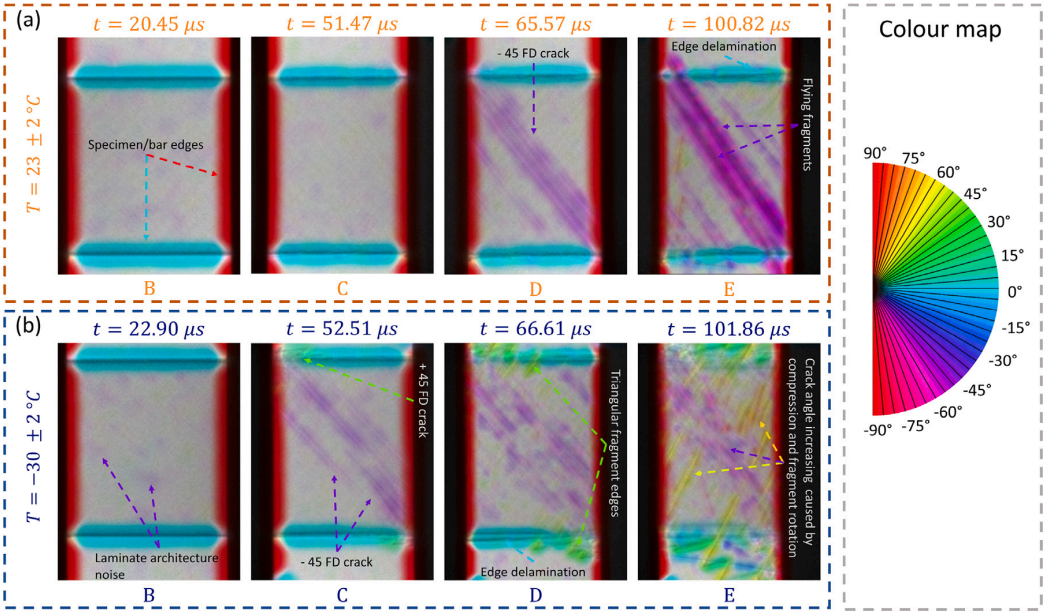


Fig. 11. Cracks highlighted on the obtained X-ray radiography based on directional features: (a) room- and (b) low-temperature specimens. For the room-temperature specimen, cracks in −45° can be recognised in Frame D and E, but no clear cracks are highlighted in +45°. Minor inter-ply delamination is shown at the upper edge in Frame D and at the both upper and lower edges in Frame E. In comparison, both ±45° FD cracks can be seen starting from Frame C in the low-temperature specimen. Obvious inter-ply delamination can be identified in Frame D and E. (For interpretation of the references to colour in this figure legend, the reader is referred to the web version of this article.).

At the early impact stage, all identified crack openings were deemed to be subpixel in size, and the crack interfaces were assumed to be largely in contact. Thus, no measurable change in X-ray transmission would be produced, and any intensity change at the detector would be dominated by phase effects. To better accommodate the directional feature of observed damage revealed by XPCI in the present study, a 2D crack identification method was applied, where the average intensity normal to the supposed crack propagation direction was determined to reduce sensitivity to Poisson noise in the image. Fig. 10a presents the 2D intensity analysis for the room-temperature specimen, where a prominent drop in intensity (highlighted by a yellow–green arrow) can be observed in Frame C ($\varepsilon \simeq 11.2\%$) with an approximate length of

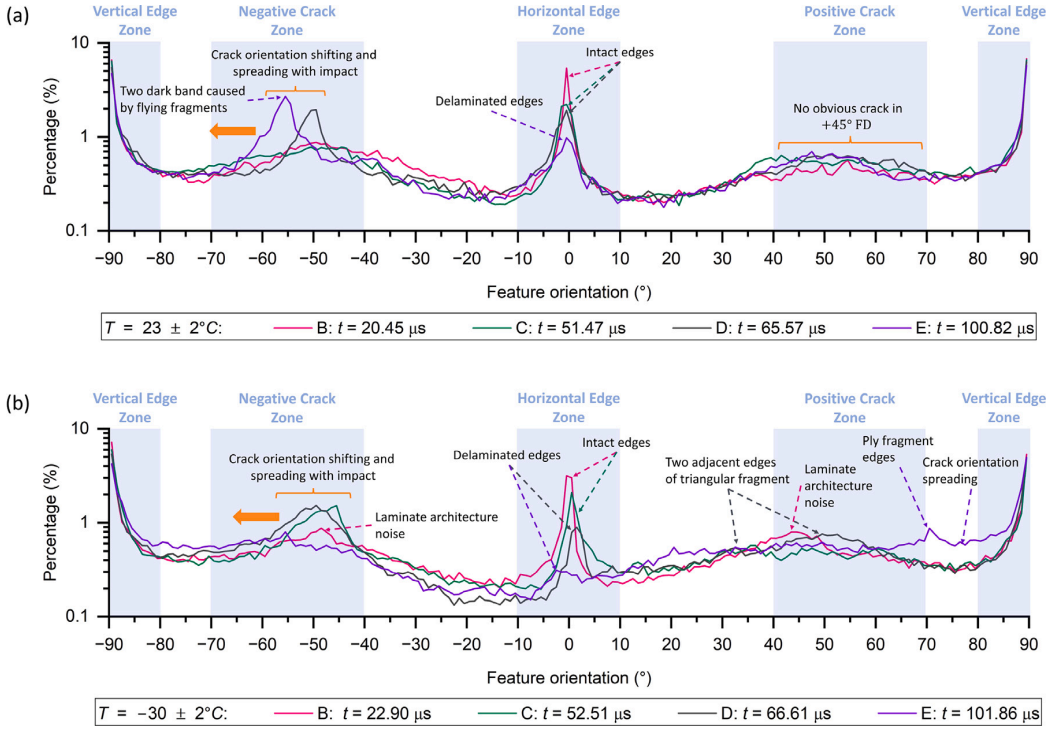


Fig. 12. Orientation distribution for the XPCI radiography: (a) room- and (b) low-temperature specimen. Vertical Edge Zone: specimen/bar vertical edge dominated zone, Negative Crack Zone: negative crack (−45° FD) dominated zone, Horizontal Edge Zone: specimen horizontal edge dominated zone, Positive Crack Zone: positive crack (+45° FD) dominated zone. The peaks in Vertical Edge Zones are mainly caused by the left and right edges of bars and specimens; the peaks in Horizontal Edge Zones result from the upper and lower edges of the specimens; the peaks in Negative Crack Zones and Positive Crack Zones are the representations of generated cracks that orientates in similar directions. (For interpretation of the references to colour in this figure legend, the reader is referred to the web version of this article.).

0.5 mm and angle of −47.0°. It results from local interference (phase contrast) in the propagated X-rays when passing through the newly generated Crack I. With further axial strain, the crack is seen to grow in width resulting in decreased X-ray absorption as shown in Fig. 10b.

A similar analysis was conducted for the low-temperature specimen (Fig. 10c) revealing an early-stage crack (Crack J) at Frame B ($\varepsilon \simeq 3.7\%$). Two narrow crack traces with an approximate length of 2 mm and 0.8 mm align on the same −45.5° line, which coincides with the −45° fibre direction (FD) at this strain (see Table 2). This placement suggests the crack had propagated along the fibres. However, at a similar strain level when the first crack is initiated in the room-temperature specimen (*i.e.*, $\varepsilon \simeq 11.2\%$), more cracks have emerged in the central region of the low-temperature specimen, with some having grown significantly (Frame C, Fig. 10d).

3.5. Observed damage evolution

Frame D to E in Fig. 9a and C to E in Fig. 9b present the rapid damage evolution in the room- and low-temperature specimens, respectively. At a similar strain level (refer to Table 2), the low-temperature specimen demonstrates a noticeably higher degree of damage. Fig. 11 illustrates XPCI highlighted using the directional feature analysis method, with the resulting orientation distributions plotted in Fig. 12. While cracks can be seen in both +45° (top-left and bottom-right corner) and −45° (central region) FD at Frame C in Fig. 11b, no damage can yet be identified at Frame C in Fig. 11a. This is also reflected by the clear peak observed in the Negative Crack Zone of Curve C in Fig. 12b, whereas the Curve C in the Negative Crack Zone in Fig. 12a remains relatively flat and even. 50% of the specimen strength had been lost at this strain in the low-temperature specimen compared to only slight strength loss (about 6%) in the room-temperature specimen.

For the room-temperature specimen at $\varepsilon \simeq 14.7\%$, multiple open cracks can be found at an angle of roughly $-50.0 \pm 2°$ to the horizontal axis (see Frame D in Fig. 9a and Fig. 11a) and are well-aligned with the deformed −45° FD indicated by the peak of Curve D at about −50° within the Negative Crack Zone in Fig. 12a. No clear cracks in +45° FD can be identified, which implies that the cracks in +45° fibre plies were still very narrow at this stage. Minor inter-ply delamination can be identified at the top-right and bottom-left corners. At the time of this frame, the stress in the specimen had reduced by about 27% compared to the peak stress.

However, at the nominally equivalent time (Frame D in Fig. 9b and 11b) for the low-temperature specimen, more cracks in both FDs appeared with triangular debris detached and flying away from the specimen in the top-left and bottom-right corners. The orientation of cracks is seen to shift to higher angles to the loading axis in the Negative Crack Zone (Curve D, Fig. 12b). Multiple interfaces are clearly visible at the lower edge of the specimen by virtue of ply delamination, resulting in the broadening of the peak of Curve D compared to Curve C within the Horizontal Edge Zone in Fig. 12b. The specimen has lost more than 85% of its strength at this time. Approximately 35 μs later (Frame E, 9b and 11b), the low-temperature specimen experienced widespread failure. A large number of cracks and detached debris can be observed throughout the radiograph, indicating severe ply breakage in the specimen.

Even at the final loading stage (Frame E, Fig. 9a and 11a), high specimen integrity was still maintained for the room-temperature specimen in contrast to the low-temperature specimen (Frame E, 9b and 11b), similar to the observations by Guedes et al. [5], Sanchez-Saez et al. [8] and Jia et al. [14]. The observable cracks were still in −45° FD plies, although some dark traces (possibly narrow cracks), which are vaguely highlighted in greenish-yellow in Frame E, Fig. 11a,

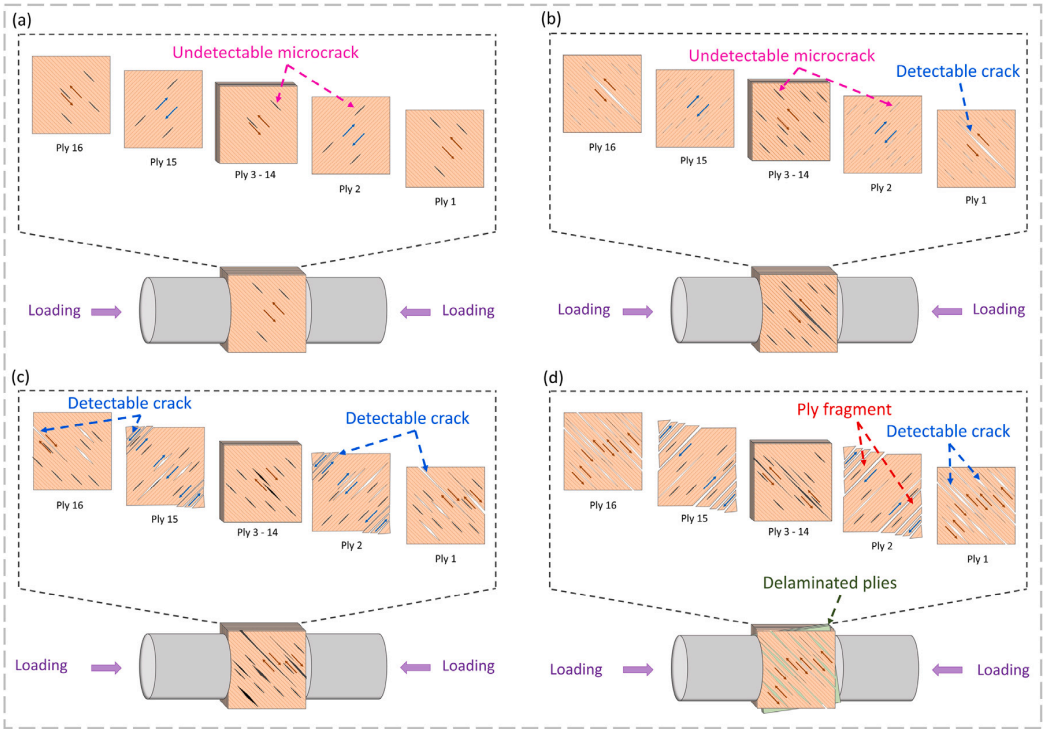


Fig. 13. Schematic of the damage evolution mechanisms of tested CFRP laminates with ply breakdowns: (a) microscale damage in subpixel size (undetectable under XPCI); (b) micro-cracks coalesce and broaden up, form detectable cracks in surface plies; (c) as compression continues, detectable cracks emerge in subsurface plies and in both FDs; (d) detectable cracks grow and cause breakage of the surface plies and ply delamination.

had just started to emerge. Ply delamination is also observed, but is less pronounced than in the low-temperature specimen. This is also reflected by the peaks within the Horizontal Edge Zone in Fig. 12a, which although broadening slightly, remains distinct throughout the compression event. The degree of damage in the room-temperature specimen is evidently lower than that of the low-temperature specimen at a similar ε possibly by virtue of the increased matrix brittleness [13] and residual stresses [42] at the fibre/matrix interface due to the lower temperature.

3.6. Failure mechanism discussion

While it has been shown that damage initiates earlier and progresses more quickly at low temperatures, all specimens appear to share a similar sequence of failure processes, namely, intra-ply cracking at the early stage, followed by a combination of intra-ply cracking and inter-ply delamination at the later stage. Fig. 13 presents a proposed mesoscale damage initiation and evolution mechanism for tested AP CFRP laminates based on these experimental observations and analysis. At early times, although there are no detectable cracks, the change in slope of the stress–strain curves indicates the material might have already undergone internal microstructural changes, possibly intra-ply microcracks. A closer study of the early-stage microscale damage under HSR loading and varying temperatures will be reported in future work.

As dynamic compression continues, intra-ply cracks grow and coalesce, as shown in Fig. 13b and supported by Frame C in Fig. 9a and Frame B in 9b. While large cracks might have already been created (*e.g.*, Frame B, Fig. 9b) possibly by stress concentration as a result of low matrix strain tolerance at low temperatures, the higher plasticity of the matrix at room temperature could enable a more even load distribution in the specimens. The resulting, more-uniform, compressive stress-state might have a positive effect in preventing, or at least delaying, the initiation and growth of cracks [20]. Thus, for CFRP laminates tested at room temperature, cracks with observable size only form at a considerably larger strain (*e.g.*, about 11.2% at Frame c in Fig. 9a) and progress slower than those tested at low temperatures.

Although the obtained X-ray radiography are projections through the entire specimen, prior knowledge of the specimen lay-up and by tracking the crack growth behaviour and timescale for debris generation, it is possible to suggest that the observable crack in both room- and low-temperature specimens first appeared in the front and back surface plies where no lateral and inter-ply shear restraints are acting, as illustrated in Fig. 13b. This is also consistent with the failure observed by Xiao et al. [21] for off-axis dynamic in-plane compression on BB CFRP. It is worth mentioning that the first damage in the room-temperature specimen (intra-ply cracking) was identified at approximately $\varepsilon = 11.2\%$ (Frame C), which is significantly earlier than the first damage captured using visible imaging by Cui et al. [20].

With increasing specimen strain, intra-ply shear stress leads to the increase of intra-ply shear strain and the formation of more intra-ply cracks in both FD directions (see Fig. 13c and supported by Frame C, Fig. 9b and 11b). As the fibres in adjacent plies are arranged perpendicular to each other (+45° and −45°), the intra-ply shear strains generated within adjacent plies are also perpendicular, giving rise to inter-ply shear stress. When the inter-ply shear stress exceeds the shear strength of the inter-ply glue layers, delamination occurs (see Fig. 13d and evidenced by Frame E for the room-temperature specimen and Frame D for the low-temperature specimen), leading ultimately to complete failure of the specimen (*e.g.*, Frame E, Fig. 9b and 11b), as observed by Cui et al. [20].

4. Conclusions

A series of HSR compression tests, synchronised to synchrotron-based MHz X-ray PCI, have been performed on AP CFRP laminates at

room and low temperature to identify the subsurface failure mechanisms responsible for the loss of strength observed at the bulk scale.

Independent of temperature, inter-ply cracking and intra-ply delamination were found to play important roles in the failure of all tested AP CFRP specimens. The observable damage was initiated in the form of intra-ply shear cracking in the surface plies along FDs as the result of the lack of lateral restraint and inter-ply shear resistance on the specimen surface. With continued deformation, the observable damage propagated into sub-layers, but the cracks still remained in good alignment with ply FDs before the associated ply fragment detached from the specimen bodies. Further deformation of specimens gives rise to the subsurface intra-ply shear in different orientations (+45° and −45° FD) between adjacent plies, causing the increase of inter-ply shear and subsequent ply delamination.

In-situ testing temperature was observed to exert notable effects on specimens' mechanical properties and timescale of failure. At low temperatures, both dried and cycled CFRP laminates exhibited higher compressive strength and apparent stiffness, and a higher amount of energy was dissipated from the bar before the peak strength was reached. The low-temperature specimens underwent a rapid strength loss and catastrophic failure, while their room-temperature counterparts demonstrated a more ductile-like behaviour after the peaks. These temperature-dependent differences in strength and energy dissipation were observed to be more prominent in specimens subjected to HTC treatment.

The present research thusly identifies the subsurface mesoscale damage mechanisms in AP CFRP laminates, and correlates this in a time-resolved manner with their mechanical response at low temperatures under HSR compressive loading. This coordinated description of thermo-mechanical and damage response can be used to develop, validate and improve advanced numerical models of CFRP laminates under complex service conditions.

CRediT authorship contribution statement

Xiyao Sun: Writing – original draft, Visualization, Validation, Methodology, Investigation, Formal analysis, Data curation, Conceptualization. **David Sory:** Writing – review & editing, Methodology, Investigation, Formal analysis. **Kai Liu:** Writing – review & editing, Validation, Conceptualization. **Bratislav Lukić:** Data curation, Methodology, Writing – review & editing. **David Simonian:** Investigation. **Kwan Lok Wong:** Investigation. **Alexander Rack:** Writing – review & editing, Resources. **David Chapman:** Writing – review & editing, Supervision, Methodology. **Nik Petrinic:** Writing – review & editing, Resources, Funding acquisition. **Daniel Eakins:** Writing – review & editing, Supervision, Resources, Project administration, Funding acquisition.

Declaration of competing interest

The authors declare that they have no known competing financial interests or personal relationships that could have appeared to influence the work reported in this paper.

Data availability

Data will be made available on request.

Acknowledgements

The authors would like to acknowledge Rolls-Royce plc, for their continued support of the University Technology Centre for Solid Mechanics at the University of Oxford. In addition, the authors gratefully acknowledge the funding for this research provided by Innovate UK grant 113190:FANTASTICAL (FAN Testing And STatistical Integrity CALibration). The ESRF, Grenoble, France is acknowledged for providing beamtime and assistance under Beamtime Proposal MA-5715. The authors would also like to thank the workshop team within the Impact and Shock Mechanics Laboratory, Begbroke Science Park for the preparation of the specimens and equipment.

References

[1] Clyne TW, Hull D. An introduction to composite materials. Third ed.. Cambridge; 2019.
[2] Irving PE, Soutis C. Polymer composites in the aerospace industry. San Diego: Elsevier Science & Technology; 2019.
[3] Wang K, Young B, Smith ST. Mechanical properties of pultruded carbon fibre-reinforced polymer (CFRP) plates at elevated temperatures. Eng Struct 2011;33(7):2154–61.
[4] Hosur MV, Alexander J, Vaidya UK, Jeelani S. High strain rate compression response of carbon/epoxy laminate composites. Compos Struct 2001;52:405–17.
[5] Guedes RM, de Moura MF, Ferreira FJ. Failure analysis of quasi-isotropic CFRP laminates under high strain rate compression loading. Compos Struct 2008;84(4):362–8.
[6] Zhao C, Zhou Z, Zhao C, Zhu H, Zhang K, Zhong J, et al. Research on compression properties of unidirectional carbon fiber reinforced epoxy resin composite (UCFREP). J Compos Mater 2021;55(11):1447–58.
[7] Ochola RO, Marcus K, Nurick GN, Franz T. Mechanical behaviour of glass and carbon fibre reinforced composites at varying strain rates. Compos Struct 2004;63(3–4):455–67.
[8] Sánchez-Sáez S, Gómez-Del Río T, Barbero E, Zaera R, Navarro C. Static behavior of CFRPs at low temperatures. Composites B 2002;33:383–90.
[9] Liu J, Zhou Z, Ma L, Xiong J, Wu L. Temperature effects on the strength and crushing behavior of carbon fiber composite truss sandwich cores. Composites B 2011;42(7):1860–6.
[10] Wei W, Rongjin H, Chuanjun H, Zhao Y, Li S, Laifeng L. Cryogenic performances of T700 and T800 carbon fibre-epoxy laminates. In: IOP conference series: materials science and engineering. Vol. 102, (1). Institute of Physics Publishing; 2015.
[11] Shi H, Sun B, Liu Q, Yang Z, Zhang Y. Properties of cryogenic epoxy resin matrix composites prepared by RTM process. In: 20th international conference on composite materials. 2015.
[12] Gómez-del Río T, Barbero E, Zaera R, Navarro C. Dynamic tensile behaviour at low temperature of CFRP using a split Hopkinson pressure bar. Compos Sci Technol 2005;65(1):61–71.
[13] Ou Y, Zhu D, Zhang H, Yao Y, Mobasher B, Huang L. Mechanical properties and failure characteristics of CFRP under intermediate strain rates and varying temperatures. Composites B 2016;95:123–36.
[14] Jia Z, Li T, Chiang Fp, Wang L. An experimental investigation of the temperature effect on the mechanics of carbon fiber reinforced polymer composites. Compos Sci Technol 2018;154:53–63.
[15] Meng J, Wang Y, Yang H, Wang P, Lei Q, Shi H, et al. Mechanical properties and internal microdefects evolution of carbon fiber reinforced polymer composites: Cryogenic temperature and thermocycling effects. Compos Sci Technol 2020;191.
[16] Weaver CW, Williams JG. Deformation of a carbon-epoxy composite under hydrostatic pressure. J Mater Sci 1975;10(8):1323–33.
[17] Pinheiro D, Longo O, Nascimento G, Couri G. Use of composite materials in carbon fiber for the recovery of small slab – calculation by analytical and computational methods. Int J Compos Mater 2017;7(1):1–7.
[18] Wang L, Kawaguchi K, Xu J, Han Q. Effects of transverse constraints on the longitudinal compressive strength of unidirectional CFRP pultruded plates and rods. Compos Struct 2019;207:740–51.
[19] Zhang X, Shi Y, Li ZX. Experimental study on the tensile behavior of unidirectional and plain weave CFRP laminates under different strain rates. Composites B 2019;164(June 2018):524–36.
[20] Cui H, Thomson D, Pellegrino A, Wiegand J, Petrinic N. Effect of strain rate and fibre rotation on the in-plane shear response of ±45° laminates in tension and compression tests. Compos Sci Technol 2016;135:106–15.
[21] Xiao J, Wu Z, Pan Z, Ouyang W, Shi L. Analysis of in-plane compression failure mechanism in carbon fiber braided composite with different off-axial angles. J Compos Mater 2022;56(13):2029–46.
[22] Garcea SC, Wang Y, Withers PJ. X-ray computed tomography of polymer composites. Compos Sci Technol 2018;156:305–19.
[23] Zwanenburg EA, Norman DG, Qian C, Kendall KN, Williams MA, Warnett JM. Effective X-ray micro computed tomography imaging of carbon fibre composites. Composites B 2023;258.
[24] Ni X, Kopp R, Kalfon-Cohen E, Furtado C, Lee J, Arteiro A, et al. In situ synchrotron computed tomography study of nanoscale interlaminar reinforcement and thin-ply effects on damage progression in composite laminates. Composites B 2021;217.
[25] Wang Y, Emerson MJ, Conradsen K, Dahl AB, Dahl VA, Maire E, et al. Evolution of fibre deflection leading to kink-band formation in unidirectional glass fibre/epoxy composite under axial compression. Compos Sci Technol 2021;213(March):108929.
[26] Wingate BP, Czabaj MW. In-situ imaging of flexure-induced fracture in tape-laminate composites using high-resolution X-ray computed tomography. Compos Sci Technol 2022;220.
[27] Watanabe T, Takeichi Y, Niwa Y, Hojo M, Kimura M. Nanoscale in situ observations of crack initiation and propagation in carbon fiber/epoxy composites using synchrotron radiation X-ray computed tomography. Compos Sci Technol 2020;197.

[28] Nie Y, Parab ND, Chu J-m, Kim G, Sun T, Fezzaa K, et al. Dynamic crack propagation from a circular defect in a unidirectional carbon fiber reinforced plastic composite. J Compos Mater 2018;52(25):3539–47.
[29] Pournoori N, Corrêa Soares G, Lukić B, Isakov M, Belone MCL, Hokka M, et al. In situ damage characterization of CFRP under compression using high-speed optical, infrared and synchrotron X-ray phase-contrast imaging. Composites A 2023;175.
[30] ASTM. Standard test method for moisture absorption properties and equilibrium conditioning of polymer matrix composite materials. Technical Report, American Society for Testing and Materials; 2004.
[31] Gray GT. Classic Split-Hopkinson Pressure Bar Testing. In: Kuhn H, Medlin D, editors. Mechanical Testing and Evaluation. 8, ASM International; 2000, p. 462–76.
[32] Weitkamp T, Tafforeau P, Boller E, Cloetens P, Valade JP, Bernard P, et al. Parallel-beam imaging at the ESRF beamline ID19: Current status and plans for the future. In: AIP conference proceedings. Vol. 1234, American Institute of Physics Inc.; 2010, p. 83–6.
[33] Escauriza EM, Olbinado MP, Rutherford ME, Chapman DJ, Jonsson JCZ, Rack A, et al. Ultra-high-speed indirect x-ray imaging system with versatile spatiotemporal sampling capabilities. Appl Opt 2018;57(18):5004.
[34] Buakor K, Zhang Y, Birnšteinová Š, Bellucci V, Sato T, Kirkwood H, et al. Shot-to-shot flat-field correction at X-ray free-electron lasers. Opt Express 2022;30(7):10633.
[35] Püspöki Z, Storath M, Sage D, Unser M. Transforms and operators for directional bioimage analysis: A survey. In: Focus on bio-image informatics. Vol. 219, Springer Verlag; 2016, p. 69–93.
[36] Wang H, Sun B, Gu B. Coupling effect of temperature and braided angle on compressive behaviors of 3D braided carbon–epoxy composite at low temperature. J Compos Mater 2017;51(18):2531–47.
[37] Feih S, Mouritz AP. Tensile properties of carbon fibres and carbon fibre-polymer composites in fire. Composites A 2012;43(5):765–72.
[38] Robert D, Caserio C. Basic principles of organic chemistry. second ed.. CA: W.A. Benjamin; 1977.
[39] Chung DDL. Carbon composites : composites with carbon fibers, nanofibers, and nanotubes. second ed.. Kidlington, Oxford, United Kingdom; 2016.
[40] Chen ZK, Yang JP, Ni QQ, Fu SY, Huang YG. Reinforcement of epoxy resins with multi-walled carbon nanotubes for enhancing cryogenic mechanical properties. Polymer 2009;50(19):4753–9.
[41] Thomson D, Quino G, Cui H, Pellegrino A, Erice B, Petrinic N. Strain-rate and off-axis loading effects on the fibre compression strength of CFRP laminates: Experiments and constitutive modelling. Compos Sci Technol 2020;195.
[42] Reed RP, Golda M. Cryogenic properties of unidirectional composites. Cryogenics 1994;34(11):909–28.

Chapter 4

CFRP's damage at micro-scale

4.1 Background and motivation

The application of XPCI in the high-strain-rate tests of CFRP laminates presented in Chapter 3 helped characterise *in-situ* damage initiation and evolution at the meso-scale. It mapped the damage mechanisms and time scale of the tested CFRP laminates with reference to the loading time and specimen strain, and therefore was able to explain the variation in the mechanical responses of the CFRP specimens at different temperatures along the loading events with the obtained imaging evidence. However, two obvious limitations of using XPCI were identified during the previous research, namely the in-plane spatial resolution (size-wise) and the out-of-plane spatial resolution (dimensional-wise). These shortcomings hindered the damage characterisation in the earlier loading stages.

4.1.1 Limitation in in-plane spatial resolution

The specimens were in the size of $5 \times 5 \times 3$ mm^3. In order to fit the specimen into the FoV, the pixel size of the XPCI system was set to be around 30×30 μm^2 (no magnifications), which makes approximately 7.5×12 mm^2 FoV. It is recommended that the features of interest should not be less than 3 times the pixel size when using CT scans [177]. Despite the enhancement brought about by introducing X-ray phase-contrast effect, it is nearly impossible to visualise the cracks whose width is smaller than one pixel width (~ 30 μm) under the current XPCI. In the tested CFRP laminates, the diameter of the carbon fibres is about 5 μm, as demonstrated in Fig.4.1. Since the intra-ply crack observed at the early loading stages was formed along the fibres, the width of the intra-ply cracks at their initiation might be even smaller than the diameter of a single fibre, and thus cannot be clearly revealed by XPCI. However, this micro-scale damage initiation and development is critical to understanding the formation of the intra-ply crack observed under XPCI at the meso-scale.

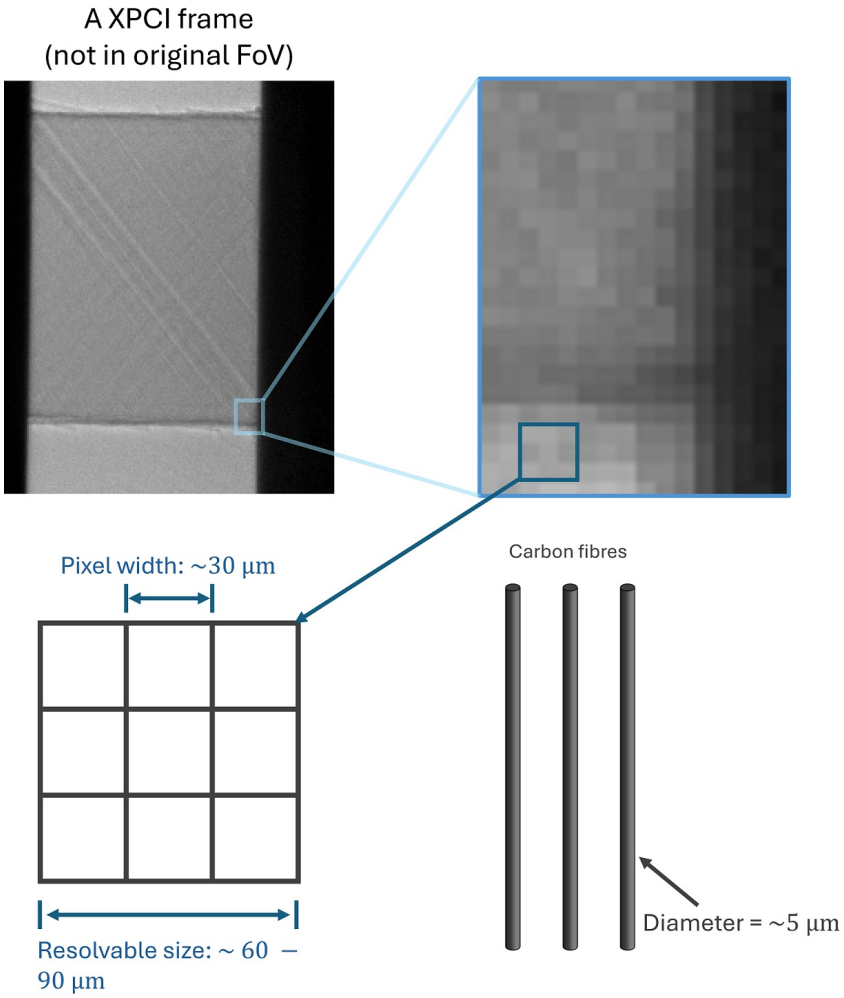


Figure 4.1: Comparison between the size of XPCI pixels and carbon fibres. The initiated matrix cracking might be smaller than the fibres, taking into consideration the epoxy's brittle behaviour. The resolution of XPCI is not sufficient for visualising damage at the micro-scale.

4.1.2 Limitation in the out-of-plane spatial resolution

In addition to constraints in pixel size, the current XPCI is, in essence, a stacking effect in the X-ray propagation direction. All interactions between the X-ray pulse and specimen structures along the X-ray transmission path were added on top of each other and projected into 2D radiographies (Fig.4.2a). Therefore, the damage developed along the depth of the specimen was shown in an overlapping 2D project pattern, including intra-ply cracks in both $+45$ and $-45\,^{\circ}$ fibre directions and inter-ply delamination (refer to Fig.4.2b for the laminate layup). The superposition of multiple X-ray interactions can obscure damage features during high-speed loading, especially the mid- to late-loading stages, at which complex damage mor-

phology has been generated along the depth of the specimens. Apart from that, although the ply layup pattern can provide some hints, the damage interpretation along the depth of the specimen is still largely limited. Other approaches and methodologies that incorporate 3D image resolution need to be explored to further investigate the damage mechanisms in this direction.

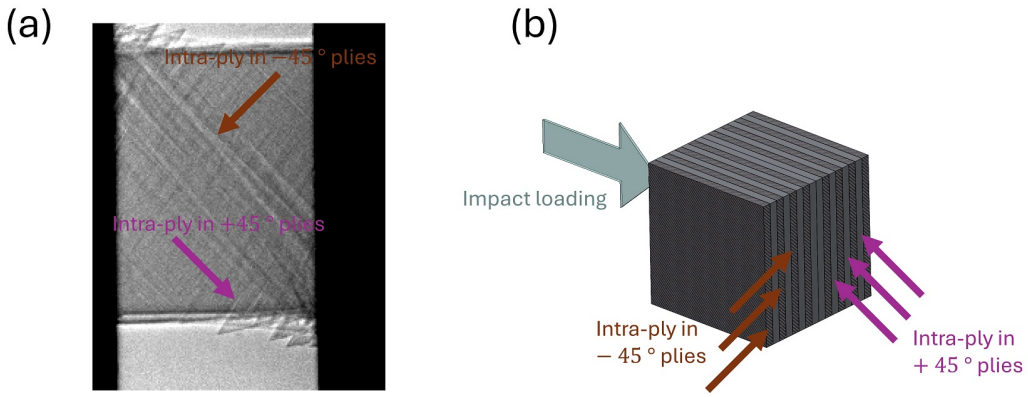


Figure 4.2: Superposition effects in XPCI 2D projects. (a) An example XPCI frame demonstrates the damage in both $+45$ and -45° plies. (b) Schematic illustrates the ply layup of the specimen along depth (X-ray propagation direction).

4.1.3 Objectives of the chapter

The consecutive observation of damage progression based on *in-situ* XPCI at the meso-scale established a framework for understanding the temperature effects on the damage mechanisms of CFRP laminates under high-strain-rate loading. However, the current bottleneck of using dynamic X-ray imaging at synchrotron facilities limits the high-rate damage characterisation at smaller scales. Novel experimental approaches are demanded to overcome this challenge. Thus, in this chapter, new experimental techniques are introduced, such as synchrotron-based phase-contrast μ-CT and high-rate strain interruption, which together enable the visualisation and analysis of damage initiation and evolution at the micro-scale. These results have complemented and expanded the results and understanding obtained from the XPCI setups. The morphology and distribution of damage along the depth of the specimens can be decoded.

4.2 Summary of Paper II

4.2.1 Material and specimen

In this research, the same CFRP laminates as in Chapter 3 were used. However, based on the findings presented in the previous chapter, hygrothermal ageing is not further considered in the current and subsequent chapters. This is because the differences in global mechanical response and observed damage mechanisms between aged and non-aged specimens were found to be limited within the scope of the present study. Therefore, the following investigations focus on isolating the effects of temperature at high-strain-rate loading. The size of the specimens was reduced to $3\times3\times3$ mm^3 (4.1) to allow for (i) reaching very high strain-rates, which requires the specimens to be short, (ii) small thermal contraction after cooling for accurate strain control, and (iii) a full-field and high-resolution phase-contrast X-ray tomography to generate the maps of micro-scale damage. It is well-known that the size of the sample can affect the mechanical response and the evolution of the damage of CFRP laminates due to heterogeneous and anisotropic composite systems [178]. Nevertheless, the intent of this study was not to characterise the mechanical properties of bulk materials for structural applications, i.e. their properties pertaining to their behaviour on the macro-scale. Instead, the goal was to map the transitions of high-strain-rate damage development observed at the micro-scale in the selected CFRP laminates as a function of temperature. The research outcomes can provide direct evidence to validate and calibrate numerical damage models for CFRP laminates under extreme loading conditions, from which the improved models can produce a better understanding and prediction at the structural level.

4.2.2 Methodology

To tackle the limitations identification in Chapter 3, a combination of strain-interrupted loading and synchrotron-based μ-CT tomography was applied. The idea of this implementation is to mechanically stop the damage progression of the specimen at the designed loading levels by preventing further deformation of the specimens (see Table 4.1). The visco-plasticity and brittleness of the CFRP laminates help to preserve the damage in recovered specimens induced by the high-strain-rate loading. The recovered specimens can then be scanned using high-resolution μ-CT at synchrotron facilities to visualise and characterise the internal micro-structural damage generated. It is worth mentioning that, although *in-situ* damage characterisation at the micro-scale, for example, performing *in-situ* μ-CT as in quasi-static

Label	Volume, mm^3	Weight, g	Designed final strain, $\%$
Room: 23 $\pm$ 2, °C			
IF1	24.85	38.20	No interrupt
IF2	26.37	40.16	No interrupt
IF3	25.92	40.06	No interrupt
RM1	25.46	39.23	2.33
RM2	24.93	38.02	2.99
RM3	26.18	40.23	3.99
RM4	25.56	39.17	8.00
RM5	25.83	39.53	13.00
Cold: -50 ± 2, °C			
IF4	25.91	39.45	No interrupt
IF5	24.42	37.64	No interrupt
IF6	23.52	36.62	No interrupt
CL1	24.85	38.48	2.33
CL2	24.56	38.11	2.66
CL3	26.10	40.02	3.32
CL4	25.73	39.39	4.32
CL5	24.94	38.23	8.31

Table 4.1: Specimen details and testing conditions. All specimens were dynamically compressed along the plane of the laminates at an approximate strain-rate of 2500 s^{-1}. The specimens that were loaded without strain interruption were labelled as "IF", while the specimens loaded with strain interruption at room and low temperatures were labelled as "RM" and "CL", respectively.

testing, is challenging due to current technology constraints, this investigation provides in-depth experimental data to complement the previously obtained *in-situ* XPCI results.

In this research, a SHPB system is also used as the loading platform, and the same bar dimensions and strain gauge setups were adopted (refer to Chapter 3 and Paper I [147]). The strain interruption of specimens is achieved primarily by installing a titanium alloy (Ti-6Al-4V) strain control collar at the interface between the incident bar and the specimen, as shown in Fig.4.3 (a and b). The strain collars were designed to have a slightly larger inner diameter than the transmitted bar, so the bar end can be slid in (Fig.4.3c). The spacers of the collars were carefully designed to be smaller than the length of the specimen, allowing for the desired levels of specimen deformation. Upon loading, the incident bar will first compress the specimens until the length of the specimens has been deformed to the same magnitude as the thickness of the spacer, at which point the end of the incident bar touches the surface of the strain control collar. The stiffness of the collar material is significantly

higher than that of the specimens. Thus, a large portion of the load is taken by the collar, which rapidly stops specimen deformation. High precision (± 10 μm) was implemented in the spacers during collar manufacturing, and a surface polish was carried out to bring the thickness tolerance close to ± 3 μm. This high-precision thickness of the spacer helped achieve an accurate strain interruption at high-strain-rate loading.

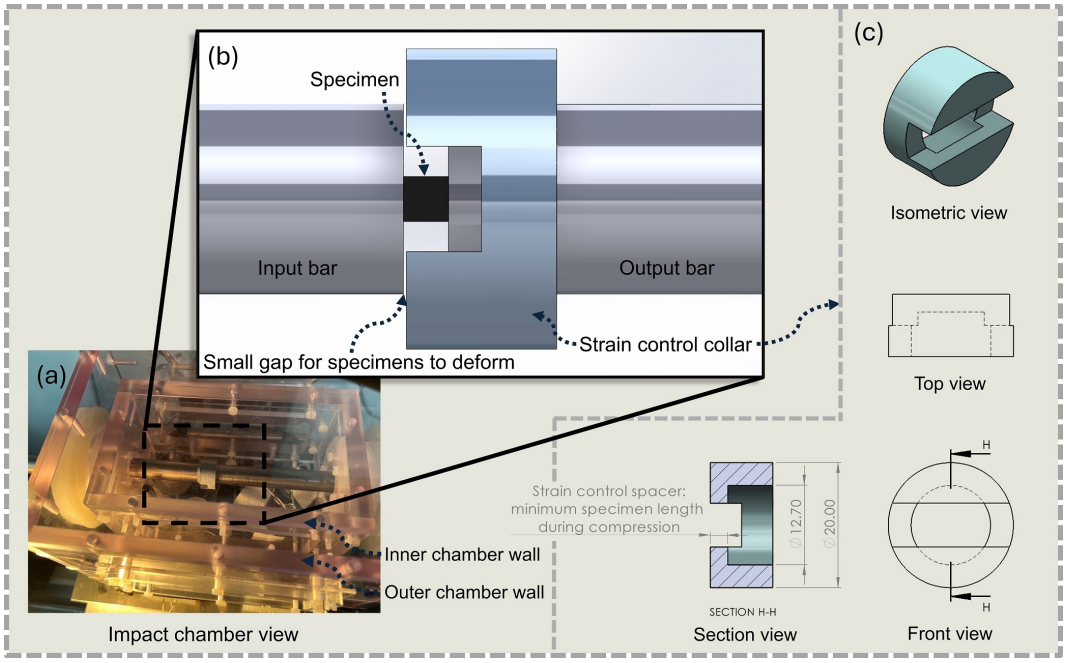


Figure 4.3: Strain interruption setups implemented on the SHPB loading system. (a) A collar is installed near the interface between the incident bar and specimen. (b) A gap is created between the end of the incident bar and the collar face to allow the desired specimen deformation. (c) Detailed dimensions of the strain control collars.

μ-CT scanning performed on synchrotron beams can achieve much higher resolutions compared to the dynamic XPCI. Fig.4.4 shows an example setup for synchrotron tomography scanning [179]. It can be seen that the X-ray pulse emitted from the storage ring is first converted into monochromatic form (polychromatic, also known as “white beam”, in the present research), and then shaped to a coherent rectangular X-ray beam with a smaller and more uniform cross-section. Specimens are placed downstream in the X-ray path on a rotation platform. During scanning, the specimens will rotate for 360 °, allowing the detectors located downstream to capture X-ray radiographies of the specimens at different angles. In the current setup at the ESRF, 6000 projections were taken, which were then used to reconstruct the 3D volumetric image data on an ESRF in-house image reconstruction system (see Paper II for details of the settings and parameters [176]). A series of filters

was applied (i.e., diamond, aluminium, and copper) to remove soft X-rays to prevent beam hardening. For a good visualisation of cracks at their initiation stage, $2.1 \times 2.1 \times 2.1$ μm^3 voxel size was adopted.

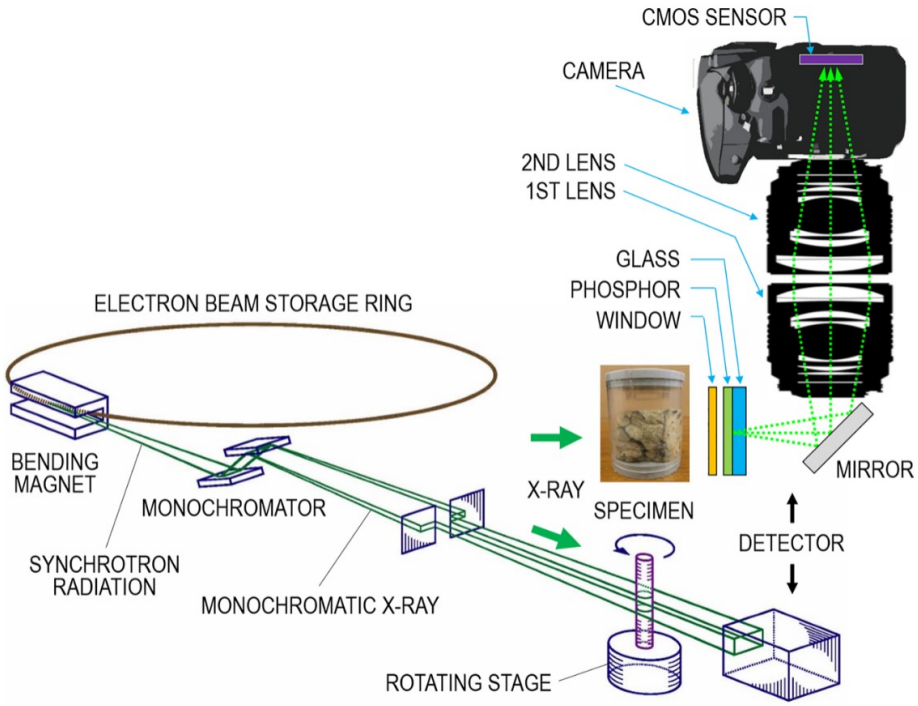


Figure 4.4: An example of a synchrotron CT setup. The produced X-ray beam is emitted from the storage ring and propagates through the specimens sitting on a rotation platform. The specimens will be rotated for 360° to allow the detector to capture X-ray radiation with specimens at different angles for the 3D volume reconstruction [161].

During high-strain-rate loading, a high-speed lighting and imaging (visible light) system was set up on the SHPB platform to record the *in-situ* global nominal deformation of the specimens, as demonstrated in Fig.4.5. This is helpful for tracking strain development and its ultimate magnitude (i.e., the interruption strain) of the specimens. It can be seen that two flashlights were mounted, with one (light 1) pointing toward the front of the specimens (facing the camera) and the other (light 2) shining light from the back of the specimens. Upon loading, the elastic compression wave will first arrive at the strain gauges mounted on the incident bar, causing a prompt voltage rise. When the voltage rise reaches the set trigger level, the flashes and the camera will be triggered with a set delay through delay generators. The high-speed camera was set to take images at one million frames per second (FPS) with a 500 ns exposure time, which provides adequate time resolution for tracking specimen strains and time duration to cover the entire compression process. The camera setting is

applied using a laptop, on which the recorded images during the loading are also stored.

Upon triggers, light 1 can provide sufficient light reflection for the speckled painting on the front, as illustrated in Fig.4.6. This facilitates the digital image correlation in the post-process based on the obtained images. In the meantime, camera 2 was needed to produce a backflash, which helped to enhance the intensity contrast at the edges of the loading rigs and specimens (Fig.4.6). The gap between the incident bar and the collar face can be clearly visualised under backflash. An efficient specimen and collar positioning can also be achieved before loading.

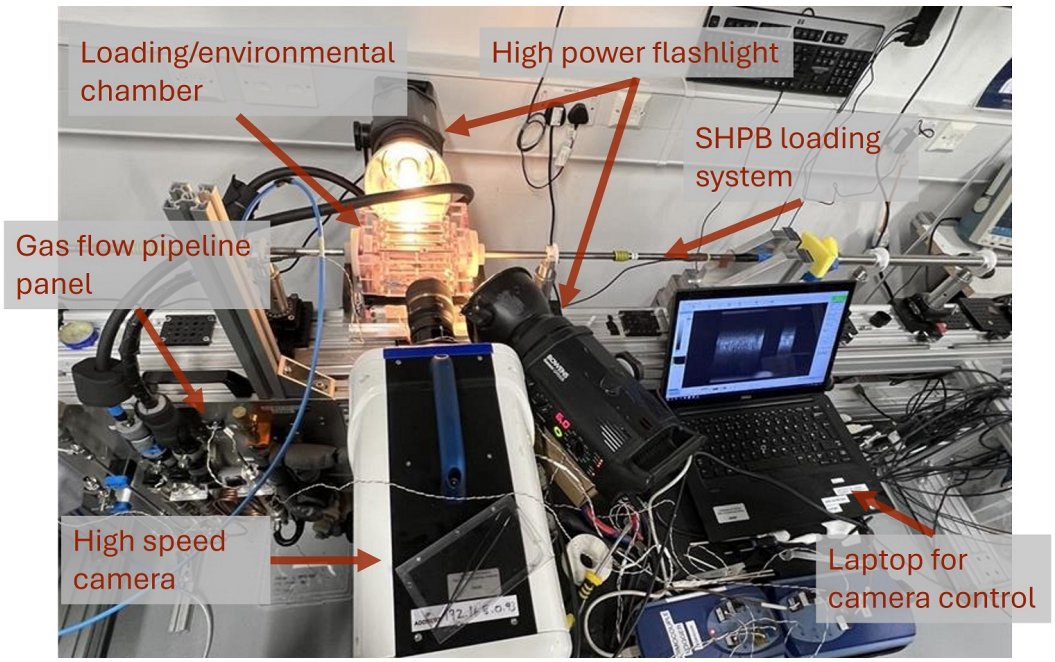


Figure 4.5: Configuration of lighting and imaging systems in the impact loading region on the SHPB platform. The camera is placed perpendicular to the loading direction, facing toward the specimens. Two flashlights were adopted, producing both front light reflection and backflash. Both the flashlights and the camera were triggered by the strain gauges on the incident bar with a set delay using delay generators. A control laptop was connected to the camera for adjusting camera parameters and recording the captured images during loading.

In terms of the damage analysis, “damage” is used as a general term in this thesis to describe all forms of microstructural degradation, including matrix cracking, fibre–matrix debonding, ply delamination, and ply detachment. Among these, only the so-called “opened damage”, characterised by the formation of void regions, can be directly identified and quantified using X-ray CT due to contrast limitations in this chapter. Therefore, the term “damage volume” (or “volume of damage”) used in this chapter specifically refers to the measurable

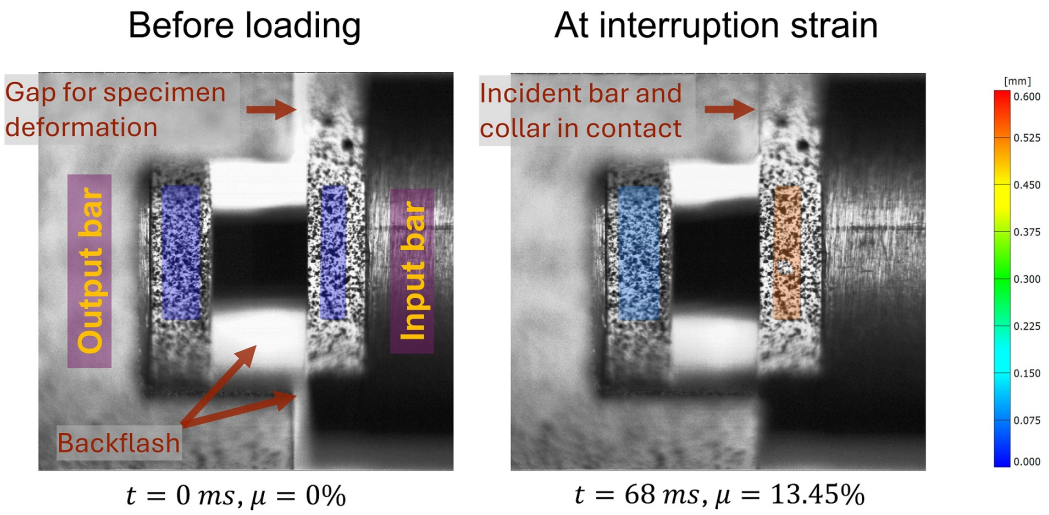


Figure 4.6: Example of captured images using the high-speed camera. Before the loading arrived at the bar/specimen interface, a clear gap can be seen between the input bar and the collar face. This gap allows the specimen to deform freely. At the interruption strain, the bar end and the collar came into contact, which stopped the load transfer to the specimen and hence interrupted the specimen deformation. The ends of the bars were painted with a white background and black speckles for tracking the displacement of the bars and the engineering strain of the specimens.

portion of damage corresponding to opened damage. In contrast, the terms "void volume" (or "volume of void") are used to represent pre-existing air bubbles formed prior to mechanical testing.

In this thesis, damage is quantified in terms of volume rather than surface area. Although damage surface area is commonly used in fracture-based analyses to characterise crack propagation and energy release rate, the present study focuses on the relationship between deformation and damage evolution across local, ply-level, and bulk-specimen scales. Given that the experimental approach is based on X-ray CT imaging, only the opened damage can be directly segmented and measured. As such, the residual damage volume after load removal provides a more consistent and quantifiable metric for describing damage evolution in relation to global stress-strain behaviour. Furthermore, the damage observed in the present study exhibits complex and interconnected 3D morphologies. Due to limitations in CT resolution and segmentation, it is challenging to ensure continuous and accurate reconstruction of all damage interfaces. As a result, estimation of damage surface area would be more sensitive to segmentation errors, whereas volume-based quantification provides a more robust and reliable measure under these conditions. The damage volume quantified from X-ray CT using conventional thresholding is sensitive to imaging and segmenta-

tion parameters, and commonly in the absence of a definitive ground truth. Therefore, the measured damage volume is more suitable for comparative analysis between specimens or testing conditions under consistent imaging and analysis procedures, rather than as an absolute measure of total damage.

4.2.3 Research findings

The present experimental setup has been shown to successfully control the strain of the specimen. Two measurements were taken to track the engineering strain of the specimens: displacement measurement of the bar ends from the obtained high-speed images (direct measurement) and displacement measurement from the strain gauges on the bars (indirect measurement). For the image-based measurement, the displacement of the bar ends was tracked by performing DIC on the speckled painting using `GOM Correlation` (Fig.4.7 (a and b)). A correlation window size of 13×13 pixels was selected to ensure that each subset contained multiple speckles, thereby providing sufficient intensity variation for robust correlation. The window distance was set to 10 pixels, resulting in a 3-pixel overlap between neighbouring subsets, which offers an appropriate balance between spatial resolution and correlation stability. The change in the distance between the ends of the incident and transmitted bars can be calculated, as shown in Fig.4.7c. Because the two sides of specimens are closely in contact with the bar ends, the distance change of bar ends can be converted into the engineering strain of the specimens, as plotted in Fig.4.7 (d and e). It is clearly shown that, after a rapid rise at the beginning, the strain of the specimens reached steady levels, indicating that the strain has been interrupted.

Apart from that, the evaluation of the specimen strain was also drawn from the elastic wave measurement of the bars using strain gauges and one-directional wave propagation theory. Foil strain gauges with a gauge length of 2 mm were employed. The gauges had a nominal resistance of $120 \pm 0.3\ \Omega$ and a gauge factor of $2.08 \pm 1\ \%$. A multi-channel signal conditioning amplifier with a 6 V excitation voltage and automatic bridge-balancing capability was used, providing a signal amplification factor of 200. As shown in Fig.4.7 (f and g), the sudden rises of stress can be seen in the stress-strain plots, which were triggered by the contact between the bar ends and the collar surfaces. Good consistency is shown between these two groups of strain measurements, indicated by a statistical strain comparison (please see Paper II - Section 3.3 [176]). It should be noted that the coefficient of

variation (CV_{ε}) shown in Fig.8a in Paper II [176] is a dimensionless quantity and is reported in percentage form for clarity. Nevertheless, the image-based measurement was used as the primary reference for damage analysis since it is a direct measurement.

Before conducting microscopic damage examinations, the bulk dimension changes of the specimens at room and low temperatures were evaluated using vernier calliper measurements. Fig.4.8a displays the specimen geometry to aid the analysis and discussion of the dimension change. It is worth recalling that the specimens at room and low temperatures are labelled as "RM" and "CL", respectively, while the increasing number indicates the increase in global strain. The most obvious difference between the dimension changes in the room and low temperature specimens is that there is basically no width change in the room-temperature specimens at the early loading stages (ie., RM1, RM2 and RM3), whereas the width direction expansion can be seen from the lowest strain of the low-temperature specimens. The cause of this macroscopic dimension change can be explained in terms of internal microstructural changes at the microscopic level in the damage analysis sections.

Fig.4.9 (a and b) show the micro-scale damage development of the room and low temperature specimens, respectively. The observed damage was categorised into six classes, namely A. No damage; B. Transverse intra-ply cracking at surface layers; C. Transverse intra-ply cracking at multiple layers; D. Inter-ply delamination; E. Inclined intra-ply cracking; and F. Surface ply detached. Generally speaking, micro-scale damage evolution is significantly more rapid at low temperature than at room temperature, similar to the meso-scale damage observed in Paper I [147]. No damage can be seen in RM1 and RM2, followed by the emergence of micro-scale intra-ply cracks in the surface and subsurface plies in RM3. Interestingly, the initiated intra-ply cracks at both surface and subsurface plies are well aligned with the in-plane diagonal line of the surface plies, suggesting a damage mechanics of mode-II shear fracture under in-plane compression. Inter-ply delamination started to show in RM4, and large-scale internal damage, involving transverse cracks, inclined cracks and ply delamination, formed when the specimen strain increased to a state as in RM5.

On the other hand, the low-temperature specimens have transverse intra-ply cracks in multiple plies from the lowest interruption strain (CL1), similar to RM3. These intra-ply cracks at multiple locations might contribute to the dimension change in the width direction of the low-temperature specimens previously observed. Although no inter-ply crack can yet be seen in CL1 and CL2, the lower permanent deformation threshold of the epoxy matrix

at lower temperatures might be the reason for the W-direction expansion in the specimens after loading. Inter-ply cracks and delamination are found in CL3 and CL4. With the development of compression and strain at low temperature, the surface ply detached from the specimen bulk on both sides. Although a large number of intra-ply cracks can be found in CL5, similar to RM5, they are mostly in the transverse direction. It is worth mentioning that the interruption strain of CL5 is similar to RM4.

Fig.4.10 demonstrates the volume of the damage as the increase of the interruption strain from a statistical point of view. It should be noted that only the opened damage (void regions with a width larger than ~ 100 µm between the newly generated interfaces after load release) was taken into consideration in these statistics owing to the limitation of segmenting small damage from the specimen background. It can be seen that the volume of opened damage developed more rapidly at lower temperatures than in the room-temperature specimens, due to the higher brittleness of the epoxy resin. This embrittlement arises from reduced molecular mobility [180, 181] and prolonged relaxation times of polymer chain segments at low temperatures [182], which suppress energy-dissipative deformation mechanisms. Specimen CL5 contains the highest volume of damage because surface ply delamination occurred, and the detached volume was also counted as damage. Fig.4.11 presents the opened damage distribution and morphology of RM4, CL4 and CL5 in a 3D space. It is clearly shown that the intra-ply cracks propagated along the fibre direction at both temperatures. Ply delamination is significantly more severe at low temperatures, as observed by comparing RM4 and CL5. RM5 does not demonstrate any ply detachment, because the inter-ply delamination has not yet propagated to the free edge of the specimen. Despite the widely spread intra-ply cracks in CL5, they remained in the transverse direction and were discrete. However, at this stage, intra-ply cracks with inclined angles were generated in RM5. They are interconnected, together with ply delaminations forming clear damage bands, potentially caused by the large visco-plastic deformation of the matrix that occurred during the loading at room temperature.

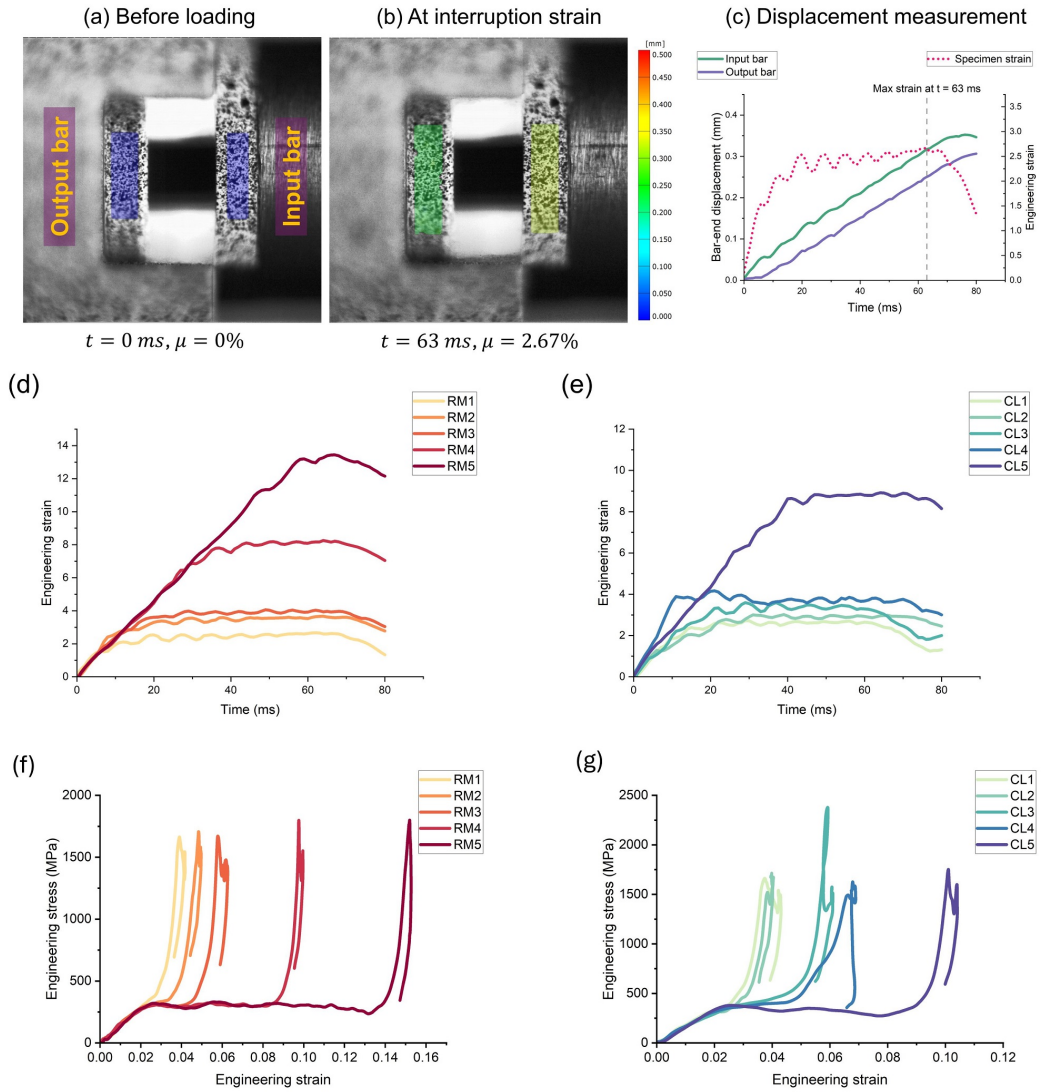


Figure 4.7: Evaluation of the specimen strain through image-based DIC measurement and strain-gauge-based wave measurement. (a) Image of the loading region before the impact arrived. (b) Image of the loading region at the interruption strain of the specimen. (c) The bar end displacement and distance tracking. The strain converted from the distance tracking for (d) the room-temperature specimens and (e) the low-temperature specimens. The stress-strain plots estimated from the wave measurement of the bars using strain gauges for (f) the room-temperature specimens and (g) the low-temperature specimens. Stable strains are shown after a rapid rise in the engineering strain-time measurements, indicating a successful interruption of the specimen strains. The sudden rises in the engineering stress-strain plot represent the same from a different measurement technique. Good agreement is seen between the two types of measurement.

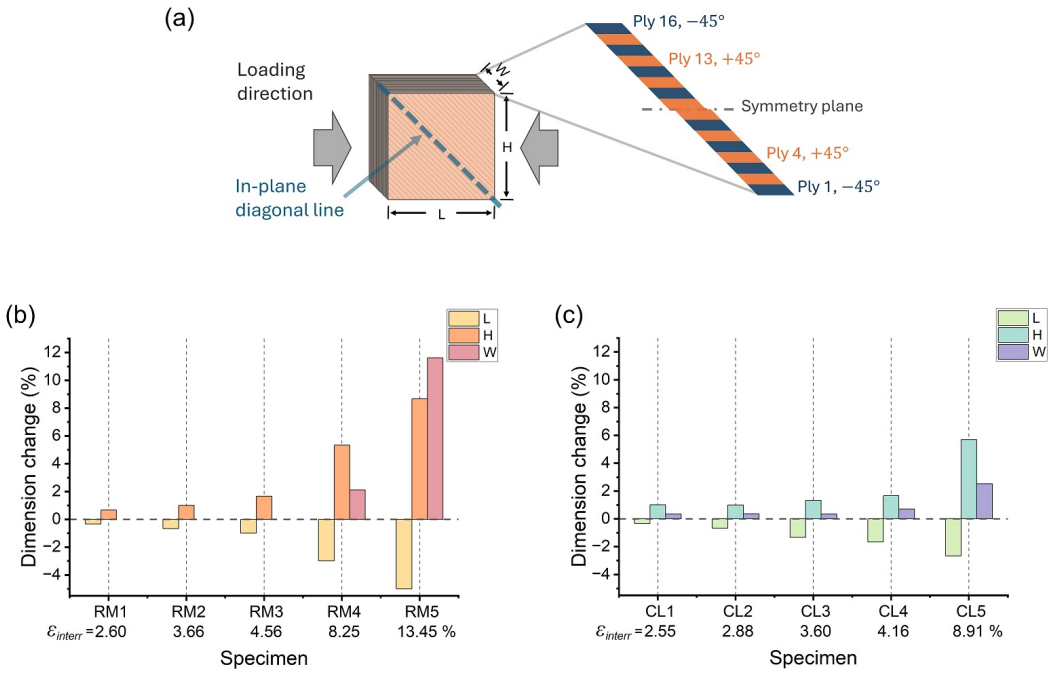


Figure 4.8: Macroscopic dimension change in the bulk specimens measured after the tests. (a) Specimen geometry, including dimension labels and ply layup. The permanent dimension change occurs after the loading for (b) the room-temperature specimens and (c) the low-temperature specimens. No width change can be seen at the room temperature until RM4, whereas evident expansion in width occurred starting from the specimen with the lowest interruption strain (i.e., CL1).

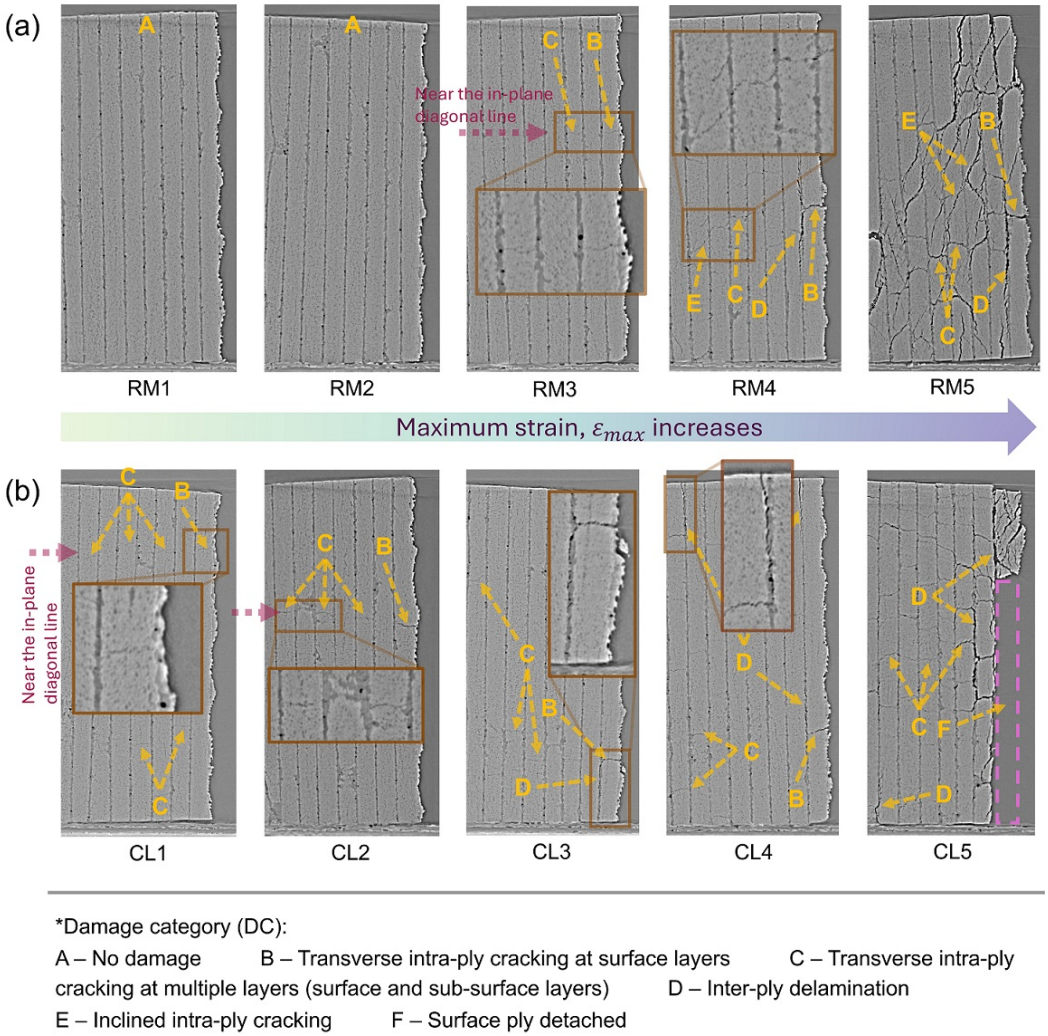


Figure 4.9: Micro-scale damage initiation and evolution in the specimens at (a) room and (b) low temperatures. The observed damage was categorised in six classes. The damage initiates and evolves more rapidly at low temperatures. Similar damage mechanisms can be seen at the early damage stages between the room and low temperature specimens, while different ones are shown at the late damage stages.

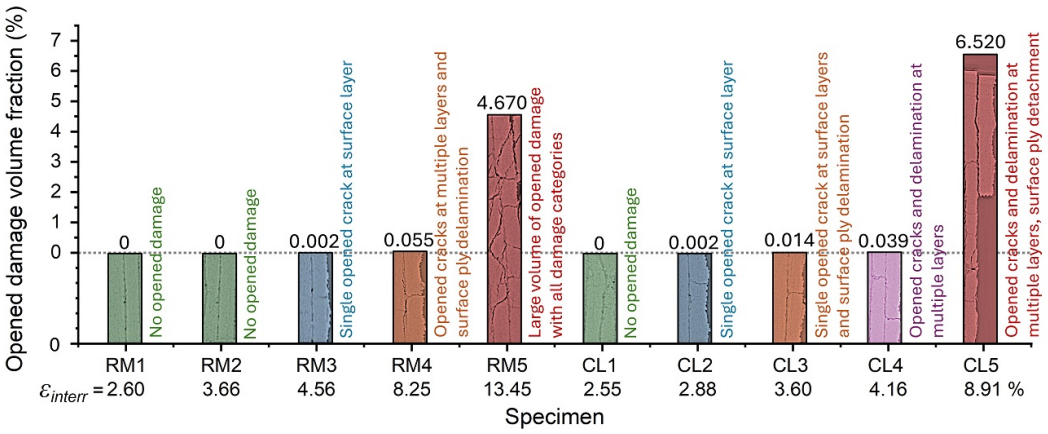


Figure 4.10: Volume statistics of the opened damage and their developments with the strain increases in the room and low temperature specimens. The volume increase of damage is more rapid in the low-temperature specimens. The damage in CL5 is significantly larger owing to the surface ply detachment on both sides of the specimens.

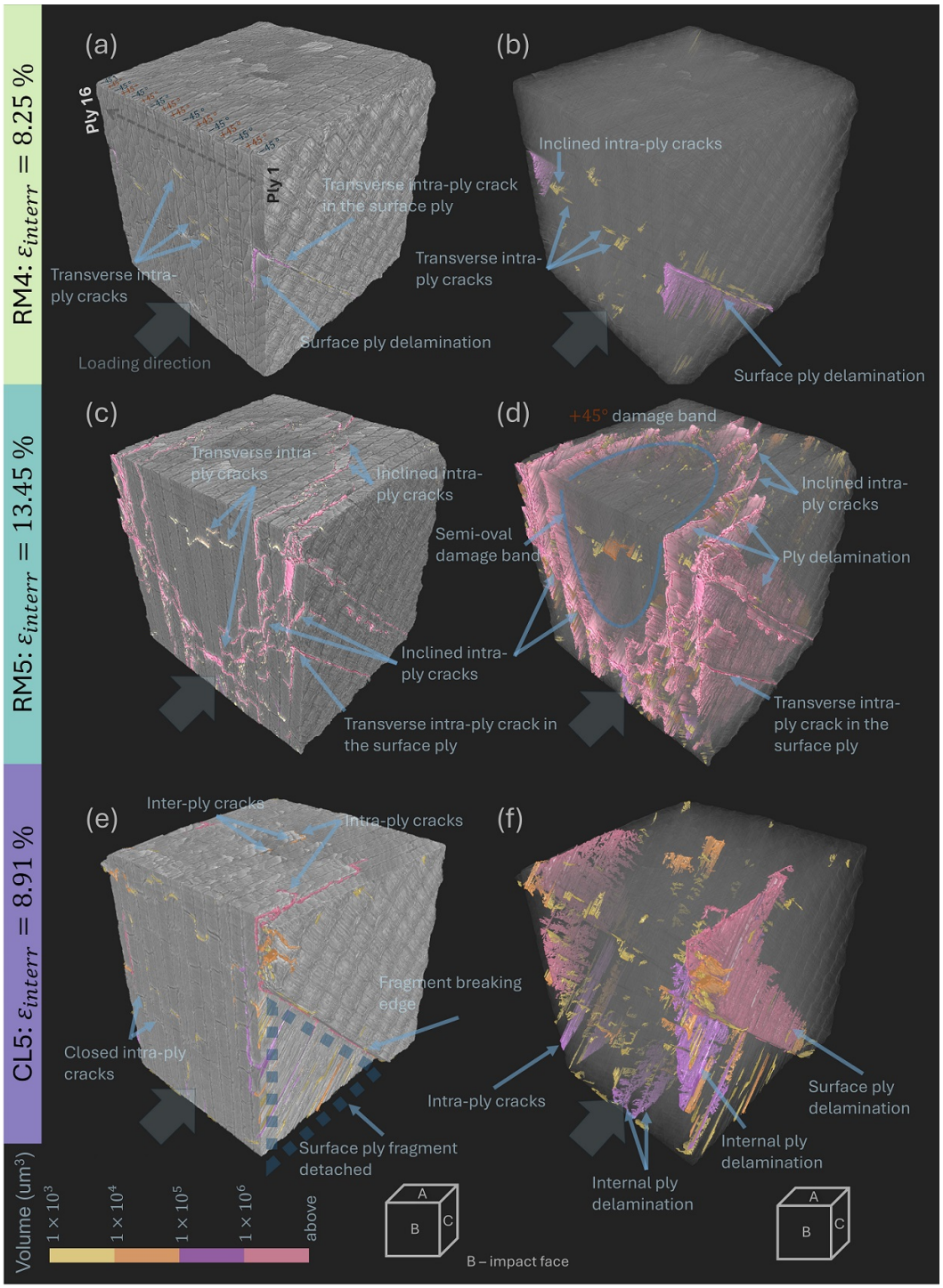


Figure 4.11: Opened damage in specimens with large interruption strain - RM4, RM5 and CL5 - visualised in 3D space. (a, c and e) are presented with solid specimen bodies to reveal the surface damage morphology and distribution, whereas those in (b, d and f) were made transparent to show the internal damage propagation. At a similar strain level, evidently larger damage can be seen in the low-temperature specimens. Prominent ply delamination at the low temperature seems to be the cause of the ply detachment in the surface plies. Discrete damage can be found in CL5, while the damage in RM5 demonstrates an interconnected pattern, forming obvious damage bands.

4.3 Chapter remarks

This chapter focuses on micro-scale damage characterisation in CFRP laminates by combining strain-interrupted loading with phase-contrast μ-CT, enabling detailed visualisation of damage initiation and evolution under varying temperature conditions. Distinct damage modes and morphologies were identified and systematically correlated with the corresponding inferred stress states. In particular, damage features containing internal void regions (i.e. opened damage) were extracted and quantitatively analysed as functions of global strain development and temperature variation.

Nevertheless, in the absence of direct measurements of local stress and strain concentrations, the underlying driving mechanisms governing damage onset and subsequent development cannot be quantitatively substantiated. To address this limitation, a DVC-based approach is proposed and will be developed in the following chapter (Chapter 5). This approach exploits the densely distributed microstructural features inherent to CFRP laminates, and thus, enables full-field strain measurements.

4.4 Paper II: Role of temperature in the development of micro-scale damage in CFRP laminates through interrupted high-rate loading and synchrotron phase-contrast μ-CT

Composites: Part A 200 (2026) 109284

Contents lists available at ScienceDirect

Composites Part A

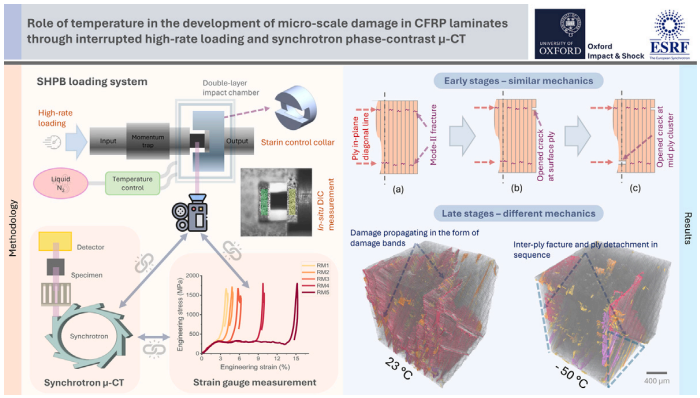
journal homepage: www.elsevier.com/locate/compositesa

Role of temperature in the development of micro-scale damage in CFRP laminates through interrupted high-rate loading and synchrotron phase-contrast μ-CT

Xiyao Sun [a], Bratislav Lukić [b,c,d], Kai Liu [a], David Sory [a], Maria Lißner [a], Justus Hoffmann [a], David Chapman [a], Nik Petrinic [a], Daniel Eakins [a,*]

[a] Department of Engineering Science, University of Oxford, Parks Road, Oxford, OX1 3PJ, UK
[b] European Synchrotron Radiation Facility, 71 Av. des Martyrs, Grenoble, 38000, France
[c] Henry Royce Institute for Advanced Materials, Department of Materials, The University of Manchester, Manchester, M13 9PL, UK
[d] Institut Max von Laue - Paul Langevin, 71 Av. des Martyrs, Grenoble, 38000, France

GRAPHICAL ABSTRACT



ARTICLE INFO

Keywords:
CFRP composites
Impact behaviour
Synchrotron X-ray tomography
Temperature-dependent damage

ABSTRACT

Understanding the evolution of damage in aerospace-grade CFRP composites after high-speed impact events is crucial for the safe design of components that can withstand dynamic loads. In this study, the temperature-dependent mechanisms of micro-scale damage in angle-ply CFRP were studied through a combination of interrupted high-rate compression experiments and synchrotron X-ray phase-contrast micro-tomography employing deep-learning-aided image analysis. Despite the earlier damage onset at low temperatures, all specimens tested have similar apparent-yield strains. The mechanisms responsible for the early damage, namely mode-II-dominant fracture in surface and subsurface plies, are observed to be similar at both low and room

* Corresponding author.
E-mail addresses: xiyao.sun@eng.ox.ac.uk (X. Sun), daniel.eakins@eng.ox.ac.uk (D. Eakins).
URL: https://shock.eng.ox.ac.uk (D. Eakins).

https://doi.org/10.1016/j.compositesa.2025.109284
Received 9 June 2025; Received in revised form 24 August 2025; Accepted 5 September 2025
Available online 17 September 2025
1359-835X/© 2025 Published by Elsevier Ltd.

temperature, with the surface ply cracks the first to develop into opened damage. After the occurrence of the middle-ply opened damage, while the room-temperature specimens dissipate energy through deformation and cracking originating from the specimen loading ends, glassy inter-ply fractures propagating from the surface towards the middle plies are the root of the rapid drop in specimen strength at low temperatures after the apparent-yield point.

1. Introduction

Carbon-fibre reinforced polymer (CFRP) composites are increasingly used in a variety of high-performance engineering applications, including aircraft, automotive, ships and satellites owing to their merits such as excellent specific strength and corrosion resistance [1–3]. However, their impact resistance is particularly important in these applications due to the inherent risk of high-speed foreign object impact during service. Off-fibre-axis compressive load resistance is normally a weakness of CFRP laminates and therefore a crucial factor that limits application [4]. As a result, understanding the nascence of damage mechanisms under high strain-rate (HSR) compression is imperative to improve the numerical simulation and design of CFRP.

While methods exist for *in-situ* investigation of subsurface damage in CFRP under quasi-static loading [5–7], experimentally capturing and characterising the damage initiation of CFRP laminates under HSR loading has been challenging because the process is normally transient. It is difficult to interrupt and resume during the loading, which gives rise to challenges in observing the internal micro-structural damage mechanisms. *In-situ* surface damage observation suggests that fibre kinking is the dominant failure mechanism for unidirectional (UD) laminates under in-plane loading [8]. Cross-ply (CP) laminates normally have slightly more complex damage as a combination of fibre kinking, ply delamination and matrix cracking owing to the introduction of 90° fibres [4,9]. Nano-scale *in-situ* crack observation performed by using synchrotron radiation X-ray computed tomography (CT) reveals that cracks in tested CFRP specimens initiated at the fibre/fibre contacting face in resin-thin regions and at fibre/resin interfaces in the resin-rich regions under opening loads [10]. Wang et al. [11] observed the formation of local fibre tilting prior to the formation of micro-scale kink-band in glass-fibre reinforced polymer (GFRP) with a similar *in-situ* X-ray CT approach. Final failure modes of CP [12], angle-ply (AP) [13], quasi-isotropic (QI) [14] and biaxial braided (BB) [15] laminates were investigated and found to be mainly inter-ply delamination under HSR in-plane compression.

The susceptibility of composites' mechanical properties to their ambient temperatures has been well established in previous research [16–20]. However, few existing studies have examined the associated micro-mechanisms of internal damage. Post-mortem inspection conducted by Sanchez-Saez et al. [21] and Ou et al. [22] indicate that both low and high temperatures can diminish the bonding strength at fibre/matrix interfaces and lead to a higher degree of fibre debonding and ply delamination. Furthermore, under tension, three-point bending and ballistic penetration, damage in CFRP laminates can develop more quickly and extensively through the bulk, with severe ply delamination taking place at lower temperatures [23–25].

Characterising the temperature effects on the damage of anisotropic composites such as CFRP laminates upon impact is an enduring challenge, which hinders the understanding of damage mechanisms and the development of damage prediction in composite engineering applications. Although the previous work [26] revealed the HSR damage evolution of CFRP laminates at different temperatures via *in-situ* dynamic X-ray imaging, only limited information was retrieved at the damage onset stage, especially through the laminate thickness. Other recent research using dynamic X-rays [27–30] suffers from similar problems owing to the low-resolution and 2D projection nature of this technology. In this context, the present research aims to investigate micro-structural damage initiation and propagation in AP CFRP laminates under HSR in-plane compression. Impact loading was precisely interrupted at specific specimen strains at varying *in-situ* testing temperatures to control the extent of damage. High-resolution synchrotron phase-contrast CT was utilised to observe the micro-scale damage at different loading stages. Finally, the micro-structural damage morphology and mechanisms of the tested specimens at different temperatures and loading stages were characterised, analysed and compared.

Table 1
Specimen details and testing conditions. All specimens were dynamically compressed along the plane of the laminates at an approximate strain-rate of 2500 s^{-1}.

Label	Volume, mm^3	Weight, g	Designed final strain, %
Room: 23 ± 2, °C			
IF1	24.85	38.20	No interrupt
IF2	26.37	40.16	No interrupt
IF3	25.92	40.06	No interrupt
RM1	25.46	39.23	2.33
RM2	24.93	38.02	2.99
RM3	26.18	40.23	3.99
RM4	25.56	39.17	8.00
RM5	25.83	39.53	13.00
Cold: −50 ± 2, °C			
IF4	25.91	39.45	No interrupt
IF5	24.42	37.64	No interrupt
IF6	23.52	36.62	No interrupt
CL1	24.85	38.48	2.33
CL2	24.56	38.11	2.66
CL3	26.10	40.02	3.32
CL4	25.73	39.39	4.32
CL5	24.94	38.23	8.31

2. Materials and methods

2.1. Material and specimen

The tested carbon-fibre reinforced polymer (CFRP) laminate is composed of a high-performance epoxy resin provided by Hexcel Corporation and "standard modulus" carbon fibres provided by Toray Industries, Inc. The laminates were autoclave-cured using the following process: heating to 180 °C at a rate of 1–2 °C/min, dwelling for 120 mins, and cooling back to room temperature at a rate of 2–5 °C/min. A hand lay-up method using UD fibre prepregs was introduced to produce a $[+45/-45]_{4s}$ AP lamination with a nominal thickness of 3 mm. The CFRP specimens were cut into small cubes ($3 \times 3 \times 3$ mm^3) to fit the field of view of the high-resolution X-ray micro-computed tomography (μ-CT). It should be noted that the small specimen size necessary for the current experimental approach might lead to the specimen response not being fully representative of the bulk or structural scale. However, the focus of the present research is to investigate the temperature effect on CFRP micro-scale damage mechanisms involving the behaviours of fibres, matrix, and their interactions under high-rate loading.

As listed in Table 1, 16 specimens in total were tested at room (23 °C) and cold temperature (−50 °C). Among them, 6 specimens (IF1 - 6) were impacted without specimen strain interruption to evaluate the overall stress–strain behaviours of the tested CFRP laminates. Based on this, 5 representative strain levels were selected as the target strain for each temperature. The loading of the remaining 10 specimens (RM1 - 5 and CL1 - 5) was interrupted at the target strains to evaluate the specimens' damage at the different loading stages.

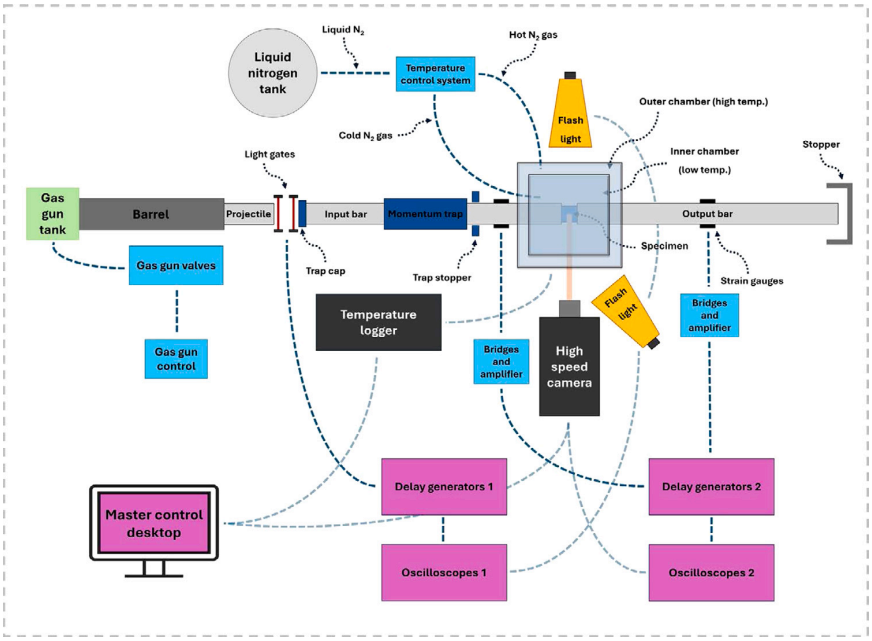


Fig. 1. Schematic of the experimental setup depicting the HSR loading apparatus, temperature control, temperature monitoring, strain recording, and imaging systems. Two flashes were set up to compensate for light obstruction caused by the strain control collars. The flash facing the front of the specimen (on the same side as the camera) was to illuminate the speckles for strain tracking; the one opposite the camera was for backlighting to locate the specimen and check for gaps at the specimen/platen interfaces.

2.2. High strain-rate loading

A split-Hopkinson pressure bar (SHPB) system was used to apply HSR in-plane loading to the CFRP specimens (see Fig. 1). The system is composed of a 200 mm striker bar, a 1300 mm input bar and a 1100 mm output bar. All the bars are made of titanium alloy (Ti-6Al-4V) with a diameter of half an inch (~12.7 mm). Two 3 mm-thick Ti-6Al-4V loading platens with the same diameter were placed between the specimens and bars to avoid the bars being damaged. A momentum trap system was installed on the input bar to prevent the secondary impact of the specimens.

Strain control collars with different spacer thicknesses were manufactured from Ti-6Al-4V titanium alloy, and were mounted at the end of the output bar, as illustrated in Fig. 2. The specimen is sandwiched between the input and output bars in the open area beside the collar spacer. Upon loading, the input bar will first compress the specimen. Once the specimen is compressed to the same thickness as the collar spacer, the input bar will come in contact with the collar spacer and create a 'hard stop' to prevent further deformation of the specimen. In this way, the thickness of the spacers was chosen to limit the maximum strain applied to the specimen.

All HSR loading tests were performed with a projectile impact velocity of about 13.8 $m\,s^{-1}$, producing an approximate strain-rate of 2500 s^{-1} onto 3 mm length specimens. Prior to the interrupted strain tests, HSR loading tests without strain interruption (impact to failure) were also conducted to evaluate the mechanical behaviours of tested CFRP laminates at room and low temperatures. It is worth mentioning that the mechanical responses of the specimens in this research mainly serve as a reference for the damage analysis. The specimen stress calculation directly adopts the cross-sectional area of the specimens, rather than following ASTM D3518/D3518M [31] for in-plane shear testing of ±45° laminates.

2.3. Test temperature control

A bespoke double-layer PMMA (polymethyl methacrylate) box was designed and manufactured as the cryogenic chamber for the HSR loading tests. During the low-temperature tests, the impact of specimens was taking place in the inner box filled with cold (approx. −80 °C) nitrogen gas. In the meantime, the hot (approx. 50 °C) nitrogen gas was injected into the outer chamber, which prevents frost and mist from forming on the inner window by removing the ambient moisture and on the outer window by maintaining the window temperature above 0 °C. The temperature control of the injection flow was achieved by using a bespoke flow and temperature control system. The system inlet was connected to a liquid nitrogen tank. The injected liquid nitrogen was first converted into gas in a nitrogen reservoir. Then, the cold nitrogen gas was divided into two flows, one flow was heated to the target testing temperature and injected into the inner chamber of the box, and another flow was heated to high temperatures and filled into the outer chamber. Temperature measurement was performed at multiple locations in the inner and outer chamber to ensure a stable temperature and mist control.

2.4. Strain control and measurement

Strain gauges were applied in these tests to monitor the stress–strain behaviours of the specimens. They were mounted 550 mm uprange of the input bar/specimen interface and 500 mm downrange of the output bar/specimen interface. By assuming one-dimensional wave propagation, the engineering stress and strain of the specimens can be estimated based on the measured bar strain and their time difference [32]. In addition, an extra strain monitor measure — a visible-light high-speed camera — was also introduced. Digital image correlation (DIC) was performed on top of the recorded images using `GOM Correlation` to monitor the specimen strain throughout the loading process. The

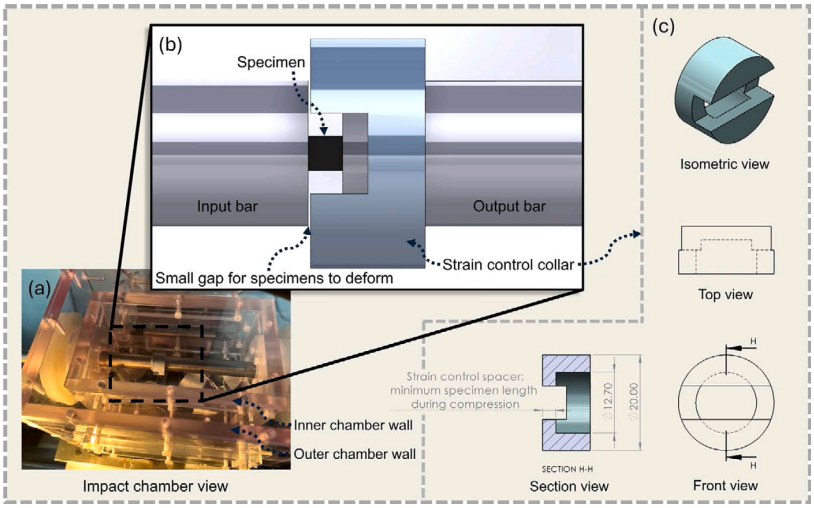


Fig. 2. Strain control collar design and setup: (a) photo of the collar mounted on the bars in the impact chamber, (b) zoom-in schematic illustration and (c) detailed drawings. The strain control collars were manufactured with high precision to produce quality specimen strain control. The tolerance of the strain control spacer was maintained within ±10 μm.

interruption strain measured by DIC was adopted as ε_{interr} (the strain reference) for damage analysis. Apart from that, the theoretical maximum specimen strain was also estimated with the assumptions of linear elastic deformation of collar materials. The peak force, F_{max} acting on the strain control collars and specimens can be obtained using,

$$F_{max} = A_b E_b \varepsilon_{b,max}, \tag{1}$$

where A_b and E_b are the cross-sectional area and the elastic modulus of the output bar. The maximum compressive strain of the output bar is noted as $\varepsilon_{b,max}$. The supporting force provided by the specimen at the point of peak loading force (F_{sp}) can be estimated as,

$$F_{sp} = A_b \sigma_{sp}. \tag{2}$$

The maximum stress of the tested CFRP laminates in the design strain interruption range (σ_{sp}) is around 300 MPa. Therefore, by assuming this value, the approximated collar spacer strain, ε_c can be represented by,

$$\varepsilon_c = \frac{F_{max} - F_{sp}}{A_c E_c}, \tag{3}$$

where A_c is the cross-sectional area of the collars that is in contact with the faces of the bar end, and E_c is the elastic modulus of the collar material. The maximum theoretical strain of the specimens, ε_t will be the summation of specimen strain before and after the collar's intervention, ε_{t1} and ε_{t2}, expressed as,

$$\varepsilon_t = \varepsilon_{t1} + \varepsilon_{t2} = \frac{(l_{sp} - d_c) + \varepsilon_c d_c}{l_{sp}}, \tag{4}$$

where the length of the specimens was noted as l_{sp}, and d_c is the thickness of the collar spacer.

Statistic analysis was carried out to assess the validity of the strain control during impact loading. The standard deviation of the four strain data sets (S_ε), including the designed strain (ε_d), theoretically calculated strain (ε_t), DIC-measured strain (ε_i) and gauge-measured strain (ε_g), can be expressed as,

$$S_\varepsilon = \sqrt{\frac{1}{4}\sum_{n=1}^{4}(\varepsilon_n - \bar{\varepsilon})^2}, \tag{5}$$

where $\bar{\varepsilon}$ stands for the mean of the four strain sets. Finally, the dispersion of the strain data is estimated using the coefficient of variation (CV_ε),

$$CV_\varepsilon = \frac{S_\varepsilon}{\bar{\varepsilon}}. \tag{6}$$

2.5. Micro-computed tomography scanning

As listed in Table 1, all specimens were scanned with μ-CT prior to the impact tests (pre-scan) to study the original state of the laminates' internal structure. Among them, 10 specimens were also scanned after the tests (post-scan) to examine and characterise the damage of specimens at different temperatures. The μ-CT scanning was performed at a synchrotron X-ray beamline - ID19 at the European Synchrotron Radiation Facility (ESRF), France with a voxel size of 2.1 × 2.1 × 2.1 μm^3. Synchrotron-based X-ray imaging can achieve higher scanning efficiency (i.e., shorter scanning times) and resolution compared to laboratory-based μ-CT by virtue of the high energy flux and microscopic source size [5]. Apart from that, by taking advantage of the brilliance and (partial-)coherence of synchrotron X-ray radiation gain through free-space propagation, the micro-damage inside the specimens can be enhanced via X-ray phase contrast tomography of weakly absorbing specimens [33]. The specimens were illuminated with a filtered white beam emitted by the beamline's wiggler insertion device located 150 m upstream of the specimens. The two sets of in-vacuum slits were used to focus the beam onto the desired field of view (FoV) and for heat moderation coming from off-axis energy spread. A series of filters (i.e., diamond, aluminium and copper) were used, providing impinging wide-spectrum radiation with a peak energy of 40 keV. The indirect detector consisted of a 3× magnification tandem lens (300 mm:100 mm, Hasselblad, Sweeden) coupled to a sCMOS camera (pco.edge 5.5, PCO AG, Germany) and a 250 μm thick LuAG:Ce scintillator. The detector was positioned 250 mm away from the specimens, allowing for sufficient edge enhancement to form through the propagation-based phase contrast effect. During a full rotation of 360 degrees, 6000 projections were taken. The 3D tomographic reconstructions were carried out with ESRF reconstruction software employing a single-distance phase-retrieval approach [34] and the ratio of the real and complex part of the refraction index (δ/β) of 120.

The pre- and post-scans were performed at two separate beamtimes. Hence, image normalisation and registration between pre- and post-scans are necessary to enable qualitative and quantitative comparisons.

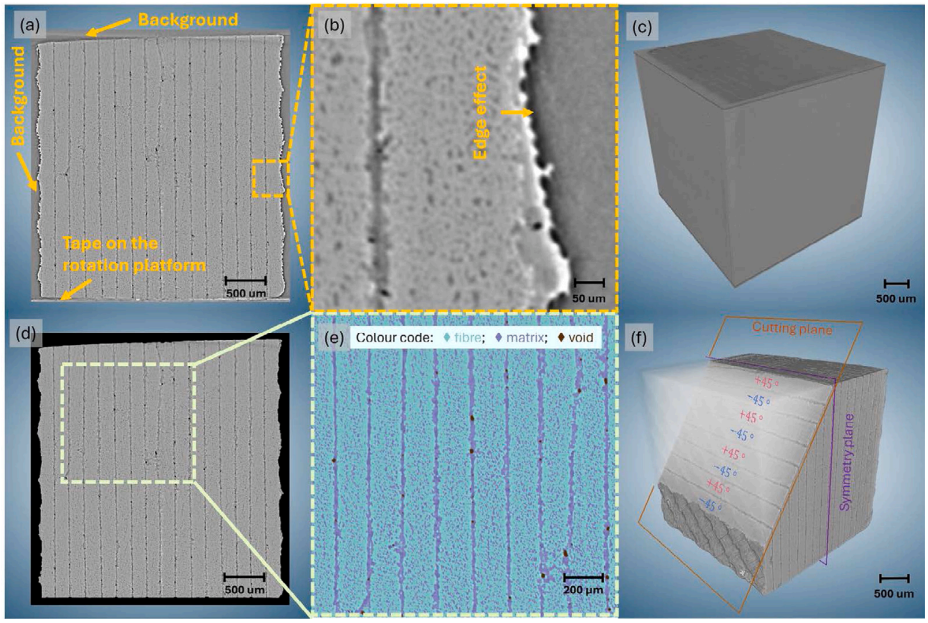


Fig. 3. Tomographic reconstruction of an original, uncompressed specimen: (a) original 2D slice, (b) magnified view, and (c) 3D volume rendering without removing the background and rotation platform; (d) 2D slice, (e) magnified view, and (f) 3D volume rendering after removing the background and rotation platform. The background cannot be removed by simple thresholding because its grey values are similar to the specimen's matrix. Additionally, the platform was a similar grey value and texture to the specimen, necessitating removal using a bespoke `Python` script.

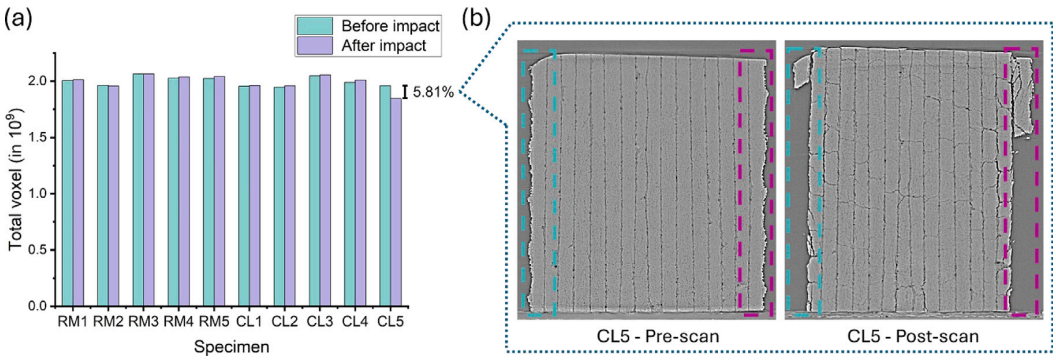


Fig. 4. (a) Total number of specimen voxels after removing backgrounds. Good agreement can be found between pre-scans and post-scans for most specimens with less than 1% differences. (b) A slice comparison between CL5 pre-scan and post-scan before removing the background showing surface plies on both sides fractured and detached from the specimen after the impact.

Image registration was implemented using image computation software - `3D Slicer` [36]. A `Python` code was developed to normalise the pre- and post-scan images. A U-Net-based deep learning model embedded in `Dragonfly 3D World` software [37] was trained and implemented together with `Python` scripts to remove the noise and unwanted background in the obtained µ-CT images. The `MaxEntropy` thresholding method was used to segment the void and damage from the specimens. The qualitative and quantitative damage analyses were then carried out using a workflow involving `ImageJ`, `Dragonfly` and `Python`.

3. Results

3.1. Specimen micro-structure

2D and 3D image visualisations are presented in Fig. 3. The background's grey value is similar to that of the specimen's matrix due to the superposition effect of X-ray phase contrast between the background (i.e. air) and specimen. Edge effects are shown along the irregular boundary of the specimens, seen as a dark and light fringe following the specimen outline (Fig. 3a and b). The specimens' internal features cannot be effectively recognised and extracted without removing the background and specimen support from the original scans (Fig. 3c). Thus, a trained deep-learning model was used and demonstrates high accuracy in this complex background recognition and segmentation scenario (Fig. 3d).

A layer of tape used to secure the specimens on the rotation platform shows a similar grey value and texture to the specimens (Fig. 3a). A custom-developed `Python` script can help aid the deep learning model in accurately segmenting the tape on the platform. As shown in Fig. 4, good volume consistency can be found between the pre-scans and post-scans of most specimens, suggesting a reliable background removal method. The discrepancy for CL5 is slightly higher (~5.81%) because

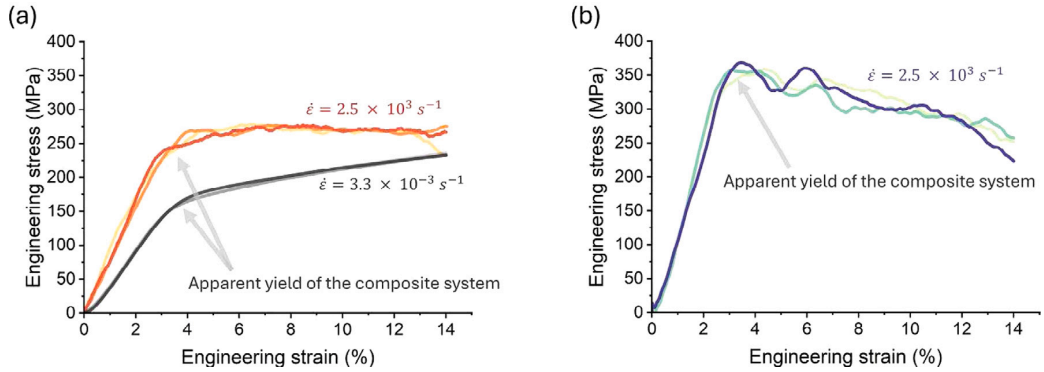


Fig. 5. Mechanical responses of the specimens at about 2.5×10^{3} s^{-1} strain rate. Stress–strain curves under impact-to-failure loading for (a) room temperature specimens with the quasi-static (3.3×10^{-3} s^{-1}) loading curves as a baseline and (b) low-temperatures specimens. Please note that the quasi-static stress–strain curves were obtained from the load cell and cross head displacement of the universal loading machine. The low-temperature specimens demonstrate evidently higher peak strength, followed by a quicker stress drop. The post-apparent-yielding behaviours of the specimens at three test conditions shift from strain hardening (quasi-static at room temperature) to stress flowing (HSR at room temperature) and then strain softening (HSR at low temperatures). "Apparent yield", in the present research, refers to the sudden change in gradient of the stress–strain responses of the specimens [35].

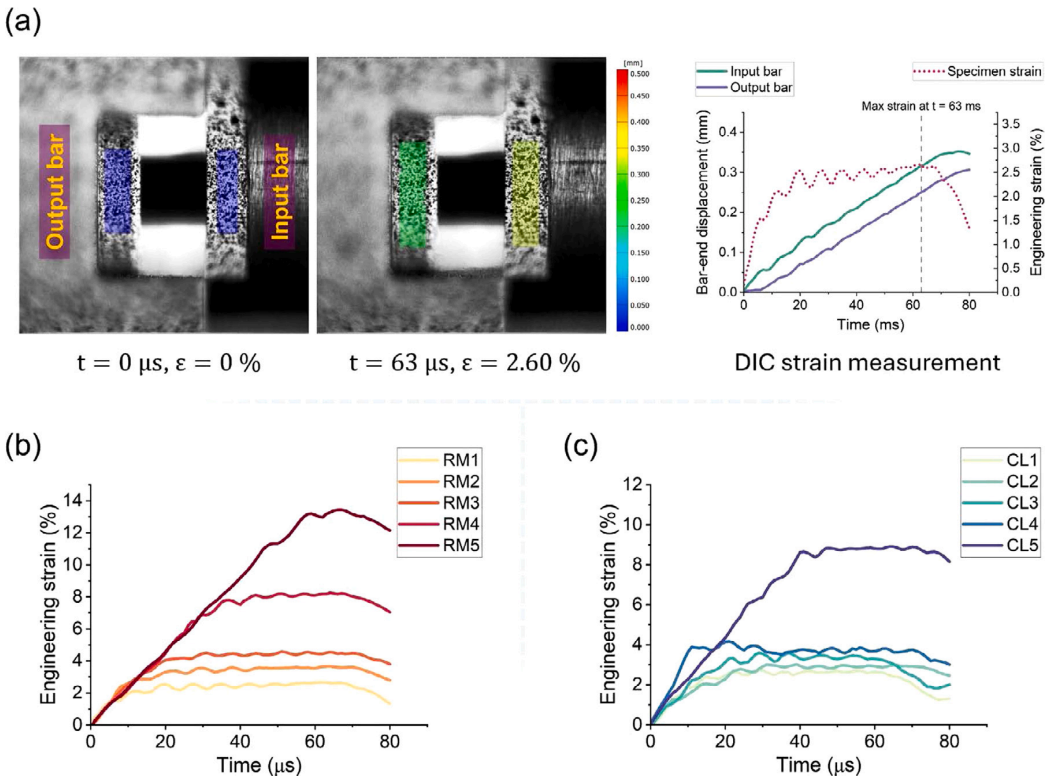


Fig. 6. Specimen strain measurement by performing DIC on visible light images captured during impact loading: (a) an example using specimen RM1 demonstrating speckle recognition and displacement tracing; strain measured for specimens at (b) room and (c) low temperatures. The sudden flattening of strain-time curves indicates the intervention of the strain control collars. The specimen strain was interrupted and maintained near the designed strain levels after the input bar end came into contact with the collars.

the surface plies detached from the laminates at large strain during the impact.

The processed specimen volume shown in Fig. 3(e and f) demonstrates +45° and −45° unidirectional plies are laid up in turn and symmetry about the middle plane forming a total of 16 plies with each in the approximate thickness of 170 μm. 5 μm-diameter carbon fibres are densely packed in each ply, resulting in an overall measured fibre volume fraction of about 60% (Fig. 3e). Voids with diameters ranging

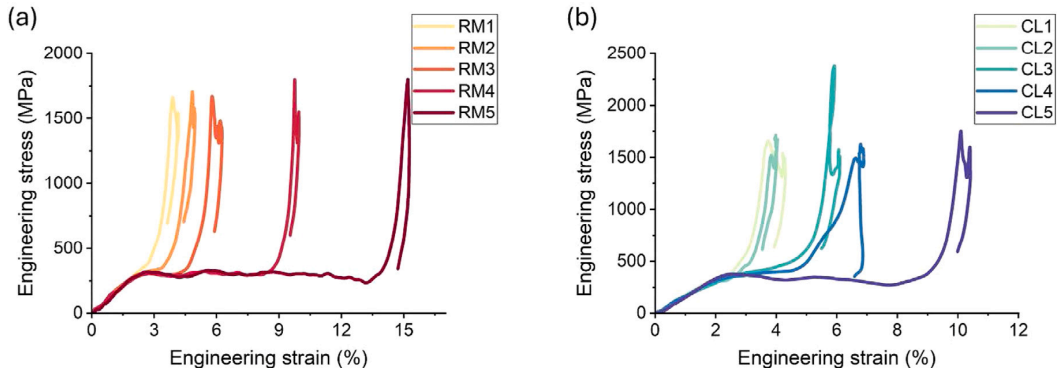


Fig. 7. Stress–strain curves of the specimens with strain interruption at (a) room and (b) low temperatures. The starting points of the sudden stress rise indicate the beginning of strain intervention.

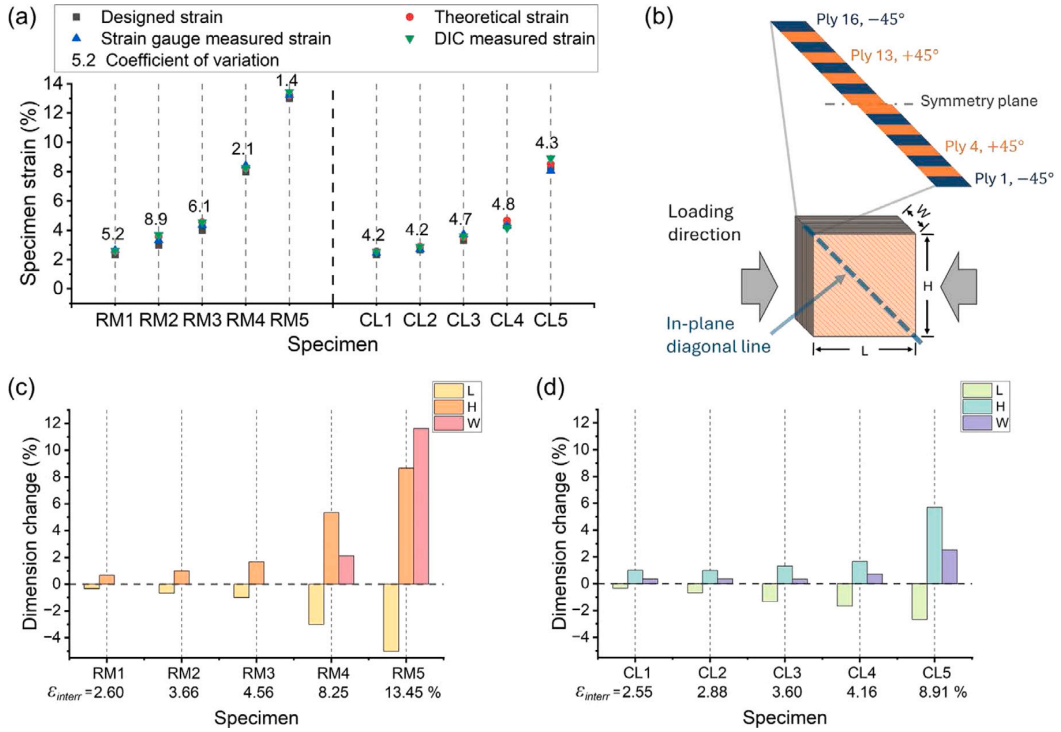


Fig. 8. Specimen dimension change after the impact: (a) comparison between designed strain, theoretically estimated strain and measured strain of specimens with the coefficients of variation; (b) specimen geometry, loading and ply configurations; dimension change induced by the impact for (c) room- and (d) low-temperature specimens. As a recap: the designed strain is the target strain from the experiment plan (see Table 1); the theoretical strain is the strain estimation based on the measured force in the bars and the mechanical properties of the specimens and collars (see Section 2.4); the strain-gauge-measured strain was obtained from the SHPB analysis (see Section 2.4); and the DIC-measured strain was determined from the high-speed images (see Section 3.3).

from 5 to 20 μm can be found in the resin-rich area between plies occupying a slight volume of around 0.2% in the specimens, similar to the data from the literature [38]. No crack-shaped defects or damage at the micro-scale level and above can be found in all the pre-scanned specimens.

3.2. Mechanical properties

Fig. 5 shows the mechanical response of the HSR load tests without interrupting the specimen strain during the loading (impact to failure). Despite the similar loading rate, the specimens tested at low temperatures exhibit significantly higher peak strength (approximately 35%) than the room-temperature specimens [26]. For the room-temperature specimens (Fig. 5a), a stable flow stress stage appears after the elastic-like deformation phase, different from an obvious strain-hardening behaviour of the specimen under quasi-static loading (~10^{-3} s^{-1}), as shown by the grey curves. In contrast, the low-temperature specimens exhibit distinct stress peaks, followed by noticeable stress drops. Nevertheless, the elastic-like deformation stage for specimens at both temperatures seems to end between 3 to 4% strain, similar to their quasi-static reference. Thus, the specimens' interruption strain (ε_{interr}), listed in Table 1, was specifically chosen to range from under 3% to over 4% strain, ensuring coverage of varying damage levels in the specimens.

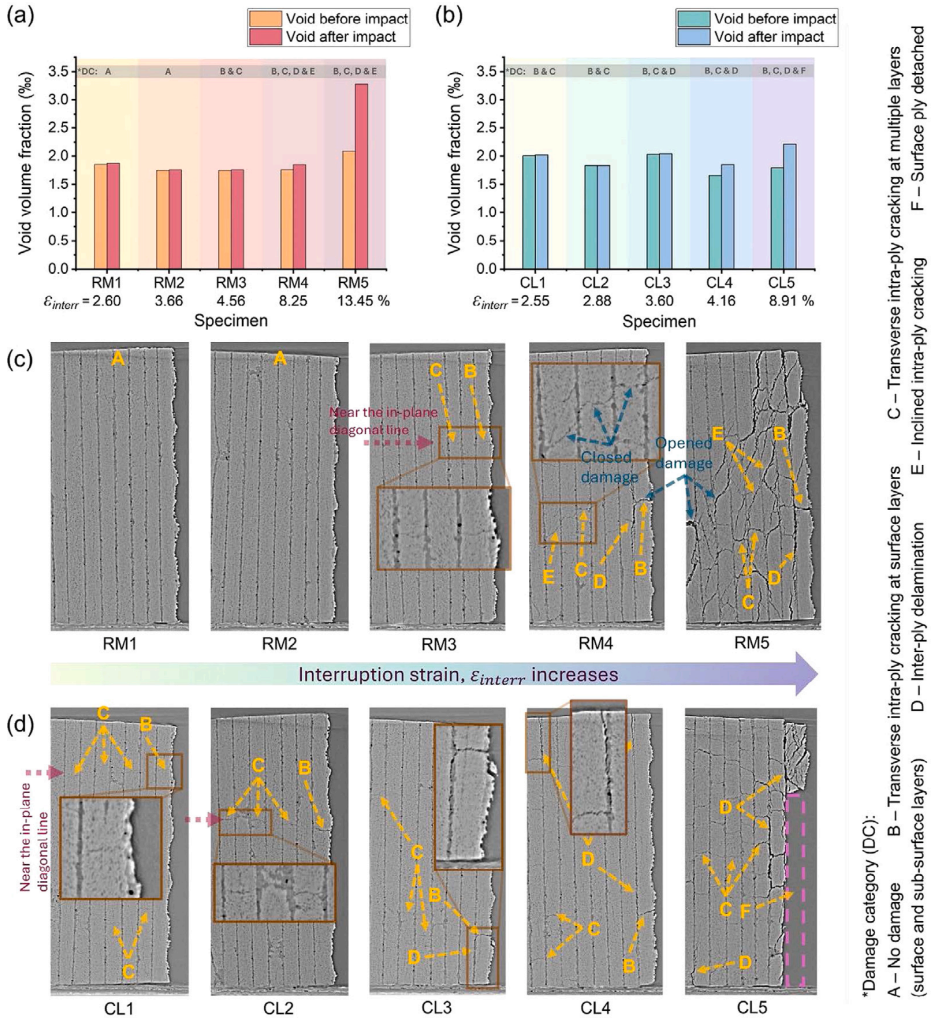


Fig. 9. Specimen internal structure change with strain increase. Void volume fractions before and after impact for (a) room- and (b) low-temperature specimens. Good void volume consistency can be found in the specimens with low ϵ_{interr}. Damage development overview shown in the symmetric half for (c) room- and (d) low-temperature specimens. The damage volume increases and the damage morphology evolves at both temperatures with increasing ϵ_{interr}.

3.3. Strain interruption

Fig. 6a demonstrate an example of strain measurement via tracking the movement of the loading platens on both sides of the specimens. The analysed strain development with time obtained from DIC for room- and low-temperature specimens are plotted in Fig. 6(b and c), respectively. The produced ϵ_{interr} increases progressively from RM1 to 5 and from CL1 to 5. The specimens experienced a free compression stage without any collar interference, reflected by a linear-like increase at the start of the loading, followed by a bar/collar interaction stage where the curves level out with observable strain oscillations. The specimen stress–strain relations extracted from strain gauge signals is presented in Fig. 7(a and b) for room- and low-temperature specimens, respectively. The sudden rises in stress also indicate the points at which the input bar ends came into contact with the strain control collars.

Together with the designed and theoretically calculated strain, in total, four sets of strain (design strain, theoretically calculated strain, DIC-measured strain and gauge-measured strain) are plotted in Fig. 8a. Statistic assessment by calculating the coefficient of variation suggests a minor dispersion (less than 10%) between the four sets of strain data for all specimens. This demonstrates the validity of the strain interruption in this impact experiment.

The nominal dimension change of the specimens after the impact was measured and is visualised in Fig. 8(c and d). The height (H) and width (W) of all specimens increased with the increasing strain at both temperatures. However, for the room-temperature specimens, there is no W change at low strains (e.g., RM1 - 3). In comparison, W increased in all low-temperature specimens after the impact. A larger dimension reduction in specimens' length (L) can also be seen in the low-temperature specimens, especially at low ϵ_{interr} (i.e., comparing between RM1 - 3 and CL1 - 4).

3.4. Damage characterisation

The internal micro-structural analysis indicates the voids occupy around 2‰ in the volume of all specimens, as shown in the column charts in Fig. 9(a and b). Good consistency in void volume can be seen between the pre-scans and post-scans, especially for the specimens with slight and mild damage (e.g., RM1 - 3 and CL1 - 3). An internal damage overview presented in Fig. 9(c and d) indicate higher ϵ_{interr}

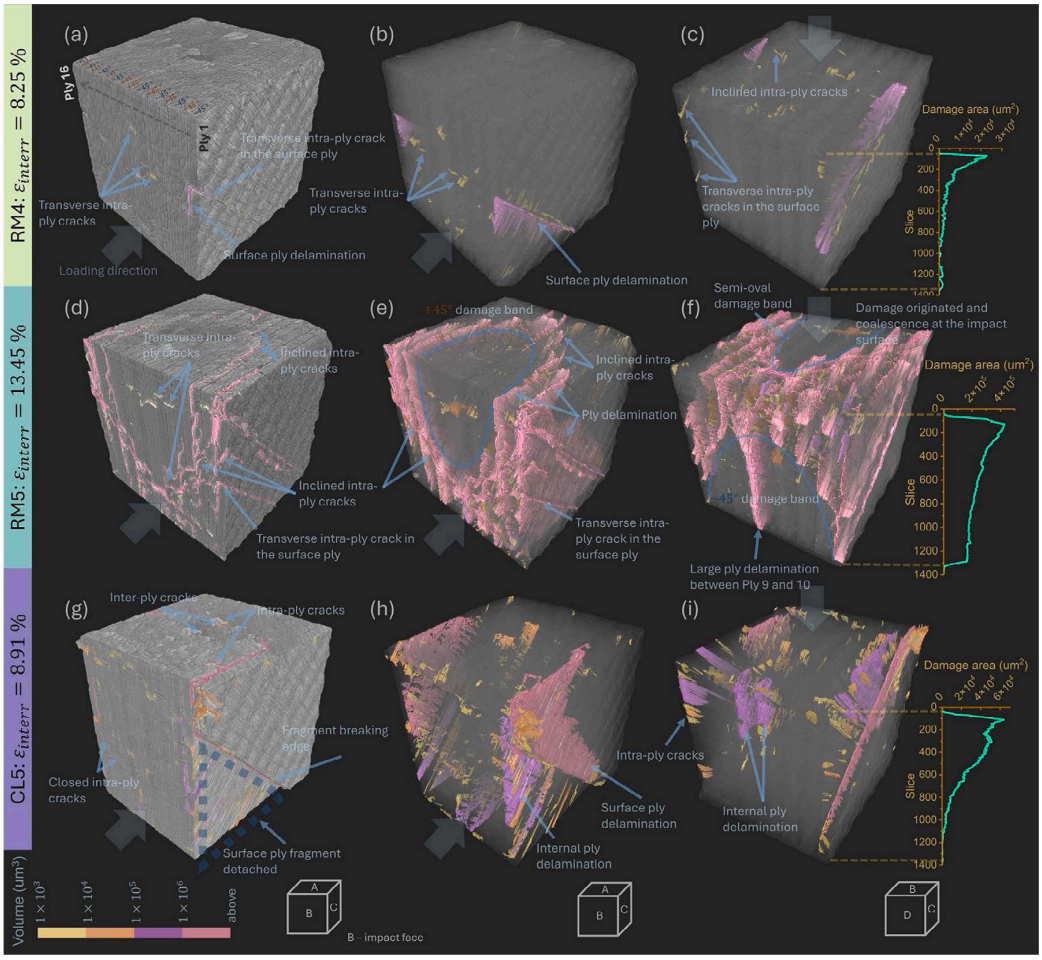


Fig. 10. Tomographic reconstructions of opened damage in tested specimens. Specimen RM4: (a) damage with solid specimen body; (b) and (c) damage with transparent specimen body. Specimen RM5: (d) damage with solid specimen body; (e) and (f) damage with transparent specimen body. Specimen CL5: (g) damage with solid specimen; (h) and (i) damage with transparent specimen body. Damage is colour-coded based on size, and the colour map is presented in the bottom-left corner. The observation directions are noted at the bottom of each figure column. The damage distributions along the loading direction are plotted next to the 3D volume reconstruction in (c), (f) and (i).

had led to larger damage in the specimens at both temperatures. More internal voids can be created during the process of loading, deforming and fracturing of RM4, RM5, CL4 and CL5.

However, the damage in low-temperature specimens appears to have an earlier initiation and more rapid evolution compared to room-temperature specimens, as observed in the previous work [26]. As shown in Fig. 9(c and d), the damage observed in the tested specimens was categorised into six types based on its morphology and state - A. No damage; B. Transverse intra-ply cracking at surface layers; C. Transverse intra-ply cracking at multiple layers; D. Inter-ply delamination; E. Inclined intra-ply cracking; and F. Surface ply detached. The damage class - 'opened damage' in the present research specifically categorises the damage or crack with the width greater than 3 pixels, that is about 6.3 μm. Maximum specimen strain, ε_{interr} was taken from the DIC measurement and set as the reference for damage development analysis.

At room temperature, the specimens have no observable micro-scale damage with low ε_{interr} (RM1 and RM2), as shown in Fig. 9c. In the specimen with ε_{interr} = 4.56% (RM3), the initiated intra-ply cracks can be seen at the surface layers propagated along the ply fibre direction and roughly aligned with the ply in-plane diagonal line (Fig. 8b) on both sides of the specimen. They slightly opened up near the impact face [26]. Apart from that, intra-ply cracks at their minimal size can also be found in the subsurface layers aligned with the surface layer intra-ply cracks in the through-width direction (highlighted by a pink arrow in Fig. 9c). The ε_{interr} of 8.25% (RM4) produces intra-ply cracks not only in surface plies but also in subsurface plies (also see Fig. 10a–c). Besides the transverse intra-ply cracks observed in RM3, inclined intra-ply cracks were also found (also see Fig. 11a). Delamination between the surface and second layers can be clearly seen. In addition, the through-length damage analysis of RM4 along the loading direction presented in Fig. 10c demonstrates the damage highly concentrates at the specimen's loading end. Similar damage distribution was also observed in existing literature [39,40].

RM5 shows that a large volume of damage can be introduced after the specimens experienced a 13.45% ε_{interr}. Intra-ply cracks and inter-ply delamination appeared throughout the specimen width (also see Fig. 10d–f). Cracks are opened and inter-connected through inclined intra-ply cracks and ply delamination forming into a branch-shaped damage morphology and rooted at the lower part of the two middle plies (Ply 8 & 9). A semi-oval damage band (also see Fig. 11b) can be found on the impact face (Face B) and its two adjacent faces (Face

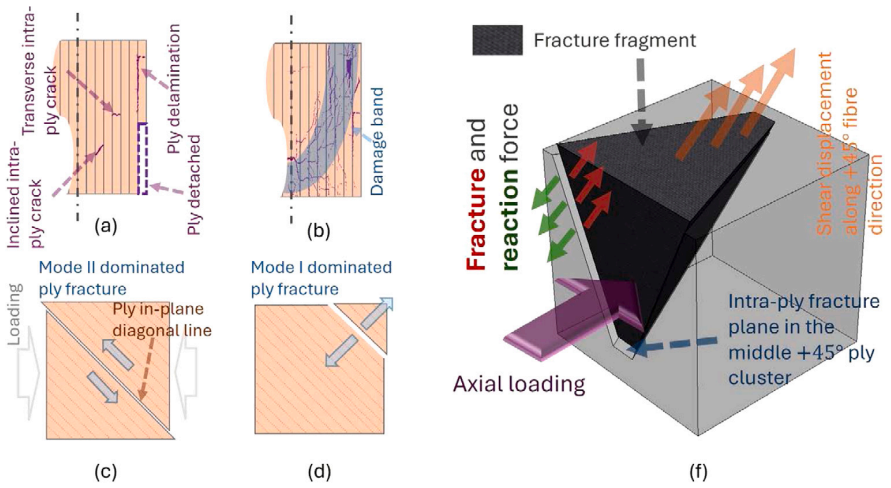


Fig. 11. Observed damage features in sketches. (a) Different types of damage and (b) damage band observing from in-plane load direction. (c) Mode-II-dominated fracture caused directly by the in-plane compression, (d) Mode-I-dominated fracture caused by inter-ply shear and (e) hypothesis of the generation of V-shaped or semi-oval-shaped fractures: the specimens under axial impact causing a chunk of fragment displacing along the middle ply fracture.

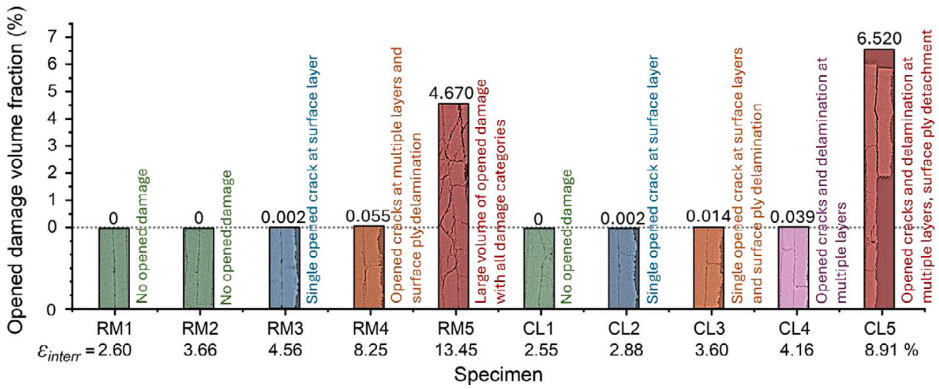


Fig. 12. Opened damage development with the specimen strain increase and the description of key damage features. The damage volume fraction for specimen CL5 includes the detached volume. At similar strain levels, the specimens at low temperatures have significantly more opened damage than their room-temperature counterparts.

A and D), as shown in Fig. 10(e and f). The damage band on Face A was mainly formed by +45° intra-ply cracks and the associated delamination, whereas −45° cracks and the associated delamination compose the damage band on Face D. The semi-oval damage band on the impact face (Face B), however, is a combination of both +45° and −45° intra-ply cracks. The 3D bulk region encompassed by the damage bands on Face A and B are prominently more intact compared to the damage band regions. The through-length damage distribution shown in Fig. 10f indicates the damage is denser near the impact face of the specimen. However, its distribution along the specimen length is much more uniform compared to RM4.

Specimens at low temperatures started to have transverse intra-ply cracks at low strain levels (Fig. 9d). Transverse intra-ply cracks can already be found in surface and subsurface plies in CL1 (ε_{interr} of 2.55%). No new damage categories were introduced in CL2 (ε_{interr} = 2.88%), but the surface ply crack had started to open up. The initiated intra-ply cracks in CL1 and CL2 also propagated along the ply fibre direction and is approximately aligned with the ply in-plane diagonal lines as the room temperature specimens (highlighted by pink arrows in Fig. 9d). At ε_{interr} = 3.60% (CL3), mild ply delamination occurred between the surface and the second plies. No obvious opened damage can be found in the rest of the regions in the specimen. On top of CL3, CL4 also has subsurface ply delamination between Ply 7 and 8. The transverse intra-ply crack that connects to the delamination opened up slightly near the impact face.

Compared to RM4 (ε_{interr} = 8.25%), a strain of 8.91% for low-temperature specimen (CL5) had resulted in larger damage as surface ply detachment on both sides of the laminates (also see Figs. 10g–i and 11a). However, ply delamination can only be found between Ply 1 & 2, 2 & 3, 7 & 8 and is symmetric about the symmetry plane (also see Fig. 10h). Despite the ply detachment, the intra-ply cracks in CL5 are mainly in the transverse direction, different from the specimens with similar ε_{interr} but at room temperature (RM4). The damage distribution of CL5 along the loading direction (Fig. 10f) also indicates a high damage concentration near the impact face. The damage has a higher uniformity than that in RM4, but it is less uniform compared to RM5.

Fig. 12 presents the volume fraction of opened damage in the tested specimens. It can be seen that the opened damage increases with the increase of ε_{interr} for the specimens at both temperatures. Specimens at low temperatures with similar ε_{interr} as the room temperature specimens have substantially larger opened damage. Considering the detached volume, there is a 6.52% damage fraction in CL5, which is even higher than the room-temperature specimens with much larger ε_{interr} (e.g., RM5).

4. Discussion

4.1. Damage development with mechanical response

Although the stress responses of the specimens between quasi-static loading (baseline), room- and low-temperature HSR loading are evidently different (Fig. 5), their apparent-yield strain (the sudden change in gradient, please see Fig. 5) all lie in the range from 3 to 4%, indicating a low sensitivity of apparent-yield strain to the changes of temperature and strain-rate within the tested ranges, as observed in the previous research [41].

Before the apparent-yield points, no micro-scale damage can be detected in RM1 and RM2 (Fig. 9c), implying that the specimens remain micro-structurally intact at room temperature. However, the specimen dimensions (mainly in L and H) changed permanently after the impact (Fig. 8c). That suggests the permanent deformation of the matrix, facilitated primarily through polymer chain rearrangement, has taken place in response to the intra-ply shear along the ±45° fibre directions. No ply delamination can be observed in RM1, RM2 and RM3 (Fig. 9c), corresponding to no permanent dimension expansion in their W direction (Fig. 8c). That is to say, before the apparent-yield point of the specimen, there is permanent deformation in L and H but not in W nor ply delamination in room-temperature specimens. At around ϵ_{interr} = 8.25%, the specimens are still in a quasi-flowing state with negligible load-bearing capacity loss as reflected in Figs. 5a and 7a. High structural integrity, i.e. lower level of damage compared to low-temperature specimens, can be seen in specimen RM4. With the appearance of large and widespread opened damage at around ϵ_{interr} = 13.45% (e.g., RM5), an evident stress drop can be found compared to the stress in the plateauing region (Fig. 7a).

In spite of the similar apparent-yield strain, the low-temperature specimens at small strains (CL1, CL2 and CL3) have already undergone permanent dimension change in all directions, including W (Figs. 8d and 9d). Given that the matrix dominates the W-direction deformation, the threshold for permanent deformation of the epoxy matrix might be lower at low temperatures [42]. The W-direction deformation was still within the fracture limit in CL1 and CL2. Delamination can only be observed at ϵ_{interr} = 3.60% (CL3 in Fig. 9d), demonstrating that ply delamination can be generated around the apparent-yield point for the specimens at low temperatures, possibly due to the embrittlement of the epoxy matrix [43]. Similarly, the transverse intra-ply cracks initiated earlier than those in the room-temperature specimens. Distinct coefficients of thermal expansion between the carbon fibres and matrix [44] can introduce thermal stresses at the fibre/matrix interface after the cooling process. In addition to the matrix embrittlement, these pre-existing stresses will further contribute to the generation of the micro-scale cracks at the fibre/matrix interfaces upon loading. After the apparent-yield point and the occurrence of ply delamination, a pronounced decrease in specimen load-bearing capacity occurred (Fig. 5b). The level of delamination develops with the permanent dimension increase in W-direction (e.g., CL3 - CL5). At about ϵ_{interr} = 8.91% (e.g., CL5), approximately 20% of the specimen's load-bearing capacity had been lost (Fig. 5b). This is notable considering that no obvious decrease in load-bearing capacity can be seen in the room-temperature specimens at a similar strain level (e.g., RM4). This sudden loss in load-bearing capacity is, in essence, the mechanical reflection of the more rapid damage development at low temperatures, which in these specimens appears to be facilitated through ply delamination.

4.2. Damage initiation mechanisms

The damage morphology analysis referring to the strain levels demonstrates that the damage initiation mechanism is similar between room- and low-temperature specimens. It is in the sequence of micro-scale intra-ply cracks in both surface and subsurface plies, intra-ply cracks opening up in surface plies, surface ply delamination, intra-ply cracks opening up in middle plies, and middle ply delamination (Fig. 9c and d). Surface ply cracks tend to open up earlier since the surface plies (with fibres in −45°) have only one side attached to the specimens and have no lateral and shear restraints on the surface sides.

At the damage initiation stage, the micro intra-ply cracks of the specimens at both temperatures are normally generated and propagate roughly along the ply in-plane diagonal line in the fibre direction (−45°). That indicates the intra-ply crack at this stage is mainly formed by ply mode II fracture where the intra-ply shear is produced by the ply fragments on opposing sides of the in-plane diagonal line displacing in opposite directions (Fig. 11c). At higher strains (e.g., RM4 and CL4), the existence of intra-ply cracks away from the ply in-plane diagonal line implies that those cracks might be produced by a mode-I/II-combined fracture (Fig. 11d). The source of this mode-I tensile stress can be the inter-ply shear in different directions caused by the deformation of neighbouring plies with different fibre directions and the volume expansion of specimens in the H-direction under L-direction compression.

The locations where opened damage appears after the surface layers for the specimens at both temperatures were found to be the cluster of two +45° plies in the middle on both sides of the symmetry plane (e.g., Fig. 9d - CL4). A Mode-II-dominated intra-ply crack was formed near the ply in-plane diagonal line (Fig. 13a) because of the *in-situ* shear strength reduction effect of clustered plies [45,46].

4.3. Difference in damage propagation

Different damage mechanisms were noticed between room- and low-temperature specimens after the opened damage occurred in the middle +45° ply cluster. With compression progression in room-temperature specimens, the fracture fragment of the middle +45° ply cluster displaces further along the +45° intra-ply fracture plane (Fig. 11f). It stretches the neighbouring plies in the +45° fibre direction, posing mode-II shear stress to −45° plies and +45° plies both in the +45° fibre direction. That causes stress concentration along a semi-oval path surrounding the centre of mass of the fracture fragment and forms the damage band on the impact surface of RM5 (Figs. 10d–f and 11f). However, this complex damage mechanic is a deduction from the damage morphology, future investigations are needed to verify this hypothesis.

Under HSR impact, the specimens do not deform uniformly along their length at the micro-scale level. High localised deformation and fracture occurred at the specimens' loading end prior to the rest of the region located deeper in the specimens' length according to the through-length damage distribution analysis in Fig. 10. The dominant open cracks in both +45 and −45° plies originate at the loading ends of the specimens, coalescing and aligning within a damage band (Fig. 13a). As the dominant open cracks propagate through specimen length, they grow along the ply fibre directions. Hence, the +45 and −45° ply cracks drift apart from each other, as shown in Fig. 13b–d. In a ply that is between two plies which have the same fibre direction (e.g., a −45° ply between two +45° plies), Mode-II-dominant cracks along the +45° fibre direction (sometimes small and discontinuous) formed and bridge the dominant cracks in the adjacent two plies (e.g., the two +45° plies), as shown in Fig. 13e. This damage propagation pattern produces the branch-shaped damage, as shown in Fig. 13d.

In contrast, specimens at low temperatures have different but simpler damage mechanisms at the later stages of loading. The observed damage morphology in low-temperature specimens implies that the epoxy matrix is stiffer and more brittle at low temperatures because of the low molecular kinetic energy. The testing temperature of −50 °C is potentially below or near the beta-relaxation temperature (T_β) of the epoxy matrix [47]. The highly restricted molecular chain movement, low internal (inter- and intra-molecular) energy absorption and poor damping properties allow the impact energy to be effectively transmitted and accumulated at the weak points in the structure (that is,

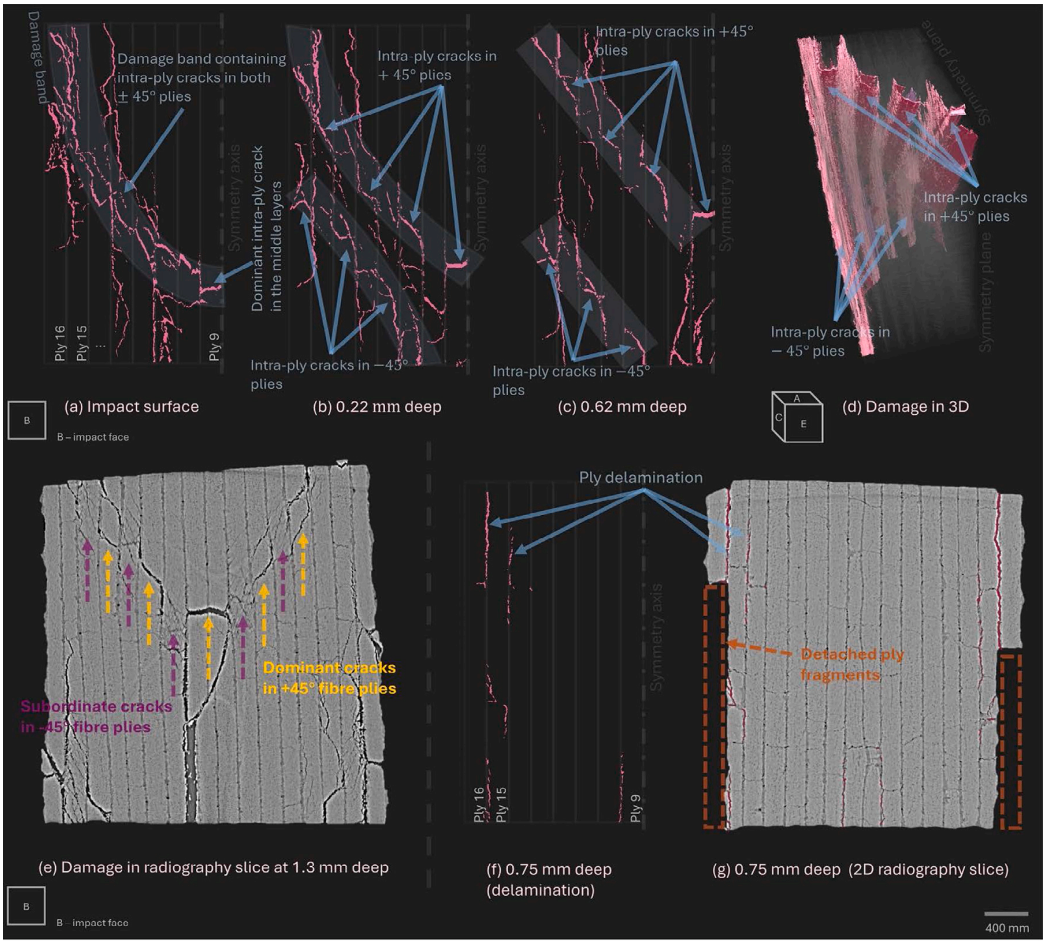


Fig. 13. Opened damage in RM5 and CL5. For RM5: opened damage (a) at 0 mm, (b) 0.22 mm and (c) 0.62 mm deep from the impact surface of the specimen, (d) in 3D view and (e) shown in radiography slice at 1.3 mm deep. Damage developed along their ply fibre directions, causing damage in +45° plies propagated and drifted away from the damage in and −45° plies. For CL5: delamination at 0.75 mm deep from the impact surface: (f) damage segmented and (g) damage in radiography slice. Ply delamination is seen between Ply 1 & 2, 2 & 3, 7 & 8 and is symmetric about the middle plane. Face E is the face opposite to the impact face (Face B).

inter-ply resin-rich regions in this case), causing rapid fractures [48, 49]. This is also indicated by the early specimen volume expansion in the W-direction before the apparent yield at low temperatures. Inter-ply weak points (i.e., the stress concentration regions) shift from the surface towards the middle layers with the continuous detachment of the outermost plies during loading, forming the damage morphology observed in Fig. 13(f and g).

5. Conclusions

The micro-scale damage mechanisms of AP CFRP laminates under high strain-rate compressive loading were investigated by combining the use of SHPB loading platform, strain and momentum interruption techniques, high-speed visible light imaging, DIC, strain gauge measurement, synchrotron-based phase-contrast X-ray μ-CT, deep-learning-aided image segmentation and visualisation. It was demonstrated that the specimen maximum strain was effectively controlled at target values. The micro-scale damage initiation and evolution of the specimens at room and low temperatures were characterised, and the associated damage mechanisms were discussed.

In general, damage in low-temperature specimens initiates earlier and progresses more rapidly. Despite the different mechanical responses at different strain rates and temperatures, the apparent-yield point of all specimens occurs in the range of 3 to 4% strain. The epoxy matrix itself, on the other hand, showcases higher brittleness at low temperatures. Although all specimens undergo permanent deformation before reaching their bulk apparent-yield stress, only the low-temperature specimens revealed intra-ply cracks, possibly attributed to the low failure strain of the matrix and the pre-existing thermal stress at the fibre/matrix interfaces. However, the existence of micro-scale intra-ply cracks does not seem to significantly impair the mechanical strength of the specimens; the rapid strength drop of the specimens is mainly dominated by inter-ply delamination. Whereas the opened cracks and delamination of room-temperature specimens initiated only after the apparent-yield point, they can be observed around the apparent-yield point at low temperatures. The opened damage for the specimens at both temperatures initiated and concentrated at the impact end of the specimens.

For specimens at both temperatures, micro-cracks caused by mode-II fracture initiated at the surface and subsurface plies, with those in the surface plies the first to develop into opened damage. As the overall strain increased, mode-I/II-combined fracture also emerged, led by the specimen volume expansion and the excessive shear strain normal to the fracture direction. While specimens at both temperatures exhibit

similar damage mechanisms initially, they show distinct ones after the occurrence of the opened damage in the middle +45° ply clusters. As the volume of opened damage increased with the strain, damage in the room-temperature specimens propagated mainly within damage bands resulting from the matrix's higher compliance. The energy was primarily dissipated through matrix deformation and crack formation. This mechanism facilitated the long strength-holding period (stress plateau) after the apparent yield. However, inter-ply delamination and the resulting ply detachment from the outer to middle plies caused by the stress accumulation at inter-ply resin-rich regions are found to be the energy dissipation mechanism of low-temperature specimens at the late loading stages. This glassy behaviour is on account of the matrix's high strength but low failure strain at low temperatures, creating a pronounced stress drop after the apparent-yield points.

The 3D characterisation of micro-scale damage in CFRP laminates detailed in this work provides unique experimental insights into temperature-dependent failure mechanisms under high-rate loading. The thermo-mechanical interpretations will help to validate and advance discrete damage models for improved design and safety assessment of composite laminates, and to enhance the mechanistic understanding of complex micro-scale damage initiation and progression under real-world conditions.

CRediT authorship contribution statement

Xiyao Sun: Writing – original draft, Visualization, Validation, Software, Methodology, Investigation, Formal analysis, Data curation, Conceptualization. **Bratislav Lukić:** Writing – review & editing, Software, Resources, Methodology, Data curation. **Kai Liu:** Methodology, Investigation. **David Sory:** Methodology, Investigation. **Maria Lißner:** Writing – review & editing. **Justus Hoffmann:** Writing – review & editing. **David Chapman:** Writing – review & editing, Supervision, Methodology, Conceptualization. **Nik Petrinic:** Resources, Project administration, Methodology, Funding acquisition. **Daniel Eakins:** Writing – review & editing, Supervision, Resources, Project administration, Methodology, Funding acquisition, Conceptualization.

Declaration of competing interest

The authors declare the following financial interests/personal relationships which may be considered as potential competing interests: Xiyao Sun reports equipment, drugs, or supplies was provided by Rolls-Royce plc. If there are other authors, they declare that they have no known competing financial interests or personal relationships that could have appeared to influence the work reported in this paper.

Acknowledgements

The authors express their thanks to Drs Yanhong Chen and Ziwen Xu for assistance with the experiments at the ESRF, and also to the technician team at Begbroke Science Park for the manufacture of all specimens and equipment. ID19 at the ESRF, Grenoble, France is acknowledged for providing standard access beamtime MA-5715 and in-house beamtime IHLS-3562. Funding for this research was provided by Innovate UK grant 113232: FANDANGO (FAN Design And iNtegrity, GO). B.L. acknowledges funding from the EPSRC (EP/W003333/1). Rolls-Royce plc is gratefully acknowledged for their continued support of the University Technology Centre in Solid Mechanics at the University of Oxford. Lastly, the authors wish to express special thanks to the late Prof Nik Petrinic, whose knowledge, guidance and support were vital to this work, and to the understanding of composites more widely.

Data availability

Data will be made available on request.

References

[1] Clyne TW, Hull D. An introduction to composite materials. Third ed.. Cambridge; 2019.
[2] Irving PE, Soutis C. Polymer Composites in the Aerospace Industry. San Diego: Elsevier Science & Technology; 2019.
[3] Wang K, Young B, Smith ST. Mechanical properties of pultruded carbon fibre-reinforced polymer (CFRP) plates at elevated temperatures. Eng Struct 2011;33(7):2154–61.
[4] Sun Q, Zhou G, Guo H, Meng Z, Chen Z, Liu H, Kang H, Su X. Failure mechanisms of cross-ply carbon fiber reinforced polymer laminates under longitudinal compression with experimental and computational analyses. Compos Part B: Eng 2019;167:147–60.
[5] Takahashi K, Higashiyama R, Xue G, Nakamura T. In situ analysis of three-dimensional microcrack propagation in cross-ply laminates using synchrotron radiation X-ray computed tomography. Compos Sci Technol 2024;258.
[6] Jiang L, Xiong H, Zeng T, Wang J, Xiao S, Yang L. In-situ micro-CT damage analysis of carbon and carbon/glass hybrid laminates under tensile loading by image reconstruction and DVC technology. Compos Part A: Appl Sci Manuf 2024;176.
[7] Zhang H, Yang L, Ren S, Wang K, Li J. In-situ experimental characterization and numerical investigation of the crack initiation of SMC composite under uniaxial tension. Compos Part A: Appl Sci Manuf 2025;188.
[8] Ploeckl M, Kuhn P, Grosser J, Wolfahrt M, Koerber H. A dynamic test methodology for analyzing the strain-rate effect on the longitudinal compressive behavior of fiber-reinforced composites. Compos Struct 2017;180:429–38.
[9] Arbaoui J, Tarfaoui M, El Malki Alaoui A. Mechanical behavior and damage kinetics of woven E-glass/vinylester laminate composites under high strain rate dynamic compressive loading: Experimental and numerical investigation. Int J Impact Eng 2016;87:44–54.
[10] Watanabe T, Takeichi Y, Niwa Y, Hojo M, Kimura M. Nanoscale in situ observations of crack initiation and propagation in carbon fiber/epoxy composites using synchrotron radiation X-ray computed tomography. Compos Sci Technol 2020;197.
[11] Wang Y, Emerson MJ, Conradsen K, Dahl AB, Dahl VA, Maire E, Withers PJ. Evolution of fibre deflection leading to kink-band formation in unidirectional glass fibre/epoxy composite under axial compression. Compos Sci Technol 2021;213(March):108929.
[12] Hosur MV, Alexander J, Vaidya UK, Jeelani S. High strain rate compression response of carbon/epoxy laminate composites. Compos Struct 2001;52:405–17.
[13] Seyednourani M, Akgun S, Ulus H, Yildiz M, Sas HS. Impact damage and low temperature effects on carbon fiber/epoxy joints: A comparative study of hybrid bolted/bonded and bolted configurations with cross-ply and angle-ply laminates. Compos Part A: Appl Sci Manuf 2025;190.
[14] Guedes RM, de Moura MF, Ferreira FJ. Failure analysis of quasi-isotropic CFRP laminates under high strain rate compression loading. Compos Struct 2008;84(4):362–8.
[15] Xiao J, Wu Z, Pan Z, Ouyang W, Shi L. Analysis of in-plane compression failure mechanism in carbon fi ber braided composite with different off-axial angles. 2022;56(13):2029–46.
[16] Katafiasz TJ, Greenhalgh ES, Allegri G, Pinho ST, Robinson P. The influence of temperature and moisture on the mode I fracture toughness and associated fracture morphology of a highly toughened aerospace CFRP. Compos Part A: Appl Sci Manuf 2021;142.
[17] Meng J, Wang Y, Yang H, Wang P, Lei Q, Shi H, Lei H, Fang D. Mechanical properties and internal microdefects evolution of carbon fiber reinforced polymer composites: Cryogenic temperature and thermocycling effects. Compos Sci Technol 2020;191.
[18] Islam MS, Benninger LF, Pearce G, Wang CH. Toughening carbon fibre composites at cryogenic temperatures using low-thermal expansion nanoparticles. Compos Part A: Appl Sci Manuf 2021;150.
[19] Körbelin J, Dreiner C, Fiedler B. Impact of temperature on LVI-damage and tensile and compressive residual strength of CFRP. Compos Part C: Open Access 2020;3.
[20] Körbelin J, Junge N, Fiedler B. Modelling of low-velocity impact and compression after impact of cfrp at elevated temperatures. Compos Part A: Appl Sci Manuf 2021;147.
[21] Sánchez-Sáez S, Gómez-Del Río T, Barbero E, Zaera R, Navarro C. Static behavior of CFRPs at low temperatures. Compos: Part B 2002;33:383–90.
[22] Ou Y, Zhu D, Zhang H, Yao Y, Mobasher B, Huang L. Mechanical properties and failure characteristics of CFRP under intermediate strain rates and varying temperatures. Compos Part B: Eng 2016;95:123–36.
[23] Li Y, Meng J, Niu G, Yang H, Wang P, Lei H, Fang D. Cryogenic damage mechanisms of CFRP laminates based on in-situ X-ray computed tomography characterization. Compos Sci Technol 2024;247:110413.
[24] Morkavuk S, Köklü U, Bağcı M, Gemi L. Cryogenic machining of carbon fiber reinforced plastic (CFRP) composites and the effects of cryogenic treatment on tensile properties: A comparative study. Compos Part B: Eng 2018;147(April):1–11.

[25] Im KH, Cha CS, Kim SK, Yang IY. Effects of temperature on impact damages in CFRP composite laminates. Compos Part B: Engineering 2001;32(8):669–82.
[26] Sun X, Sory D, Liu K, Lukić B, Simonian D, Wong KL, Rack A, Chapman D, Petrinic N, Eakins D. Effect of temperature on high strain-rate damage evolving in cfrp studied by synchrotron-based MHz X-ray phase contrast imaging. Compos Part B: Eng 2024;279.
[27] Nie Y, Parab ND, Chu J-m, Kim G, Sun T, Fezzaa K, Sterkenburg R, Chen WW. Dynamic crack propagation from a circular defect in a unidirectional carbon fiber reinforced plastic composite. J Compos Mater 2018;52(25):3539–47.
[28] Pournoori N, Corrêa Soares G, Lukić B, Isakov M, Belone MCL, Hokka M, Kanerva M. In situ damage characterization of CFRP under compression using high-speed optical, infrared and synchrotron X-ray phase-contrast imaging. Compos Part A: Appl Sci Manuf 2023;175.
[29] Song P, Chapman DJ, Graham AM, Lukić B, Rack A, Siviour CR. Thermomechanical characterisation of a thermoplastic polymer and its short glass fibre reinforced composite: Influence of fibre, fibre orientation, strain rates and temperatures. Compos Part A: Appl Sci Manuf 2024;180.
[30] Rodríguez-Sereno JM, Pernas-Sánchez J, Artero-Guerrero JA, Rack A, Vaz-Romero A, López-Puente J, Varas D, Naya F, Cohen A, Lukić B. Experimental compressive damage analysis on holed laminates under dynamic loadings using in-situ MHz synchrotron X-ray phase contrast imaging. Compos Struct 2025;359.
[31] ASTM. Standard Test Method for In-Plane Shear Response of Polymer Matrix Composite Materials by Tensile Test of a 645° Laminate 1. Technical Report, American Society for Testing and Materials; 2018.
[32] Gray G. Classic split-hopkinson pressure bar testing. ASM Handb 2000;8.
[33] Le TH, Dumont PJ, Orgéas L, Favier D, Salvo L, Boller E. X-ray phase contrast microtomography for the analysis of the fibrous microstructure of SMC composites. Compos Part A: Appl Sci Manuf 2008;39(1):91–103.
[34] Paganin D, Mayo SC, Gureyev TE, Miller PR, Wilkins SW. Simultaneous phase and amplitude extraction from a single defocused image of a homogeneous object. J Microsc 2002;206(1):33–40.
[35] Fuller J, Wisnom MR. Pseudo-ductility and damage suppression in thin ply CFRP angle-ply. Compos: Part A 2015;64–71.
[36] Kikinis R, Pieper SD, Vosburgh KG. 3D slicer: A platform for subject-specific image analysis, visualization, and clinical support. In: Intraoperative imaging and image-guided therapy. New York, NY: Springer New York; 2014, p. 277–89.
[37] D'Imprima E, Garcia Montero M, Gawrzak S, Ronchi P, Zagoriy I, Schwab Y, Jechlinger M, Mahamid J. Light and electron microscopy continuum-resolution imaging of 3D cell cultures. Dev Cell 2023;58(7):616–32.
[38] Little JE, Yuan X, Jones MI. Characterisation of voids in fibre reinforced composite materials. NDT E Int 2012;46(1):122–7.
[39] Song Z, Wang Z, Ma H, Xuan H. Mechanical behavior and failure mode of woven carbon/epoxy laminate composites under dynamic compressive loading. Compos Part B: Eng 2014;60:531–6.
[40] Zhao J, Guo L, Zhang L, Wang X, Tang Y, Li Z. Experimental investigations on the in-plane dynamic compressive behavior and upper limit of constant strain rate for 2D twill weave carbon fiber reinforced composite. Compos Part B: Eng 2021;220.
[41] Gu J, Bai Y, Zhao Z, Zhang C. Temperature and strain rate sensitivity of modulus and yield strength of epoxy resin under compressive loads. Polymer 2024;295.
[42] Chen H, Song P, Commins T, Graham A, Trivedi AR, Siviour CR. Characterization and modelling of bisphenol-a type epoxy polymer over a wide range of rates and temperatures. Polymer 2022;249.
[43] Araki W, Asahi D, Adachi T, Yamaji A. Time-temperature dependency of mode II fracture toughness for bisphenol a type epoxy resin. J Appl Polym Sci 2005;96(1):51–5.
[44] Ruiz-Iglesias R, Cappello R, Thomsen OT, Dulieu-Barton JM. Estimating the coefficients of thermal expansion of carbon fibre composite materials using infrared thermography. Compos Part A: Appl Sci Manuf 2025;198.
[45] Dvorak GJ, Laws N. Analysis of Progressive Matrix Cracking In Composite Laminates II. First Ply Failure. Technical Report.
[46] Camanho PP, Dávila CG, Pinho ST, Iannucci L, Robinson P. Prediction of in situ strengths and matrix cracking in composites under transverse tension and in-plane shear. Compos Part A: Appl Sci Manuf 2006;37(2):165–76.
[47] Reyes LQ, Swan SR, Gan H, Seraji SM, Zhang J, Varley RJ. The role of β relaxations in determining the compressive properties of an epoxy amine network modified with POSS and mono-functional epoxy resins. Polym Test 2021;93.
[48] Shito N, Sato M. Electrical and mechanical properties of anhydride-cured epoxy resins. J Polym Sci Part C: Polym Symp 1967;16(2):1069–78.
[49] Vryonis O, Vaughan AS, Andritsch T, Morshuis PH, Claverie A. On molecular dynamics and charge transport in a flexible epoxy resin network. Materials 2022;15(18).

Chapter 5

CFRP's damage at micron-scale

5.1 Background and motivation

The previous investigation presented in Chapter 4 extended the damage characterisation to the micro-scale level and further analysed the spatial distribution of damage by decomposing it along the lamination direction of the specimens. In-depth investigations of damage morphology, volume, and distribution were conducted at representative loading and strain stages, which were then further anchored to the *in-situ* damage probing with XPCI in the first work package (Paper I) in this DPhil research. Generally speaking, the volume of damage increases with the strains of the specimens, regardless of temperature. However, at low temperatures, micro-scale damage initiates earlier and develops more rapidly than at room temperature. Specimen lateral expansion can be found at the early loading stage at low temperatures, whereas the room-temperature specimens only show it at the middle loading stages. In addition, the onset of damage is in the form of intra-ply micro-cracks in multiple layers at both room and low temperatures. With compression progression, intra-ply cracks propagate, leading to inter-ply delamination. This should be the main cause of the sudden stress drop in the specimens under loading.

However, despite the systematic characterisation of opened damage (micro-scale damage), the damage that was closed after load release (micron-scale damage, width less than 5 μm) could not be extracted and quantified. In addition to that, the evaluation of the damage micro-mechanics was performed mainly by reverse deduction from the damage morphology and distribution. Characterisation and analysis based on direct internal stress and strain measurements remained difficult.

5.1.1 Micron-scale damage characterisation

Synchrotron-based μ-CT scanning is an effective method for visualising and characterising damage in specimens. Unlike at quasi-static loading rates, performing direct *in-situ* CT scans at high-strain-rate loading is not achievable with current technologies. One of the main drawbacks of the previous approach, which interrupted the specimen strain and examined the damage using μ-CT scanning, is that the volume of the damage could be reduced after releasing the load, as demonstrated in Fig.5.1. During the early to mid loading stages, large cracks, especially those in the surface plies, can still exhibit void regions within their crack contours. However, for small cracks or cracks in the internal plies, the edges on both sides of the crack have been closed after load removal, which effectively diminishes the X-ray absorption contrast effect. Although the phase-contrast effect in the current μ-CT setup can reveal these small cracks, they are usually less than 2 pixels in width (about $2-4$ μm) and thus difficult to segment from the background material.

Conventional image segmentation relies on the intensity contrast between the target features and the background. For the CFRP image data obtained from the synchrotron CT scan, the closed cracks have an intensity similar to that of the intact epoxy resins. Using intensity-based image segmentation to highlight closed cracks will inevitably also include some intact epoxy regions, as illustrated in Fig.5.2. Some advanced machine-learning- and deep-learning-based image segmentation methods can achieve good results in other image processing applications when the intensity difference is trivial. However, they are otherwise ineffective in the present case, due to the limited quantity of training data, the small size of the cracks relative to the pixels, and the subtle morphology difference between the small cracks and the inter-ply matrix regions.

5.1.2 Micro-mechanics measurement and analysis

In addition to the problem of segmenting small cracks, it is also difficult to characterise the micro-mechanics inside the specimen based on the previous μ-CT scanning due to the lack of direct measurement. The comments made on the internal mechanics of the specimens were mainly derived from the observed damage. The tested CFRP laminates are a type of heterogeneous material, which means the configuration, arrangement, and different properties of the components might result in complex stress and strain localisation within the specimens. The prevalent method for performing local strain characterisation in quasi-static

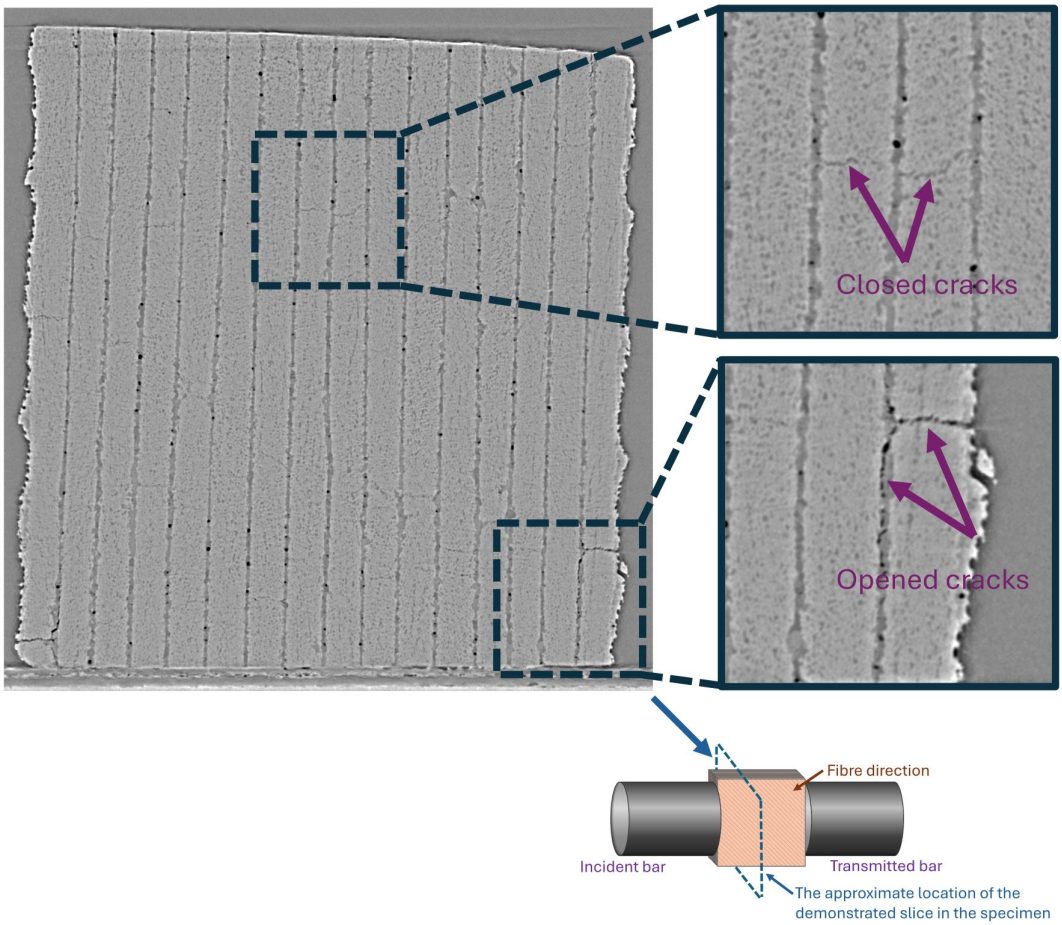


Figure 5.1: Comparison between the opened and closed cracks in a single X-ray radiography. Void regions can be seen inside the opened cracks, whereas the edges on both sides of the closed cracks have come back in contact after removing the load.

loading conditions is using synchrotron-based *in-situ* tomography. However, it is currently not feasible in high-strain-rate testing due to technology constraints. Therefore, a novel experimental strategy, which involves a combination of advanced image data acquisition, pre-processing, post-processing, and strain-damage interactive analysis, was developed.

5.1.3 Objectives of the chapter

Considering the limitations in previous research (Chapter 4), this chapter aims to further extend the results on the basis of micro-scale damage characterisation with micron-scale cracks quantification and strain localisation measurement. Existing studies have predominantly focused on local displacement and strain characterisation under quasi-static loading conditions, using techniques such as *in-situ* CT and DVC [183, 184]. In contrast, the short

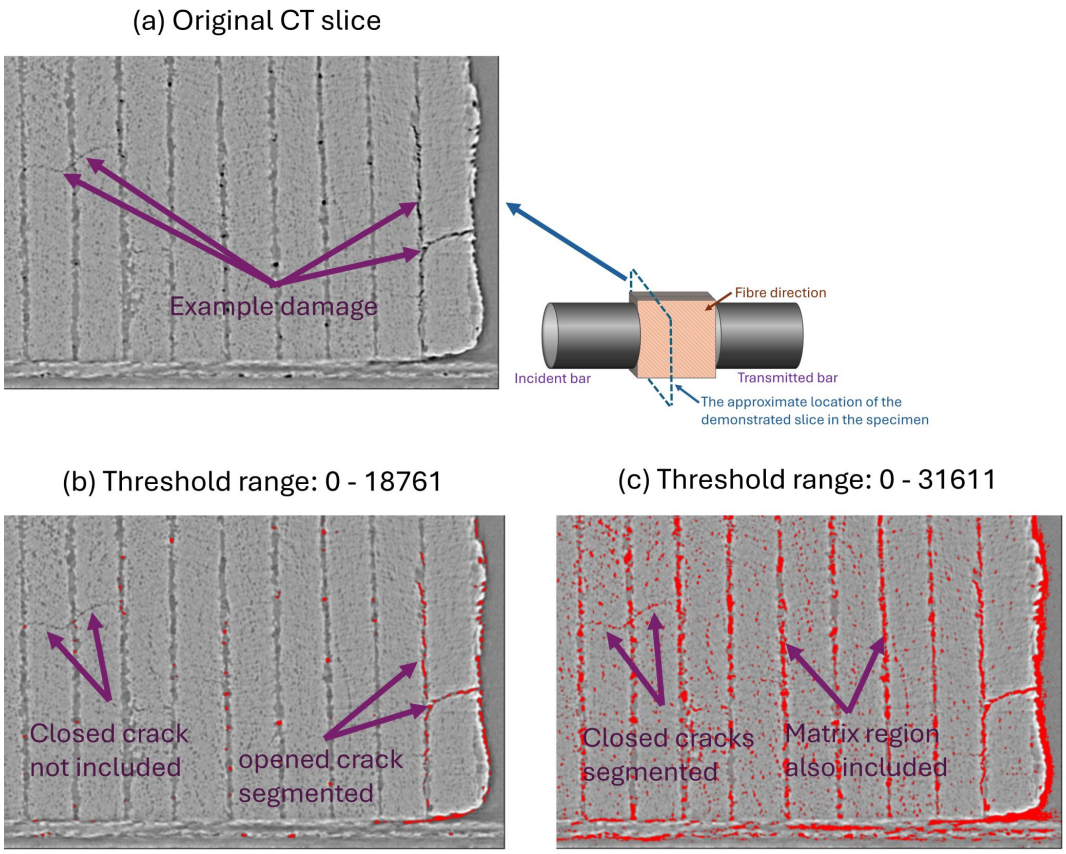


Figure 5.2: Difficulties of segmenting closed cracks with conventional thresholding methods. (a) The original tomography slice with both closed and opened cracks. (b) Segmenting the slice with a thresholding range from 0 to 18761. (c) Segmenting the slice with a thresholding range from 0 to 31611. Closed cracks cannot be accurately differentiated from the background material owing to the similar intensity between the closed cracks and the matrix.

duration of high-strain-rate loading poses significant challenges for image data acquisition, correlation, and processing, preventing *in-situ* characterisation. Therefore, a sequential workflow needs to be developed, described in this chapter, which enables the acquisition of high-quality image data, robust pre-processing, accurate three-dimensional microscopic displacement computation and damage segmentation, as well as informative post-processing in the high-strain-rate context. The measured and calculated strain localisation can help evaluate the stress distribution and state inside the specimens, which, on the other hand, explains the micro-mechanics of the different damage types and locations under high-strain-rate loading conditions. This integrated analysis of strain localisation and damage distribution is expected to consolidate the understanding of the temperature effects on damage initiation and evolution mechanisms in CFRP laminates at the micron-level.

5.2 Summary of Paper III

5.2.1 Material and specimen

The results presented in this chapter were produced based on an extended analysis of the experimental data acquired in Chapter 4. Two testing temperatures were investigated - room and low (around 23 and -50 °C, respectively). The deformation of the specimens along the loading axis was interrupted during high-strain-rate loading to preserve damage at different loading stages. Three strain-interruption levels, ranging from 2.5% to 4.5% (engineering strain along loading axis), were selected, which are around the apparent yield of the bulk specimens to reveal damage at early stages. They are labelled as RM1 to RM3 for the room-temperature specimens, and CL1 to CL3 for the low-temperature specimens, where increasing number implies increasing interrupted strain.

5.2.2 Methodology

Research strategy

Micron-scale damage characterisation and local strain computation are mainly achieved through DVC. In existing studies, DVC is usually implemented based on the reconstructed *in-situ* μ-CT images with in-house X-rays or at synchrotron light sources, such as the ESRF, APS and SLS, where specimens can be scanned more rapidly [185, 183, 186, 184]. When the displacement of the loading heads reaches the target levels, the force exerted on the specimens will be retained. Then the X-ray imaging process begins while the specimen rotates for 360 ° with the external loading condition remaining unchanged [187, 188]. This method has been approved as an effective way to observe damage initiation and development inside specimens. In the case that densely-distributed structural features exist in specimens allowing feature correlation, local displacement computation can be carried out to analyse the strain distribution and localisation [189, 190].

However, existing attempts are mainly under quasi-static loading conditions. It is currently impossible to interrupt and retain load during at high strain rates because of the short duration of dynamic loading. Therefore, the present research adopted a compromised strategy, which is performing DVC on carefully recovered specimens with residual local displacements after unloading through a pair of pre- and post-loading scans (Fig.5.3). An effective characterisation of strain localisation and an accurate segmentation of micron-damage were

achieved, taking advantage of the patterned structures of CFRP and the low elastic deformation threshold of the matrix, especially at low temperatures.

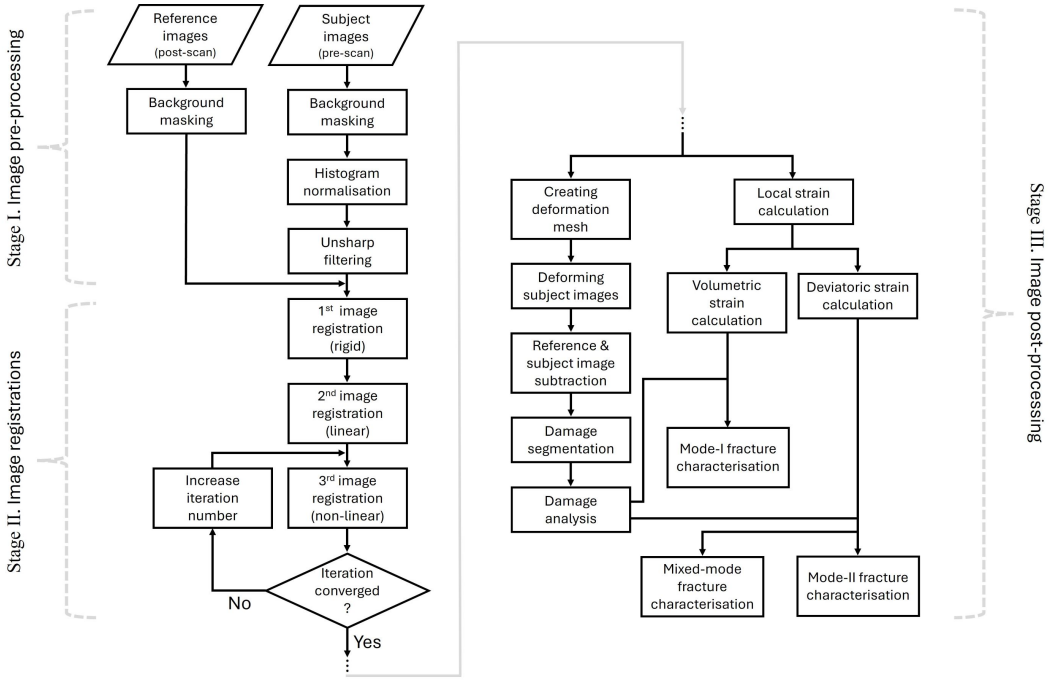


Figure 5.3: Data acquisition, image processing, strain computation, and damage analysis flowchart in three stages: image pre-processing (including image acquisition strategy), image registrations, and image post-processing.

Feasibility - textured structure

An important prerequisite, above all others, for performing DVC on the target specimens is the presence of densely arranged internal structures to which the correlation can be anchored. For the specimens and loading design in the present case, which are $[\pm 45]_{4s}$ laminates under uniaxial compression, slicing the obtained CT data from the cross-sectional direction perpendicular to the loading direction will show a clear textured structure, as shown in Fig.5.4, by virtue of the impregnation of carbon fibres in the epoxy matrix. Upon loading, an off-fibre-axis load will be applied to the CFRP laminates, causing fibre displacement. This dislocation of fibres produces high-quality features for performing image correlations and local strain calculation.

Feasibility - residual strain and damage

Another aspect that must be taken into consideration is the mechanical properties of the CFRP laminates. Due to technological limitations, the current approach is a semi-*in-situ* probing of deformation and damage, which means that the loading states will not be main-

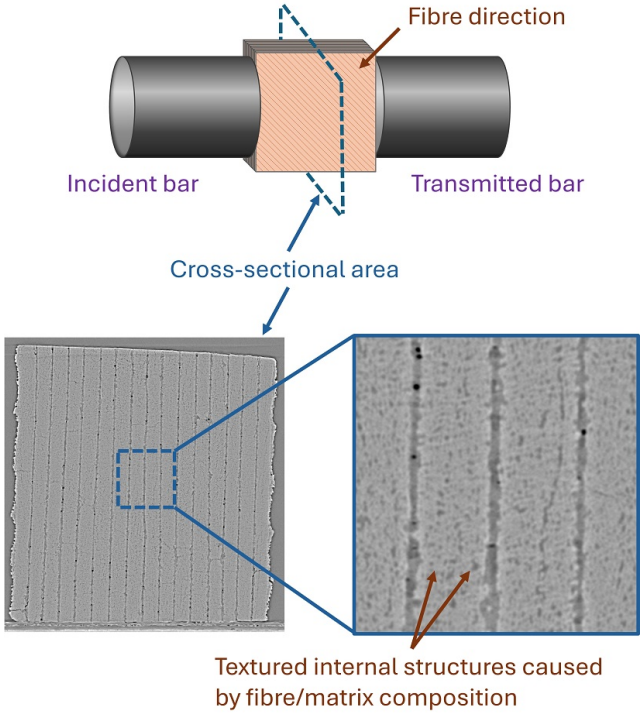


Figure 5.4: Internal microstructures of the tested CFRP specimens in the cross-sectional direction perpendicular to the loading. A clear textured structure can be seen created by the impregnation of the carbon fibres in the epoxy matrix.

tained while performing μ-CT scan. Hence, the characterisation achieved in the present studies is, in essence, on the residual deformation and damage after loading removal. Assessing the as-is states of specimens during loading largely relies on the quantification of residual strains. Therefore, it might be misleading or invalid if the tested material has a large elastic or visco-elastic domain, so that the local deformation of the specimens can return to their original state when the load is released.

It is well-known that epoxy commonly exhibits non-linear visco-elastic, visco-plastic and brittle fracture behaviours at different loading stages, which can result in considerable residual strain, especially at low temperatures [123, 191]. It should be noticed that, although material strain can recover mostly to its original state in the non-linear visco-elastic regime, noticeable residual strain at the microscopic level can still exist [192, 193], especially under elevated temperatures (Fig. 5.5) [194]. When CFRP laminates are subjected to a high-strain-rate loading, the heterogeneous configuration inside the laminates can cause rapid stress concentration and temperature elevation in the epoxy matrix, leading to local stress states exceeding permanent deformation thresholds. At low testing temperature, on the

other hand, the threshold for the onset of damage in the CFRP epoxy matrix was observed to be significantly lower [195]. These could be potential sources of residual strain after load removal, characterising which can benefit the interpretation of damage mechanisms in CFRP laminates.

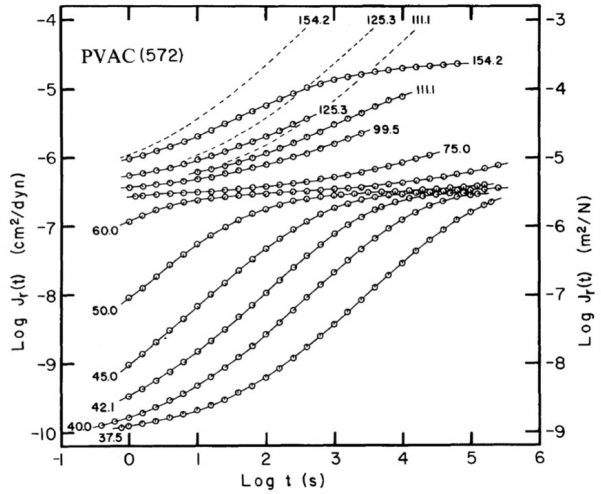


Figure 5.5: Change of recoverability of polymers at elevated temperatures. J_r (solid lines with circle markers) is the recoverable shear compliance of the polymer material. Dashed lines represent the total creep compliance, J. It can be seen that at high temperatures, J_r and J have obvious differences even at early loading stages, indicating a poor recoverability [176].

Pre- and post-scan

In addition to the conventional post-mortem CT scan after loading (post-scan), a pre-scan, which scans the specimens in their pristine state, is also needed to establish a base-line reference. Since pre- and post-scans were conducted separately in time, it is crucial to maintain the imaging parameters as close as possible. That is because the two sets of image data - pre-scans (Fig.5.6a) and post-scans (Fig.5.6b) - need to be registered to each other for performing image correlation. Despite the fact that an image pre-processing step is inevitable, similar scanning parameters can produce a good starting point. Nevertheless, it is impossible to apply the exact same scan conditions between pre- and post-scan since the synchrotron X-ray source varies constantly, as well as other changing factors such as specimen position and deformation (Fig.5.6c).

Image pre-processing

Because of the persistent image difference between pre-scan and post-scan, image pre-processing is an indispensable step to bring these two groups of image data to a com-

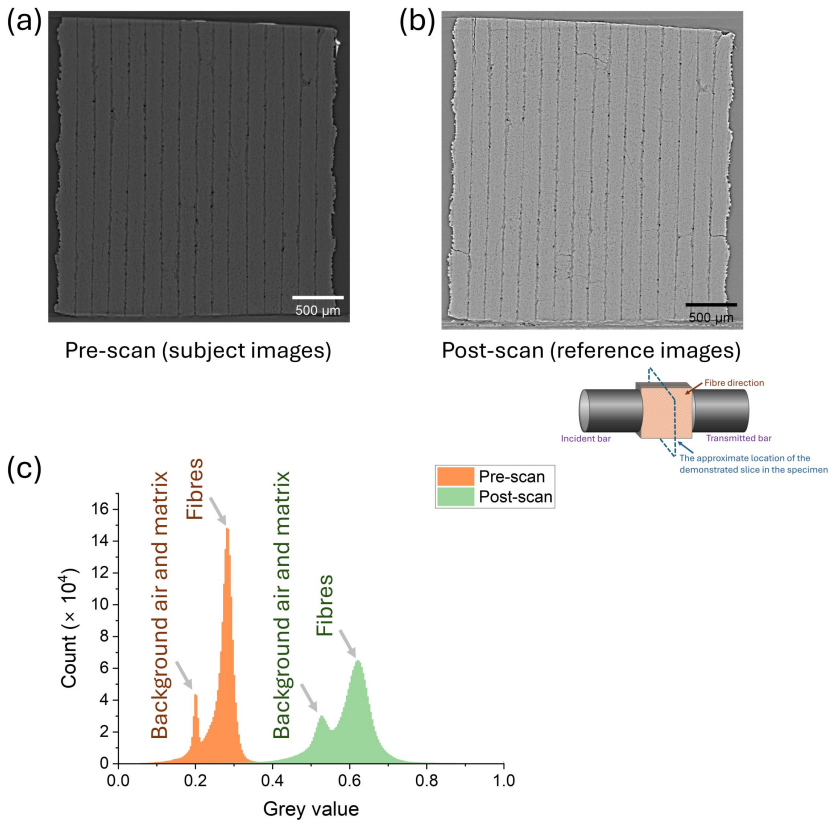


Figure 5.6: Comparison between pre- and post-scan slices in roughly the same location in a specimen. (a) Pre-scan: CT scan performed before loading. (b) Post-scan: CT scan performed after loading. (c) Grey value distribution for pre- and post-scan slices. Although the same scanning parameters were implemented, differences in the resulting images can still be seen.

parable state. The image registrations in the next step rely on the intensity gradient in the pre- and post-scan images; effective image pre-processing can significantly increase the image registration efficiency and accuracy. This pre-processing stage is mainly composed of three steps, namely background removal, histogram normalisation, and unsharp filtering. A background mask for each image volume was generated to remove the unwanted background in the CT slices. This helps reduce the computation time in the image registration step and produces quality damage visualisation in the post-processing step. Background segmentation in the present study was performed in two stages. First, the regions corresponding to the rotation platform (used to rotate the specimens during CT scanning) were cropped from the images using a custom edge-detection script written in `Python`. Next, background removal was carried out in `Dragonfly 3D World` (commercial software) using a U-Net-based deep-learning model. The model was trained on manually labelled images

to optimise segmentation accuracy, particularly along irregular laminate boundaries where strong phase-contrast edge effects were present. The trained model was then applied to the full image datasets to segment all images across all specimens. Intensity normalisation was also performed using an in-house `Python` script. Pixel intensities within the region of interest (RoI) (i.e., specimen-only images after background removal) were flattened into 1D arrays for both the reference and subject images to estimate their intensity distributions. A monotonic intensity mapping function from the subject to the reference distribution was then constructed through interpolation (cumulative distribution function matching) and applied to the subject image on a pixel-wise basis to obtain the normalised 2D image. Lastly, implementing unsharp masking with a `Python` script using a Gaussian blur radius of 2 - 4 pixels and a masking weight of 0.3 - 0.4 further tuned the intensity gradients and contrast between different components in the CT slices. Fig.5.7 demonstrates the effectiveness of image pre-processing using a pair of pre-scan and post-scan CT slices (Fig.5.7 (a and b)) with statistical comparisons (Fig.5.7 (c and d)).

Image registration

Three rounds of image registrations were carried out to accurately match the pre-scan image (subject images) to the post-scan image (reference images), as shown in Fig.5.3. The first image registration is a rigid image transformation, which coarsely matches the pre- and post-scans without deforming the subject images. By eliminating large misalignment between the pre- and post-scan at this step, the computation time and accuracy in the following step - linear image registration (the second image registration) - can be significantly improved. On top of the rigid image transformation, the linear image transformation applies a single transformation function, ϕ, to the subject images and deforms the subject images linearly towards the reference images. After these two rounds of image registrations, the pre-scan and post-scan should already be mostly aligned. However, the accuracy is not sufficient to reveal the micron-scale cracks set out in the objective of this study. Thus, non-linear image registration (the third image registration) takes place, which implements local (sub-volume) image transformation based on small-scale features in the images. This local deformation of subject images relative to the reference image can effectively highlight micron-scale differences between the subject and reference images, hence revealing the induced damage in specimens. Please refer to Paper III [196] for detailed explanations of the theory, settings, parameters, and strategy of performing DVC on the obtained image

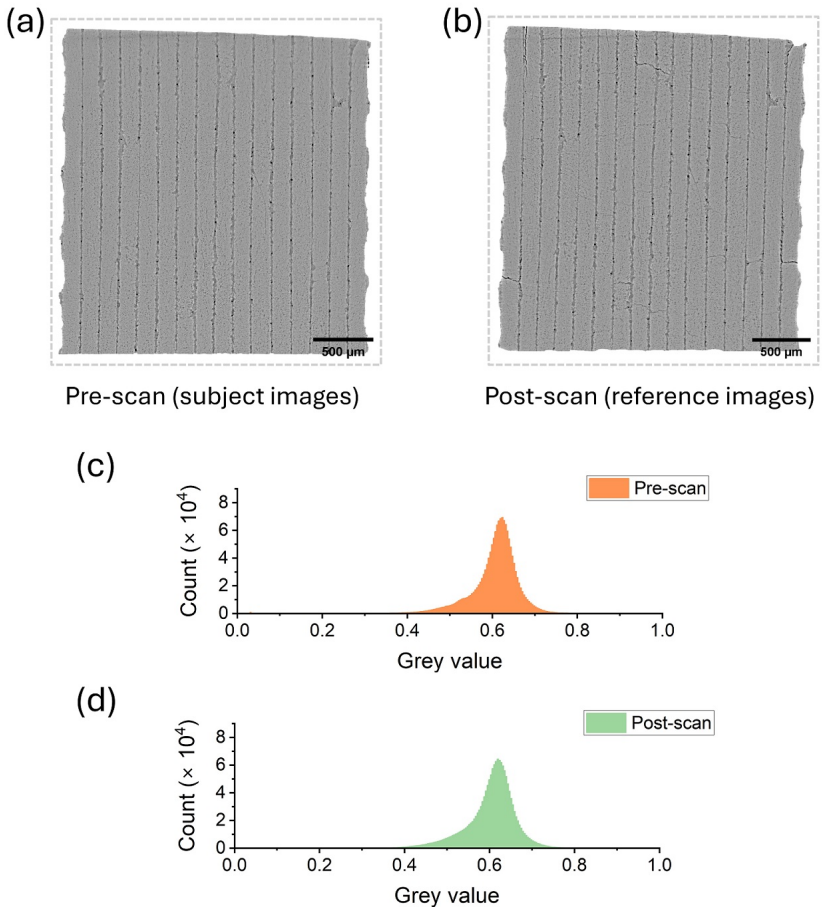


Figure 5.7: An example demonstrating the effectiveness of image pre-processing. (a) Pre-processed pre-scan image. (b) Pre-processed post-scan image. (c) The grey value distribution of the pre-scan image after normalisation. (d) The grey value distribution of the post-scan image. The pre-processed images are in a much more comparable state compared to those in Fig.5.6.

data.

Image post-processing

There are three objectives in the image post-processing stage: 1. segmenting the micron-scale cracks from the specimens; 2. identifying the strain localisation in the specimens; 3. performing integrated analysis involving the segmented micron-scale cracks and strain localisation, explaining the damage micro-mechanics. Micron-scale damage can be revealed through image calculation between the registered subject and reference images. This is to highlight the newly-generated structures (i.e., cracks) on the post-scans with respect to the pre-scans. This DVC-based damage analysis is subject to uncertainties arising from the limited spatial resolution of µ-CT, particularly when the detected crack widths approach the resolution limit. Although DVC-assisted registration improves damage identi-

fication by compensating for deformation and extracting structured residuals, the quantified damage volume remains dependent on image acquisition, registration, and segmentation procedures. Therefore, the reported damage metrics are interpreted as estimated and trend-based measures rather than absolute quantifications. Two types of strain were computed during image registration using DVC, namely the volumetric strain and the deviatoric strain. After combining the observed micron-scale damage and strain localisation, high deviatoric strain can imply the damage formed in the mode-II-dominated fracture triggered by shear, while localised volumetric strain can suggest the involvement of opening stress in some damaged regions, and thus a mode-I fracture. Subsequently, a mixed-mode fracture can result in a comparable weight of contribution between the volumetric and deviatoric strain.

5.2.3 Research findings

Local displacement

The local displacement vectors in the specimens were determined by finding the transformation function of each element on the grid (staggered correlation), as presented in Fig.5.8. These local displacement vector fields demonstrate the dimension change of the specimens in greater detail compared to a bulk dimension measurement only conducted in Paper II [176]. This directional displacement measurement confirms the influence of fibre directions on the specimen deformation under high-strain-rate loading. The local displacement along the fibre directions in individual plies is clearly shown.

From a bulk specimen point of view, the dimension expansion in the height direction is seen in the specimens at all loading stages, regardless of the temperature, by virtue of the off-fibre-axis loading directions [197]. In this case, the principal strain of the plies was mainly along the $+45$ or -45 ° fibre directions, causing this lateral expansion in the height direction (90 and -90 °) of the specimens (strain components perpendicular to the in-plane loading direction). In addition, no apparent expansion in the width direction can be observed at room temperature until the strain is equal to about 4.56%. Compared to that, a slight outward displacement (in the specimen width direction) of the surface plies can be identified in low-temperature specimens at early loading stages (e.g., CL1, $\varepsilon_{interr} = 2.55\%$). The displacement localisation and magnitude increase with increasing global engineering strain, but they are relatively higher in low-temperature specimens at a certain strain level.

Micron-scale damage and strain analysis

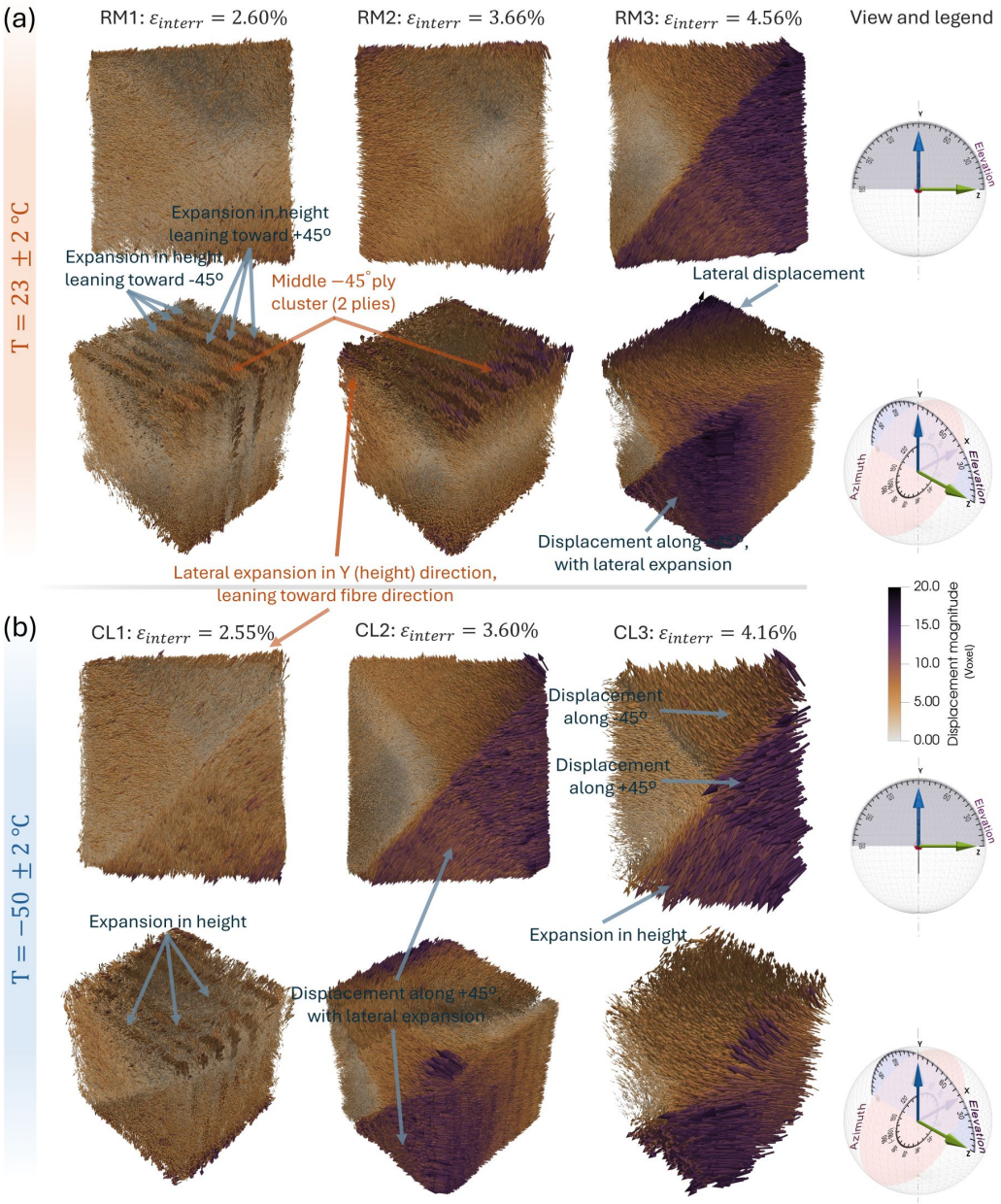


Figure 5.8: Development of local displacement vectors for the specimens at (a) room and (b) low temperatures. The local displacement and its development show clear directional features regardless of temperatures and loading stages in the tested CFRP laminates. Local displacement evolves more rapidly at low temperatures. Degrees noted are the fibre directions instead of the absolute directions.

The extracted micron-scale damage and calculated strain localisation can be analysed integratively. Overall, specimens have a similar micron-scale damage initiation mechanism regardless of temperature, which is intra-ply cracking along the fibre-direction diagonal of the plies. Although at low temperatures, this damage initiation is significantly earlier compared to room-temperature specimens. At room temperature, no evident shear localisation and damage can be found until $\varepsilon_{interr} = 4.56\%$ (refer to Fig. 10 in Section 5.3). Despite the same mechanism, the initiated cracks are mainly located in a few piles near the surface (refer to Fig. 9 - RM3 in Section 5.3), forming an obvious contrast to low-temperature specimens (e.g., CL1), where the intra-ply cracks are spread through the thickness of the specimens, as shown in Fig. 5.9.

From the damage distribution presented in Fig.5.9a, it can be seen that the micron-scale damage (closed cracks) with a thickness of 2 to 4 µm was successfully segmented from the specimen background. Micron-scale intra-ply cracks were generated in multiple layers through the lamination direction of the specimens at the lowest interruption strain (e.g., $\varepsilon_{interr} = 2.55\%$) at low temperatures. They propagated along the fibre directions from one free edge to another and concentrated near the fibre-direction diagonal in each ply. In accordance with that, shear strain concentration can also be found at this location (Fig.5.9b). Taking into account that very little volumetric strain exists at this location (fibre-direction diagonal of the ply) (Fig.5.9c), the observed micron-scale intra-ply cracks should be mainly induced by shear during loading (mode-II-dominated fracture).

Regarding the intra-ply cracks away from the fibre-direction diagonal of the plies, they are mainly located near the corners and perpendicularly intersect the off-fibre-direction diagonal of the current plies. That is to say, the discrete intra-ply cracks that can be seen at the corners of a -45 ply, although in -45 position, spread along the fibre-direction diagonals of its neighbouring plies (i.e., $+45$ plies). Also taking into account that the volumetric and deviatoric strain have comparable intensities at this damage location, these intra-ply cracks near the corners should be caused by the combination of in-plane shear and opening stress (mixed-model fracture). The opening load can be induced by the interaction between the neighbouring plies that have different fibre directions (inter-ply shear coupling) and the Poisson effect under uniaxial compression.

When the strain increased to about 3.60%, a good location match is still maintained between the visualised damage and the strain. A notable volume increase can be observed

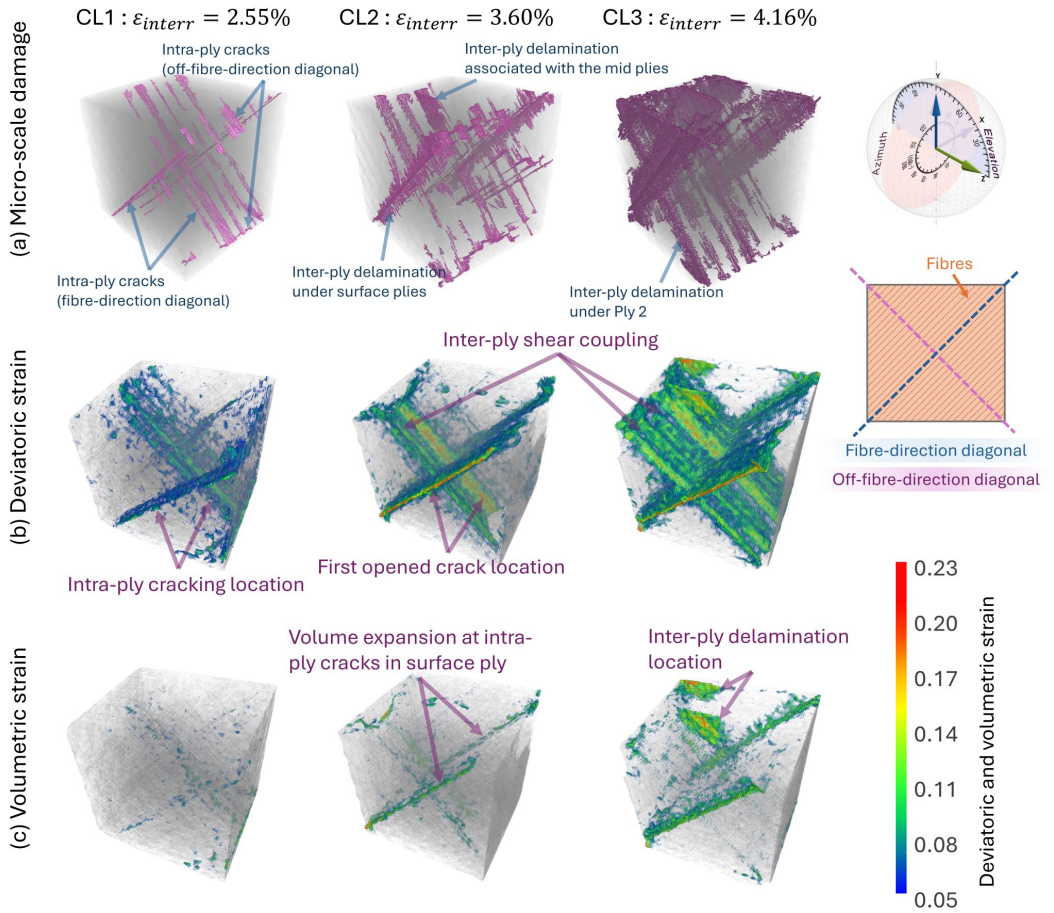


Figure 5.9: Distribution and development of (a) the micron-scale damage, (b) the deviatoric strain, and (c) the volumetric strain in low temperature specimens. The locations of the intra-ply cracks coincide with the shear strain localisation. At the locations of inter-ply delamination, prominent volumetric strain can be seen.

in basically all the segmented intra-ply cracks, including both surface-ply and subsurface cracks, and at both fibre- and off-fibre-direction diagonal locations. Correspondingly, evident stress localisation can be found in the surface plies and the mid plies. The shear coupling effect between the neighbouring plies had become more prominent, as visualised in a nearly contiguous shear band across the specimen lamination direction. In addition to that, minor delamination of the surface and mid plies has just initiated. No obvious strain localisation can yet be seen.

At $\varepsilon_{interr} = 4.16\%$, the volume of damage increased further, together with a wider damage distribution. As a reflection of high-level strain localisation, two major shear bands had formed in the specimens throughout the laminate thickness, demonstrating a more evident shear transfer effect between plies with different fibre directions. Noticeable volumetric

strain is shown at the location of surface intra-ply crack and all delamination (Fig.5.9c), which indicates, on top of the shear strain localisation presented in Fig.5.9b, volumetric strain also played an important role at these locations at around 4.16% strain.

Specimens at room temperature share similar mechanical and damage mechanics as their low-temperature counterparts. The main differences lie in that the micron-damage in low-temperature initiates and evolves more rapidly, with its damage morphology in a more discrete pattern. At room temperature, internal strain localisation substantially increases together with the occurrence of damage only after the apparent yield in the global response, whereas low-temperature specimens start to show damage and rapid local strain accumulation at early global strain (before apparent yield). Detailed comparison of the displacement, strain, and damage between room- and low-temperature specimens can be found in Paper III attached in Section 5.3 [196].

Inter-ply shear coupling

To further explain the inter-ply shear coupling effect between adjacent plies with different fibre directions, the deviatoric and volumetric strain distribution of a 2D slice was extracted from the volume and shown in Fig.5.10, with the slice location and the fibre direction indicated. A clear shear band is visualised along the fibre direction in both the deviatoric and volumetric strain fields, suggesting that both shear deformation and volume expansion took place in this region. In addition to that, another strain localisation band can also be seen, especially in the deviatoric strain field, perpendicular to the fibre direction of the current ply but parallel to the fibre direction of the neighbouring plies.

This observed strain localisation along the off-fibre-direction diagonal of the ply proves that a cutting-through-fibre strain localisation was generated in the current ply, resulting from the stress and deformation in the neighbouring plies. Plies in $+45$ and -45 ° fibre directions interact in a staggered form under high-strain-rate loading and create two nearly contiguous shear bands (one along the $+45$ ° fibre direction and the other one along the -45 ° fibre direction, see Fig. 5.9b-CL3) through the thickness of specimens. The clear existence of the inter-ply shear transfer effect indicates that, at this stage, the test subject is no longer in a pure in-plane shear state to a considerable degree. Measuring shear properties of laminates with the classic assumption of pure in-plane shear under uniaxial loading [101] presents an obvious risk at high-strain-rate loading and low temperatures.

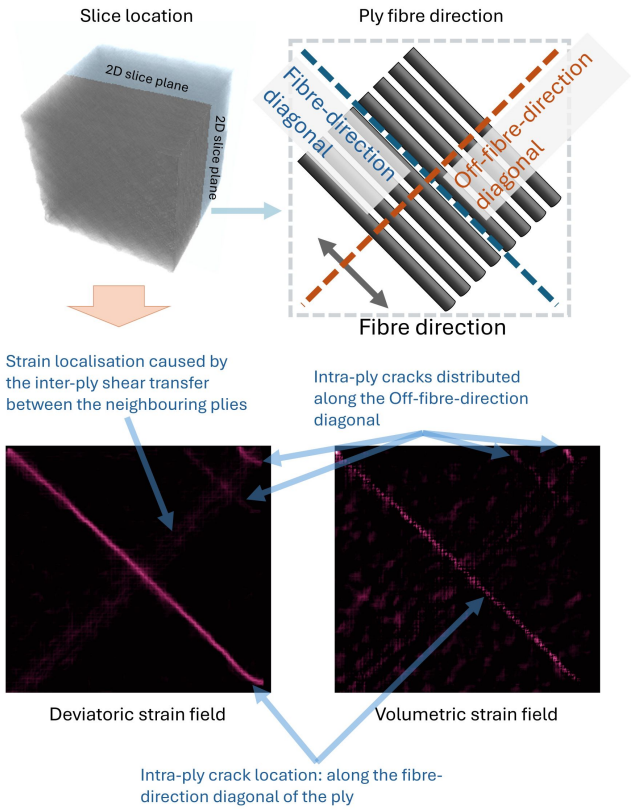


Figure 5.10: Deviatoric and volumetric strain distribution of a 2D slice in CL3, with the location and the fibre direction of the slice demonstrated on the top. Both deviatoric and volumetric strain bands are visualised along the fibre direction of the current ply. In addition, a shear localisation band can also be seen perpendicular to the fibre direction of the current ply but along the fibre direction of the neighbouring plies, which is caused by the inter-ply shear transfer effect.

5.3 Chapter remarks

This chapter demonstrates a robust and reliable implementation of DVC, enabled by a carefully controlled imaging setup between the pre- and post-loading scans. High-quality image registration was achieved through a tailored image pre-processing procedure combined with a coarse-to-fine correlation strategy. The effectiveness of the proposed workflow is evidenced by stable convergence under a stringent correlation threshold and by the accurate extraction of fine cracks. The resulting three-dimensional strain fields enabled clear decomposition and visualisation of deviatoric and volumetric strain concentrations in RoI, thereby providing quantitative support for the analysis of underlying damage mechanisms.

By integrating the results of this chapter into the overall DPhil study, a comprehensive investigation of damage mechanisms in $\pm 45^{\circ}$ CFRP laminates under dynamic uniaxial com-

pression is established, explicitly accounting for temperature effects. The work spans multiple dimensions: from the meso-scale to the micro-scale in length, from global mechanical response to localised strain concentration in scope, from two-dimensional planar observation to three-dimensional volumetric characterisation in space, and from staged behaviour to sequential observation with microsecond-level temporal resolution. Finally, the findings provide critical insight into the validity and limitations of the classical assumption of pure in-plane shear in $\pm 45^{\circ}$ CFRP laminates subjected to high-strain-rate uniaxial loading at low temperatures.

5.4 Paper III: 3D micro-mechanics of a CFRP laminate under high-rate and varying temperature loading using digital volume correlation

Composites Part B 321 (2026) 113693

Contents lists available at ScienceDirect

Composites Part B

journal homepage: www.elsevier.com/locate/composites

3D micro-mechanics of a CFRP laminate under high-rate and varying temperature loading using digital volume correlation

Xiyao Sun [a], Bratislav Lukić [b,c,d], Yanhong Chen [a], Ziwen Xu [a], David Chapman [a], Daniel Eakins [a,*]

[a] Department of Engineering Science, University of Oxford, Parks Road, Oxford, OX1 3PJ, UK
[b] European Synchrotron Radiation Facility, 71 Av. des Martyrs, Grenoble, 38000, France
[c] Henry Royce Institute for Advanced Materials, Department of Materials, The University of Manchester, Manchester, M13 9PL, UK
[d] Institut Max von Laue - Paul Langevin, 71 Av. des Martyrs, Grenoble, 38000, France

ARTICLE INFO

Keywords:
Fibre-reinforced-polymer composites
Impact behaviour
Temperature effects
Synchrotron X-ray tomography
Digital volume correlation (DVC)
Microscopic strain analysis
Damage micro-mechanics

ABSTRACT

Understanding microscopic damage mechanics in laminated CFRP at high-strain-rate (HSR) loading and extreme temperatures remains an enduring challenge. Using X-ray tomography coupled with digital volume correlation (DVC), three-dimensional local displacement/strain fields and segmented micron-scale intra-ply cracking were quantified, revealing damage micro-mechanics at HSR. Local deformation exhibits strong directionality that intensifies with increasing strain and decreasing temperature, accompanied by earlier and more rapid damage development at low temperature. Strain-damage correspondence indicates both Mode-II-dominated and mixed-mode (I/II) intra-ply cracking, while delamination shows a stronger Mode-I contribution but remains mixed-mode. Inter-ply kinematic constraint and shear transfer between adjacent plies with mismatched fibre orientations were directly visualised and characterised under HSR loading, particularly at low temperature. Together with the spatially non-uniform and asynchronous development of local deformation through the laminate thickness, these results highlight substantial departures from the nominal in-plane shear state commonly assumed for uniaxial ±45° laminate tests under extreme conditions.

1. Introduction

Carbon-fibre-reinforced polymer (CFRP) has been extensively used in the transport industry, where reducing weight yields direct improvement of energy and cost efficiency. Despite numerous advantages, such as high strength-to-weight ratios, corrosion resistance, and design flexibility [1], the anisotropic architectures of CFRP and the different mechanical, physical, and chemical properties of the components can lead to complex damage mechanisms both internally and on the surface [2]. Under high-strain-rate (HSR) loading and/or low temperatures, the damage in CFRP can propagate rapidly after initiation, causing sudden failure of structures resulting from the time–temperature superposition effects of the polymer matrix [3–5]. Investigating the micro-scale damage initiation and mechanics of CFRP under HSR loading, particularly in conjunction with temperature-dependent behaviour, is therefore of particular importance [6–8].

Several existing studies have investigated the micro-scale damage mechanisms of continuous fibre-reinforced polymer (FRP) composites under different loading configurations. Damage was found to initiate in the form of micro-cracks and fibre micro-kinking when the continuous FRP is under compression [9–11]. In tensile tests, fibre breaking, debonding, and pull-out are commonly observed on top of matrix damage [12–15]. Similar damage characteristics have also been reported in composite tubular structures and hybrid laminates [16–18]. For laminates loaded off-axis, such as angle-ply (AP) FRP (± 45°), fibre reorientation is usually induced under both tensile and compressive load, which could considerably alter the stress state, especially in large deformation stages [19,20]. Furthermore, under bending load, in addition to inter-fibre cracking, large-scale damage such as ply delamination could also initiate during the early stages of damage due to the high inter-laminate shear stress [21,22].

The strain-rate sensitivity of FRP's damage primarily depends on the relative contribution of matrix during loading, since it is significantly more rate-dependent than the fibres in most FRP composites [23–25]. Earlier matrix cracking can often be seen in FRP composites under impact loading [26]. Compared to damage caused by quasi-static loading, damage produced at HSR compression and tension is more prone to concentrate at or near the loading surface [27–29]. Under dynamic bending and shear loading, more fibre fractures can be observed in

* Corresponding author.
E-mail address: daniel.eakins@eng.ox.ac.uk (D. Eakins).

https://doi.org/10.1016/j.compositesb.2026.113693
Received 13 February 2026; Received in revised form 10 April 2026; Accepted 14 April 2026
Available online 17 April 2026
1359-8368/© 2026 Published by Elsevier Ltd.

contrast to quasi-static loading [30]. Ballistic impact can also result in matrix cracking and ply delamination in FRP [31]. However, its failure is, in essence, dominated by fibre shear and tensile failure [32].

Although investigations of FRP's HSR damage mechanisms at varying temperatures are limited, most existing studies agree that both high and low temperatures can weaken the overall performance of FRP composites, albeit through different mechanisms, especially when the matrix plays an important role [33,34]. As a result of polymers' temperature sensitivity, high temperatures tend to diminish the matrix strength and fibre/matrix bonding at the interfaces, whereas polymer embrittlement at low temperatures impairs the overall energy absorption of composites under loading [35–38]. For example, a transition in damage mechanism (reduced matrix cracking but increased fibre/matrix debonding) was observed in ±45° FRP laminates when the test temperature was changed from low to high [39].

FRP laminates are naturally suitable for performing digital volumetric correlation (DVC) following *in-situ* X-ray computed tomography (CT) by virtue of their high fibre packing density [40–42]. While the combination of *in-situ* CT and DVC has been widely adopted in quasi-static testing [43–47], the three-dimensional (3D) characterisation of internal damage and micro-mechanics at HSR loading is still a challenge. Investigations of damage mechanisms at HSR loading in existing research mainly rely on post-mortem inspections [48,49]. A previous study [50] observed rapid subsurface damage initiation and evolution in CFRP *in situ* under low-temperature impact at the meso-scale using X-ray phase-contrast imaging (XPCI), but damage characterisation was limited by available spatial resolution and the 2D nature of the XPCI technique. Under similar testing conditions, a follow-up study quantitatively analysed opened damage (i.e., damage that contains internal void regions) in CFRP laminates using micro-computed tomography (μ-CT) at intermediate-to-late loading stages using conventional image processing techniques [51]. However, the mechanisms of microscopic damage inception under HSR impact and varying temperatures, particularly the coupling between local strain localisation and ultra-fine ply cracking at early loading stages, have not yet been quantitatively resolved.

Therefore, utilising the datasets of the experimental campaign reported in our previous study [51], which focused on opened damage at intermediate-to-late loading stages, the present study shifts the analysis to early-stage damage and introduces a fundamentally different framework by incorporating pre-loading μ-CT scans and applying a dedicated DVC-based approach to resolve microscopic strain–damage interactions. The loading was interrupted at predefined strain levels to preserve early-stage damage. Through DVC-enabled volumetric registration, this approach enables (i) segmentation of micron-scale cracks (2–4 μm), (ii) computation of high-resolution microscopic strain fields over sub-volumes (~16.8 ×16.8 ×16.8 μm^3), and (iii) direct correlation between strain localisation and crack initiation. This integrated strain–damage analysis within a unified volumetric framework provides unique mechanistic insights into early-stage damage evolution as functions of strain and temperature, which were not accessible through conventional experiment, imaging, and post-processing protocols under HSR loading.

2. Materials and methodology

2.1. Material

The investigated CFRP laminates embedded "standard modulus" carbon fibres (Toray Industries, Inc.) in a high-performance epoxy resin (Hexcel Corporation) to produce unidirectional (UD) fibre/epoxy prepregs. The laminates were manufactured by laying up 16 layers of the UD prepregs following the stacking sequence of $[+45/-45]_{4s}$ and resulting in a fibre volume fraction of around 60% (calculated from fibre/matrix weight fractions and constituent densities provided by the suppliers, and independently verified by μ-CT image segmentation), as illustrated in Fig. 1a. The [+45/−45] laminate configuration was selected as a representative in-plane off-fibre-axis loading scenario. Unlike UD laminates, its dual fibre-orientation architecture enables direct investigation of inter-ply interactions between plies with different fibre directions. At the same time, compared to quasi-isotropic (QI) laminates, the [+45/−45] configuration promotes clearer localisation of internal stress and strain, thereby facilitating high-quality data acquisition and analysis under off-fibre-axis and shear-dominated loading conditions. Under quasi-static loading (approximately at $\dot{\varepsilon} = 3.3 \times 10^{-1}$ s^{-1}), the in-plane shear strength (τ_{21}) and shear modulus (G_{21}) of the CFRP laminate were measured as 82.6 MPa and 2.96 GPa, respectively. The curing process was implemented using an autoclave machine, which raised the temperature to 180 °C at a rate of 1–2 °C min^{-1}, held for 120 min, and then reduced to room temperature at a rate of 2–5 °C min^{-1}. The produced 3 mm thick CFRP panels were then cut into 3 × 3 × 3 mm^3 for HSR testing and μ-CT scanning. This specimen size was selected to satisfy the requirements of full-field synchrotron μ-CT imaging and sufficient voxel resolution for DVC analysis, while ensuring stable dynamic testing conditions.

2.2. Loading and temperature

HSR compression was performed using a split-Hopkinson pressure bar (SHPB) system along the laminate in-plane direction (Fig. 1b). This SHPB system was configured with a set of half-inch (about 12.7 mm) Ti-6Al-4V titanium alloy bars with lengths of 200, 1300, and 1100 mm for the striker, input and output bars, respectively. Two sets of strain gauges were mounted on the bars, one at 550 mm distance from the input-bar/specimen interface and the other at 500 mm distance from the output-bar/specimen interface. Two 3 mm-thick Ti-6Al-4V loading platens were used at the bar/specimen interfaces to protect the bar ends from being damaged by the specimens. Secondary loading was prevented by implementing a momentum trap on the input bar so that the recovered specimens only contain damage imposed by a single compression event.

A strain interruption technique was employed to impose different levels of deformation and damage to the specimens. This was achieved by installing precision-manufactured strain control collars at the interface between the output bar and the specimens, as shown in Fig. 1c. Collar spacers of different thicknesses were manufactured and subsequently hand-polished to achieve a dimensional tolerance of ±3 μm. Once the length of the specimens has been compressed to the same level as the thickness of the collar spacers, the input bar end and the collars will come into direct contact and produce a "sudden stop" to the specimen deformation. The target interruption strains (ε_{interr}) were designed in accordance with the non-interrupted response of the specimens tested under similar conditions [51]. The impact velocity of the striker bar was ~13.8 m s^{-1}, yielding an engineering strain rate of ~2500 s^{-1} onto 3 mm long specimens. In addition to strain-gauge measurements, a high-speed camera was synchronised with loading to record deformation images *in situ* and directly deduce the specimen ε_{interr} by two-dimensional (2D) digital image correlation (DIC).

The tests were conducted at 23 °C and −50 °C (± 2 °C) to study the role of temperature in the damage mechanisms at high rates. The −50 °C condition represents typical ambient temperatures encountered at civil aircraft cruising altitudes and is particularly relevant given the increased brittleness of typical epoxy matrix in the temperature range associated with β-relaxation [52]. The initial temperature was achieved through a bespoke temperature control system for HSR SHPB testing. The cool nitrogen gas originating from an LN2 dewar was heated, regulated and injected into a double-walled impact/temperature chamber (Fig. 1c) as both a cooling and heating agent. During the experiment, the inner chamber was maintained at the target testing temperature; meanwhile, the outer "isolation" chamber was heated to prevent moisture and frost from forming on the observation windows. More details on HSR loading, strain interruption, and temperature control setups can be found in previous research [51].

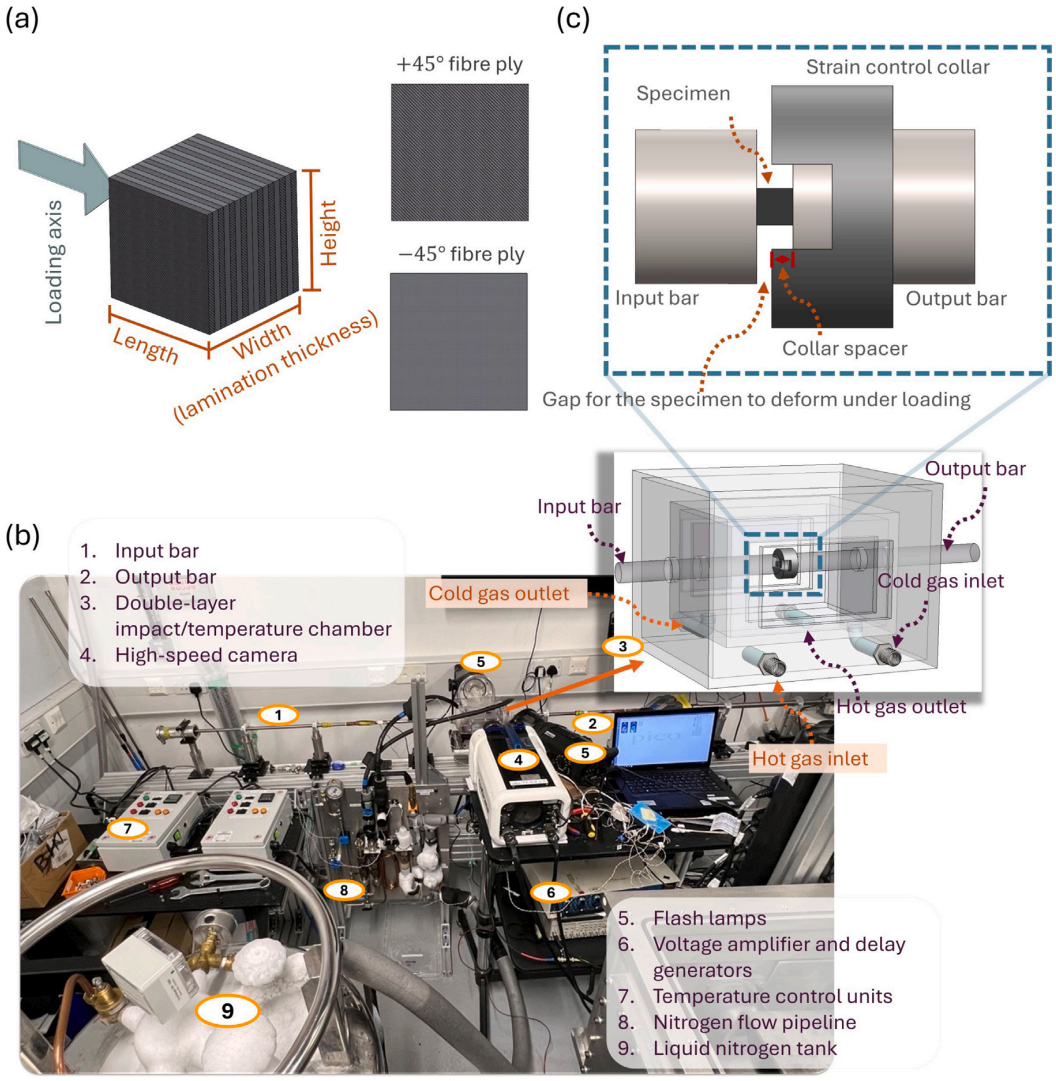


Fig. 1. Schematic of the specimens, loading, temperature control, and imaging setups. (a) The specimen geometry formed by stacking plies with +45 and −45° fibre pies, (b) a SHPB loading platform mounted with high-speed imaging and temperature control systems, and (c) the zoom-in views of the double-layer impact/temperature chamber and the strain interruption setup.

2.3. X-ray imaging strategy

The internal structures of the laminate specimens were examined with synchrotron-based phase-contrast μ-CT on Beamline ID19 at the European Synchrotron Radiation Facility (ESRF). The high photon flux and small effective X-ray source size enable rapid scanning at high spatial resolution (effective pixel size of 2.1 μm × 2.1 μm in this study) while providing propagation-based phase-contrast enhancement [53]. Compared with absorption-contrast imaging alone, phase-contrast propagation improves the visibility of weakly absorbing features and interfaces, facilitating micron-scale damage detection. Based on the phase-contrast tomograms, DVC was applied to quantify loading-induced permanent deformation by correlating volume pairs acquired before loading (pre-scan) and after loading (post-scan) at selected loading stages. The resulting 3D displacement field was then used for micro-scale image registration, enabling accurate voxel-wise comparison between scans, and robust extraction and analysis of both residual strain and micron-scale damage. This analysis pipeline will be discussed in detail in the following sections.

For each experimental condition (interruption strain level and temperature), one specimen was analysed using the full DVC workflow. This was constrained by the requirement of paired pre- and post-loading synchrotron μ-CT scans and the limited availability of beamtime. Mechanical repeatability was verified through multiple SHPB tests under identical conditions, and additional specimens characterised by post-scans exhibited consistent damage morphology and evolution trends. For a given temperature, the physically coherent evolution of global response, damage morphology, and local strain localisation across increasing interruption strain levels further supports the mechanistic consistency of the observed damage processes.

2.4. Image pre-processing

The methodology for image processing and damage analysis in HSR loading testing is presented in Fig. 2. Due to the much longer acquisition time relative to the loading event, X-ray tomography cannot be carried out continuously, as in the case of quasi-static tests. However, scanning specimens at separate times (pre- and post-scans) can

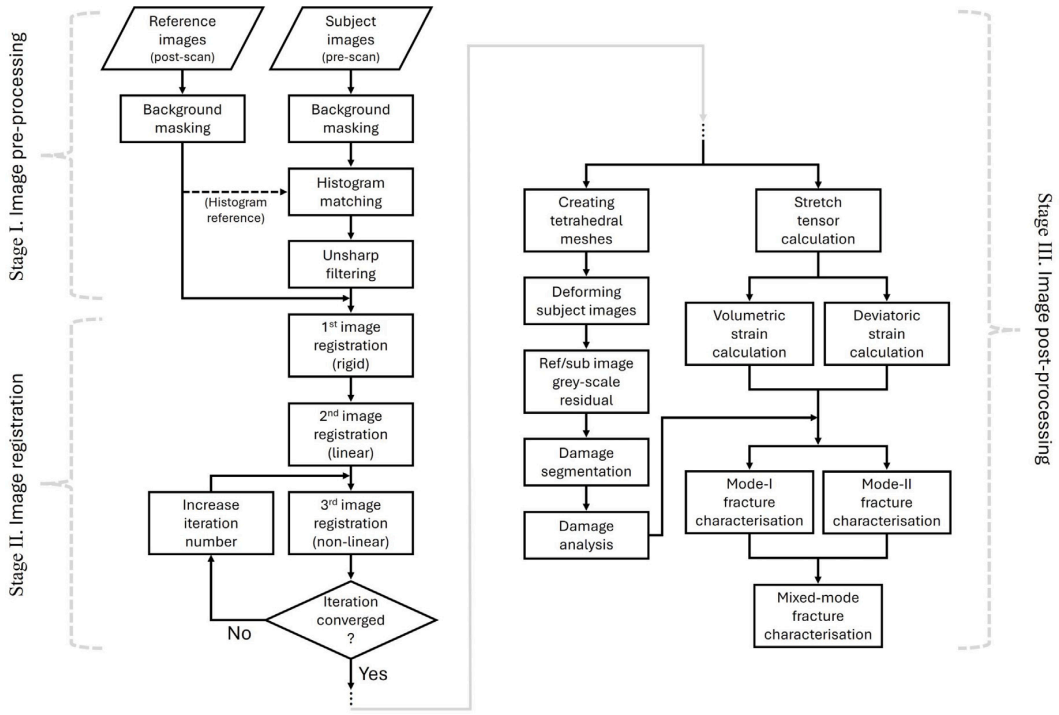


Fig. 2. Data acquisition, image processing, damage segmentation, and micro-mechanics analysis flowchart. Stage I involved histogram matching of the subject scans to the reference scans prior to image registration. These pre-processing steps improved grey-scale consistency and ensured robust correlation and numerical convergence. At Stage II, image registration was conducted in three steps (rigid, linear, and non-linear) to achieve correlation from coarse to fine. Stage III performed damage segmentation and strain calculation, which, in combination, help characterise the micro-mechanics of the segmented damage.

lead to dissimilarities that originate from fine differences in the X-ray beam and imaging parameters. Thus, prior to image registration, image normalisation was necessary to compensate for differences encountered during post-scans, as shown in Fig. 2, Stage I. During this process, post-scans (images of damaged specimens) were selected as references to avoid distortion of the damage features. High-accuracy boundary detection and specimen/background segmentation are required for full-field damage visualisation and characterisation, enabling the study of boundary effects in AP laminates. This was achieved by creating region of interest (RoI) masks using a deep-learning model based on the U-Net architecture integrated in the `Dragonfly 3D World` software [54]. Next, histograms of pre- and post-scans were matched, and an unsharp masking was applied to help minimise the difference in intensity gradients between the two sets of scans. These image pre-processing procedures can effectively enhance gradient-based feature recognition, resulting in good calculation convergence and less computational cost.

2.5. Image registration

The spatial correspondence between the two tomography datasets was then established through image registration and transformation (Fig. 2, Stage II). First, a rigid image transformation (the 1st image registration) was performed in `3D Slicer` [55] to eliminate large-scale specimen misalignment, which, if present, would substantially increase computational cost and reduce robustness during subsequent registration. The 2nd image registration applied a global linear (affine) coordinate transformation to the subject volumes using the `SPAM` analysis toolkit [56], following,

$$\mathbf{X}' = \mathbf{F}\mathbf{X} + \mathbf{t}, \tag{1}$$

where $\mathbf{X}'$ and $\mathbf{X}$ denote the voxel coordinates in the reference volumes and the subject volumes, respectively ($\mathbf{X}'$, $\mathbf{X} \in \mathbb{R}^3$). $\mathbf{F} \in \mathbb{R}^{3\times3}$ stands for the transformation (deformation) gradient tensor, and $\mathbf{t} \in \mathbb{R}^3$ is the translation vector [57]. The assembled linear deformation matrix $\boldsymbol{\phi}$ is written in homogeneous coordinates ($\mathbf{X}_h = [\mathbf{X}^\mathsf{T}\ 1]^\mathsf{T}$) as,

$$\boldsymbol{\phi} = \begin{bmatrix} F_{xx} & F_{xy} & F_{xz} & t_x \\ F_{yx} & F_{yy} & F_{yz} & t_y \\ F_{zx} & F_{zy} & F_{zz} & t_z \\ 0 & 0 & 0 & 1 \end{bmatrix}, \tag{2}$$

such that the transformation can be written explicitly as

$$\begin{bmatrix} X'_x \\ X'_y \\ X'_z \\ 1 \end{bmatrix} = \begin{bmatrix} F_{xx} & F_{xy} & F_{xz} & t_x \\ F_{yx} & F_{yy} & F_{yz} & t_y \\ F_{zx} & F_{zy} & F_{zz} & t_z \\ 0 & 0 & 0 & 1 \end{bmatrix} \begin{bmatrix} X_x \\ X_y \\ X_z \\ 1 \end{bmatrix}. \tag{3}$$

With the obtained ϕ as an initial guess, the 3rd image registration correlated the reference and subject volumes within local regions by segmenting the volumes using structured grids and solving the non-rigid transformation fields. This was achieved by minimising an error function $\mathcal{T}(\phi)$ defined over a correlation sub-volume $\boldsymbol{\Omega}_\mathbf{s}$ in the reference volume,

$$\mathcal{T}(\phi) = \tfrac{1}{2} \sum_{\mathbf{X}' \in \boldsymbol{\Omega}_\mathbf{s}} \left[T(\mathbf{X}') - I\left(\phi^{-1}(\mathbf{X}')\right) \right]^2, \tag{4}$$

where $T(\mathbf{X}')$ denotes the voxel intensity of the reference evaluated at coordinate $\mathbf{X}'$, and $I(\cdot)$ represents the voxel intensity of the subject evaluated at the mapped coordinates. The optimal transformation parameters were obtained by iteratively updating $\boldsymbol{\phi}$ such that,

$$\frac{\partial \mathcal{T}}{\partial \boldsymbol{\phi}} = \mathbf{0}, \tag{5}$$

which was solved using a Newton–Raphson optimisation until the norm of the gradient $\nabla\mathcal{T}(\boldsymbol{\phi})$ falls below the prescribed convergence threshold (0.01 in the present calculation).

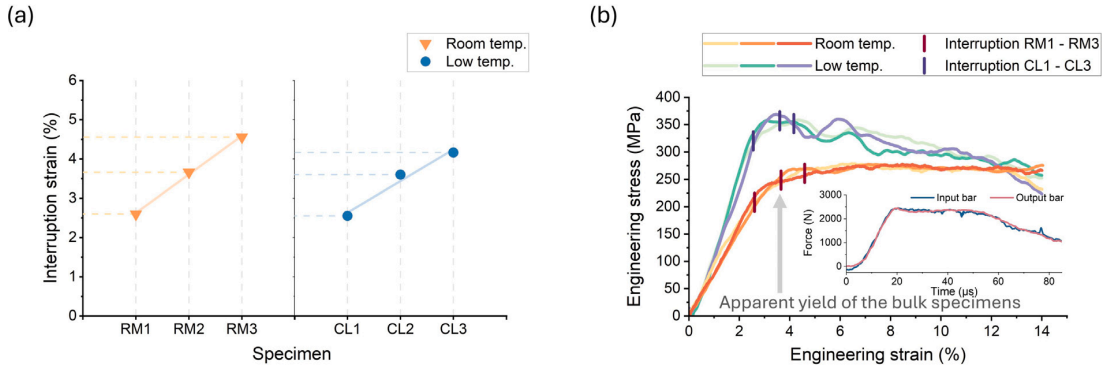


Fig. 3. Interruption strain levels for the specimens. (a) The measured strain levels at interruptions show a gradually increasing trend from RM1 to RM3 and from CL1 to CL3. (b) The loading stages of the specimens at the interrupted strain levels are demonstrated, in comparison with the non-interrupted stress–strain curves of the same CFRP laminates tested under similar loading conditions [51]. For clarity, only the pre-failure regime of the stress–strain response is displayed; catastrophic failure of the room-temperature specimens occurs at larger strains. The curves are shown in engineering form (axial engineering strain) and used to mark interruption stages rather than to present converted in-plane shear constitutive data. A representative input and output force–time history from a non-interrupted test is shown in the inset. The forces are in close agreement prior to peak stress, demonstrating dynamic stress equilibrium during SHPB loading.

A hierarchical coarse-to-fine strategy was adopted to improve convergence robustness. The DVC computation started with a coarse correlation sub-volume and progressively refined the solution using smaller window sizes, each iteration building upon the previously obtained transformation field. Specifically, the sub-volume size was reduced from 64 × 64 × 64 voxels to 8 × 8 × 8 voxels, with a decrement of 4 voxels per iteration.

2.6. Image post-processing and analysis

The local transformations derived from the preceding image registration were then input into two analysis tracks — damage segmentation and strain calculation, as illustrated in Fig. 2, Stage III. Tetrahedral meshes were generated to discretise the subject volumes. Local transformations obtained from DVC analysis were applied to these meshes, allowing consistent deformation of the subject volumes with respect to the measured displacement fields [56]. This enabled accurate mapping of the subject volumes onto the reference volumes, providing the basis for subsequent damage segmentation. Next, both deformed and undeformed subject volumes were subtracted from the reference volumes to calculate the grey-scale residuals r_{def} and r_{undef}, respectively, following,

$$\mathbf{r_{def}} = \mathbf{I_{ref}} - \mathbf{I_{obj}^{def}}, \tag{6}$$

$$\mathbf{r_{undef}} = \mathbf{I_{ref}} - \mathbf{I_{obj}}, \tag{7}$$

where $\mathbf{I_{ref}}$ is the reference volumes (post-scans). $\mathbf{I_{obj}}$ and $\mathbf{I_{obj}^{def}}$ denote the object volumes (pre-scans) before and after deformation according to the obtained transformations, respectively. Subsequently, the standard deviation (**STD**) for r_{def} and r_{undef} can be calculated to assess the effectiveness of DVC analysis using,

$$\mathbf{STD} = \sqrt{\frac{1}{N}\sum_{i=1}^{N}(x_i - \mu)^2}, \tag{8}$$

where N and μ represent the total number of voxels and the mean intensity in the computing volumes, x_i is the intensity of each voxels. The resulting r_{def} can also be used to highlight the structural differences between $\mathbf{I_{ref}}$ and $\mathbf{I_{obj}^{def}}$ (e.g., cracks generated during loading). From there, micron-scale crack segmentation can be accomplished using maximum entropy image thresholding to create damage masks for qualitative and quantitative analysis. Visualisation and analysis of local residual displacement, strain concentration, and micron-scale damage were performed through the combined use of `Dragonfly` 3D `World` [54], `ImageJ` [58], `ParaView` [59], and developed `Python` scripts.

In the strain calculation, microscopic local strain was computed directly from the transformation matrix for each sub-volume (8 × 8 × 8 voxels, approximately 16.8×16.8×16.8 μm^3) on the structured grid. The local deformation gradient **F** was obtained by linking eight neighbouring grid nodes [56], following,

$$\mathbf{F} = \mathbf{I} + \frac{d\mathbf{u}}{d\mathbf{X}'}, \tag{9}$$

where **I** is the identity matrix, and $\nabla\mathbf{u}$ denotes the gradient of the displacement tensor. The right stretch tensor **U** was derived using polar decomposition [60], expressed as,

$$\mathbf{F} = \mathbf{RU}, \tag{10}$$

$$\mathbf{U} = (\mathbf{F}^{\mathrm{T}}\mathbf{F})^{1/2}, \tag{11}$$

where **R** is a proper orthogonal rotation ($\mathbf{R}^{\mathrm{T}}\mathbf{R} = \mathbf{I}$, $\det \mathbf{R} = +1$). The stretch tensor can be multiplicatively decomposed into an isotropic and a deviatoric part as,

$$\mathbf{U} = \mathbf{U}_{iso} \cdot \mathbf{U}_{dev}, \tag{12}$$

where $\mathbf{U}_{\mathrm{iso}} = J^{1/3}\mathbf{I}$ represents the volumetric stretch associated with the local volume change $J = \det(\mathbf{F})$, and $\mathbf{U}_{\mathrm{dev}} = J^{-1/3}\mathbf{U}$ captures the isochoric (shape-changing) deformation. Volumetric and deviatoric deformation measures were analysed together with the segmented damage, as they highlight different deformation modes and therefore different damage mechanisms. In particular, local volumetric expansion is indicative of opening-dominated processes (Mode I), whereas deviatoric deformation and shear localisation are commonly associated with sliding-dominated mechanisms (Mode II).

3. Results and discussion

3.1. Interrupted strain comparison

The interrupted strain levels achieved in both room- and low-temperature specimens are shown in Fig. 3a, increasing from ~2.5% to 4.5% for subsequent specimens (i.e., RM1 to RM3, CL1 to CL3). The relative global stress–strain stages of the specimens at the interruption points can be evaluated by comparing with the non-interrupted responses obtained from similar loading and environmental conditions, as presented in Fig. 3b. It should be noted that the stress–strain curves

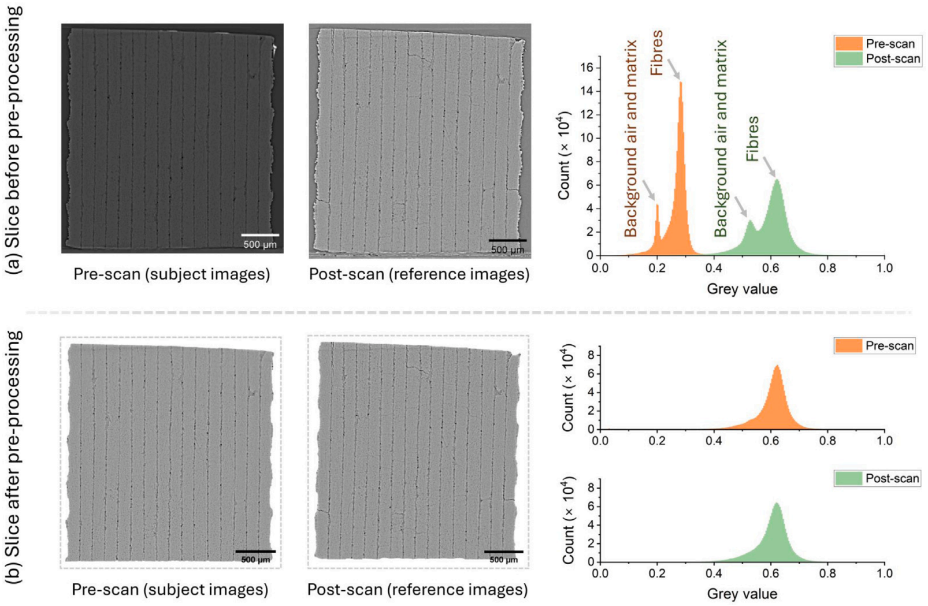


Fig. 4. Image pre-processing results. (a) The X-ray μ-CT slices and their histograms of specimen CL2 before and after loading. (b) The same X-ray μ-CT slices and their histograms after the pre-processing. It can be seen that the image background has been removed, and the grey-scale distribution of the slices has been matched. The grey-scale gradients between features are in a comparable state across pre- and post-scans.

are presented in engineering form. As the maximum deformation remains below 5% in all interruption cases, engineering strain, which is commonly adopted in ±45° laminate testing in accordance with ASTM D3518/D3518M [61], is considered appropriate. Within this small deformation range, the difference between engineering and true strain measures is negligible for the purposes of the present damage and strain localisation analysis. The interrupted strain level was acquired from direct displacement measurement using DIC, the detailed analysis of which is discussed in the previous study [51]. The strain of the specimens (RM1–RM3 at room temperature and CL1–CL3 at low temperature) was interrupted in the vicinity of the apparent yield, allowing the study of the microscopic damage evolution throughout the critical transition from nominal elastic to inelastic bulk deformation regimes.

3.2. Pre-processed image analysis

The same specimen scanned at separate times on the same synchrotron beamline can possess different grey-scale distributions and gradients, as shown in the X-ray μ-CT slices in Fig. 4a. The grey scale of the empty region (the air), the specimen resting platform, and the resin-rich regions are intertwined, because of the low X-ray absorption of the epoxy matrix and the presence of phase-contrast effects. For each of the histograms, the left-side peak (the relatively lower one), together with its base, is a composition of these three components, making the background (the air and platform) difficult to subtract using a thresholding method. The use of a bespoke `Python` code and a U-Net-based deep-learning algorithm (integrated in `Dragonfly 3D World`) enabled the accurate removal of the background (see the no background slices and single-peak histograms in Fig. 4b) through edge, gradient, and texture detection. Hence, the registration, analysis, and visualisation of the images in later stages would not include the background regions.

After removing the background, discrepancies in the histograms between the pre- and post-scans were still evident (Fig. 4a). Given that this DVC analysis was a grey-scale gradient-based calculation, comparable distributions and contrast were needed for good convergence and feature registration. Therefore, the pre-scan histogram was matched (cumulative histogram mapping) to the post-scan histogram, and unsharp filtering was applied. Fig. 4b displays the same X-ray radiography slices as in Fig. 4. The histograms of the two slices, one from the pre-scan and the other from the post-scan, exhibit highly comparable structures and grey scales, meaning that the gradient differences between the components, such as the voids, matrix, and fibres, in these pre- and post-scan slices have been matched.

3.3. Image registration effectiveness

The image registration processes performed in the present research are essential for identifying fine cracks and other microscopic damage signatures, such as deformation. Fig. 5 showcases the effectiveness of image registration between the pre- and post-scans. Overlay and subtraction between unaltered pre- and post-scan slices demonstrate clear misalignment, particularly recognisable at the specimen's edges (top-row images in Fig. 5). However, after being deformed through image registration, the pre-scan (50% opacity) became barely visible when overlaid on the post-scan. A substantial reduction in grey-scale residuals can be found in the subtraction image with a drop in STD from 17.68 to 6.35, indicating a significantly higher degree of comparability between the post-scan and the deformed pre-scan (bottom-row images in Fig. 5).

The notation, coordinate, and naming conventions used in the data analysis are specified in Fig. 6, in which Fig. 6a shows the dimension notation and ply layup of the CFRP specimens. Fig. 6b is the spherical coordinate system adopted in the displacement vector analysis. The XY plane is parallel to the impact face of the specimens, and the loading was applied along the Z axis towards the −Z direction. The naming of cracks with different morphologies is illustrated in Fig. 6c. Intra-ply cracks that are shown to be 1 to 2 pixels in width were named as micron-scale intra-ply cracks, while wider ones with obvious internal void space between the edges were labelled as opened cracks. In addition, inter-ply delamination is the separation of two adjacent plies in the resin-rich regions.

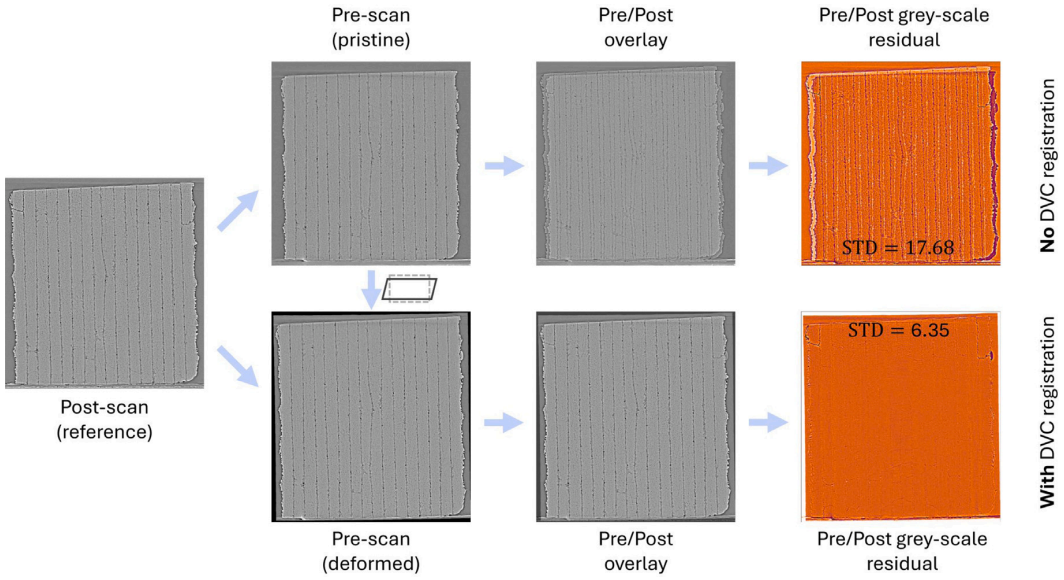


Fig. 5. Image registration before (top row) and after (bottom row) DVC. Image overlay and subtraction results are displayed to demonstrate the feature matching between pre- and post-scans. A good match can be found after performing DVC, evidenced by a clearer overlay image result and significantly homogenised (reduced STD) grey-scale residuals.

3.4. Micro-scale displacement analysis

Specimen internal displacements produced from the DVC analysis are demonstrated in Fig. 7. The arrows point to the displacement directions, and the magnitude of the displacement is indicated by the length and colour map. For each specimen, two views – front (YZ plane) and isometric – are presented. It can be seen that at equivalent strain levels (each column in Fig. 7), the specimens tested at low temperature exhibit earlier and larger displacements with greater localisation. The internal local displacements of the specimens show a strong directional feature influenced by the internal structures of the laminates, mainly the fibre directions and the ply stacking sequence. This directional feature is more evident in specimens with larger interrupted strains or at similar strains but lower temperatures. Large surface ply displacement (above 10 voxels) along the fibre direction (+45°) can be found in RM3, CL2 and CL3, identified by arrows with longer length and darker colours. For specimens with small interrupted strains, such as RM1, RM2, and CL1, lateral expansion in the Y direction (the height direction of the specimens) is prominent with inclinations towards the fibre directions in individual plies.

The statistical analysis of the vector direction and magnitude is presented in Fig. 8. For each specimen, three plots were produced based on displacement vectors — direction histogram (DH), accumulated magnitude histogram with normalised colourmap (AMH-NC), and accumulated magnitude histogram with fixed-range colourmap (AMH-FC). The DH plots illustrate the distribution of vector directions in each specimen. In the AMH-NC plots, the magnitude of each displacement vector is accumulated within each direction bin, enabling visualisation of the accumulated vector magnitude in different directions using a colour map normalised to the maximum and minimum values in the volume. This representation facilitates the assessment of the alignment between the direction and magnitude distributions. For instance, an overall flattening of the intensity distribution from DH to AMH-NC (i.e., a higher degree of spatial uniformity in AMH-NC compared to DH) can indicate a mismatch of the peak intensity between the direction and magnitude distribution. Lastly, the AMH-FC plots employ a fixed colour scale, allowing direct and consistent comparisons of accumulated vector magnitudes across specimens.

Interestingly, in specimen RM1, displacement is highly concentrated in the specimen's in-plane direction (length and height). Four labelled high-intensity regions, denoted RM1-1, RM1-2, RM1-3 and RM1-4 in Fig. 8, reveal a pronounced tendency for in-plane displacement along the specimen's length and height directions. These displacements lean towards +45 or −45° fibre directions in each ply (also see RM1 in Fig. 7). Despite the existence of Poisson's effect, the noticeable specimen expansion in the height direction (90 and −90°) in this stage is fundamentally induced by the off-fibre-axis loading, which drives ply displacement along +45 or −45° fibre directions. The displacement in the specimen width direction remains minimal, as evidenced by the vertically aligned intensity distribution centred at about 90 and −90° in the azimuth [62]. As ϵ_{interr} increases to 3.66% (RM2), a modest increase in width-direction displacement becomes apparent, as indicated by the higher intensities observed in Zones RM2-1 and RM2-2 when compared to RM1 (Fig. 8). Specimen RM3 represents a further development of this behaviour, characterised by a clear rotation of the dominant displacement direction. Zone RM3-1 exhibits a strong in-plane displacement approximately aligned with the +45° fibre direction, accompanied by an outward component in the specimen width direction (i.e., the −X direction in the global spherical coordinate system). Meanwhile, Zone RM3-2 is approximately the central symmetry of RM3-1, showing a corresponding displacement pattern on the opposite side of the specimen (also see RM3 in Fig. 7). Similarly, Zones RM3-3 and RM3-4 describe displacement components that intersect the RM3-1 and RM3-2 directions at approximately 90° in the −45° fibre plies. Owing to the alternating stacking sequence of the +45 and −45° fibre ($[+45/-45]_{4s}$ layup), the inter-ply interaction in orthogonal fibre orientations gives rise to a coherent band of displacement directions, as shown in RM3, Fig. 8.

It is notable that, for RM1 and RM2, the AMH-NC plots exhibit a pronounced flattening relative to the corresponding DH plots once the accumulated vector magnitudes are incorporated, whereas the AMH-NC plot for RM3 remains broadly similar to its DH plot. The evident flattening observed in RM1 and RM2 arises from an intensity mismatch between the direction distribution and the magnitude distribution of the displacement vectors. This indicates that, although a large number of vectors in RM1 and RM2 were orientated along similar directions,

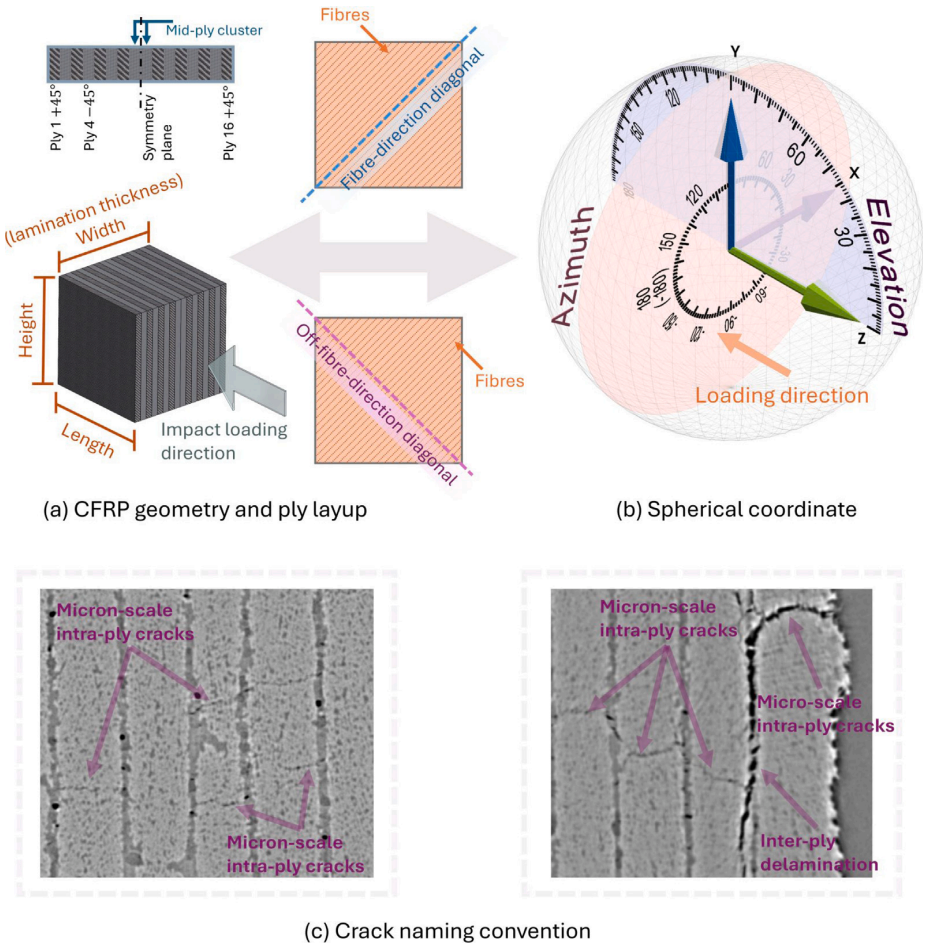


Fig. 6. Notation and coordination systems used in analysis. (a) The geometry and ply layup of the CFRP laminates are demonstrated, together with the illustration of two types of diagonals that are used in the damage micro-mechanics discussion. (b) The 3D spherical coordinate system is used to indicate the direction of displacement vectors in a 3D space. (c) The naming convention for different damage morphologies.

forming well-defined direction clusters, their magnitudes are relatively small and more spatially dispersed. In other words, at this stage, the localisation of displacement magnitude is markedly weaker than the localisation of displacement direction. In contrast, no pronounced flattening is observed in the AMH-NC plot of RM3 when compared with its DH plot, indicating that, at higher strain levels, the direction distribution is in good agreement with the corresponding magnitude distribution. Furthermore, a clear trend of increasing direction distribution and growing in magnitude with increasing ε_{interr} can be identified in the displacements by cross-comparing RM1, RM2 and RM3 using the AMH-FC plots. This evolution is attributed to the progressive development of volume expansion, contraction, and shear deformation along the three specimen dimensions.

CL1 exhibits the lowest ε_{interr} among low-temperature specimens. While similar in-plane displacement patterns and limited specimen width expansion can be observed, similarly to RM1 and RM2, the displacement of CL1 is highly localised within Zone CL1-1, as highlighted in Fig. 8. This pronounced localisation is indicative of a brittle deformation behaviour under low-temperature conditions [39]. Although CL2 was interrupted at $\varepsilon_{interr} = 3.60\%$, it already demonstrates the formation of a nearly coherent displacement band, comparable to that observed in RM3 at a higher strain level ($\varepsilon_{interr} = 4.56\%$). Nevertheless, the displacement field in CL2 remains more strongly localised than its room-temperature counterpart, observed from the AMH-FC plots. The DH plot of CL3 shows that the displacement vectors are highly concentrated in four distinct zones, labelled CL3-1, CL3-2, CL3-3 and CL3-4 in Figs. 7 and 8 (CL3). Zones CL3-1 to CL3-3 correspond to the displacement vectors influenced predominantly by the +45° fibre direction, whereas the displacement in CL3-4 is approximately aligned with the −45° fibre direction. Moreover, the displacement vectors opposing the loading direction are also observed in CL3 and are labelled Zone CL3-5. This behaviour indicates that the residual deformation along the specimen length direction (i.e., the ± Z axis) in CL3 is significantly larger than that observed at room temperature (RM3).

Similarly to RM3, the AMH-NC plots for CL1 to CL3 show only marginal flattening when compared with the corresponding DH plots, indicating a high degree of consistency between the direction and magnitude distribution of the displacement vectors. In particular, this consistency emerges at a much lower strain level in low-temperature specimens ($\varepsilon_{interr} = 2.55\%$) than at room temperature, where a comparable behaviour is only observed at 4.56%. This observation further suggests a higher degree of displacement localisation (both in magnitude and direction) in CFRP under low-temperature conditions at a microscopic scale. Meanwhile, the progressively enhanced AMH-FC distributions from CL1 to CL3 reflect the continued development of internal deformation with increasing global strain, following a trend similar to that observed in the room-temperature specimens.

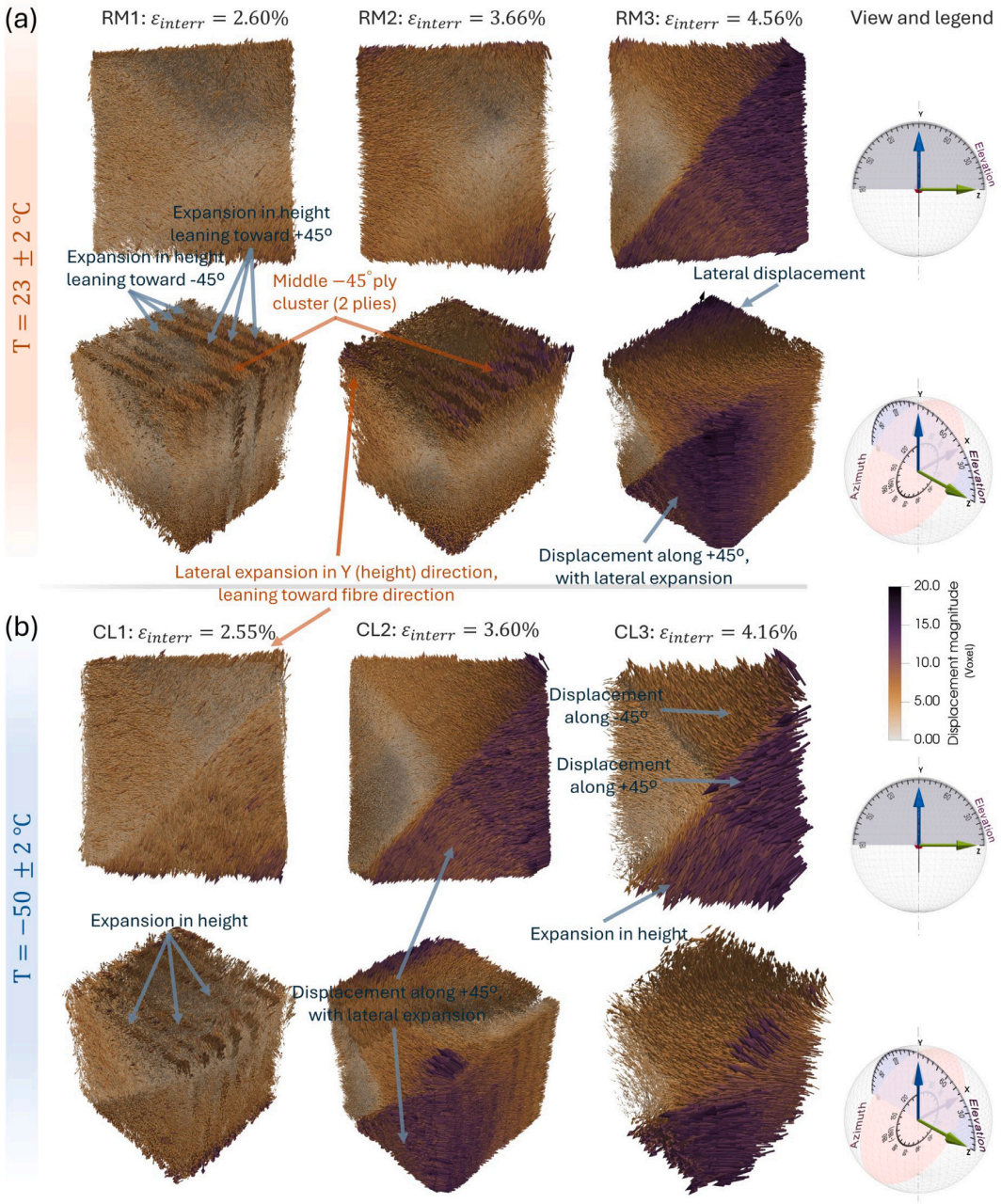


Fig. 7. 3D microscopic displacement vectors calculated from DVC for specimens at (a) room and (b) low temperatures. Two views are presented for each specimen. The directions of the displacement vectors are consistent with the arrow directions, and the colour code and the length of the arrows indicate their magnitude. Prominent directionality is observed in the specimens at both temperatures, with the low-temperature ones being more pronounced at similar strains. An evident correlation between displacement direction and fibre/ply arrangement is visualised. More direction indications can be found in Fig. 6. (For interpretation of the references to colour in this figure legend, the reader is referred to the web version of this article.)

3.5. Micron-scale damage analysis

The spatial distribution, quantity, and propagation characteristics of micron-scale damage within the specimens are presented in Fig. 9a, extracted using the image processing workflow proposed in this study. An example 2D slice from specimen CL1 is shown in Fig. 9b, revealing the presence of micron-scale cracks (approximately 2–4 pixels in width) and their segmentation. Given that the detected crack widths approach the effective spatial resolution limit of the μ-CT system, the identification of such fine damage features does not rely solely on conventional grey-level thresholding. Instead, the present approach is based on DVC-assisted registration of paired pre- and post-loading scans, allowing newly formed damage to be identified from structured residuals after deformation compensation. Similar strategies have been adopted in recent studies for resolving fine-scale damage in tested specimens using DVC [42,43]. In addition, the segmented cracks show

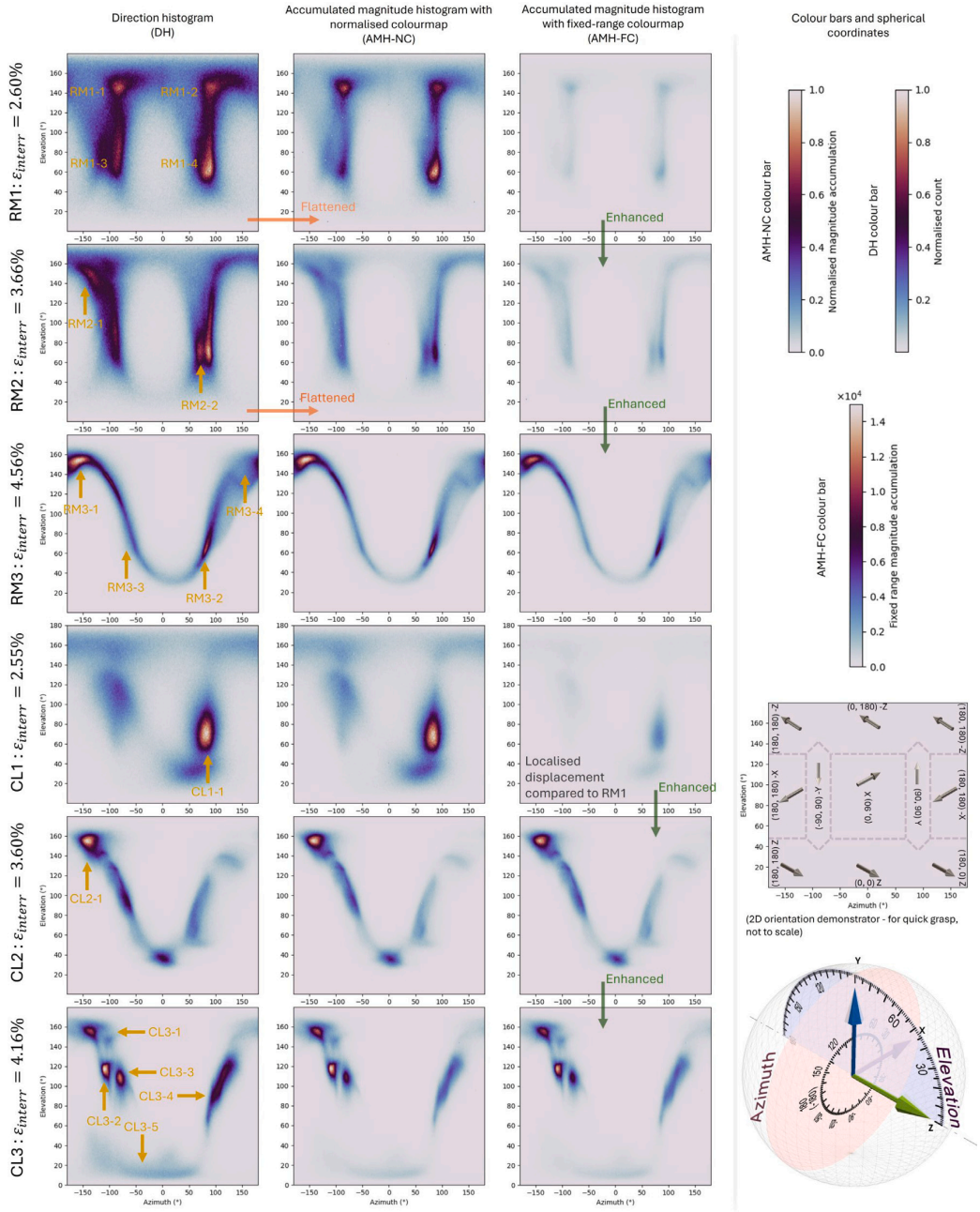


Fig. 8. Distribution plots for the direction and magnitude of the microscopic displacement in the specimens. The DH plots demonstrate the direction distribution of the displacement vectors. The AMH-NC plots incorporate the vectors' magnitude into the DH plots to visualise the consistency between the direction and magnitude distributions. The AMH-FC normalise the plots with the same colour scale to form a clear comparison across specimens. The distribution plots should be interpreted in conjunction with the spherical coordinate and 2D demonstrator at the side. More direction indications can be found in Fig. 6. (For interpretation of the references to colour in this figure legend, the reader is referred to the web version of this article.)

clear spatial correspondence with visually identifiable cracks in the raw images (Fig. 9b), providing additional independent evidence for the physical relevance of the detected damage features. Quantitative estimation of damage volume fractions is summarised in Fig. 9c to illustrate the progressive growth of damage across the specimens. These quantities are interpreted as estimated and trend-based metrics rather than absolute volumetric measurements. The present study focuses on elucidating crack initiation mechanisms through the spatial correlation between damage morphology and microscopic strain localisation. The spatial agreement between the extracted cracks and the independently computed strain fields further supports the reported damage evolution trends.

Despite being subjected to comparable levels of interrupted global strain, the low-temperature specimens exhibit a markedly accelerated development of micron-scale damage compared with their room-temperature counterparts. No resolvable damage is detected in RM1

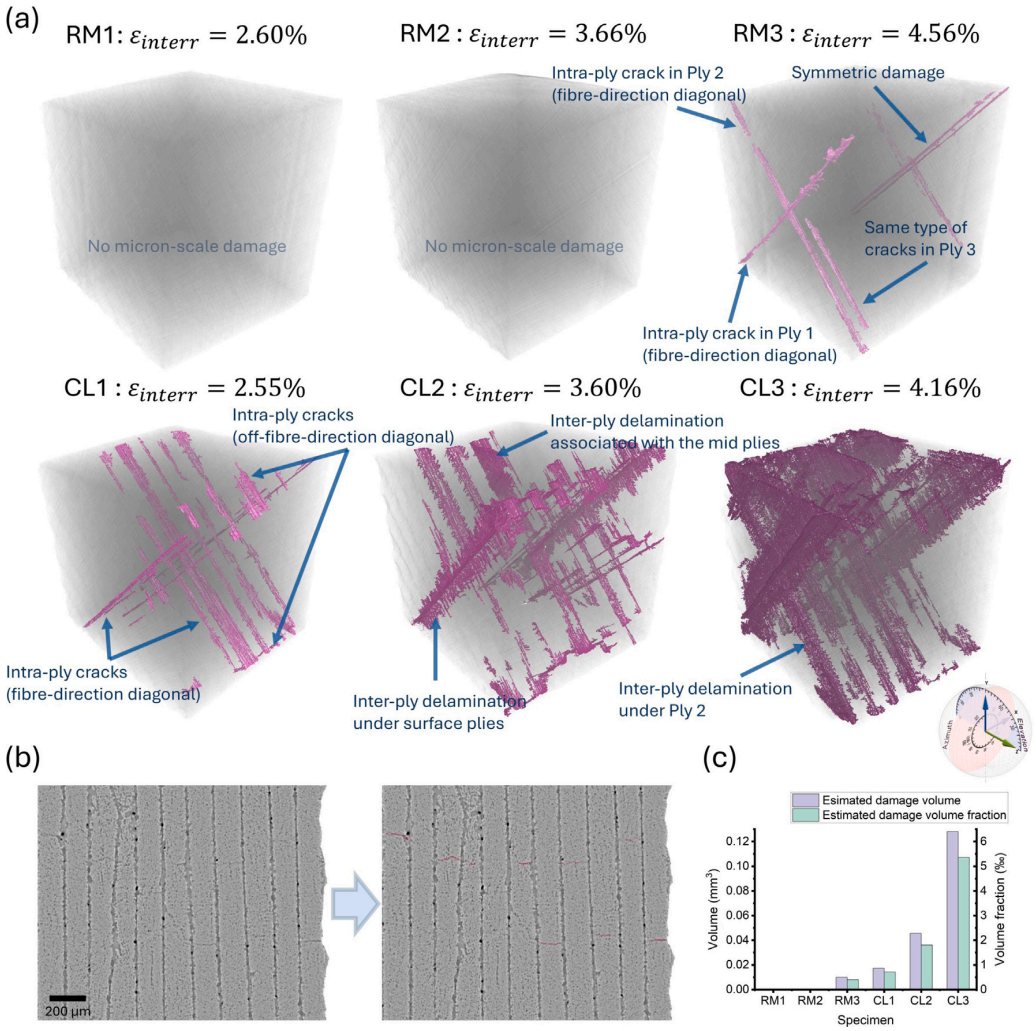


Fig. 9. Segmented damage at micron-scale and above in the specimens. (a) The damage segmentation and visualisation show the damage initiation and evolution with increasing axial strain level. (b) Representative comparison between visually identifiable micron-scale cracks and DVC-assisted crack segmentation on the same μ-CT slice. Arrows indicate cracks identifiable in the raw image, while the red overlays denote the corresponding segmented damage features obtained using the proposed pipeline, demonstrating the consistency between visual inspection and automated detection. (c) The damage volume statistics of the specimens at different axial strain levels. The quantified damage volume and corresponding volume fraction are influenced by factors such as image acquisition consistency, pre-processing, registration accuracy, and segmentation thresholding. The presented results are therefore intended to illustrate the relative evolution and overall trend of damage growth across different strain levels, rather than to provide absolute volumetric quantification. The proposed experimental and analysis workflow enables high-quality recognition and segmentation of the micron-cracks. Micron-cracks initiate before the apparent yield of the low-temperature specimens and develop significantly more rapidly than the room-temperature specimens.

and RM2, corresponding to stages before and approximately at the global apparent yield, respectively. Micron-scale intra-ply cracks first emerge in the room-temperature specimens when ε_{interr} increases to approximately 4.56% (RM3). These cracks are predominantly confined in a very limited number (two in the present case) of plies underneath the surface ply, aligned with the fibre directions on both sides of the laminate, and concentrated along the fibre-direction diagonals within individual plies (see Fig. 6a for ply geometry notation).

In contrast, resolvable cracks are already present in the low-temperature specimens at the lowest interrupted strain level investigated ($\varepsilon_{interr} = 2.55\%$ for CL1), which is prior to the global apparent yield and approximately at the end of the nominal elastic regime, as indicated in Fig. 3b. Although these cracks are very small in width, they are distributed more uniformly across the plies throughout the specimen lamination thickness. Similar enhanced damage distributions in AP CFRP at low temperatures have also been reported under quasi-static loading conditions [39]. The segmented cracks are larger and more contiguous in the two surface plies (Ply 1 and 16) and in the two middle plies (−45° mid-ply cluster — Ply 8 and 9), indicating elevated stress concentrations in these regions. In addition, several discrete intra-ply cracks oriented along the off-fibre-direction diagonals (see Fig. 6a for ply geometry notations) are observed near the impact surface. Building upon the crack morphology observed in CL1, specimen CL2 exhibits additional damage in the form of mild inter-ply delamination between Ply 1 and 2, and between Ply 15 and 16, which is spatially connected to the intra-ply cracking in the surface plies. Similar inter-ply delamination is also observed between Ply 7 and 8, linking to intra-ply cracks in the middle plies (Ply 8 and 9). This behaviour suggests that stress redistribution following the onset of intra-ply cracking can promote inter-ply delamination [19]. Damage in CL3 further increases

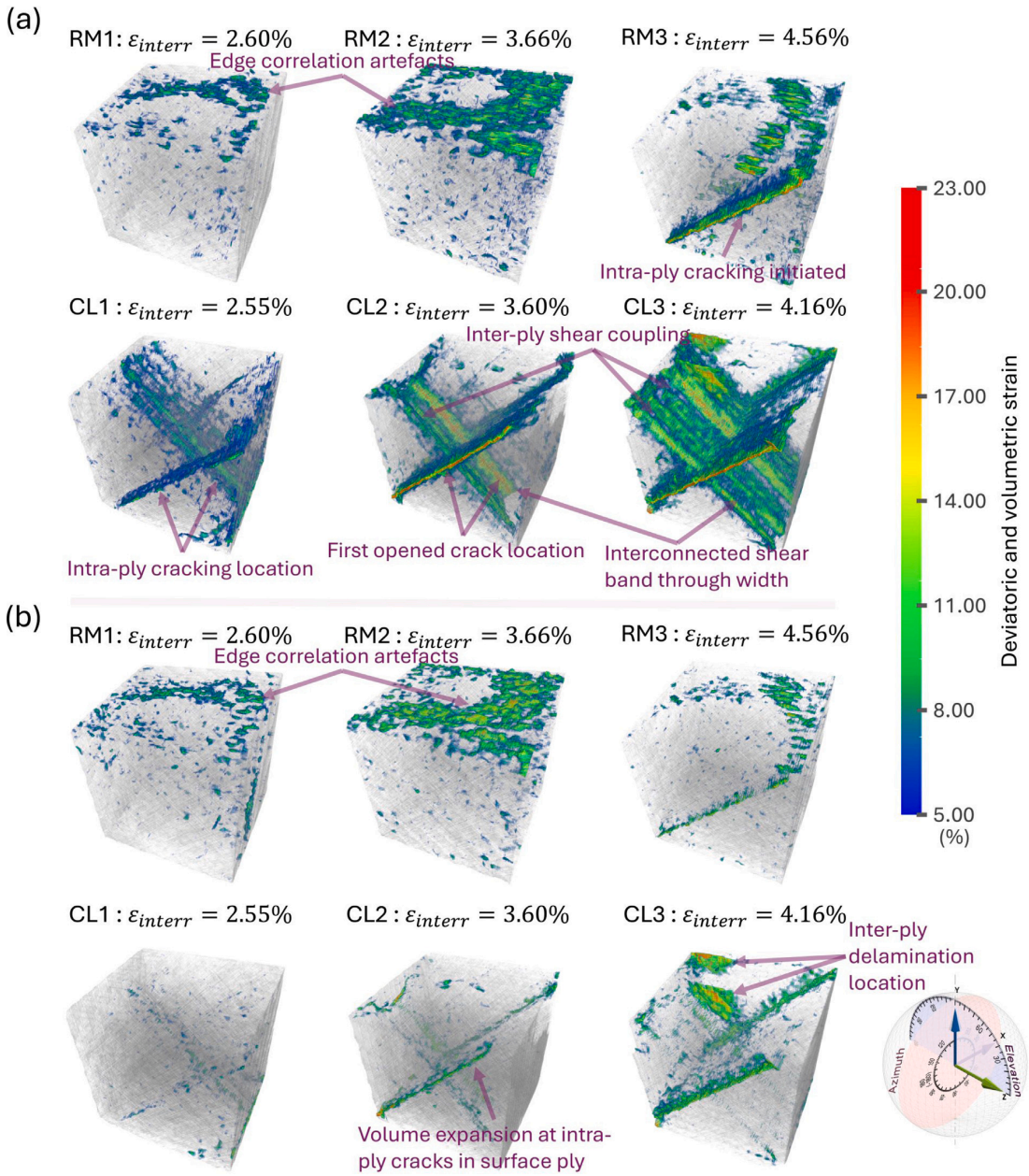


Fig. 10. Distribution and intensity of (a) deviatoric and (b) volumetric components in specimen local strain. Both strain components develop more rapidly at low temperatures. The deviatoric strain propagates along the fibre directions, forming shear bands. High volumetric strain is observed between plies in the delamination regions. The location and magnitude of the strain are in good agreement with the segmented damage, which reveals the damage micro-mechanics. Both Mode-II-dominant and mixed-mode fractures are found in intra-ply cracking, whereas ply delamination shows predominantly mixed-mode features, with a notable contribution from volumetric behaviour.

in volume relative to CL2, with inter-ply delamination extending to the interfaces between Ply 2 and 3, and between Ply 14 and 15. This delaminate progression pattern indicates a surface-to-inner propagation trend [51].

3.6. Microscopic strain analysis

The 3D distribution of the local deviatoric and volumetric residual strain within the tested specimens is illustrated in Fig. 10. For RM1 and RM2, no evident localisation of either deviatoric or volumetric strain exceeding 5% is observed within the bulk of the specimens. The apparent strain localisation visible near the top surface of the strain fields is attributed to edge correlation artefacts arising from imperfect background removal and edge artefacts in the original X-ray images. Consistent with this observation, no resolvable damage is detected at these stages, as shown in Fig. 9a for RM1 and RM2. At room temperature, when ε_{interr} increases to 4.56% (RM3), a pronounced localisation of deviatoric strain emerges within the surface ply. The

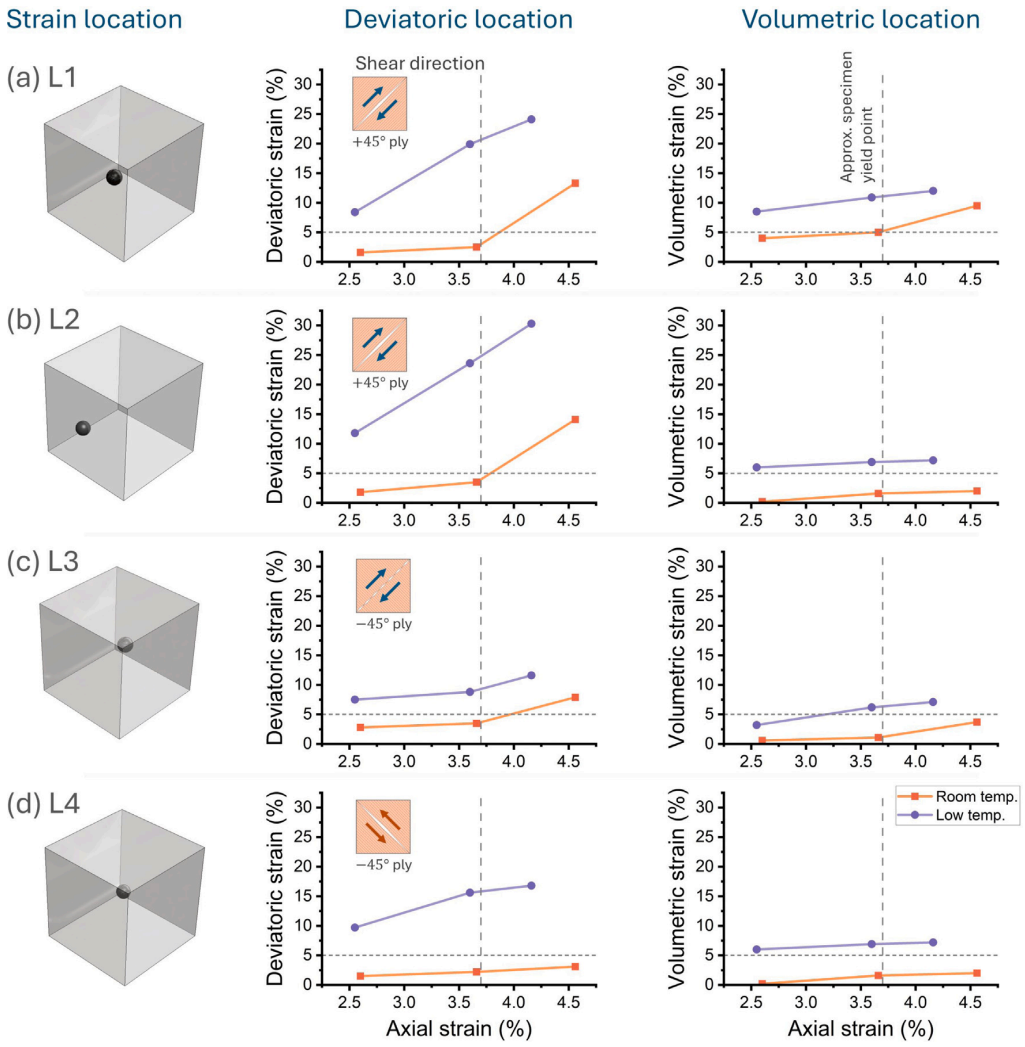


Fig. 11. Microscopic strain development at four representative locations: (a) L1, (b) L2, (c) L3, and (d) L4. The deviatoric strain shows a more pronounced increase compared to the volumetric strain, as the selected locations are all on the deviatoric-dominated high-strain bands. L1 and L2 lie in the surface ply (Ply 1 or 16) along the high-strain band, presenting noticeable strain increases with the increasing macroscopic strain. L3 sits at the same ply location as L1 but on the underlying ply (Ply 2 or 15). A clear shear strain localisation can be observed along the off-fibre-direction diagonal of the ply (perpendicular to the fibre direction) at L3, causing inter-ply shear transfer and a contiguous shear band through laminate thickness. L4 represents the increase of the strain propagated along the −45 °C fibre direction in the mid-ply cluster.

concentrated deviatoric strain aligns approximately with the local fibre direction and spatially coincides with the intra-ply cracks observed near the fibre-direction diagonal of the ply, as shown for RM3 in Fig. 9a. At these regions of damage/strain localisation, the deviatoric strain magnitude is significantly greater than the corresponding volumetric strain, indicating that the associated intra-ply cracking is predominantly shear-dominated. This behaviour is more clearly demonstrated in Fig. 11(a and b).

All low-temperature specimens exhibit a pronounced deviatoric deformation behaviour similar to that observed in RM3. Its degree of deviatoric deformation increases progressively from CL1 to CL3, concomitant with the growth of intra-ply damage, as shown in Fig. 9a. The highest concentrations of deviatoric strain are located in the surface plies and mid-ply clusters, where opened cracks are first observed. In these damage regions, the deviatoric strain displays both a broader spatial distribution and a higher intensity. In contrast, at locations dominated by inter-ply delamination in CL3, volumetric strain becomes comparatively more pronounced, indicating that volumetric deformation plays a more significant role in the delamination process. Combined with the inter-ply shear induced by excessive intra-ply shear along mismatched fibre directions (+45 and −45°) [19,63], this deformation state promotes prominent mixed-mode (Mode I and Mode II) fracture behaviour in the delamination regions.

The plots in Fig. 11 describe the evolution of local strain with increasing axial strain at several representative locations (L1–L4). At all locations, the local strain exhibits a clear increasing trend with increasing global axial strain. By adopting an approximate apparent yield point of the laminate at ~3.7% based on non-interrupted stress–strain measurements [51], it is evident that room-temperature specimens experience a prominent increase in local strain primarily after the apparent yield point. In contrast, low-temperature specimens show a rapid increase in local strain throughout all three strain steps, indicating an earlier activation of localised deformation mechanisms.

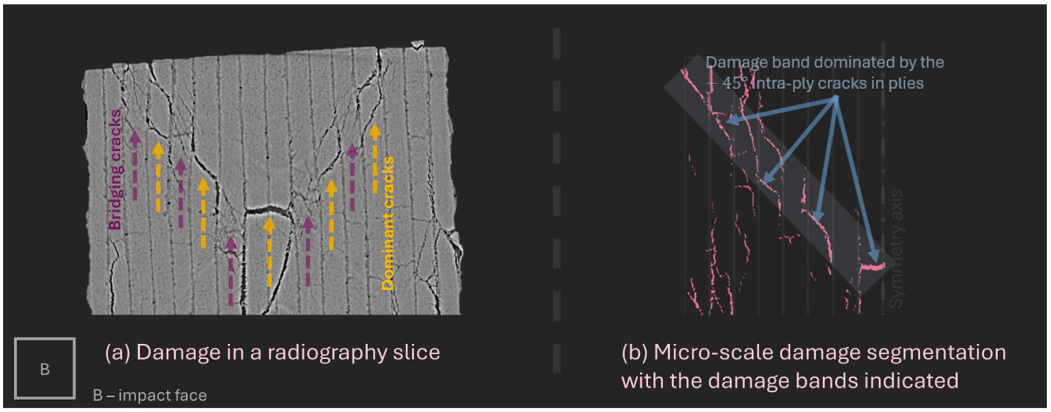


Fig. 12. A radiography slice from literature [51] showing the dominant cracks and the bridging cracks: (a) the tomography slice and (b) the segmentation of the opened cracks. The dominant cracks were generated primarily by in-plane shear, and thus, Mode-II dominated. In contrast, the mixed-mode fracture is the driving mechanism of the bridging cracks, which can be small in size and spatially discrete.

The locations L1 (near the corner) and L2 (in the centre) were situated within Ply 1, which is the surface plies with +45° fibres in the specimens. Similar strain histories can be found between these two locations, as they belong to the same shear localisation band (see Fig. 10). At both locations, the strain response is characterised by Mode-II-dominated cracking aligned with the +45° fibre direction. Location L3 corresponds to the same corner position as L1 but lies within Ply 2, a −45° ply, and therefore aligns with the off-fibre-direction diagonal of that ply (see notations in Fig. 6a). The pronounced strain localisation observed at L3 along the +45° fibre direction indicates significant shear deformation perpendicular to the local fibre orientation (−45°), corresponding to cut-through-fibre shear. This cut-through-fibre shear, in combination with along-fibre shear induced by direct ply compression, drives the initiation of discrete intra-ply cracks distributed along the off-fibre-direction diagonal, as shown in Fig. 9b. Given the comparable contributions of deviatoric and volumetric strain at L3, these discrete intra-ply cracks are likely governed by mixed-mode fracture. The opening component of the fracture is attributed to inter-ply shear coupling and Poisson-driven transverse deformation under global uniaxial compression. Location L4 is situated within the middle −45° ply cluster, where a high level of shear localisation is already observed at the lowest strain level (CL1), similar to the behaviour in the surface plies. This observation explains the early onset of opened damage in the mid-ply cluster reported in the previous study [51].

In fact, the phenomenon observed at L3 is not confined to a single ply, but can extend across multiple adjacent plies, forming a contiguous through-laminate-thickness shear band (see CL1–CL3 in Fig. 10a). These cutting-through-fibre shear bands become increasingly prominent in low-temperature specimens and at higher strain levels. The resulting intra-ply cracks distributed along the off-fibre-direction diagonal in −45° fibre plies bridge the dominant intra-ply cracks aligned with the fibre-direction diagonal in +45° fibre plies, giving rise to a continuous damage band across the laminate thickness, as shown in Fig. 12, which is observed in the previous study [51]. As a result of shear acting perpendicularly through the fibre direction, these bridging cracks tend to remain small and discrete in size.

Although the magnitude of the shear strain at L3 is lower than that observed at L1, the in-plane shear coupling across the lamination thickness of ±45 CFRP (see CL1–CL3 in Fig. 10a) clearly showcases the interactive stress transfer between adjacent pies with mismatched fibre orientations. This analysis provides quantitative evidence that the local deformation state departs from the nominal in-plane shear response assumed when interpreting uniaxial tests of ±45 laminates [61], Instead, a pronounced through-thickness gradient develops, characterised by a “mixed-mode” stress–strain state. This mechanistic insight helps rationalise the reported sensitivity of the apparent shear response to specimen geometry and boundary conditions, as well as the macroscopic surface strain non-uniformity measured by full-field techniques [64,65]. Importantly, while uniaxial loading may lead to an overestimation of the apparent shear stiffness prior to the apparent yield of the laminates [66] due to inter-ply shear coupling and cut-through-fibre shear, the early damage onset and strain localisation in surface plies indicate a spatial non-uniform and temporal unsynchronised stress development across the laminate thickness. This behaviour can, in turn, result in an underestimation of the ply shear strength at failure [61]. Under HSR loading and extreme temperatures, these uncertainties are expected to be further amplified by rate-dependent [26] and temperature-dependent [50] matrix/interface behaviour, as well as fibre-reorientation effects [19], promoting stronger localisation [67] and inter-ply constraint-driven deviations [61] from a uniform shear state.

It is worth noting that, although the present study quantifies residual displacements and strains, these measurements can still be indicative of *in-situ* deformation processes and the associated stress state during loading. This is particularly relevant for epoxy matrices, which typically exhibit a limited elastic regime under HSR loading and/or low temperatures [68–70]. Under such conditions, localised permanent deformation may develop even when the macroscopic response appears predominantly viscoelastic. This behaviour is driven by pronounced strain localisation and the associated thermal (adiabatic) softening, which can promote irreversible microstructural deformation during loading [71–73].

By superimposing the segmented damage masks with the deviatoric strain fields (Fig. 13), a strong spatial correspondence is observed between the locations of the intra-ply cracks and regions of high strain localisation. Here, the residual strain evaluated in the vicinity of crack tips is used as an indicative measure of the localised deformation retained after unloading. Owing to the limited spatial resolution of the correlation sub-volume and the known challenges of DVC near displacement discontinuities, these values should be interpreted as a conservative proxy for the *in-situ* crack-tip deformation rather than the instantaneous peak strain. Based on five representative cracks, the estimated local residual strain associated with epoxy cracking can reach ~6% or higher, which is plausible given the reported large-strain deformation capacity of epoxy resins under loading [74,75].

4. Conclusion

This study demonstrates the application of DVC to CFRP laminates subjected to HSR loading under room- and low-temperature

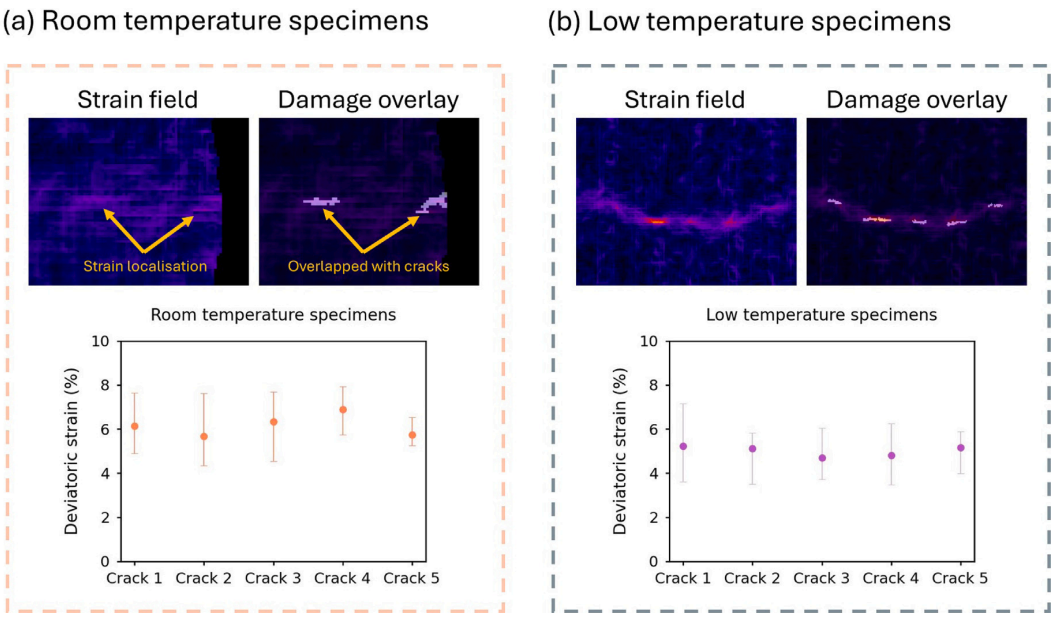


Fig. 13. The correlation of the locations between the shear strain localisation and damage regions at (a) room temperature and (b) low temperatures, demonstrating a good consistency. A statistical measurement of the residual strain at the crack tips was performed to evaluate the microscopic strain of matrix cracking under the loading condition.

conditions. A systematic workflow encompassing image acquisition, pre-processing, registration, and post-processing was established, enabling robust reconstruction of microscopic displacement/strain fields and subsequent micron-scale crack segmentation and quantification. By combining the segmented damage with the measured local kinematics, the evolution and micro-mechanics of damage under the prescribed loading and environmental conditions were characterised.

The results show that fibre and laminate configurations strongly govern the directionality and localisation of microscopic displacement and strain. Localisation becomes more pronounced at higher interrupted strain levels and at lower temperatures. Compared with room-temperature specimens, the low-temperature specimens exhibit an earlier onset of damage and localised deformation, occurring prior to the apparent laminate yield.

Across all specimens, damage locations show a strong spatial correspondence with regions of high local strain. The primary intra-ply cracks along the fibre-direction diagonals are predominantly Mode-II dominated, whereas the discrete intra-ply cracks distributed along the off-fibre-direction diagonals near specimen corners exhibit mixed-mode characteristics. Inter-ply delamination is associated with a comparatively larger volumetric deformation component, indicating a stronger Mode-I contribution, while remaining mixed-mode in nature. Moreover, the inter-ply kinematic constraint and associated shear coupling between adjacent plies with mismatched fibre orientations under off-axis loading were evidenced and quantified under HSR conditions. In combination with spatial non-uniform and asynchronous development of local deformation through the laminate thickness, these findings reveal pronounced through-thickness deformation gradients and systematic departures from the nominal in-plane shear state typically assumed when interpreting uniaxial tests of ±45° laminates. This provides a mechanistic basis for the reported sensitivity of apparent shear response to specimen geometry and boundary conditions, while offering guidance for improved characterisation of CFRP shear properties, particularly under HSR loading and extreme temperature conditions.

CRediT authorship contribution statement

Xiyao Sun: Writing – original draft, Visualization, Validation, Software, Methodology, Investigation, Formal analysis, Data curation, Conceptualization. **Bratislav Lukić:** Writing – review & editing, Software, Resources, Methodology, Data curation, Conceptualization. **Yanhong Chen:** Writing – review & editing, Investigation. **Ziwen Xu:** Writing – review & editing, Investigation. **David Chapman:** Writing – review & editing, Supervision, Methodology, Conceptualization. **Daniel Eakins:** Writing – review & editing, Supervision, Resources, Project administration, Methodology, Funding acquisition, Conceptualization.

Declaration of competing interest

The authors declare the following financial interests/personal relationships which may be considered as potential competing interests: Xiyao Sun, Yanhong Chen, Ziwen Xu reports financial support was provided by Rolls- Royce plc. Bratislav Lukic reports financial support was provided by Engineering and Physical Sciences Research Council. If there are other authors, they declare that they have no known competing financial interests or personal relationships that could have appeared to influence the work reported in this paper.

Acknowledgements

The authors would like to acknowledge Rolls-Royce plc, for their continued support of the University Technology Centre in Solid Mechanics at the University of Oxford. In addition, the authors hereby acknowledge the funding for this research provided by Innovate UK grant 113232: FANDANGO (FAN Design And iNtegrity, GO). B.L. acknowledges funding from the EPSRC, United Kingdom (EP/W003333/1). The ESRF, Grenoble, France, is acknowledged for providing beamtime and assistance. The authors would also like to thank the workshop team at the Advanced Technology Institute, Oxford University Begbroke Science Park, for all the specimens and equipment machining.

Data availability

Data will be made available on request.

References

[1] Calvo JV, Feito N, Giner E. A simplified fatigue characterization of defective CFRP laminates with infrared thermography. Compos Struct 2025;367.
[2] Poggenpohl L, Holthusen H, Simon JW. Failure zone homogenization for modeling damage- and debonding-induced softening in composites including gradient-extended damage at finite strains. Int J Plast 2022;154.
[3] López-Puente J, Zaera R, Navarro C. The effect of low temperatures on the intermediate and high velocity impact response of CFRPs. Compos Part B: Eng 2002;33:559–66.
[4] Chen C, Zhang C, Zhao Z, Wang Y, Wong SC, Li Y. Effect of fiber reinforcement and fabrication process on the dynamic compressive behavior of PEEK composites. Int J Mech Sci 2019;155:170–7.
[5] Zhang Z, Hou S, Mao Y, He L, Han X. Rate-related study on the ply orientation of carbon fiber reinforced epoxy composite laminates. Int J Mech Sci 2020;188.
[6] Kayrıcı M, Taser HH. Experimental investigation of the effect of fabric wrapping method and autoclave curing on the mechanical and thermal degradation of carbon nanotube doped and undoped carbon composite pipes. Polym Compos 2024;45:12885–98.
[7] Özkılıç YO, Madenci E, Safonov A, Gemi L, Yazman S. Comprehensive evaluation of tensile properties, damage mechanisms, and predictive modeling of pultruded GFRP after elevated temperatures. Compos Part B: Eng 2025;304.
[8] Demiral M, Köklü U, Yazman S, Gemi L, Morkavuk S. Unveiling the impact resilience of GFRP and CFRP: A cryogenic exploration through experiment and FE simulation. Compos Part B: Eng 2026;310.
[9] Hamdi K, Moreau G, Aboura Z. Digital image correlation, acoustic emission and in-situ microscopy in order to understand composite compression damage behavior. Compos Struct 2021;258.
[10] Wang Y, Emerson MJ, Conradsen K, Dahl AB, Dahl VA, Maire E, Withers PJ. Evolution of fibre deflection leading to kink-band formation in unidirectional glass fibre/epoxy composite under axial compression. Compos Sci Technol 2021;213:108929.
[11] Bai Y, Vallée T, Keller T. Delamination of pultruded glass fiber-reinforced polymer composites subjected to axial compression. Compos Struct 2009;91:66–73.
[12] Pupurs A, Goutianos S, Brondsted P, Varna J. Interface debond crack growth in tension-tension cyclic loading of single fiber polymer composites. Compos Part A: Appl Sci Manuf 2013;44:86–94.
[13] f. Su Y, y. Zhang T, Sun H, h. Ma L, Zhou W. Cryogenic damage behavior of carbon fiber reinforced polymer composite laminates via fiber-optic acoustic emission. Compos Part A: Appl Sci Manuf 2024;186.
[14] Morkavuk S, Köklü U, Bağcı M, Gemi L. Cryogenic machining of carbon fiber reinforced plastic (CFRP) composites and the effects of cryogenic treatment on tensile properties: A comparative study. Compos Part B: Eng 2018;147:1–11.
[15] Özkılıç YO, Madenci E, Gemi L. Tensile and compressive behaviors of the pultruded GFRP Lamina. Turk J Eng 2020;4:169–75.
[16] Gemi L, Köklü U, Yazman S, Morkavuk S. The effects of stacking sequence on drilling machinability of filament wound hybrid composite pipes: Part-1 mechanical characterization and drilling tests. Compos Part B: Eng 2020;186.
[17] Gemi L, Azeem M, Yazman S, Kayrıcı M, Gök O. Investigation of mechanical properties and damage development of filament wound GFRP composite pipes by ring tensile test. Necmettin Erbakan Üniversitesi Fen ve Mühendislik Bilimleri Dergisi; 2024.
[18] Erhan F, Gemi L, Yazman S, Morkavuk S, Köklü U. A comprehensive investigation into the influence of variation in the stacking sequence on the mechanical behaviour and drilling machinability of basalt fiber-reinforced composite tubes. Compos Part B: Eng 2025;299.
[19] Serna Moreno MC, Horta Muñoz S. Pseudo-ductile effects in ±45° angle-ply CFRP laminates under uniaxial loading: Compression and cyclic tensile test. Compos Part B: Eng 2022;233.
[20] Fuller J, Wisnom MR. Pseudo-ductility and damage suppression in thin ply CFRP angle-ply. Compos: Part A 2015;64–71.
[21] Fiedler B, De Jong C, Hobbiebrunken T, Hojo M, Schulte K. Micro/macro-mechanical approach of first ply failure in CFRP. J Mater Sci 2006;41:6760–7.
[22] Wingate BP, Czabaj MW. In-situ imaging of flexure-induced fracture in tape-laminate composites using high-resolution X-ray computed tomography. Compos Sci Technol 2022;220.
[23] Hou JP, Ruiz C. Measurement of the properties of woven CFRP T300 / 914 at different strain rates. Compos Sci Technol 2000;60:2829–34.
[24] Ivančević D, Ratković J, Giannaros E. Strain rate-dependent failure modelling of impact damage in laminated CFRP structures. Compos Struct 2024;330.
[25] Rodríguez-Sereno JM, Pernas-Sánchez J, Artero-Guerrero JA, López-Puente J. On the importance of strain rate dependence in high velocity impacts of woven CFRP fragments: Experimental and numerical methodology. Int J Impact Eng 2025;198.
[26] Cui H, Thomson D, Pellegrino A, Wiegand J, Petrinic N. Effect of strain rate and fibre rotation on the in-plane shear response of ±45° laminates in tension and compression tests. Compos Sci Technol 2016;135:106–15.
[27] Pournoori N, Corrêa Soares G, Orell O, Palola S, Hokka M, Kanerva M. Adiabatic heating and damage onset in a pultruded glass fiber reinforced composite under compressive loading at different strain rates.. Int J Impact Eng 2021;147.
[28] Song Z, Wang Z, Ma H, Xuan H. Mechanical behavior and failure mode of woven carbon/epoxy laminate composites under dynamic compressive loading. Compos Part B: Eng 2014;60:531–6.
[29] Zhao J, Guo L, Zhang L, Wang X, Tang Y, Li Z. Experimental investigations on the in-plane dynamic compressive behavior and upper limit of constant strain rate for 2D twill weave carbon fiber reinforced composite. Compos Part B: Eng 2021;220.
[30] Yu J, Huang J, Zhang L, Yu S, Guo L, Huang T. Dynamic response and damage mechanisms of 2D plain weave hybrid composites under the out-of-plane punch shear loading. Int J Impact Eng 2025;197.
[31] Liu J, Li Y, Huang M, Zhang Y, Lu Y, Dong L. Prediction of low-velocity impact mechanical response and damage in thermoplastic composites considering elastoplastic behavior. Int J Impact Eng 2024;194.
[32] Zhang N, Zhou G, Guo X, Xuan S, Wei D, Wang X, Cai D. High-velocity impact damage and compression after impact behavior of carbon fiber composite laminates: Experimental study. Int J Impact Eng 2023;181.
[33] Mazzuca P, Firmo JP, Correia JR, Castilho E. Influence of elevated temperatures on the mechanical properties of glass fibre reinforced polymer laminates produced by vacuum infusion. Constr Build Mater 2022;345.
[34] Aklilu G, Adali S, Bright G. Long-term effects of low and high temperatures on the mechanical performance of hybrid FRP composite laminates: Experimental and model assessment. Compos Part C: Open Access 2023;11.
[35] Katafiasz TJ, Greenhalgh ES, Allegri G, Pinho ST, Robinson P. The influence of temperature and moisture on the mode I fracture toughness and associated fracture morphology of a highly toughened aerospace CFRP. Compos Part A: Appl Sci Manuf 2021;142.
[36] Körbelin J, Junge N, Fiedler B. Modelling of low-velocity impact and compression after impact of CFRP at elevated temperatures. Compos Part A: Appl Sci Manuf 2021;147.
[37] Sánchez-Sáez S, Gómez-Del Río T, Barbero E, Zaera R, Navarro C. Static behavior of CFRPs at low temperatures. Compos: Part B 2002;33:383–90.
[38] Li Y, Meng J, Niu G, Yang H, Wang P, Lei H, Fang D. Cryogenic damage mechanisms of CFRP laminates based on in-situ X-ray computed tomography characterization. Compos Sci Technol 2024;247:110413.
[39] Bai Y, Zhao Z, Duan S, Wang P, Li Y, Lei H. Internal shear damage evolution of CFRP laminates ranging from -100 °C to 100 °C using in-situ X-ray computed tomography. Compos Sci Technol 2025;259.
[40] Lee S, Jo E, Ji W. Digital volume correlation technique for characterizing subsurface deformation behavior of a laminated composite. Compos Part B: Eng 2020;194.
[41] Hong S, Yuan Z, Pan D, Kuang C, Dong B, Fan S. Digital-volume-correlation-assisted crack extraction using X-ray computed tomography images of cementitious materials. Cem Concr Compos 2025;158.
[42] Wang Y, Chen Q, Luo Q, Li Q, Sun G. Characterizing damage evolution in fiber reinforced composites using in-situ X-ray computed tomography, deep machine learning and digital volume correlation (DVC). Compos Sci Technol 2024;254.
[43] Kuang C, Ghosh S, Michel A. Enhanced detection of fine damage in composite materials using integrated X-ray computed tomography, digital volume correlation, and U-net. J Build Eng 2024;98.
[44] Mehdikhani M, Breite C, Swolfs Y, Soete J, Wevers M, Lomov SV, Gorbatikh L. Digital volume correlation for meso/micro in-situ damage analysis in carbon fiber reinforced composites. Compos Sci Technol 2021;213.
[45] Zhang H, Yang L, Ren S, Wang K, Li J. In-situ experimental characterization and numerical investigation of the crack initiation of SMC composite under uniaxial tension. Compos Part A: Appl Sci Manuf 2025;188.
[46] Jiang L, Xiong H, Zeng T, Wang J, Xiao S, Yang L. In-situ micro-CT damage analysis of carbon and carbon/glass hybrid laminates under tensile loading by image reconstruction and DVC technology. Compos Part A: Appl Sci Manuf 2024;176.
[47] Pirzada TJ, Liu D, Ell J, Barnard H, Šulák I, Galano M, Marrow TJ, Ritchie RO. In situ observation of the deformation and fracture of an alumina-alumina ceramic-matrix composite at elevated temperature using x-ray computed tomography. J Eur Ceram Soc 2021;41:4217–30.
[48] Léonard F, Stein J, Soutis C, Withers PJ. The quantification of impact damage distribution in composite laminates by analysis of X-ray computed tomograms. Compos Sci Technol 2017;152:139–48.
[49] Bull DJ, Spearing SM, Sinclair I, Helfen L. Three-dimensional assessment of low velocity impact damage in particle toughened composite laminates using micro-focus X-ray computed tomography and synchrotron radiation laminography. Compos Part A: Appl Sci Manuf 2013;52:62–9.
[50] Sun X, Sory D, Liu K, Lukić B, Simonian D, Wong KL, Rack A, Chapman D, Petrinic N, Eakins D. Effect of temperature on high strain-rate damage evolving in CFRP studied by synchrotron-based MHz X-ray phase contrast imaging. Compos Part B: Eng 2024;279.

[51] Sun X, Lukić B, Liu K, Sory D, Lißner M, Hoffmann J, Chapman D, Petrinic N, Eakins D. Role of temperature in the development of micro-scale damage in CFRP laminates through interrupted high-rate loading and synchrotron phase-contrast μ -CT. Compos Part A: Appl Sci Manuf 2026;200:109284.
[52] Reyes LQ, Swan SR, Gan H, Seraji SM, Zhang J, Varley RJ. The role of β relaxations in determining the compressive properties of an epoxy amine network modified with POSS and mono-functional epoxy resins. Polym Test 2021;93.
[53] Bull DJ, Helfen L, Sinclair I, Spearing SM, Baumbach T. A comparison of multi-scale 3D X-ray tomographic inspection techniques for assessing carbon fibre composite impact damage. Compos Sci Technol 2013;75:55–61.
[54] Inc. Comet Technologies Canada. Dragonfly 3D world (version 2025.1). 2025.
[55] Fedorov A, Beichel R, Kalpathy-Cramer J, Finet J, Fillion-Robin JC, Pujol S, Bauer C, Jennings D, Fennessy F, Sonka M, Buatti J, Aylward S, Miller JV, Pieper S, Kikinis R. 3D slicer as an image computing platform for the quantitative imaging network. Magn Reson Imaging 2012;30:1323–41.
[56] Stamati O, Andò E, Roubin E, Cailletaud R, Wiebicke M, Pinzon G, Couture C, Hurley R, Caulk R, Caillerie D, Matsushima T, Bésuelle P, Bertoni F, Arnaud T, Laborin A, Rorato R, Sun Y, Tengattini A, Okubadejo O, Colliat J-B, Saadatfar M, Garcia F, Papazoglou C, Vego I, Brisard S, Dijkstra J, Birmpilis G. Spam: Software for practical analysis of materials. J Open Source Softw 2020;5:2286.
[57] Gurtin ME. An Introduction to Continuum Mechanics. vol. 158, New York: Academic Press; 1981.
[58] Schindelin J, Arganda-Carreras I, Frise E, Kaynig V, Longair M, Pietzsch T, Preibisch S, Rueden C, Saalfeld S, Schmid B, Tinevez JY, White DJ, Hartenstein V, Eliceiri K, Tomancak P, Cardona A. Fiji: An open-source platform for biological-image analysis. 2012.
[59] Ahrens J, Geveci B, Law C. ParaView: An end-user tool for large-data visualization. In: Visualization handbook. Elsevier; 2005, p. 717–31.
[60] Hackett RM. Polar decomposition. Hyperelasticity primer. Cham: Springer International Publishing; 2018, p. 9–18.
[61] ASTM. D3518 - test method for in-plane shear response of polymer matrix composite materials by tensile test of a 45 laminate. West Conshohocken, PA: ASTM; 2018, Technical Report.
[62] Matsuda T, Goto K, Kubota N, Ohno N. Negative through-the-thickness Poisson's ratio of elastic-viscoplastic angle-ply carbon fiber-reinforced plastic laminates: Homogenization analysis. Int J Plast 2014;63:152–69.
[63] Burhan M, Scalici T, Ullah Z, Kazancı Z, Catalanotti G. A three-dimensional finite fracture mechanics model to predict free edge delamination in angle-ply laminates. Eng Fract Mech 2024;306.
[64] Long Y, Qi C, Han R, Guo C, Qiao H, Hao W. Influence of width on the tensile properties of ±45° fiber-reinforced composites using DIC and AE. Mater Des 2026;261.
[65] Merzkirch M, An Q, Forster AM. In-Plane Shear Response of GFRP Laminates by ±45° and 10° Off-axis Tensile Testing using Digital Image Correlation. Gaithersburg: National Institute of Standards and Technology; 2019, Technical Report.
[66] Horta Muñoz S, Serna Moreno MC. Tension–compression biaxial test with ±45° symmetric angle-ply laminates for determining the pure shear response in principal material directions of a lamina. Compos Part B: Eng 2023;261.
[67] Chakraborty A, Roy S. Shear localization and shear banding: A review about the complex interplay between material, microstructural and process variables. 2024.
[68] Griffith JC, Wang S, Palubiski DR, Ramakrishnan KR, Rochat S, Giuliani F, Walls-Bruck M, Hamerton I. Investigating the microcracking behaviour of a commercial epoxy matrix under cryogenic conditions. Compos Part A: Appl Sci Manuf 2025;199.
[69] Buckley CP, Harding J, Hou JP, Ruiz C, Trojanowski A. Deformation of thermosetting resins at impact rates of strain. Part I: Experimental study. J Mech Phys Solids 2001;49:1517–38.
[70] Bhagoria P, Bharadwaj MR, Kumar R, Yadav K, Tiwari V. Mechanical and fracture behaviour of epoxy polymer under extreme low temperature and high strain rate conditions. Int J Adhes Adhes 2025;140.
[71] Xia Z, Shen X, Ellyin F. An assessment of nonlinearly viscoelastic constitutive models for cyclic loading: The effect of a general loading/unloading rule. Mech Time-Depend. Mater 2005;9:281–300.
[72] Starkova O, Buschhorn ST, Mannov E, Schulte K, Aniskevich A. Creep and recovery of epoxy/MWCNT nanocomposites. Compos Part A: Appl Sci Manuf 2012;43:1212–8.
[73] Plazek DJ. The temperature dependence of the viscoelastic behavior of poly(vinyl acetate). Polym J 1980;12:43–53.
[74] Kumar R, Bhagoria P, Bharadwaj MR, Tiwari V. From quasi-static to dynamic: Experimental study of mechanical and fracture behaviour of epoxy resin. Int J Impact Eng 2025;195.
[75] Goldberg RK, Roberts GD. Strain rate sensitivity of epoxy resin in tensile and shear loading. National Aeronautics and Space Administration; 2005, Technical Report.

Chapter 6

Conclusion and outlook

The Earth's environment, long considered stable and familiar, is increasingly at risk as global warming accelerates due to the combined effects of industrial pollution and natural climate variability. The increase in subsequent hazards, such as wildfires, droughts, and sea level rise, is profoundly changing the trajectory of human development in the foreseeable future. Reducing the environmental impact caused by living and industrial activities cannot be further ignored. All sectors and elements in society worldwide need to contribute towards this goal for the sustainable development of civilisation. For transportation industries, especially the aerospace sector, in the absence of a significant energy revolution, the use of lightweight structural materials is deemed to be one of the most effective routes. Reducing the self-weight of the transportation vehicles can directly promote energy efficiency, but at the cost of using previously non-existent, unfamiliar, and unconfident materials, such as artificial composites – CFRP. It is particularly an unparalleled challenge in the aerospace sector owing to the high safety requirements, originating from the nature of low accident rates but catastrophic consequences. To confront this challenge from an engineering and material point of view, the failure mechanisms of CFRP at extreme conditions need to be further investigated to eliminate the redundant over-design. In light of this, the present thesis provides a systematic guideline for the investigation methodology and an in-depth understanding of the damage initiation and evolution mechanisms of CFRP laminates at high strain-rate and extreme temperatures using cutting-edge synchrotron X-ray imaging technologies.

6.1 Research aim, scope, and challenges

The aim of this thesis is to develop a time-resolved experimental framework for investigating multi-scale damage initiation and evolution in CFRP laminates under high-strain-rate loading and varying temperature conditions, and to establish direct links between subsurface

damage mechanisms and the corresponding macroscopic and local mechanical response.

The scope of this research is limited to the experimental investigation of ± 45 ° CFRP laminates subjected to dynamic compression under controlled temperature conditions. The work focuses on *in-situ* and semi-*in-situ* X-ray-based damage characterisation across multiple length scales, and aims to provide mechanistic understanding rather than fully generalised predictive models or comprehensive coverage of all laminate configurations and loading scenarios.

The realisation of this aim is challenged by several factors associated with both the material system and the experimental conditions. Firstly, the anisotropic laminate architecture of CFRP leads to complex and interacting damage mechanisms, which cannot be adequately captured by surface observations or post-mortem analysis alone. Subsurface and time-resolved probing is therefore required to resolve damage initiation and progression.

Secondly, the transient nature of high-strain-rate loading introduces significant experimental constraints. Loading events occur within microseconds and cannot be paused or controlled in the same manner as quasi-static tests, making direct *in-situ* 3D imaging extremely challenging. Existing techniques are often limited either in temporal resolution or spatial resolution, and are therefore unable to capture the full evolution of internal damage.

Finally, the integration of environmental control with dynamic loading and high-resolution imaging presents additional complexity. Temperature control systems must be designed to avoid interference with X-ray propagation, while maintaining stable and representative testing conditions. Addressing these combined challenges requires the development of specialised experimental setups and analysis methodologies, which form the foundation of the present research.

6.2 Methodological contributions and new capabilities

This thesis establishes an integrated experimental and analytical framework for a time-resolved characterisation of multi-scale damage in CFRP laminates under high-strain-rate loading and varying temperature conditions. The methodological contributions can be summarised in terms of three key capabilities.

An experimentation and analysis framework for CFRP that synchronises high-strain-rate loading, synchrotron XPCI, and temperature control was developed, enabling *in-situ*

observation and characterisation of subsurface damage evolution at the meso-scale. By integrating SHPB-based loading with high-speed X-ray imaging and precise signal synchronisation, this approach allows direct temporal correlation between damage evolution and global stress-strain response, which is not accessible using conventional post-mortem techniques.

An experimental methodology combining strain-interrupted loading with synchrotron phase-contrast µ-CT was established to extend damage characterisation to the micro-scale. This approach overcomes the limitation that high-strain-rate loading cannot be paused for full-field imaging, by preserving representative damage states at selected strain levels. It enables 3D reconstruction of internal damage morphology and provides detailed spatial information on damage distribution and evolution.

A DVC-based workflow was developed for quantifying local displacement and strain fields at the micron scale. By leveraging the intrinsic microstructural features of CFRP laminates, the approach enables robust image registration and full-field strain measurement, allowing the direct linkage between microscopic strain localisation and damage initiation. This represents a transition from purely morphological characterisation to mechanically informed damage analysis.

Together, these methodological developments advance the field from post-mortem and predominantly surface-based observations towards a time-resolved, process-oriented, and cross-scale investigation of damage in CFRP laminates. The framework provides a transferable methodology for studying complex composite damage under extreme thermomechanical conditions.

6.3 Integrated multi-scale mechanistic conclusions

The combined experimental and analytical approaches developed in this thesis enable a unified and cross-scale understanding of damage initiation and evolution in $\pm 45\,^{\circ}$ CFRP laminates under high-strain-rate loading and varying temperature conditions. The key mechanistic findings can be synthesised into a consistent damage evolution framework linking meso-, micro-, and micron-scale observations.

Damage initiation across all investigated length scales is dominated by matrix-controlled mechanisms, primarily in the form of intra-ply cracking aligned with fibre directions. At the meso-scale, such cracking is initially observed at surface plies due to reduced lateral con-

straint, while micro- and micron-scale analyses reveal that similar damage can simultaneously initiate within subsurface plies, especially at low temperatures. The DVC-derived strain fields further demonstrate that these cracks are closely associated with inter-fibre shear localisation, indicating the governing damage modes.

The transition from distributed intra-ply cracking to inter-ply delamination represents a critical stage in damage evolution. Across all scales, delamination is consistently observed to initiate from the edges of intra-ply cracks and propagate along ply interfaces. This transition coincides with the rapid loss of load-bearing capacity in the global stress-strain response, establishing a direct link between specific damage mechanisms and macroscopic mechanical behaviour. This finding provides strong experimental evidence that delamination, rather than fibre failure and in-plane cracking, governs the collapse of $\pm 45\,^{\circ}$ laminates under high-strain-rate compression.

Temperature is found not to influence the fundamental sequence of damage mechanisms, but the temporal progression and spatial distribution of damage. At low temperatures, damage initiates earlier and evolves more rapidly, with a more discrete and brittle damage pattern. In contrast, room-temperature specimens exhibit more expanded and interconnected damage, leading to gradual stress degradation and the presence of a post-peak plateau. This demonstrates that temperature primarily affects the kinetics of damage evolution and the balance between brittle and ductile-like responses. Importantly, the integration of XPCI, interrupted µ-CT, and DVC analyses reveals a consistent correspondence between damage morphology and local strain fields. The agreement between independently observed damage features and strain localisation patterns provides direct evidence linking microstructural damage processes to the underlying mechanical driving forces. This establishes a mechanistically informed interpretation of damage evolution, rather than based solely on post-mortem morphology.

Overall, this work advances the understanding of damage in CFRP laminates from isolated observations at individual scales to a coherent, time-resolved, and physically grounded description of damage evolution across multiple length scales. It provides a framework for interpreting the interaction between strain localisation, damage initiation, and global mechanical response under extreme thermomechanical conditions.

6.4 Limitations

Despite the advances achieved in this thesis, several limitations should be acknowledged. First, the present study focuses on a specific material system, namely ± 45 ° CFRP laminates under high-strain-rate axial compression. While this configuration is well-suited for investigating shear-dominated damage mechanisms, the findings cannot be directly generalised to other laminate architectures, material systems, or loading configurations, such as tensile, bending, or impact-dominated conditions.

In addition, the experimental observations are constrained by the capabilities of the employed imaging techniques. The *in-situ* XPCI approach provides time-resolved information but is limited to 2D projection imaging, whereas the synchrotron µ-CT analysis offers 3D structural information but is restricted to interrupted (post-loading) states. As a result, fully time-resolved 3D characterisation of damage evolution under high-strain-rate loading remains unattainable with current synchrotron imaging capabilities.

The quantification of damage based on X-ray CT is inherently limited by spatial resolution and contrast. Only opened damage (i.e., void-like features) can be reliably detected and segmented at late loading stages, while other forms of damage, such as micro-cracking and fibre-matrix debonding in largely deformed specimens, may remain unresolved. Consequently, the reported damage volume represents the measurable portion of damage and is more suitable for comparative analysis than as an absolute measure of total damage.

Furthermore, the DVC-based strain analysis is subject to uncertainties associated with image resolution, registration accuracy, and segmentation procedures. Although the use of DVC enables the identification of strain localisation and its correlation with damage initiation, the accuracy of segmented damage volume is influenced by imaging quality and the lack of a definitive ground truth.

Finally, due to the experimental complexity of high-strain-rate synchrotron-based testing, the number of repeat experiments is limited. The results presented in this thesis, therefore, emphasise mechanistic understanding and trend identification rather than statistical generalisation. These limitations define the scope of the present work and provide the basis for the future research directions outlined in the following section.

6.5 Future work

Building upon the limitations identified in the present study, several directions for future research are proposed to further advance the understanding of damage mechanisms in CFRP laminates. Firstly, the present work is limited to $\pm 45\,^{\circ}$ laminates under high-strain-rate compression. Future studies should extend the developed experimental framework to a wider range of laminate configurations, including UD, CP, and QI laminates, as well as different loading modes such as tension, bending, torsion and other impacts. This would enable a more comprehensive understanding of damage mechanisms across different stress states and structural applications.

Apart from that, a key limitation of the current approach lies in the separation between time-resolved 2D imaging and 3D post-mortem characterisation. Future work should focus on the development of fully time-resolved 3D imaging techniques, for example, through ultrafast tomography or advanced reconstruction algorithms, to directly capture the evolution of damage in 3D during high-strain-rate loading.

Improvements in spatial resolution and damage quantification methods are required to better resolve fine-scale damage mechanisms. The integration of higher-resolution imaging, machine-learning-based segmentation, and uncertainty quantification techniques would enable more reliable identification of micro-cracks, fibre-matrix debonding, and other sub-resolution damage features.

Furthermore, the robustness of DVC-based strain analysis can be enhanced by developing improved correlation algorithms, multi-scale registration strategies, and systematic uncertainty assessment frameworks. This would allow more accurate quantification of local strain fields and strengthen the link between strain localisation and damage initiation.

In addition, increasing the number of repeat experiments and incorporating statistical analysis would improve the reliability and generalisability of the observed trends. This is particularly important for capturing variability in composite materials and validating mechanistic interpretations.

Beyond experimental developments, the integration of the present multi-scale experimental data with numerical modelling represents an important direction for future work. The obtained datasets provide valuable physical benchmarks for validating and calibrating multi-scale modelling approaches, particularly those based on representative volume elements (RVEs) and hierarchical modelling frameworks. This integration would enable more accu-

rate prediction of damage initiation and evolution under complex loading and environmental conditions.

Lastly, the experimental and analytical framework developed in this thesis is transferable to a broader range of composite systems and environmental conditions. Future research may extend this approach to other material systems, including woven composites, hybrid laminates, and ceramic matrix composites, as well as to more complex environmental conditions such as combined temperature, moisture, and fatigue loading. Such studies would contribute to a more comprehensive understanding of composite behaviour in real engineering applications.

6.6 Concluding remarks

In conclusion, this thesis advances the investigation of damage in CFRP laminates under high-strain-rate loading and varying temperature conditions from post-mortem observations towards a time-resolved, process-oriented, and multi-scale understanding. By integrating synchrotron-based X-ray imaging techniques with tailored experimental and analytical methodologies, the work establishes a direct linkage between subsurface damage evolution and mechanical response, providing new insights into the mechanisms governing composite failure under extreme thermomechanical conditions.

Beyond the specific findings, this research demonstrates the potential of combining advanced imaging and data analysis techniques to overcome long-standing experimental limitations in high-rate composite testing and temperature control. The developed framework not only enhances mechanistic understanding but also provides a foundation for future integration with predictive modelling approaches. It is expected that such experimentally informed multi-scale methodologies will contribute to more reliable design and reduced conservatism in the use of composite materials in demanding engineering applications.

Bibliography

[1] Mar-Bal Incorporated, “History of composite materials,” 2022. [Online]. Available: https://www.mar-bal.com/applications/history-of-composites

[2] J. Hale, “Boeing 787 from the ground up,” *AERO*, no. 24, pp. 17–23, 2006.

[3] J. Segui, “Protecting aircraft composites from lightning strike damage,” *COMSOL Blog*, 6 2015. [Online]. Available: https://www.comsol.com/blogs/protecting-aircraft-composites-from-lightning-strike-damage

[4] D. Blanco, E. M. Rubio, R. Lorente, and M. A. Sáenz-Nuño, “Lightweight structural materials in open access: Latest trends,” *Materials*, vol. 14, no. 21, 11 2021.

[5] Rolls-Royce, “Future products,” 2022. [Online]. Available: https://www.rolls-royce.com/innovation/ultrafan.aspx

[6] R. G. Boeman and N. L. Johnson, “Development of a cost competitive, composite intensive, body-in-white,” Society of Automotive Engineers, Tech. Rep., 2002.

[7] D. Lang and D. W. Radford, “Cost, draping, material and partitioning optimization of a composite rail vehicle structure,” *Materials*, vol. 15, no. 2, 1 2022.

[8] C. Yang, Y. Gao, W. Guo, Y. Yang, P. Xu, and M. S. Alqahtani, “High-velocity impact behaviour of curved GFRP composites for rail vehicles: Experimental and numerical study,” *Polymer Testing*, vol. 116, 12 2022.

[9] A. Ulbricht, F. Zeidler, F. Bilkenroth, and S. Soltysiak, “Structural lightweight components for energy-efficient rail vehicles using high performance composite materials,” in *Transportation Research Procedia*, vol. 72. Elsevier B.V., 2023, pp. 1685–1692.

[10] A. J. Sobey, J. I. Blake, and R. A. Shenoi, “Optimisation of composite boat hulls using first principles and design rules,” *Ocean Engineering*, vol. 65, pp. 62–70, 2013.

[11] A. Mouritz, E. Gellert, P. Burchill, and K. Challis, “Review of advanced composite structures for naval ships and submarines,” *Composite Structures*, vol. 53, no. 1, pp. 21–42, 7 2001.

[12] R. A. Shenoi and F. L. M. Violette, “A study of structural composite tee joints in small boats,” *Journal of Composite Materials*, vol. 24, pp. 644–666, 1989.

[13] M. A. Seif, U. A. Khashaba, and R. Rojas-oviedo, “Residual stress measurements in CFRE and GFRE composite missile shells,” *Composite Structures*, vol. 79, no. 2, pp. 261–269, 7 2007.

[14] J. Esslinger, R. Evans, and G. Snyder, “Design of high performance missile structures utilizing advanced composite material technologies,” in *Proceedings of the Second International Conference on Intelligent Processing and Manufacturing of Materials*. IEEE, 1999, pp. 331–337. [Online]. Available: http://ieeexplore.ieee.org/document/792503/

[15] J. C. Bruhl, A. H. Varma, and W. H. Johnson, “Design of composite SC walls to prevent perforation from missile impact,” *International Journal of Impact Engineering*, vol. 75, pp. 75–87, 2015.

[16] J. W. Lim and D. G. Lee, “Development of the hybrid insert for composite sandwich satellite structures,” *Composites Part A: Applied Science and Manufacturing*, vol. 42, no. 8, pp. 1040–1048, 8 2011.

[17] H. Bansemir and O. Haider, “Fibre composite structures for space applications-recent and future developments,” *Cryogenics*, vol. 38, no. 1, pp. 51–59, 1998.

[18] D. Zhengchun, Z. Mengrui, W. Zhiguo, and Y. Jianguo, “Design and application of composite platform with extreme low thermal deformation for satellite,” *Composite Structures*, vol. 152, pp. 693–703, 2016.

[19] Y. Zhang, Y. Su, F. Chen, and K. Yang, “Axial compressive test and a new stress-strain model of CFRP-confined damaged high-strength concrete,” *Construction and Building Materials*, vol. 490, p. 142476, 9 2025.

[20] P. Ayough, W. Zeng, Y.-H. Wang, E. Rasa, Y.-T. Peng, M. Su, A. Y. Elghazouli, and M. Elchalakani, “Experimental assessment of CFST beam-columns strengthened with CFRP grid-reinforced ultra-high-strength engineered cementitious composites,” *Construction and Building Materials*, vol. 475, p. 141204, 5 2025.

[21] X. Wang, Z. Zhang, and P. Zhuge, “Transient analysis of a novel full submersible floating offshore wind turbine with CFRP tendons,” *Ocean Engineering*, vol. 266, p. 112686, 12 2022.

[22] E. Greenhalgh and M. Hiley, “The assessment of novel materials and processes for the impact tolerant design of stiffened composite aerospace structures,” *Composites Part A: Applied Science and Manufacturing*, vol. 34, no. 2, pp. 151–161, 2 2003.

[23] G. Balaganesan and V. Chandra Khan, “Energy absorption of repaired composite laminates subjected to impact loading,” *Composites Part B: Engineering*, vol. 98, pp. 39–48, 8 2016.

[24] U. A. Khashaba, R. Othman, and I. M. Najjar, “Development and characterization of structural adhesives for aerospace industry with alumina nanoparticles under shear and thermo-mechanical impact loads,” *Proceedings of the Institution of Mechanical Engineers, Part G: Journal of Aerospace Engineering*, vol. 234, no. 2, pp. 490–507, 2 2020.

[25] C. Zhang, G. Lu, and T. Suo, “Impact Dynamics for Advanced Aerospace Materials and Structures,” *Journal of Aerospace Engineering*, vol. 36, no. 4, 7 2023.

[26] Y. Karsandik, B. Sabuncuoglu, B. Yildirim, and V. V. Silberschmidt, “Impact behavior of sandwich composites for aviation applications: A review,” *Composite Structures*, vol. 314, 6 2023.

[27] C. Reuter, K. H. Sauerland, and T. Tröster, “Experimental and numerical crushing analysis of circular CFRP tubes under axial impact loading,” *Composite Structures*, vol. 174, pp. 33–44, 8 2017.

[28] J. J. Andrew and H. N. Dhakal, “Sustainable biobased composites for advanced applications: recent trends and future opportunities – A critical review,” *Composites Part C: Open Access*, vol. 7, 3 2022.

[29] A. H. Davies, “The development and use of glass fibres,” *Journal of the Royal Society of Arts*, vol. 105, no. 5002, pp. 437–455, 1957. [Online]. Available: http://www.jstor.org/stable/41366061

[30] P. Mallick, *Fiber-Reinforced Composites*, 3rd ed., P. Mallick, Ed. Boca Raton: CRC Press, 11 2007. [Online]. Available: https://www.taylorfrancis.com/books/9781420005981

[31] A. A. Griffith, “VI. The phenomena of rupture and flow in solids,” *Philosophical Transactions of the Royal Society of London. Series A, Containing Papers of a Mathematical or Physical Character*, vol. 221, no. 582-593, pp. 163–198, 1 1921. [Online]. Available: https://royalsocietypublishing.org/rsta/article/221/582-593/163/44073/VI-The-phenomena-of-rupture-and-flow-in-solids

[32] B. A. Newcomb, “Processing, structure, and properties of carbon fibers,” *Composites Part A: Applied Science and Manufacturing*, vol. 91, pp. 262–282, 12 2016.

[33] R. F. Gibson, *Principles of Composite Material Mechanics*, 4th ed. Florida: CRC Press, 2 2016, no. 8.5.2017. [Online]. Available: https://www.taylorfrancis.com/books/9781498720724

[34] D. Hull and T. W. Clyne, *An Introduction to Composite Materials*. Cambridge University Press, 8 1996. [Online]. Available: https://www.cambridge.org/core/product/identifier/9781139170130/type/book

[35] R. M. Jones, *Mechanics of Composite Materials*. CRC Press, 10 2018. [Online]. Available: https://www.taylorfrancis.com/books/9781498711067

[36] D. Gay, S. V. Hoa, and S. W. Tsai, *Composite Materials*. CRC Press, 12 2002. [Online]. Available: https://www.taylorfrancis.com/books/9781420031683

[37] J. Zhang, G. Lin, U. Vaidya, and H. Wang, “Past, present and future prospective of global carbon fibre composite developments and applications,” *Composites Part B: Engineering*, vol. 250, 2 2023.

[38] V. L. Tiemann, “CFRP Laminate Structure,” 6 2021. [Online]. Available: https://www.swms.de/caesa/cfrp-laminate-structure/#chfy-coo-check-save

[39] J. Cheng, H. Ji, J. Qiu, T. Takagi, T. Uchimoto, and N. Hu, “Novel electromagnetic modeling approach of carbon fiber-reinforced polymer laminate for calculation of eddy currents and eddy current testing signals,” *Journal of Composite Materials*, vol. 49, no. 5, pp. 617–631, 3 2015.

[40] A. M. Pawlak, T. Górny, L. Dopierała, and P. Paczos, “The use of CFRP for structural reinforcement - literature review,” *Metals*, vol. 12, no. 9, 9 2022.

[41] A. Odeh, M. A. Al-Shugaa, H. J. Al-Gahtani, and F. Mukhtar, “Analysis of laminated composite plates: A comprehensive bibliometric review,” *Buildings*, vol. 14, no. 6, p. 1574, 5 2024.

[42] M. R. Zakaria, F. N. A. M. Sabri, and H. M. Akil, “Advanced hybrid fiber-reinforced composites for high material performance,” in *Composite Materials: Manufacturing, Properties and Applications*, I.-M. Low and Y. Dong, Eds. San Diego: Elsevier Ltd., 2021, pp. 53–64. [Online]. Available: http://dx.doi.org/10.1016/B978-0-12-820512-9.00022-8

[43] S. J. Lewis, “The use of carbon fibre composites on military aircraft,” *Composites Manufacturing*, vol. 5, no. 2, pp. 95–103, 1994.

[44] S. Chand, “Carbon fibers for composites,” *Journal of Materials Science*, vol. 35, no. 6, pp. 1303–1313, 2000.

[45] A. P. Mouritz, “Manufacturing of fibre-polymer composite materials,” in *Introduction to Aerospace Materials*, Adrian P. Mouritz, Ed. Cambridge, UK: Elsevier, 2012, pp. 303–337. [Online]. Available: https://linkinghub.elsevier.com/retrieve/pii/B9781855739468500145

[46] D. Pinheiro, O. Longo, G. Nascimento, and G. Couri, “Use of composite materials in carbon fiber for the recovery of small slab – calculation by analytical and computational methods,” *International Journal of Composite Materials*, vol. 7, no. 1, pp. 1–7, 2017.

[47] C. W. Weaver and J. G. Williams, “Deformation of a carbon-epoxy composite under hydrostatic pressure,” *Journal of Materials Science*, vol. 10, no. 8, pp. 1323–1333, 1975.

[48] H. Wang, X. Zhang, Y. Duan, and L. Meng, “Experimental and numerical study of the interfacial shear strength in carbon fiber/epoxy resin composite under thermal loads,” *International Journal of Polymer Science*, vol. 2018, pp. 1–8, 2018.

[49] X. Zhang, Y. Shi, and Z. X. Li, “Experimental study on the tensile behavior of unidirectional and plain weave CFRP laminates under different strain rates,” *Composites Part B: Engineering*, vol. 164, no. June 2018, pp. 524–536, 2019.

[50] B. Wang, B. He, Z. Wang, S. Qi, D. Zhang, G. Tian, and D. Wu, “Enhanced impact properties of hybrid composites reinforced by carbon fiber and polyimide fiber,” *Polymers*, vol. 13, no. 16, 8 2021.

[51] T. K. Kim, J. S. Park, S. H. Kim, and W. T. Jung, “Structural behavior evaluation of reinforced concrete using the fiber-reinforced polymer strengthening method,” *Polymers*, vol. 13, no. 5, pp. 1–18, 3 2021.

[52] S. Ranabhat, “Delta Boeing 767 heavily damaged by hail storm,” 7 2023. [Online]. Available: https://samchui.com/2023/07/24/delta-boeing-767-heavily-damaged-by-hail-storm/

[53] P. Amalaraj, “Terrifying pictures show huge damage to front of Airbus which was hit by a bird strike after taking off from Spanish airport,” 8 2025. [Online]. Available: https://www.msn.com/en-in/news/world/terrifying-pictures-show-huge-damage-to-front-of-airbus-struck-by-bird-after-taking/-off-from-spain/ar-AA1JPMNs?apiversion=v2&domshim=1&noservercache=1&noservertelemetry=1&batchservertelemetry=1&renderwebcomponents=1&wcseo=1

[54] Plenumchamber, “JT8D engine after bird strike,” 7 2007. [Online]. Available: https://commons.wikimedia.org/wiki/File:JT8D_Engine_after_Bird_Strike.jpg

[55] ASTM International, “D3410/D3410M − Test Method for Compressive Properties of Polymer Matrix Composite Materials with Unsupported Gage Section by Shear Loading,” West Conshohocken, PA, Tech. Rep. 3, 2003. [Online]. Available: https://store.astm.org/d3410_d3410m-16e01.html

[56] R. T. Durai Prabhakaran, G. A. Ormondroyd, and G. Zhongwei, “Flax/epoxy composite beams - Simulation of flexural stresses,” *Materials Today: Proceedings*, vol. 8, pp. 760–768, 2019.

[57] J. Wen, Z. Xia, and F. Choy, “Damage detection of carbon fiber reinforced polymer composites via electrical resistance measurement,” *Composites Part B: Engineering*, vol. 42, no. 1, pp. 77–86, 1 2011.

[58] A. E. Coronado Mondragon, C. E. Coronado Mondragon, P. J. Hogg, and N. Rodríguez-López, “A design process for the adoption of composite materials and supply chain reconfiguration supported by a software tool,” *Computers and Industrial Engineering*, vol. 121, pp. 62–72, 7 2018.

[59] M. Bazli, H. Ashrafi, A. Jafari, X. L. Zhao, R. K. Singh Raman, and Y. Bai, “Effect of fibers configuration and thickness on tensile behavior of GFRP laminates exposed to harsh environment,” *Polymers*, vol. 11, no. 9, 2019.

[60] S. M. Zaharia, C. O. Morariu, A. Nedelcu, and M. A. Pop, “Experimental study of static and fatigue behavior of CFRP-balsa sandwiches under three-point flexural loading,” *BioResources*, vol. 12, no. 2, pp. 2673–2689, 5 2017.

[61] T. Zhao, J. Yang, J. Chen, and S. Guan, “Review of carbon fiber-reinforced sandwich structures,” *Polymers and Polymer Composites*, vol. 30, pp. 1–17, 2022.

[62] B. He, B. Wang, Z. Wang, S. Qi, G. Tian, and D. Wu, “Mechanical properties of hybrid composites reinforced by carbon fiber and high-strength and high-modulus polyimide fiber,” *Polymer*, vol. 204, 9 2020.

[63] N. Bouhfid, M. Raji, R. Boujmal, H. Essabir, M.-O. Bensalah, R. Bouhfid, and A. e. k. Qaiss, “Numerical modeling of hybrid composite materials,” in *Modelling of Damage Processes in Biocomposites, Fibre-Reinforced Composites and Hybrid Composites*. Elsevier, 2019, pp. 57–101. [Online]. Available: https://linkinghub.elsevier.com/retrieve/pii/B9780081022894000059

[64] J. Zhang, K. Chaisombat, S. He, and C. H. Wang, “Hybrid composite laminates reinforced with glass/carbon woven fabrics for lightweight load bearing structures,” *Materials and Design*, vol. 36, pp. 75–80, 2012.

[65] S. Ekşi and K. Genel, “Comparison of mechanical properties of unidirectional and woven carbon, glass and aramid fiber reinforced epoxy composites,” *Acta Physica Polonica A*, vol. 132, no. 3, pp. 879–882, 2017.

[66] G. Yamamoto, K. Koizumi, and T. Okabe, “Tensile strength of unidirectional carbon fiber-reinforced plastic composites,” in *Strength of Materials*, H. Jaramillo S., J. Arnaldo Avila, and C. Chen, Eds. IntechOpen, 3 2020, p. 13. [Online]. Available: https://www.intechopen.com/books/strength-of-materials/tensile-strength-of-unidirectional-carbon-fiber-reinforced-plastic-composites

[67] H. Hamada, N. Oya, K. Yamashita, and Z. I. Maekawa, “Tensile strength and its scatter of unidirectional carbon fibre reinforced composites,” *Journal of Reinforced Plastics and Composites*, vol. 16, no. 2, pp. 119–130, 1 1997. [Online]. Available: https://journals.sagepub.com/doi/10.1177/073168449701600202

[68] L. Wang, K. Kawaguchi, J. Xu, and Q. Han, “Effects of transverse constraints on the longitudinal compressive strength of unidirectional CFRP pultruded plates and rods,” *Composite Structures*, vol. 207, pp. 740–751, 1 2019.

[69] D. D. Chung, “Polymer-matrix composites,” in *Carbon Fiber Composites*, D. D. Chung, Ed. Newton, MA: Elsevier, 1994, ch. 6, pp. 85–123. [Online]. Available: https://linkinghub.elsevier.com/retrieve/pii/B9780080500737500105

[70] P. Alam, D. Mamalis, C. Robert, C. Floreani, and C. M. Ó Brádaigh, “The fatigue of carbon fibre reinforced plastics - A review,” *Composites Part B: Engineering*, vol. 166, pp. 555–579, 6 2019.

[71] F. Al-Mahmoud, A. Castel, and R. François, “Modelling of flexural behaviour of RC beams strengthened with NSM CFRP rods including serviceability,” *European Journal of Environmental and Civil Engineering*, vol. 17, no. 7, pp. 532–553, 7 2013.

[72] M. Fuwa, A. R. Bunsell, and B. Harris, “Tensile failure mechanisms in carbon fibre reinforced plastics,” *Journal of Materials Science*, vol. 10, no. 12, pp. 2062–2070, 1975.

[73] S. K. Gopalraj and T. Kärki, “A finite element study to investigate the mechanical behaviour of unidirectional recycled carbon fibre/glass fibre–reinforced epoxy composites,” *Polymers*, vol. 13, no. 18, 2021.

[74] C. C. Chamis, “Micromechanics strength theories,” The National Aeronautics and Space Administration, Cleveland, Tech. Rep., 1974. [Online]. Available: https://ntrs.nasa.gov/citations/19750040810

[75] F. L. Matthews, “Compression,” in *Mechanical Testing of Advanced Fibre Composites*, J. Hodgkinson, Ed. Cambridge: Woodhead Publishing, 2000, pp. 75–99. [Online]. Available: https://fliphtml5.com/zurx/bxho/basic

[76] N. Geier, “Influence of fibre orientation on cutting force in up and down milling of UD-CFRP composites,” *International Journal of Advanced Manufacturing Technology*, vol. 111, no. 3-4, pp. 881–893, 2020.

[77] J. Brunbauer and G. Pinter, “Effects of mean stress and fibre volume content on the fatigue-induced damage mechanisms in CFRP,” *International Journal of Fatigue*, vol. 75, pp. 28–38, 2015.

[78] Y. Wang, S. C. Garcea, and P. J. Withers, “Computed tomography of composites,” *Comprehensive Composite Materials II*, vol. 7, pp. 101–118, 2017.

[79] Y. Wang, T. L. Burnett, Y. Chai, C. Soutis, P. J. Hogg, and P. J. Withers, “X-ray computed tomography study of kink bands in unidirectional composites,” *Composite Structures*, vol. 160, pp. 917–924, 2017.

[80] L. A. Feldkamp, L. C. Davis, and J. W. Kress, “Practical cone-beam algorithm,” *Journal of the Optical Society of America A*, vol. 1, no. 6, p. 612, 6 1984. [Online]. Available: https://opg.optica.org/abstract.cfm?URI=josaa-1-6-612

[81] J. Hapke, F. Gehrig, N. Huber, K. Schulte, and E. T. Lilleodden, “Compressive failure of UD-CFRP containing void defects: In situ SEM microanalysis,” *Composites Science and Technology*, vol. 71, no. 9, pp. 1242–1249, 2011.

[82] C. A. Volkert and A. M. Minor, “Focused Ion Beam Micromachining,” *MRS Bulletin*, vol. 32, no. May, pp. 389–399, 2007.

[83] J. A. Taillon, C. Pellegrinelli, Y. L. Huang, E. D. Wachsman, and L. G. Salamanca-Riba, “Improving microstructural quantification in FIB/SEM nanotomography,” *Ultramicroscopy*, vol. 184, pp. 24–38, 2018.

[84] Y. Wang, M. J. Emerson, K. Conradsen, A. B. Dahl, V. A. Dahl, E. Maire, and P. J. Withers, “Evolution of fibre deflection leading to kink-band formation in unidirectional glass fibre/epoxy composite under axial compression,” *Composites Science and Technology*, vol. 213, no. 3, p. 108929, 9 2021.

[85] M. R. Piggott and B. Harris, “Compression strength of carbon, glass and Kevlar-49 fibre reinforced polyester resins,” *Journal of Materials Science*, vol. 15, no. 10, pp. 2523–2538, 1980.

[86] E. Maire, C. Le Bourlot, J. Adrien, A. Mortensen, and R. Mokso, “20 Hz X-ray tomography during an in situ tensile test,” *International Journal of Fracture*, vol. 200, no. 1-2, pp. 3–12, 2016.

[87] M. J. Emerson, A. B. Dahl, K. Conradsen, and V. A. Dahl, “Insegt fibre: A user-friendly software for individual fibre segmentation,” in *ICCM International Conferences on Composite Materials*, vol. 2019-Augus, 2019. [Online]. Available: https://backend.orbit.dtu.dk/ws/portalfiles/portal/190197001/ICCM22_Full_Paper_Submission_monj.pdf

[88] E. W. Godwin, “Tension,” in *Mechanical Testing of Advanced Fibre Composites*, J. Hodgkinson, Ed. Cambridge: Woodhead Publishing, 2000. [Online]. Available: https://fliphtml5.com/zurx/bxho/basic

[89] ASTM International, “D3039/D3039M — Test Method for Tensile Properties of Polymer Matrix Composite Materials,” American Society for Testing and Materials, West Conshohocken, PA, Tech. Rep. 3, 9 2008. [Online]. Available: http://www.astm.org/cgi-bin/resolver.cgi?D3039D3039M-08

[90] K. Majerski, B. Surowska, J. Bienias, P. Jakubczak, and M. Ostapiuk, “Experimental investigation on the influence of fibers orientation on the failure of carbon hybrid laminates,” *Aircraft Engineering and Aerospace Technology*, vol. 86, no. 4, pp. 307–311, 2014.

[91] Q. Sun, Z. Meng, G. Zhou, S. P. Lin, H. Kang, S. Keten, H. Guo, and X. Su, “Multi-scale computational analysis of unidirectional carbon fiber reinforced polymer composites under various loading conditions,” *Composite Structures*, vol. 196, no. March, pp. 30–43, 2018.

[92] BS, “ISO 527-5 – Plastics – Determination of tensile properties: Part 5: Test conditions for unidirectional fibre-reinforced plastic composites,” British Standards, Tech. Rep., 2009. [Online]. Available: https://www.iso.org/standard/52991.html

[93] W. Chen, Y. Liu, Z. Jiang, L. Tang, Z. Liu, and L. Zhou, “Modeling of compressive strength for unidirectional fiber reinforced composites with nanoparticle modified epoxy matrix,” *Materials*, vol. 12, no. 23, 2019.

[94] M. H. Ikbal, A. Ahmed, W. Qingtao, Z. Shuai, and L. Wei, “Hybrid composites made of unidirectional T600S carbon and E-glass fabrics under quasi-static loading,” *Journal of Industrial Textiles*, vol. 46, no. 7, pp. 1511–1535, 2017.

[95] ASTM International, “D695 − Test Method for Compressive Properties of Rigid Plastics,” American Society for Testing and Materials, West Conshohocken, PA, Tech. Rep., 1 2026. [Online]. Available: https://store.astm.org/d0695-26.html

[96] ——, “D6641/D6641M −Test Method for Compressive Properties of Polymer Matrix Composite Materials Using a Combined Loading Compression (CLC) Test Fixture,” American Society for Testing and Materials, West Conshohocken, PA, Tech. Rep., 11 2009. [Online]. Available: https://store.astm.org/d6641_d6641m-16e02.html

[97] ISO, “ISO 14126 − Fibre-reinforced plastic composites − Determination of compressive properties in the in-plane direction Composites,” International Organization for Standardization, Tech. Rep., 1999. [Online]. Available: https://www.iso.org/standard/80371.html

[98] H. Cui, D. Thomson, A. Pellegrino, J. Wiegand, and N. Petrinic, “Effect of strain rate and fibre rotation on the in-plane shear response of ±45° laminates in tension and compression tests,” *Composites Science and Technology*, vol. 135, pp. 106–115, 2016.

[99] F. Weng, Y. Fang, M. Ren, J. Sun, and L. Feng, “Effect of high strain rate on shear properties of carbon fiber reinforced composites,” *Composites Science and Technology*, vol. 203, p. 108599, 2 2021.

[100] D. Thomson, G. Quino, H. Cui, A. Pellegrino, B. Erice, and N. Petrinic, “Strain-rate and off-axis loading effects on the fibre compression strength of CFRP laminates: Experiments and constitutive modelling,” *Composites Science and Technology*, vol. 195, 7 2020.

[101] ASTM International, “D3518/D3518M — Test Method for In-Plane Shear Response of Polymer Matrix Composite Materials by Tensile Test of a 45° Laminate,” American

Society for Testing and Materials, West Conshohocken, PA, Tech. Rep., 11 2018. [Online]. Available: https://store.astm.org/d3518_d3518m-18.html

[102] ISO, "ISO 14129 — Fibre-reinforced plastic composites — Determination of the in-plane shear stress/ shear strain response, including the in-plane shear modulus and strength, by the ± 45° tension test method," International Organization for Standardization, Tech. Rep., 12 1997. [Online]. Available: https://www.iso.org/standard/23641.html

[103] J. P. Hou and C. Ruiz, "Measurement of the properties of woven CFRP T300 / 914 at different strain rates," *Composites Science and Technology*, vol. 60, pp. 2829–2834, 2000.

[104] Q. G. Wu, Q. K. Wang, L. Zu, Y. X. Wu, Q. Zhang, G. M. Zhang, J. H. Fu, B. Z. Wang, and L. C. Zhou, "Dynamic In-Plane Shear Mechanical Behavior of Carbon Fiber/Epoxy Composite at Different Temperatures," *Mechanics of Composite Materials*, vol. 60, no. 5, pp. 863–874, 11 2024.

[105] J. Lienhard and W. Böhme, "Characterisation of resin transfer moulded composite laminates under high rate tension, compression and shear loading," *Engineering Fracture Mechanics*, vol. 149, pp. 338–350, 11 2015.

[106] N. Zhang, X. Qian, Q. Zhang, G. Zhou, S. Xuan, X. Wang, and D. Cai, "On strain rate effect and high-velocity impact behavior of carbon fiber reinforced laminated composites," *Thin-Walled Structures*, vol. 194, 1 2024.

[107] C. Soutis, "Carbon fiber reinforced plastics in aircraft construction," *Materials Science and Engineering A*, vol. 412, no. 1-2, pp. 171–176, 2005.

[108] M. O. Richardson and M. J. Wisheart, "Review of low-velocity impact properties of composite materials," *Composites Part A: Applied Science and Manufacturing*, vol. 27, no. 12 Part A, pp. 1123–1131, 1996. [Online]. Available: http://dx.doi.org/10.1016/1359-835X(96)00074-7

[109] S. Abrate, "Impact on laminated composites: Recent advances," *Applied Mechanics Reviews*, vol. 47, no. 11, pp. 517–544, 1994.

[110] ——, “Damage in laminates from low-velocity impacts,” in *Dynamic Deformation, Damage and Fracture in Composite Materials and Structures*, 2nd ed., V. Silberschmidt, Ed. Elsevier, 2016, pp. 35–69.

[111] C. Soutis and P. T. Curtis, “Prediction of the post-impact compressive strength of CFRP laminated composites,” *Composites Science and Technology*, vol. 56, no. 6, pp. 677–684, 1996.

[112] Z. Hashin, “Failure Criteria for Unidirectional Fiber Composites,” *Journal of Applied Mechanics*, vol. 47, pp. 329–334, 1980. [Online]. Available: http://www.asme.org/terms/Terms_Use.cfm

[113] Instron, “Drop tower impact testing,” Instron, Tech. Rep., 2020. [Online]. Available: https://www.instron.com/wp-content/uploads/2024/06/POD-Tensile-Impact_v2.pdf

[114] F. Pinto, “Drop tower tensile impact testing for high strain rate measurements,” 2021. [Online]. Available: https://www.instron.com/en/resources/blog/2021/july/drop-tower-tensile-impact-testing-for-high-strain-rate-measurements/

[115] Y. Ou, D. Zhu, H. Zhang, Y. Yao, B. Mobasher, and L. Huang, “Mechanical properties and failure characteristics of CFRP under intermediate strain rates and varying temperatures,” *Composites Part B: Engineering*, vol. 95, pp. 123–136, 6 2016.

[116] Instron, “Instron 9400 series impact drop tower system,” 2020. [Online]. Available: https://www.instron.com/-/media/literature-library/products/2020/02/9400-series-drop-tower-brochure.pdf?la=en

[117] R. W. Rydin, M. B. Bushman, and V. M. Karbhari, “The Influence of Velocity in Low-Velocity Impact Testing of Composites Using the Drop Weight Impact Tower,” *Journal of Reinforced Plastics and Composites*, vol. 14, no. 2, pp. 113–127, 2 1995. [Online]. Available: https://journals.sagepub.com/doi/10.1177/073168449501400202

[118] P. R. Sreenivasan and S. K. Ray, *Encyclopedia of Materials: Science and Technology*, 2nd ed., K.H. Jürgen Buschow, Robert W. Cahn, Merton C. Flemings, and Edward J. Kramer, Eds. Elsevier, 2001. [Online]. Available: https://www.sciencedirect.com/referencework/9780080431529/encyclopedia-of-materials-science-and-technology

[119] W. Chen and B. Song, *Split Hopkinson (Kolsky) Bar*, 1st ed., ser. Mechanical Engineering Series. Boston, MA: Springer US, 2011. [Online]. Available: https://link.springer.com/10.1007/978-1-4419-7982-7

[120] B. Song, K. Connelly, J. Korellis, W. Y. Lu, and B. R. Antoun, "Improved Kolsky-bar design for mechanical characterization of materials at high strain rates," *Measurement Science and Technology*, vol. 20, no. 11, 2009.

[121] D. Casem, "Miniature Kolsky bar Methods," in *Advances in Experimental Impact Mechanics*, Bo Song, Ed. Elsevier, 1 2022, pp. 149–189. [Online]. Available: https://linkinghub.elsevier.com/retrieve/pii/B9780128233252000108

[122] M. May, S. Arnold-Keifer, V. Landersheim, D. Laveuve, C. Contell Asins, and M. Imbert, "Bird strike resistance of a CFRP morphing leading edge," *Composites Part C: Open Access*, vol. 4, 3 2021.

[123] C. Buckley, J. Harding, J. Hou, C. Ruiz, and A. Trojanowski, "Deformation of thermosetting resins at impact rates of strain. Part I: Experimental study," *Journal of the Mechanics and Physics of Solids*, vol. 49, no. 7, pp. 1517–1538, 7 2001.

[124] A. E. Mayr, W. D. Cook, and G. H. Edward, "Yielding behaviour in model epoxy thermosets-I. Effect of strain rate and composition," *Polymer*, vol. 39, no. 16, 1997.

[125] J. I. Perry and S. M. Walley, "Measuring the Effect of Strain Rate on Deformation and Damage in Fibre-Reinforced Composites: A Review," *Journal of Dynamic Behavior of Materials*, vol. 8, no. 2, pp. 178–213, 6 2022.

[126] Y. Zhou, D. Jiang, and Y. Xia, "Tensile mechanical behavior of T300 and M40J fiber bundles at different strain rate," *Journal of Materials Science*, vol. 36, no. 4, pp. 919–922, 2 2001.

[127] Q. Bing and C. T. Sun, "Modeling and testing strain rate-dependent compressive strength of carbon/epoxy composites," *Composites Science and Technology*, vol. 65, no. 15-16 SPEC. ISS., pp. 2481–2491, 12 2005.

[128] H. Al-zubaidy, X. Zhao, and R. Al-mahaidi, "Mechanical characterisation of the dynamic tensile properties of CFRP sheet and adhesive at medium strain rates," *Composite Structures*, vol. 96, pp. 153–164, 2013.

[129] R. M. Guedes, M. F. de Moura, and F. J. Ferreira, “Failure analysis of quasi-isotropic CFRP laminates under high strain rate compression loading,” *Composite Structures*, vol. 84, no. 4, pp. 362–368, 8 2008.

[130] H. Paul, M. Isakov, N. Ledford, S. Nagasawa, and M. May, “Evaluation of the strain rate dependent behavior of a CFRP using two different Hopkinson bars,” *ECCM 2018 - 18th European Conference on Composite Materials*, pp. 24–28, 2020.

[131] Y. Sawamura, Y. Yamazaki, S. Yoneyama, and J. Koyanagi, “Multi-scale numerical simulation of impact failure for cylindrical CFRP,” *Advanced Composite Materials*, vol. 30, no. 1, pp. 19–38, 2020.

[132] K. Gliesche, T. Hübner, and H. Orawetz, “Investigations of in-plane shear properties of ±45° carbon/epoxy composites using tensile testing and optical deformation analysis,” *Composites Science and Technology*, vol. 65, no. 2, pp. 163–171, 2 2005.

[133] F. Liu, L. Grotz, Y. Cui, and K. Kirane, “Experimental dataset on the in-plane tensile, shear, and compressive properties of a carbon-epoxy twill woven composite,” *Data in Brief*, vol. 45, no. 108650, 2022.

[134] H. Koerber, J. Xavier, and P. P. Camanho, “High strain rate characterisation of unidirectional carbon-epoxy IM7-8552 in transverse compression and in-plane shear using digital image correlation,” *Mechanics of Materials*, vol. 42, no. 11, pp. 1004–1019, 11 2010.

[135] J. López-Puente and S. Li, “Analysis of strain rate sensitivity of carbon/epoxy woven composites,” *International Journal of Impact Engineering*, vol. 48, pp. 54–64, 10 2012.

[136] W. Tan and B. Liu, “A physically-based constitutive model for the shear-dominated response and strain rate effect of carbon fibre reinforced composites,” *Composites Part B: Engineering*, vol. 193, 7 2020.

[137] M. Santos and J. Santos, “Ultrasonic C-scan techniques for the evaluation of impact damage in CFRP,” *Materialprüfung*, vol. 63, no. 2, pp. 131–37, 2021.

[138] C. Garnier, M.-l. Pastor, F. Eyma, and B. Lorrain, “The detection of aeronautical defects in situ on composite structures using Non Destructive Testing,” *Composite Structures*, vol. 93, no. 5, pp. 1328–1336, 2011.

[139] M. Cuartas, P. Marie-laetitia, W. Hélène, C. Arthur, and K. Moussa, “Application of non destructive testing to the detection of aeronautical defects in composite structure,” in *Nonconventional Technologies*, 2013. [Online]. Available: https://hal.science/hal-02285220v1

[140] I. K. Giannopoulos, M. Yasaee, and N. Maropakis, “Ballistic impact and virtual testing of woven frp laminates,” *Journal of Composites Science*, vol. 5, no. 5, 5 2021.

[141] F. Léonard, J. Stein, C. Soutis, and P. J. Withers, “The quantification of impact damage distribution in composite laminates by analysis of X-ray computed tomograms,” *Composites Science and Technology*, vol. 152, no. 2017, pp. 139–148, 2017.

[142] D. J. Bull, L. Helfen, I. Sinclair, S. M. Spearing, and T. Baumbach, “A comparison of multi-scale 3D X-ray tomographic inspection techniques for assessing carbon fibre composite impact damage,” *Composites Science and Technology*, vol. 75, pp. 55–61, 2013.

[143] J. Xiao, Z. Wu, Z. Pan, W. Ouyang, and L. Shi, “Analysis of in-plane compression failure mechanism in carbon fiber braided composite with different off-axial angles,” *Journal of Composite Materials*, vol. 56, no. 13, pp. 2029–2046, 6 2022. [Online]. Available: https://journals.sagepub.com/doi/10.1177/00219983221077485

[144] J. Als-Nielsen and D. McMorrow, *Elements of Modern X-ray Physics*, 2nd ed. Chichester, West Sussex: Wiley, 3 2011. [Online]. Available: https://onlinelibrary.wiley.com/doi/book/10.1002/9781119998365

[145] C. A. MacDonald, *An introduction to X-ray physics, optics, and applications*, C. A. MacDonald, Ed. Princeton: Princeton University Press, 2017. [Online]. Available: https://assets.press.princeton.edu/chapters/s11052.pdf

[146] S. D. Auweter, J. Herzen, M. Willner, S. Grandl, K. Scherer, F. Bamberg, M. F. Reiser, F. Pfeiffer, and K. Hellerhoff, “X-ray phase-contrast imaging of the breast - Advances towards clinical implementation,” *British Journal of Radiology*, vol. 87, no. 1034, 2014.

[147] X. Sun, D. Sory, K. Liu, B. Lukić, D. Simonian, K. L. Wong, A. Rack, D. Chapman, N. Petrinic, and D. Eakins, “Effect of temperature on high strain-rate damage evolving in CFRP studied by synchrotron-based MHz X-ray phase contrast imaging,” *Composites Part B: Engineering*, vol. 279, 6 2024.

[148] Q. B. Dou, K. R. Wu, T. Suo, C. Z. X. Guo, Y. Z. Guo, W. G. Guo, and Y. L. Li, "Experimental methods for determination of mechanical behaviors of materials at high temperatures via the split Hopkinson bars," *Acta Mechanica Sinica*, vol. 36, pp. 1275–1293, 2020.

[149] Y. Nie, N. D. Parab, J.-m. Chu, G. Kim, T. Sun, K. Fezzaa, R. Sterkenburg, and W. W. Chen, "Dynamic crack propagation from a circular defect in a unidirectional carbon fiber reinforced plastic composite," *Journal of Composite Materials*, vol. 52, no. 25, p. 3539–3547, 2018.

[150] N. D. Parab, J. T. Black, B. Claus, M. Hudspeth, J. Sun, K. Fezzaa, and W. W. Chen, "Observation of Crack Propagation in Glass Using X-ray Phase Contrast Imaging," *International Journal of Applied Glass Science*, vol. 5, no. 4, pp. 363–373, 12 2014.

[151] A. Cohen, D. Levi-Hevroni, P. Fridman, D. Chapman, A. Rack, M. P. Olbinado, A. Yosef-Hai, and D. Eakins, "In-situ radiography of a split-Hopkinson bar dynamically loaded materials," *Journal of Instrumentation*, vol. 14, no. 6, 2019.

[152] A. Rack, M. Scheel, L. Hardy, C. Curfs, A. Bonnin, and H. Reichert, "Exploiting coherence for real-time studies by single-bunch imaging," *Journal of Synchrotron Radiation*, vol. 21, no. 4, pp. 815–818, 2014.

[153] E. M. Escauriza, J. P. Duarte, D. J. Chapman, M. E. Rutherford, L. Farbaniec, J. C. Jonsson, L. C. Smith, M. P. Olbinado, J. Skidmore, P. Foster, T. Ringrose, A. Rack, and D. E. Eakins, "Collapse dynamics of spherical cavities in a solid under shock loading," *Scientific Reports*, vol. 10, no. 1, pp. 1–16, 2020.

[154] D. E. Eakins and D. J. Chapman, "X-ray imaging of subsurface dynamics in high-Z materials at the Diamond Light Source," *Review of Scientific Instruments*, vol. 85, no. 12, 2014.

[155] E. M. Escauriza, M. P. Olbinado, M. E. Rutherford, D. J. Chapman, J. C. Z. Jonsson, A. Rack, and D. E. Eakins, "Ultra-high-speed indirect x-ray imaging system with versatile spatiotemporal sampling capabilities," *Applied Optics*, vol. 57, no. 18, p. 5004, 2018.

[156] A. Jadhav, E. Woldesenbet, and S. S. Pang, “High strain rate properties of balanced angle-ply graphite/epoxy composites,” *Composites Part B: Engineering*, vol. 34, no. 4, pp. 339–346, 6 2003.

[157] H. Raza, O. Rodera, K. Carpenter, T. Pärnänen, J. Jokinen, M. Kanerva, and J. Bayandor, “Predictive methods for initiation of delamination and intra-laminar damage in carbon fibre reinforced polymer laminates subject to impact,” *Aeronautical Journal*, vol. 128, no. 1323, pp. 846–874, 5 2024.

[158] D. Ivančević, J. Ratković, and E. Giannaros, “Strain rate-dependent failure modelling of impact damage in laminated CFRP structures,” *Composite Structures*, vol. 330, 2 2024.

[159] N. Pournoori, G. Corrêa Soares, B. Lukić, M. Isakov, M. C. L. Belone, M. Hokka, and M. Kanerva, “In situ damage characterization of CFRP under compression using high-speed optical, infrared and synchrotron X-ray phase-contrast imaging,” *Composites Part A: Applied Science and Manufacturing*, vol. 175, 12 2023.

[160] S. Li, D. Chen, Y. Yuan, C. Gao, Y. Cui, H. Wang, X. Liu, M. Liu, and Z. Wu, “Influence of flexible molecular structure on the cryogenic mechanical properties of epoxy matrix and carbon fiber/epoxy composite laminate,” *Materials and Design*, vol. 195, 10 2020.

[161] R. Ruiz-Iglesias, R. Cappello, O. T. Thomsen, and J. M. Dulieu-Barton, “Estimating the coefficients of thermal expansion of carbon fibre composite materials using infrared thermography,” *Composites Part A: Applied Science and Manufacturing*, vol. 198, 11 2025.

[162] Y. Li, J. Meng, J. Luo, P. Wang, J. Ma, Z. Zhao, and H. Lei, “Cryogenic mechanics and damage behaviors of carbon fiber reinforced polymer composites,” *Composites Part A: Applied Science and Manufacturing*, vol. 169, 6 2023.

[163] J. Chen, B. Li, B. Gu, and B. Sun, “Molecular dynamics insights into temperature-dependent interfacial properties and failure behaviors of carbon fiber/epoxy composites,” *Composite Structures*, vol. 374, 12 2025.

[164] C. Soutis and D. Turkmen, “Moisture and Temperature Effects of the Compressive Failure of CFRP Unidirectional Laminates,” *Journal of Composite Materials*, vol. 31,

no. 8, pp. 832–849, 4 1997. [Online]. Available: https://journals.sagepub.com/doi/10.1177/002199839703100805

[165] J. Körbelin, N. Junge, and B. Fiedler, “Modelling of low-velocity impact and compression after impact of CFRP at elevated temperatures,” *Composites Part A: Applied Science and Manufacturing*, vol. 147, 8 2021.

[166] T. Gómez-del Río, E. Barbero, R. Zaera, and C. Navarro, “Dynamic tensile behaviour at low temperature of CFRP using a split Hopkinson pressure bar,” *Composites Science and Technology*, vol. 65, no. 1, pp. 61–71, 1 2005.

[167] M. Castres, J. Berthe, E. Deletombe, and M. Brieu, “Experimental evaluation of the elastic limit of carbon-fibre reinforced epoxy composites under a large range of strain rate and temperature conditions,” *Strain*, vol. 53, no. 6, 12 2017.

[168] Z. Jia, T. Li, F.-p. Chiang, and L. Wang, “An experimental investigation of the temperature effect on the mechanics of carbon fiber reinforced polymer composites,” *Composites Science and Technology*, vol. 154, pp. 53–63, 1 2018.

[169] J. Meng, Y. Wang, H. Yang, P. Wang, Q. Lei, H. Shi, H. Lei, and D. Fang, “Mechanical properties and internal microdefects evolution of carbon fiber reinforced polymer composites: Cryogenic temperature and thermocycling effects,” *Composites Science and Technology*, vol. 191, 5 2020.

[170] M. S. Islam, E. Melendez-Soto, A. G. Castellanos, and P. Prabhakar, “Investigation of woven composites as potential cryogenic tank materials,” *Cryogenics*, vol. 72, pp. 82–89, 12 2015.

[171] S. Morkavuk, U. Köklü, M. Bağcı, and L. Gemi, “Cryogenic machining of carbon fiber reinforced plastic (CFRP) composites and the effects of cryogenic treatment on tensile properties: A comparative study,” *Composites Part B: Engineering*, vol. 147, pp. 1–11, 8 2018.

[172] L. Yang, Z. Li, H. Xu, and Z. Wu, “Prediction on residual stresses of carbon/epoxy composite at cryogenic temperature,” *Polymer Composites*, vol. 40, no. 9, pp. 3412–3420, 9 2019.

[173] M. Di Ludovico, F. Piscitelli, A. Prota, M. Lavorgna, G. Mensitieri, and G. Manfredi, "Improved mechanical properties of CFRP laminates at elevated temperatures and freeze-thaw cycling," *Construction and Building Materials*, vol. 31, pp. 273–283, 6 2012.

[174] ASTM International, "D5229/D5229M – Test Method for Moisture Absorption Properties and Equilibrium Conditioning of Polymer Matrix Composite Materials," American Society for Testing and Materials, West Conshohocken, PA, Tech. Rep., 3 2020. [Online]. Available: https://store.astm.org/d5229_d5229m-20.html?_gl=1*1phveww*_gcl_au*ODc2MzkzMzIuMTc3NzgwMjY1NA

[175] G. Gray, "Classic Split-Hopkinson Pressure Bar Testing," *ASM Handbook*, vol. 8, 2000. [Online]. Available: www.asminternational.org

[176] X. Sun, B. Lukić, K. Liu, D. Sory, M. Lißner, J. Hoffmann, D. Chapman, N. Petrinic, and D. Eakins, "Role of temperature in the development of micro-scale damage in CFRP laminates through interrupted high-rate loading and synchrotron phase-contrast μ-CT," *Composites Part A: Applied Science and Manufacturing*, vol. 200, p. 109284, 1 2026.

[177] E. Maire and P. J. Withers, "Quantitative X-ray tomography," *International Materials Reviews*, vol. 59, no. 1, pp. 1–43, 1 2014.

[178] Z. P. Bazant, I. M. Daniel, and Z. Li, "Size Effect and Fracture Characteristics of Composite Laminates," *Journal of Engineering Materials and Technology*, vol. 118, no. 3, pp. 317–324, 7 1996.

[179] K. Umetani, T. Okamoto, K. Saito, Y. Kawata, and N. Niki, "36M-pixel synchrotron radiation micro-CT for whole secondary pulmonary lobule visualization from a large human lung specimen," *European Journal of Radiology Open*, vol. 7, 1 2020.

[180] J. D. Ferry, *Viscoelastic properties of polymers*, 3rd ed., J. D. Ferry, Ed. Wiley, 1980. [Online]. Available: https://pearl-hifi.com/06_Lit_Archive/14_Books_Tech_Papers/Ferry_John/Viscoelastic_Properties_of_Polymers_Ferry_3rd_Edn.pdf

[181] K. S. Khare and F. R. Phelan, "Integration of Atomistic Simulation with Experiment Using Time-Temperature Superposition for a Cross-Linked Epoxy Network," *Macromolecular Theory and Simulations*, vol. 29, no. 2, 3 2020.

[182] L. Q. Reyes, S. R. Swan, H. Gan, S. M. Seraji, J. Zhang, and R. J. Varley, "The role of β relaxations in determining the compressive properties of an epoxy amine network modified with POSS and mono-functional epoxy resins," *Polymer Testing*, vol. 93, 1 2021.

[183] H. Zhang, L. Yang, S. Ren, K. Wang, and J. Li, "In-situ experimental characterization and numerical investigation of the crack initiation of SMC composite under uniaxial tension," *Composites Part A: Applied Science and Manufacturing*, vol. 188, 1 2025.

[184] T. J. Pirzada, D. Liu, J. Ell, H. Barnard, I. Šulák, M. Galano, T. J. Marrow, and R. O. Ritchie, "In situ observation of the deformation and fracture of an alumina-alumina ceramic-matrix composite at elevated temperature using x-ray computed tomography," *Journal of the European Ceramic Society*, vol. 41, no. 7, pp. 4217–4230, 7 2021.

[185] C. Kuang, S. Ghosh, and A. Michel, "Enhanced detection of fine damage in composite materials using integrated X-ray computed tomography, digital volume correlation, and U-Net," *Journal of Building Engineering*, vol. 98, 12 2024.

[186] L. Jiang, H. Xiong, T. Zeng, J. Wang, S. Xiao, and L. Yang, "In-situ micro-CT damage analysis of carbon and carbon/glass hybrid laminates under tensile loading by image reconstruction and DVC technology," *Composites Part A: Applied Science and Manufacturing*, vol. 176, 1 2024.

[187] S. Hong, Z. Yuan, D. Pan, C. Kuang, B. Dong, and S. Fan, "Digital-volume-correlation-assisted crack extraction using X-ray computed tomography images of cementitious materials," *Cement and Concrete Composites*, vol. 158, 4 2025.

[188] Y. Wang, Q. Chen, Q. Luo, Q. Li, and G. Sun, "Characterizing damage evolution in fiber reinforced composites using in-situ X-ray computed tomography, deep machine learning and digital volume correlation (DVC)," *Composites Science and Technology*, vol. 254, 7 2024.

[189] S. Lee, E. Jo, and W. Ji, "Digital volume correlation technique for characterizing subsurface deformation behavior of a laminated composite," *Composites Part B: Engineering*, vol. 194, 8 2020.

[190] M. Mehdikhani, C. Breite, Y. Swolfs, J. Soete, M. Wevers, S. V. Lomov, and L. Gorbatikh, “Digital volume correlation for meso/micro in-situ damage analysis in carbon fiber reinforced composites,” *Composites Science and Technology*, vol. 213, 9 2021.

[191] P. Bhagoria, M. R. Bharadwaj, R. Kumar, K. Yadav, and V. Tiwari, “Mechanical and fracture behaviour of epoxy polymer under extreme low temperature and high strain rate conditions,” *International Journal of Adhesion and Adhesives*, vol. 140, 6 2025.

[192] Z. Xia, X. Shen, and F. Ellyin, “An assessment of nonlinearly viscoelastic constitutive models for cyclic loading: The effect of a general loading/unloading rule,” *Mechanics of Time-Dependent Materials*, vol. 9, no. 4, pp. 281–300, 2005.

[193] O. Starkova, S. T. Buschhorn, E. Mannov, K. Schulte, and A. Aniskevich, “Creep and recovery of epoxy/MWCNT nanocomposites,” *Composites Part A: Applied Science and Manufacturing*, vol. 43, no. 8, pp. 1212–1218, 8 2012.

[194] D. J. Plazek, “The Temperature Dependence of the Viscoelastic Behavior of Poly(vinyl acetate),” *Polymer Journal*, vol. 12, no. 1, pp. 43–53, 1 1980. [Online]. Available: https://www.nature.com/doifinder/10.1295/polymj.12.43

[195] J. C. Griffith, S. Wang, D. R. Palubiski, K. R. Ramakrishnan, S. Rochat, F. Giuliani, M. Walls-Bruck, and I. Hamerton, “Investigating the microcracking behaviour of a commercial epoxy matrix under cryogenic conditions,” *Composites Part A: Applied Science and Manufacturing*, vol. 199, 12 2025.

[196] X. Sun, B. Lukić, Y. Chen, Z. Xu, D. Chapman, and D. Eakins, “3D micro-mechanics of a CFRP laminate under high-rate and varying temperature loading using digital volume correlation,” *Composites Part B: Engineering*, vol. 321, p. 113693, 7 2026.

[197] M. C. Serna Moreno and S. Horta Muñoz, “Pseudo-ductile effects in ±45° angle-ply CFRP laminates under uniaxial loading: Compression and cyclic tensile test,” *Composites Part B: Engineering*, vol. 233, 3 2022.